

AFC512-TR 97-0439

**Final Technical Report  
for  
Mechanics of Widespread Fatigue Damage  
&  
Life Enhancement Methodologies  
for  
Aging Aerospace Structures**

Georgia Tech Grant Number B-15-F43

United States Air Force Contract Number:  
F49620-93-1-0270

Sponsored by:  
United States Air Force  
Air Force Office of Scientific Research  
110 Duncan Avenue, Suite B115  
Bolling Air Force Base, DC 20332-5113

Principal Investigator: Satya N. Atluri

Georgia Institute of Technology  
Computational Mechanics Center  
Room 225 French Building  
Atlanta, GA 30332-0356

**DISTRIBUTION STATEMENT A**

Approved for public release  
Distribution Unlimited

May 1997

QUALITY INSPECTED 3

19971003 046

Approved for  
distribution

AIR FORCE OFFICE OF SCIENTIFIC RESEARCH (AFOSR)  
NOTICE OF THE  
THIS TECHNICAL REPORT IS  
APPROVED FOR  
DISTRIBUTION  
AND IS  
DISTRIBUTED  
STANDARD  
21-001 AFOSR-97-0439

REPORT DOCUMENTATION PAGE			Form Approved OMB No. 0704-0188	
<small>Public reporting burden for this collection of information is estimated to average 1 hour per response, including the time for reviewing instructions, searching existing data sources, gathering and maintaining the data needed, and completing and reviewing the collection of information. Send comments regarding this burden estimate or any other aspect of this collection of information, including suggestions for reducing this burden, to Washington Headquarters Services, Directorate for Information Operations and Reports, 1215 Jefferson Davis Highway, Suite 1204, Arlington, VA 22202-4302, and to the Office of Management and Budget, Paperwork Reduction Project (0704-0188), Washington, DC 20503.</small>				
1. AGENCY USE ONLY (Leave blank)		2. REPORT DATE May 1997		3. REPORT TYPE AND DATES COVERED final Technical Report 4-15-93 to 12-14-96
4. TITLE AND SUBTITLE "Mechanics of wide-spread Fatigue Damage & Life Enrichment Methodologies for Aging Aerospace Structures"			5. FUNDING NUMBERS F49620-93-1-0270	
6. AUTHOR(S) Dr. Satya Atluri				
7. PERFORMING ORGANIZATION NAME(S) AND ADDRESS(ES) Georgia Institute of Technology Computational Mechanics Center Room 225, French Building			8. PERFORMING ORGANIZATION REPORT NUMBER  3	
9. SPONSORING/MONITORING AGENCY NAME(S) AND ADDRESS(ES) Air Force Office of Scientific Research, NA 110 Duncan Ave, Suite B 115 Bolling AFB, DC 20332-8050			10. SPONSORING/MONITORING AGENCY REPORT NUMBER	
11. SUPPLEMENTARY NOTES				
12a. DISTRIBUTION AVAILABILITY STATEMENT  Approved for public release; distribution unlimited.			12b. DISTRIBUTION CODE	
13. ABSTRACT (Maximum 200 words)  The major aircraft structural situation considered in this research is that of a thin skin stiffened by orthogonal frames and stringers, with the possibility of a lap joint. Effects on this situation considered in this research are: (1) impact by foreign objects, (2) fatigue damage due to repetitive loading, and (3) corrosion damage. Various theoretical models, pertaining to the response of the subject aircraft structure to these effects, have been considered: (1) the Finite Element Alternating Method (FEAM) applied to a single crack, (2) FEAM applied to Multiple Site Damage (MSD), and others. An analysis is also presented which pertains to the repair of cracks by application of a composite patch using adhesive.				
14. SUBJECT TERMS			15. NUMBER OF PAGES	
			16. PRICE CODE	
17. SECURITY CLASSIFICATION OF REPORT  Unclassified	18. SECURITY CLASSIFICATION OF THIS PAGE  Unclassified	19. SECURITY CLASSIFICATION OF ABSTRACT  Unclassified	20. LIMITATION OF ABSTRACT  UL	

# TABLE OF CONTENTS

<b>CHAPTER</b>	<b>1</b>
<b>I Damage Tolerance, Integrity, and Durability of Built-up Metallic Structures</b>	<b>1</b>
§ 1.1 The Displacement Compatibility Method . . . . .	4
§ 1.1.1 Sheet displacements . . . . .	5
§ 1.1.2 Stiffener displacements . . . . .	11
§ 1.1.3 Fastener displacements . . . . .	13
§ 1.1.4 Compatibility of displacements . . . . .	13
§ 1.1.5 Crack-tip stress intensity factor . . . . .	16
§ 1.1.6 Summary . . . . .	17
§ 1.2 The FEAM for a Cracked Stiffened Panel . . . . .	18
§ 1.2.1 A hierarchical methodology and the FEAM . . . . .	18
§ 1.2.2 Details of extracting the isolated skin model . . . . .	23
§ 1.2.3 Numerical examples . . . . .	27
§ 1.3 Residual Strength of Aircraft Structures with a Single Dominant Flaw (Discrete Source Damage) . . . . .	32
§ 1.3.1 Introduction . . . . .	32
§ 1.3.2 Computational models . . . . .	36
§ 1.3.3 Single dominant multi-bay crack in the skin . . . . .	40
§ 1.3.4 Two-bay crack with holes near the crack tip . . . . .	42
§ 1.3.5 Long crack and MSD in lap splice . . . . .	44
§ 1.3.6 Two-bay cracking at lap splice . . . . .	56
§ 1.4 Residual Strength of Aircraft Structures under Discrete Source Damage: Use of Elastic-Plastic Fracture Mechanics . . . . .	58
§ 1.4.1 Automated evaluation of residual strength in the presence of widespread fatigue damage . . . . .	62
§ 1.4.2 Two-bay longitudinal cracks at various locations . . . . .	69
§ 1.4.3 Interaction of multiple longitudinal cracks . . . . .	71
§ 1.4.4 Circumferential cracks . . . . .	74
§ 1.5 Widespread Fatigue Damage Threshold . . . . .	87
§ 1.5.1 Residual strength analyses . . . . .	88
§ 1.5.2 Fatigue crack growth analyses . . . . .	93
§ 1.5.3 Conclusions . . . . .	95

§ 1.6	Degradation of Residual Strength in the Presence of MSD: Stable Tearing Analyses . . . . .	97
§ 1.6.1	Prediction methodology . . . . .	98
§ 1.6.2	NIST multiple site damage experiments . . . . .	101
§ 1.6.3	Resistance curve calculation - generation phase . . . . .	104
§ 1.6.4	Prediction of single crack tests - application phase (1) . . . . .	110
§ 1.6.5	Prediction of MSD tests - application phase (2) . . . . .	112
§ 1.6.6	Conclusions . . . . .	131
§ 1.7	Crack-Bulging in a Pressurized Aircraft Fuselage: Large Deformation Analyses . . . . .	132
§ 1.7.1	Introduction . . . . .	132
§ 1.7.2	Computational models . . . . .	135
§ 1.7.3	Numerical results . . . . .	137
§ 1.8	Fatigue Life Estimation & Linkup of MSD Cracks Due to Fatigue: Generic Methodology and Illustrative Examples . . . . .	148
§ 1.8.1	Introduction . . . . .	148
§ 1.8.2	Multiple-site-damage near a row of fastener-holes in a bonded fuselage-lap-joint: A Model Problem . . . . .	150
§ 1.8.3	Analysis of load transfer through fastener and adhesive bonding in a fuselage lap-splice joint . . . . .	158
§ 1.8.4	The finite element alternating method for MSD near a row of fastener holes . . . . .	159
§ 1.8.5	Multiple site damage near a row of fastener holes . . . . .	161
§ 1.8.6	Effect of residual stresses in the fastener hole . . . . .	165
§ 1.9	Growth of Multiple Cracks and Their Linkup in a Fuselage Lap Joint: A Realistic Aircraft Structure . . . . .	174
§ 1.9.1	Problem definition . . . . .	176
§ 1.9.2	Analytical approach . . . . .	179
§ 1.9.3	Results and observations . . . . .	182
§ 1.10	Prediction of Fatigue Crack Growth and Linkup for a Full Scale Curved Stiffened Panel . . . . .	194
§ 1.10.1	Foster-Miller curved panel test . . . . .	194
§ 1.10.2	Computational models . . . . .	196
§ 1.10.3	Fatigue crack growth analysis . . . . .	199
§ 1.10.4	Results and discussions . . . . .	201
§ 1.11	Residual Life and Strength Estimates of Aircraft Structural Components with <i>MSD/MED</i> . . . . .	203
§ 1.11.1	Computational framework . . . . .	205
§ 1.11.2	An example computation: <i>MSD/MED</i> at a frame stringer junction . . . . .	207
§ 1.12	Fatigue Growth of Surface Flaws . . . . .	213



§ 1.12.1	Introduction . . . . .	213
§ 1.12.2	Cracks emanating from rivet holes . . . . .	217
§ 1.12.3	Fatigue crack growth . . . . .	219
§ 1.12.4	Variable amplitude loading . . . . .	224
§ 1.12.5	Discussion . . . . .	232
§ 1.13	Composite Patch Repair Technology . . . . .	234
§ 1.13.1	Repair of center or edge cracks in unstiffened panels . .	235
§ 1.13.2	Repair of cracks near loaded fastener holes in a lap joint	251
§ 1.13.3	Three-dimensional analysis of surface-flaws with and with- out repairs . . . . .	263
§ 1.14	Analysis of Repaired Cracks in Pressurized Aircraft Fuselages .	274
§ 1.14.1	Methodology . . . . .	279
§ 1.14.2	Analysis of repaired cracks . . . . .	282
§ 1.14.3	Effects of Adhesive Nonlinearity, thermal Cycling & Debond- ing . . . . .	298
§ 1.15	Fracture and Fatigue Analysis of Curved or Kinked Cracks Near Fastener Holes . . . . .	318
§ 1.15.1	A computational model . . . . .	320
§ 1.15.2	Conclusion . . . . .	328
§ 1.16	Interaction of Engine Rotor Fragments with Containment Struc- tures . . . . .	328
§ 1.17	Finite Element Analysis of Engine Rotor Failure and Containment	328
§ 1.17.1	Introduction . . . . .	329
§ 1.17.2	The engine casing impacted by a single rigid blade . . .	334
§ 1.17.3	Interaction among two blades and the casing . . . . .	338
§ 1.17.4	Interaction between a single blade and the containment ring	339
§ 1.17.5	Interaction among a single blade fragment, containment ring and other rotor blades . . . . .	340
§ 1.17.6	Interaction between a three bladed fragment and the con- tainment ring . . . . .	345
§ 1.17.7	Interaction among a three bladed fragment, containment ring and the other rotor blades . . . . .	345
§ 1.17.8	Tri-hub rotor burst failure . . . . .	351
§ 1.17.9	Conclusions . . . . .	352

## CHAPTER I

### DAMAGE TOLERANCE, INTEGRITY, AND DURABILITY OF BUILT-UP METALLIC STRUCTURES

In this chapter, we discuss the damage tolerance, integrity, and durability of metallic built-up structures. While the methodologies presented are generic in nature, for illustration purpose, the discussion is focused in stiffened aircraft structures. In a typical commercial aircraft, the fuselage is made of a thin skin that is stiffened by frames and stringers; and the skin is attached to these stiffening elements through flexible fasteners. Also, a lap joint along the longitudinal direction may exist when the lower skin and the upper skin overlap. A typical construction is illustrated in Fig. 1.1. Typical damage scenarios in which an aircraft is expected

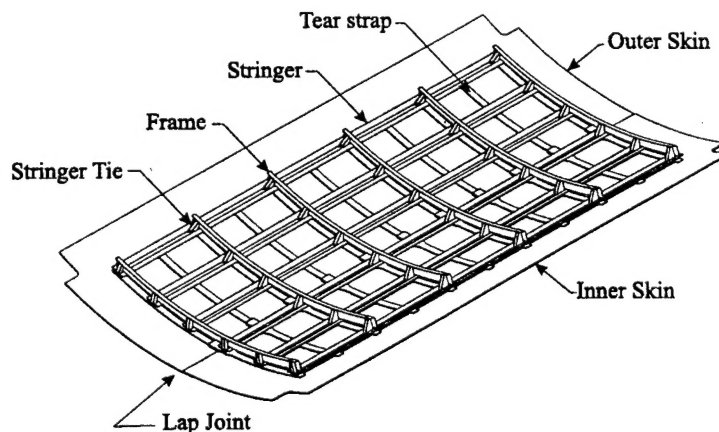


Figure 1.1: A typical construction of a commercial aircraft

to retain its structural integrity are: impact by foreign objects or fragments of a disintegrated engine; fatigue damages due to repetitive loadings; corrosion damages, etc. In a typical damage tolerance analysis, damages are modeled as cracks, either in the longitudinal direction or in the circumferential direction. Due to the

internal cabin pressure, a typical aircraft panel is subjected to circumferential loading as well as longitudinal (axial) loading. In addition to the internal cabin pressure, the fuselage bending in the longitudinal direction can induce a significant axial loading on the aircraft panel. To determine the damage tolerance capability of an aircraft and to assess the integrity of the damaged aircraft, the reduction in the load-carrying capacity of an aircraft due to the presence of cracks must be assessed.

Due to the complexity of the aircraft structure, it is impossible to analyze the entire aircraft in detail in a single numerical analysis. Thus, a hierarchical analysis approach is required. In a hierarchical analysis, a global analysis is first performed to obtain the load flow in the aircraft fuselage; at that stage, the details of the structure are greatly simplified. Stringers and frames can be modeled as beams; rivets can be modeled as shear springs, etc. Based on the results of the global analysis, a detailed local model can be constructed to study more accurately the local details near the damage. The "global-local" methodology is a generic computational tool to assess the structural integrity and durability of complex engineering structures.

In assessing the structural integrity of cracked fuselage panels, especially in the presence of multiple-site-damage, an accurate evaluation of the stress-intensity factors (or other fracture parameters), is required. If the ordinary finite element method is used for such purposes, especially in linear elastic fracture, proper numerical modeling of the crack-tip singularities is necessary [Atluri (1986)]. Even if indirect methods such as the "stiffness-derivative approach" or the "equivalent domain integral approach" are used, the relatively fine meshes needed near the crack-tips make the computation prohibitively expensive, especially in the case of complex geometrical shapes of fuselage structures with stringers, stiffeners and lap joints, etc., and with multiple cracks. In order to circumvent these difficulties, alternative computational strategies are mandatory. One such novel alternative scheme is the so-called "displacement-compatibility-method" (DCM), developed some twenty years ago by Swift (1974, 1984). It is based on the classical redundant force method [or "Flexibility Matrix" method] for statically indeterminate structures, as developed by Argyris and Kelsey in the 1950's. In this scheme, the effects of stiffeners, and flexible fasteners, attached to the skin were taken into account through the displacement compatibility conditions, and a linear-superposition principle. Since Swift used analytical solutions for displacement fields only for an infinite cracked panel, the method is anti-conservative in the case of finite-sized panels (or when the ratio of crack size to panel size is not very small). It is also difficult to generalize the DCM method to the case of multiple cracks of arbitrary size and at arbitrary locations in the panel, or to account for geometric and material nonlinearities.

To circumvent these difficulties and shortcomings in the analysis of multiple cracks [multi-site-damage in the presence of a lead-crack] in finite-sized flat stiffened panels, a "finite element/alternating method" (FEAM) [which is based on the more common finite element stiffness method] is preferable. In this method, a very coarse finite element mesh is first used to compute the reactions of the fasteners (used to fasten the stringers and stiffeners) on the sheet, while accounting for broken stiffeners, if any, as well as the broken ligaments of the crack; but ignoring the detailed stress-state near the crack-tip. In this way, the free-body diagram of the cracked sheet alone may be constructed, with the applied loading on the sheet being the fastener reactions as well as the external loading. The "alternating method" (described in Chapter III) is then used to compute the stress-intensity factors for the (multiply-) cracked sheet, while still using the same very coarse finite element grid. In this way, one can dramatically reduce the computational time as well as the data preparation time, as compared to the conventional finite element stiffness method or the "flexibility matrix" based DCM method. Furthermore, the FEAM is ideally suited for analyzing the multiple-site-damage (MSD) situation (including plasticity effects), as in the case of cracks emanating from a row of fastener holes in a lap-joint in a fuselage.

In order to enhance the life of damaged engineering structures in general, and cracked aging aircraft structures in particular, the repair technique which uses adhesively bonded Boron/epoxy composite patches is being widely considered as a cost-effective and reliable method [Baker and Jones (1988)]. For a successful implementation of this repair technique, however, a thorough understanding of the effect of various design parameters of repair, on the crack-tip stress intensity factors, is necessary. These design parameters include: the size, thickness and material properties of the composite patch, and the mechanical properties and thickness of the adhesive layer. Other issues that must be understood for a successful implementation of composite patch repairs include: (i) the effect of adhesive nonlinearity; (ii) the effects of residual stresses in the metal panel due to elevated temperature curing of the patch; (iii) the effect of thermal cycling (ground to flight altitude) on the fatigue growth of the patched crack; (iv) the effect of interaction of multiple patches; (v) the effect of debonding of the patch, on the fatigue growth of the underlying crack, etc. Early work in this area includes that by Greif and Sanders (1965); Arin (1974) who considered the effect of a single stringer that is used to reinforce the crack; and those by Erdogan and Arin (1972); Atluri and Kathiresan (1978); Jones and Callinan (1979); Rose (1981); Kan and Ratwani (1981); Sethuraman and Maiti (1989), using finite element methods or semi-analytical methods. In most of these

cases, only patches of infinite size, or very narrow strip type patches, are considered. Furthermore, the ensemble of results presented in the above references is still not sufficient for rational design purposes. A detailed general methodology for analyzing the effects of composite patches applied to cracked metallic structures was presented recently by Park, Ogiso, and Atluri (1992); Nagaswamy, Pipkins, and Atluri (1996); and Chow and Atluri (1997). These approaches will be discussed later in this chapter.

### § 1.1 The Displacement Compatibility Method

In a stiffened panel, the far-field applied load is transmitted to the sheet in a complex way. The stiffeners and the fasteners (both of which are flexible) exert tractions on the sheet. Thus, the stress intensity factor at the tip of a crack in the sheet depends on these tractions exerted on the sheet by the fasteners. Swift (1974) developed a "flexibility matrix" approach to determine the fastener tractions exerted on the sheet. Since this method has its root in the classical "redundant force method", it is generally known as the "Displacement Compatibility Method" (DCM).

The "redundant force method" was first introduced in the area of aircraft structural analysis, by Argyris and Kelsey in the 1950's. In this approach, which is used to analyse statically indeterminate structures, the redundant forces are first removed from the system. Their magnitudes are later determined by enforcing the condition of compatibility of displacement [hence the name "Displacement Compatibility Method"] at the points where the redundant forces act. This leads to a "flexibility matrix equation" (which is linear for linear structural mechanics) from which the redundant force vector is solved for.

In the Displacement Compatibility Method, displacements in the cracked sheet at each fastener location are made compatible with those in the stiffening elements, taking full account of stiffener bending and fastener shear flexibility. The "redundant force method" (and hence the DCM) is a dual to the now standard finite element displacement method which leads to a "stiffness matrix equation" (which is linear for linear structural mechanics) from which nodal displacements are solved for. Thus, it is worthwhile to remark here that while Swift (1984)'s DCM is based on a "flexibility matrix approach", the Finite Element Alternating Method (FEAM) to be described subsequently is based on a "stiffness matrix" approach. It is for this reason, that FEAM can be far more easily implemented in a global/local strategy, using the currently available commercial software, which are, without exception, based on the finite element stiffness method.

The following development of DCM is due to Swift (1984).

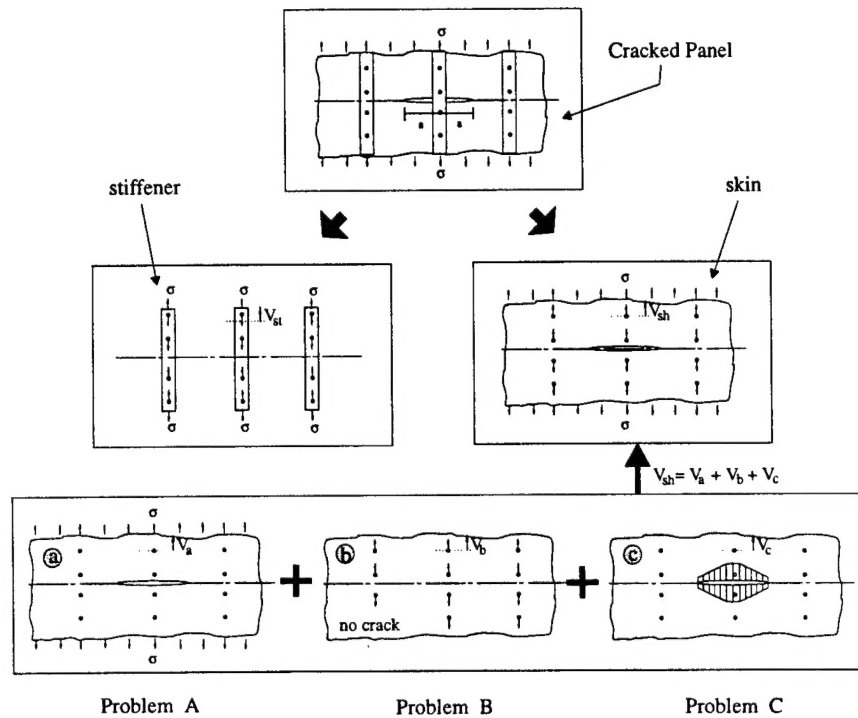


Figure 1.2: Displacement Compatibility Method (DCM)

### § 1.1.1 Sheet displacements

For the two bay crack with a broken central stiffener, the displacements in the cracked sheet,  $v_{sh}$ , are obtained by a superposition of the three cases shown in Fig. 1.2. The displacements resulting from these three cases are

1.  $V_a$ , the displacement in the infinite cracked sheet due to the applied gross stress  $\sigma$  [see Problem A in Fig. 1.2];
2.  $V_b$ , the displacement in the uncracked infinite sheet due to all the stiffener fastener loads [see Problem B in Fig. 1.2]; and
3.  $V_c$ , the displacements in the infinite cracked sheet, due to a traction applied on the crack face, which is equal and opposite to the traction at the location

of the crack in the uncracked sheet, due to fastener loads as in Case 2 [see Problem C in Fig. 1.2].

*Displacement  $V_a$  in a center-cracked sheet due to the far field loading*

The displacements at the rivet locations in the cracked sheet, due to the far field stress  $\sigma$ , can be determined using the well known Westergaard (1939) solution, as described briefly below.

It is shown in ?? that the equilibrium equation will be satisfied if the stress components are expressed in terms of stress functions  $\phi(x,y)$  in the following fashion.

$$\sigma_x = \frac{\partial^2 \phi}{\partial y^2}, \quad \sigma_y = \frac{\partial^2 \phi}{\partial x^2}, \quad \tau_{xy} = -\frac{\partial^2 \phi}{\partial x \partial y} \quad (1.1)$$

The stress function  $\phi(x,y)$  must satisfy the biharmonic equation

$$\frac{\partial^4 \phi}{\partial x^4} + 2 \frac{\partial^4 \phi}{\partial x^2 \partial y^2} + \frac{\partial^4 \phi}{\partial y^4} = 0 \quad (1.2)$$

in order to satisfy the compatibility equation (Eq. ??).

Westergaard's stress function  $\phi$ , where

$$\phi = \text{Re} \bar{Z} + y \text{Im} \bar{Z} \quad (1.3)$$

and

$$\bar{Z} = \frac{d\bar{Z}}{dz}, \quad Z = \frac{dZ}{dz}, \quad \text{and} \quad Z' = \frac{dZ}{dz}$$

would satisfy the biharmonic equation (Eq. 1.2). Thus, the complex function  $Z$  that satisfies the boundary condition for a specific problem is the solution for the given problem.

Use of Eq. 1.3 in Eq. 1.1 results in the following equations for the components of stress

$$\begin{cases} \sigma_x = \text{Re} Z - y \text{Im} Z' \\ \sigma_y = \text{Re} Z + y \text{Im} Z' \end{cases} \quad (1.4)$$

Substitution of Eq. 1.4 into the strain-stress relations results in

$$\epsilon_y = \frac{[(1-\nu) \text{Re} Z + (1+\nu) y \text{Im} Z']}{E} \quad (1.5)$$

where  $\epsilon_y$  is the strain in the  $y$  direction and  $\nu$  is the Poisson's ratio.

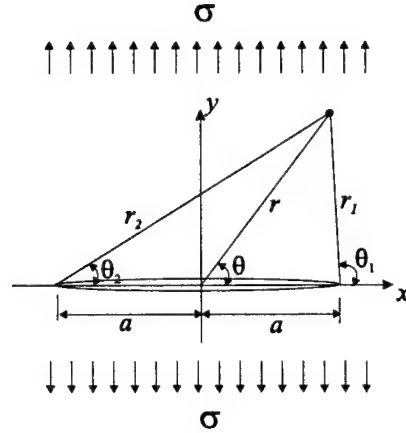


Figure 1.3: A center cracked sheet subjected to uniaxial far field load

Integration of Eq. 1.5 gives the following equation for displacement  $V$  in the cracked sheet

$$V = \frac{[2\text{Im}\bar{Z} - (1 + \nu)y\text{Re}Z]}{E} \quad (1.6)$$

The following stress function [Wetgeraad (1939)] would satisfy the boundary conditions at the crack surface for the infinite sheet.

$$Z = \frac{\sigma z}{\sqrt{z^2 - a^2}} \quad (1.7)$$

where  $\sigma$  is the tension stress at  $\infty$  in all directions.

Since the actual problem considered has an applied stress  $\sigma$  only as  $y \rightarrow \infty$ , adding a term to cancel out the effect of  $\sigma_x$  as  $x \rightarrow \infty$ , and substituting the resulting stress functions in Eq. 1.6, yields the following equation for the skin displacement in a uniaxially loaded cracked sheet.

$$V_a = \frac{\sigma}{E} \left\{ 2\sqrt{r_1 r_2} \sin\left(\frac{\theta_1 + \theta_2}{2}\right) - \frac{(1 + \nu)yr[\cos(\theta - \theta_1/2 - \theta_2/2)]}{\sqrt{r_1 r_2}} + \nu y \right\} \quad (1.8)$$

$$\equiv \sigma v_a \quad (1.9)$$

where the geometric parameters  $r_1$ ,  $r_2$ ,  $\theta_1$ ,  $\theta_2$  and  $r$ ,  $\theta$  are defined in the Fig. 1.3.



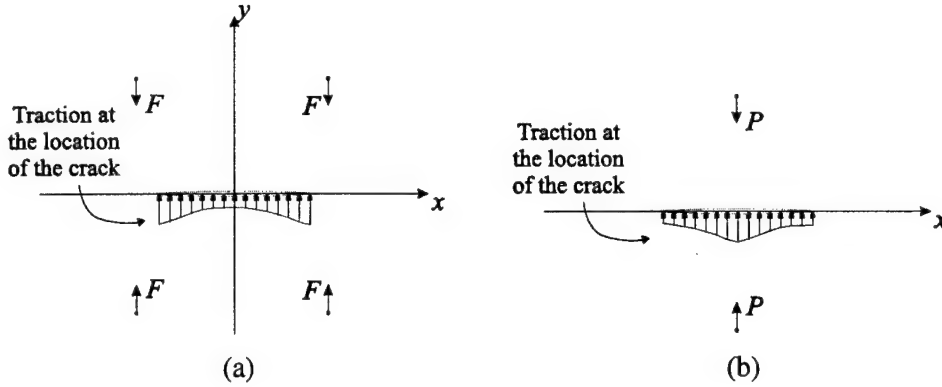


Figure 1.4: An infinite sheet subjected to (a) four fastener loads; (b) two fastener loads

*Displacement  $V_b$  in an uncracked sheet due to fastener loadings*

The stress distribution in an infinite sheet resulting from a concentrated force  $F$  can be determined from the work of Love (1944), as follows

$$\sigma_y = \frac{Fy(1+\nu)}{4\pi t(x^2+y^2)} \left[ \frac{3+\nu}{1+\nu} - \frac{2x^2}{x^2+y^2} \right] \quad (1.10)$$

The corresponding displacements are given by

$$V_F = \frac{Fy(1+\nu)}{4\pi tE} \left[ \frac{3-\nu}{2} \log(x^2+y^2) + \frac{(1+\nu)x^2}{x^2+y^2} \right] + C \quad (1.11)$$

where  $x$  and  $y$  are measured from the load point,  $C$  is a constant of integration, and  $t$  is the sheet thickness. Eq. 1.11 contains a singularity. The singularity can be eliminated by distributing the concentrated force  $F$  uniformly over the rivet diameter  $D$ . Using Eq. 1.11 to obtain the displacement of an elemental load and integrating the effect over the rivet diameter will yield an expression free from singularity. The resulting expression can then be used to obtain the displacement due to the fastener loads.

The displacement due to a system of four fastener loads, exerted symmetrically about the crack by the two intact outer stiffeners [see Fig. 1.4(a)], is

$$V_\alpha(x_i, y_i, x_j, y_j) = \frac{F(1+\nu)(3-\nu)}{16\pi Et} \left\{ (X_A+1) \log \left[ \frac{(X_A+1)^2 + Y_A^2}{(X_A+1)^2 + Y_B^2} \right] \right.$$

$$\begin{aligned}
& - (X_A - 1) \log \left[ \frac{(X_A - 1)^2 + Y_A^2}{(X_A - 1)^2 + Y_B^2} \right] + (X_B + 1) \log \left[ \frac{(X_B + 1)^2 + Y_A^2}{(X_B + 1)^2 + Y_B^2} \right] \\
& - (X_B - 1) \log \left[ \frac{(X_B - 1)^2 + Y_A^2}{(X_B - 1)^2 + Y_B^2} \right] + 4 \left( \frac{1 - \nu}{3 - \nu} \right) \\
& \times \left[ Y_A \tan^{-1} \left( \frac{2Y_A}{Y_A^2 + X_A^2 - 1} \right) + Y_A \tan^{-1} \left( \frac{2Y_A}{Y_A^2 + X_B^2 - 1} \right) \right. \\
& \quad \left. - Y_B \tan^{-1} \left( \frac{2Y_B}{Y_B^2 + X_B^2 - 1} \right) - Y_B \tan^{-1} \left( \frac{2Y_B}{Y_B^2 + X_A^2 - 1} \right) \right] \} \quad (1.12)
\end{aligned}$$

$$\equiv F v_{\alpha} \quad (1.13)$$

where  $X_A = (2/D)(x_i - x_j)$ ,  $X_B = (2/D)(x_i + x_j)$ ,  $Y_A = (2/D)(y_i - y_j)$ ,  $Y_B = (2/D)(y_i + y_j)$ . The index  $i$  labels the rivet locations where displacements are computed, and the index  $j$  labels the systems of fastener loads.

The displacement due to a pair of fastener loads, exerted symmetrically by the broken center stiffener on the center line of the crack [see Fig. 1.4(b)], is

$$\begin{aligned}
& V_{\beta}(x_i, y_i, y_j) \\
& = \frac{P(1 + \nu)(3 - \nu)}{16\pi Et} \left\{ (X_C + 1) \log \left[ \frac{(X_C + 1)^2 + Y_A^2}{(X_C + 1)^2 + Y_B^2} \right] \right. \\
& \quad - (X_C - 1) \log \left[ \frac{(X_C - 1)^2 + Y_A^2}{(X_C - 1)^2 + Y_B^2} \right] + 4 \left( \frac{1 - \nu}{3 - \nu} \right) \\
& \quad \times \left[ Y_A \tan^{-1} \left( \frac{2Y_A}{Y_A^2 + X_C^2 - 1} \right) - Y_B \tan^{-1} \left( \frac{2Y_B}{Y_B^2 + X_C^2 - 1} \right) \right] \} \quad (1.14)
\end{aligned}$$

$$\equiv P v_{\beta} \quad (1.15)$$

where  $X_C = (2/D)x_i$ .

The displacement at the  $i$ th rivet location due to all fastener loads is

$$V_b(x_i, y_i) = \sum_j F_j v_{\alpha_j} + \sum_j P_j v_{\beta_j} \quad (1.16)$$

where  $F_j$  and  $P_j$  are the fastener loads in the corresponding load system.

#### *Displacement $V_c$ in a center-cracked sheet due to the crack surface load*

The stress in the uncracked sheet along the  $x$  axis, where the actual crack is located, due to the fastener forces in the uncracked sheet, can be obtained from Eq. 1.10 by transfer of axis.

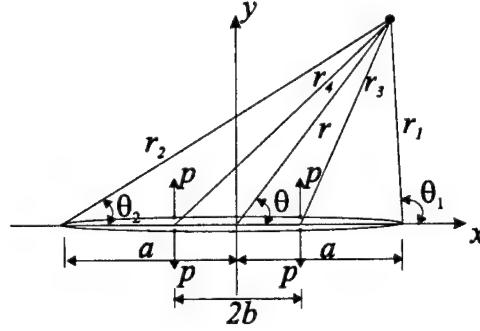


Figure 1.5: A center-cracked sheet subjected to crack surface point loads

$$\sigma_y(x, 0) = -\frac{(1+\nu)y_1}{2\pi t} \left[ \sum_j F_j \alpha(x_j, y_j, b) + \sum_j P_j \beta(y_j, b) \right] \quad (1.17)$$

where

$$\alpha(x_j, y_j, b) = \frac{3+\nu}{1+\nu} \left[ \frac{1}{(b-x_j)^2 + y_j^2} + \frac{1}{(b+x_j)^2 + y_j^2} \right] - \frac{2(b-x_j)^2}{[(b-x_j)^2 + y_j^2]^2} - \frac{2(b+x_j)^2}{[(b+x_j)^2 + y_j^2]^2} \quad (1.18)$$

$$\beta(y_j, b) = \frac{3+\nu}{1+\nu} \left[ \frac{1}{b^2 + y_j^2} \right] - \left[ \frac{\sqrt{2}b}{b^2 + y_j^2} \right]^2 \quad (1.19)$$

The displacement  $V_c$  (see Fig. 1.2) is obtained by applying an equal and opposite traction over the crack face to cancel out the stress caused by the rivet forces  $F_j$  and  $P_j$ . The displacement caused by this stress distribution can be obtained from Eq. 1.6 by using a complex stress function derived by Irwin (1957) for the center-cracked sheet with a pair of point forces opening the crack [see Fig. 1.5].

$$Z = \frac{2Pa}{t\pi(z^2 - b^2)} \sqrt{\frac{1 - (b/a)^2}{1 - (a/z)^2}} \quad (1.20)$$

Substituting  $t\sigma_y(x, 0) db$  for  $P$ , and integrating over half the crack length leads to the following expression for  $V_c$ .

$$V_c = -\frac{(1+\nu)y_j}{2\pi^2 E t} \left[ \sum_j F_j \int_0^a \alpha(x_j, y_j, b) \epsilon(x_i, y_i, b) db + \sum_j P_j \int_0^a \beta(y_j, b) \epsilon(x_i, y_i, b) db \right] \quad (1.21)$$

where  $\alpha$  and  $\beta$  are given by Eq. 1.18 and Eq. 1.19, and  $\epsilon$  is given by

$$\begin{aligned} \epsilon(x_i, y_i, b) = & \log \left[ \frac{(a^2 - b^2) + \sqrt{a^2 - b^2} (BC + AD) + r_1 r_2}{(a^2 - b^2) - \sqrt{a^2 - b^2} (BC + AD) + r_1 r_2} \right] \\ & - \frac{y_i (1 + \nu) \sqrt{(a^2 - b^2)}}{r_1 r_2 r_3^2 r_4^2} \\ & \{ (x_i^2 - b^2 - y_i^2) [x_i (AC - BD) + y_i (BC + AD)] \\ & - 2x_i y_i [x_i (BC + AD) - y_i (AC + BD)] \} \end{aligned} \quad (1.22)$$

where  $A = \sqrt{r_i + x_i - a}$ ,  $B = \sqrt{r_i - x_i + a}$ ,  $C = \sqrt{r_2 + x_i + a}$ , and  $D = \sqrt{r_2 - x_i - a}$ .

Numerical integration is, in general, necessary to evaluate the integrals in Eq. 1.21.

The total sheet displacement, denoted by  $V_{sh}$  in Fig. 1.2, is:

$$V_{sh} = V_a + V_b + V_c$$

or

$$V_{shi} = V_{ai} + V_{bi} + V_{ci}$$

for the displacement at  $i$ th rivet location.

### § 1.1.2 Stiffener displacements

#### *Outer, intact stiffener displacements*

The outer stiffener is assumed to be supported on three frames running normal to the stiffeners. The center frame is on the skin crack centerline. Stiffener extension at the fastener shear face is determined because of axial loads and bending from fastener loads and direct loads resulting from axial stresses. Stiffener bending is induced since the fastener shear faces are offset from the stiffener neutral axis. The average bending moment between each fastener, obtained through the use of the three-moment-equation, is given by [Swift (1974)]:

$$M_{A_i} = \sum_{j=i}^{2n} CF_j - \left[ \frac{3C}{2L^3} \sum_{j=n+1}^{2n} F_j (2Ly_j - y_j^2) \right] \left[ L - \frac{y_{i-1} + y_i}{2} \right] \quad (1.23)$$

Stiffener displacement caused by bending from fastener loads is given by

$$\delta_{M_i} = \frac{C}{EI} \sum_{j=n+1}^i M_{A_j} [y_j - y_{j-1}] \quad (1.24)$$

Stiffener displacement resulting from direct fastener loads is given by

$$\delta_{D_i} = \frac{1}{AE} \sum_{j=n+1}^i F_j y_j + \frac{y_i}{AE} \sum_{j=i+1}^{2n} F_j \quad (1.25)$$

Stiffener displacement resulting from gross stress is given by

$$\delta_{G_i} = \frac{\sigma y_i}{E} \quad (1.26)$$

where  $C$  is the distance from neutral axis to shear face,  $I$  is the stiffener inertia,  $L$  is the distance between supports,  $n$  is the number of active fasteners per stiffener, and  $y$  is the rivet coordinate from crack centerline.

Thus, at each fastener location in each of the out-stiffeners, the stiffener displacement,  $V_{st_i}$ , is given by

$$V_{st_i} = \delta_{M_i} + \delta_{D_i} + \delta_{G_i} \quad (1.27)$$

#### *Center broken stiffener displacements*

The center stiffener is assumed to be broken at the center of the skin crack. It is assumed to be supported by a frame at the break and two other frames at each side of the break. The average bending moment between each fastener is given by

$$M_{A_i} = \sum_{j=i}^i CP_j - \left[ \frac{C}{L} \sum_{j=n+1}^n P_j \left( \frac{5}{4} - \frac{3y_j}{4L^2} \right) \right] \left[ \frac{y_{i+1} + y_i}{2} \right] \quad (1.28)$$

Stiffener displacement resulting from bending due to fastener loads is given by

$$\delta_{M_i} = \frac{C}{EI} \sum_{j=i}^{n-1} M_{A_j} (y_{i+1} - y_j) \quad (1.29)$$

Stiffener displacement resulting from direct load is given by

$$\delta_{D_i} = \frac{1}{AE} \sum_{j=1}^i P_j (y_n - y_j) + \frac{1}{AE} \sum_{j=i+1}^{n-1} P_j (y_n - y_j) \quad (1.30)$$

Thus, at each fastener location in the central broken stiffener, the stiffener displacement  $V_{st_i}$  is given by

$$V_{st_i} = \delta_{M_i} + \delta_{D_i} \quad (1.31)$$

### § 1.1.3 Fastener displacements

The DCM is based on the displacement compatibility between the cracked skin and the stiffener, after accounting for the rivet displacement. Thus, the stiffener plus rivet displacements are made equal to skin displacements at each of the rivet locations. It is of interest to note that the rivet contribution to stiffener plus rivet displacement is more than 75%, and is therefore an extremely important consideration. Errors up to 50% in crack-tip stress intensity factors can result by neglecting fastener displacements [Swift (1984)].

It has been determined by tests [Swift (1974)] that the elastic displacement in shear can be represented by the following empirical relation

$$\delta_R = \frac{F}{ED} \left[ A + C \left( \frac{D}{B_1} + \frac{D}{B_2} \right) \right] \quad (1.32)$$

where  $F$  is the applied load,  $E$  is the modulus of sheet material,  $D$  is the rivet diameter,  $B_1$  and  $B_2$  are thickness of joined sheets.  $A = 0.5$  for aluminium rivets; and  $A = 1.666$  for steel fasteners.  $C = 0.8$  for aluminium rivets; and  $C = 0.86$  for steel fasteners.

### § 1.1.4 Compatibility of displacements

The fastener forces on the panel are obtained from the solution of a set of simultaneous equations based on the compatibility relations enforced at each of the fastener locations in the two outer stiffeners,  $V_{sh_i} = V_{st_i} + \delta_{R_i}$ , and a similar relation for the central broken stiffener. Compatibility at the center broken stiffener is given by

$$\begin{aligned} & \sum_{j=n+1}^{2n} F_j \left[ v_\alpha(x_n, y_n, x_j, y_j) - \frac{(1+\nu)y_j}{2\pi^2 EB} \int_0^a \alpha(x_j, y_j, b) \epsilon(x_n, y_n, b) db \right] \\ & - \sum_{j=1}^n P_j \left[ v_\beta(x_n, y_n, y_j) - \frac{(1+\nu)y_j}{2\pi^2 EB} \int_0^a \beta(y_j, b) \epsilon(x_n, y_n, b) db \right] \end{aligned}$$

$$\begin{aligned}
& +\delta_{R_n} - \delta_{D_i} - \delta_{M_i} - \delta_{R_i} \\
& - \sum_{j=n+1}^{2n} F_j \left[ v_\alpha(x_i, y_i, x_j, y_j) - \frac{(1+\nu)y_j}{2\pi^2 EB} \int_0^a \alpha(x_j, y_j, b) \varepsilon(x_i, y_i, b) db \right] \\
& + \sum_{j=1}^n P_j \left[ v_\beta(x_i, y_i, y_j) - \frac{(1+\nu)y_j}{2\pi^2 EB} \int_0^a \beta(y_j, b) \varepsilon(x_i, y_i, b) db \right] \\
& = \sigma v_a(x_i, y_i) - \sigma v_a(x_n, y_n)
\end{aligned} \tag{1.33}$$

$$\tag{1.34}$$

Compatibility at the outer intact stiffener is given by:

$$\begin{aligned}
& \delta_{D_i} + \delta_{M_i} + \delta_{R_i} \\
& - \sum_{j=n+1}^{2n} F_j \left[ v_\alpha(x_i, y_i, x_j, y_j) - \frac{(1+\nu)y_j}{2\pi^2 EB} \int_0^a \alpha(x_j, y_j, b) \varepsilon(x_i, y_i, b) db \right] \\
& + \sum_{j=1}^n P_j \left[ v_\beta(x_i, y_i, y_j) - \frac{(1+\nu)y_j}{2\pi^2 EB} \int_0^a \beta(y_j, b) \varepsilon(x_i, y_i, b) db \right] \\
& = \sigma v_a(x_i, y_i) - \delta_{G_i}
\end{aligned} \tag{1.35}$$

A system of simultaneous equations is set up from these compatibility equations, to solve for the fastener loads  $F_j$  and  $P_j$ . The matrix is  $2n \times 2n$  in size where  $n$  is the number of active fasteners assumed in each of the center and outer stiffeners. A value of  $n$  of 15 is usually adequate for the broken central stiffener case[Swift (1984)].

The compatibility matrix is made up of a series of sections formed by terms of the compatibility equations. The section *DCC* is a  $14 \times 14$  matrix of skin displacements at each of the center stiffener rivets resulting from center stiffener rivet loads. Only the first 14 rivets are considered in this matrix since all the displacements at the broken center stiffener are made relative to the fifteenth, most remote rivet from the crack, and this is considered separately. *DCC* is formed from the eighth term of Eq. 1.33, The section *DCO* is a  $14 \times 15$  matrix of skin displacements at each of the center stiffener rivets resulting from outer stiffener rivet loads.

*DCO* is formed from the seventh term of Eq. 1.33. Both *DCC* and *DCO* are initially formulated as  $15 \times 15$  matrices. The fifteenth row in *DCC* is replaced by a series of ones. The reason for this is to form the fifteenth equation, which is the equilibrium for the broken central stiffener and equates the sum of the rivet loads to the load in the stiffener beyond the fifteenth rivet. The fifteenth column of *DCC* is replaced by the rivet flexibility of the fifteenth rivet in the center stiffener,

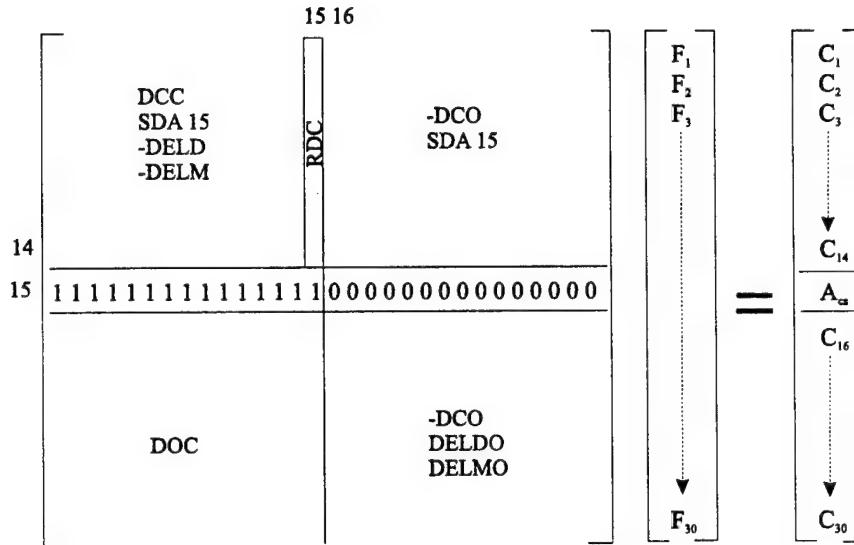


Figure 1.6: Matrix of compatibility equations for two bay crack with center broken stiffener [Adopted from Swift (1984)]

obtained from Eq. 1.32. The section *SDA15* is a  $14 \times 30$  matrix representing the skin displacement at the fifteenth rivet in the center stiffener. This displacement is the one to which all center stiffener displacement are referenced. The first 14 columns are formed from *DCC* with  $i$  equal to 15. Column 15 in this matrix is eventually replaced by *RDC*, based on Eq. 1.32. Columns 16 to 30 are formed from *DCO* with  $i$  equal to 15, that is, displacement at the fifteenth rivet. All the 14 rows in this matrix are identical to each other. The section *DELD* is a  $14 \times 14$  matrix of center stiffener displacements resulting from rivet direct loads. The matrix is formulated from Eq. 1.30 plus the third term of Eq. 1.35. The section *DELM* is a  $14 \times 14$  matrix of center stiffener displacements resulting from bending. It is formed by first obtaining a matrix *DDELM*, which is a matrix of increments of stiffener displacement resulting from bending. For example,  $\Delta\delta M_1$ , (*DDELM*<sub>1</sub>) is the extension of the center broken stiffener between the first and second rivets.  $\Delta\delta M_2$  (*DDELM*<sub>2</sub>) is the center stiffener extension between the second and third rivets and so forth. The total displacement at the  $i$ th rivet is given by Eq. 1.29. *DELM* is formed by first summing the elements of the *DDELM* matrix. The section *DOC* is a  $15 \times 15$  matrix of skin displacements at each of the outer stiffener rivets resulting from center stiffener rivet loads. *DOC* is formed from the fifth term of



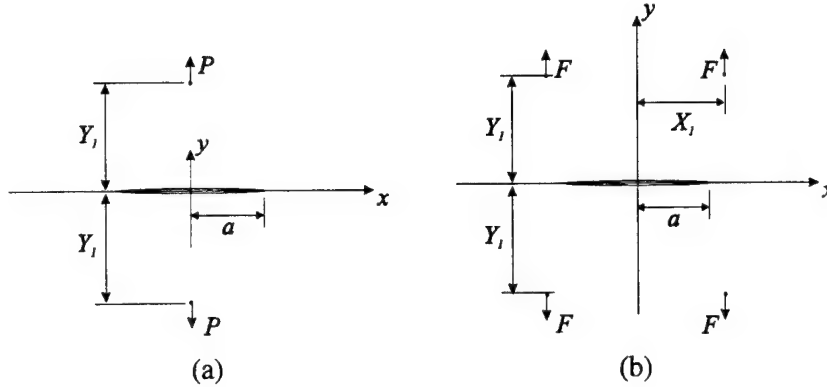


Figure 1.7: A center-cracked sheet subjected to (a) a pair of fastener loads; (b) a system of four fastener loads

Eq 1.35 where  $j$  is 1 to 15, and  $i$  is 15 to 30. The  $i, j$  notation reflects the skin displacement at the  $i$ th rivet resulting from the  $j$ th rivet load. The section  $DOO$  is a  $15 \times 15$  matrix of skin displacements at each of the outer stiffener rivets resulting from outer stiffener rivet loads.  $DOO$  is formed from fourth term of Eq. 1.35. The section  $DELDO$  is a  $15 \times 15$  matrix of outer stiffener displacements resulting from rivet direct loads and is formulated from first and third terms of Eq 1.35, or Eqs 1.25 and 1.32. The section  $DELMO$ , is a  $15 \times 15$  matrix of outer stiffener displacements resulting from bending. It is formed by first obtaining a matrix  $DDELMO$ , which is a matrix of increments of outer stiffener displacements caused by bending. For example,  $\Delta\delta M_1$ , ( $DDELMO_1$ ) is the extension of the outer stiffener between the first and second rivets.  $\Delta\delta M_2$  ( $DDELMO_2$ ) is the extension of the outer stiffener between the second and third rivets. The total deflection at the  $i$ th rivet is given by the second term of Eq 1.35 or Eq. 1.29. The matrix  $DELMO$  is formed by summing the elements of the  $DDELMO$  matrix.

*The final compatibility matrix is inverted and solved for fastener loads.*

#### § 1.1.5 Crack-tip stress intensity factor

Crack-tip stress intensity factors caused by each pair of center stiffener fastener loads as shown in Fig. 1.7(a) are given by Paris (1960)

$$K_{cs} = \frac{\sqrt{a}P}{2t\sqrt{\pi}} \left[ \frac{2a^2 + (3+\nu)Y_1^2}{(a^2 + Y_1^2)^{3/2}} \right] \quad (1.36)$$

For each set of outer stiffener fastener loads, as shown in Fig. 1.7(b), the stress intensity is given by Paris (1960)

$$K = \frac{2FY_1\sqrt{\pi a}}{\pi t} \left[ \left( \frac{3+\nu}{2} \right) I_1 - (1+\nu) I_2 \right] \quad (1.37)$$

where

$$I_1 = \frac{\beta}{Y_1 \sqrt{(Y_1^2 + a^2 - X_1^2)^2 + 4X_1^2 Y_1^2}} \quad (1.38)$$

$$I_2 = \frac{\left[ (a^2 + X_1^2) Y_1^2 + (a^2 - X_1^2)^2 \right] \beta^2 + X_1^2 Y_1^2 (Y_1^2 - a^2 + X_1^2)}{2Y_1 \beta \left[ (Y_1^2 + a^2 - X_1^2)^2 + 4X_1^2 Y_1^2 \right]^{3/2}} \quad (1.39)$$

$$\beta = \frac{1}{\sqrt{2}} \left[ (Y_1^2 + a^2 - X_1^2) + \sqrt{(Y_1^2 + a^2 - X_1^2)^2 + 4X_1^2 Y_1^2} \right]^{1/2}$$

where  $X_1$  and  $Y_1$  are defined in Fig. 1.7

Total stress intensity is obtained by superposition for each set of active fasteners, paying attention to load direction, and the effects of overall stress.

### § 1.1.6 Summary

The displacement compatibility method (DCM) uses a simplified computational model to compute the stress intensity factors for a cracked panel. In the simplified model, the displacement compatibility condition between a center-cracked infinite sheet and the stiffener system, both subjected to the far field loading and the fastener loads, is used to form a system of equations to solve for the fastener loads. Thus, it is essentially a redundant-force-method, wherein the displacement compatibility condition is used to solve for the redundant (statically indeterminate) forces. Based on the superposition principle, analytical solutions for i) a center-cracked infinite sheet subjected to uniaxial far field load, ii) a center-cracked infinite sheet subjected to point load at crack surface, and iii) an uncracked infinite sheet subjected to a point load, are used to determine the displacement for the sheet. The use of these infinite body solutions would, in general, result in anti-conservative results for cracks in finite panels. The traction at the location of the crack for the uncracked sheet, subjected to the fastener loads, is cancelled by the applied load at the crack surface of the center-cracked panel. The stiffener system is solved using the classical beam theory. The resulting linear equation system is small, in the order of the number of rivets.

However, the simplified model uses analytical solutions for an infinite sheet, and the effect of boundaries is ignored. This is anti-conservative. To include the boundary effects and possible plasticity effects, the finite element alternating method is preferable. Since it is difficult to incorporate the displacement compatibility requirements, as in the flexibility matrix approach of DCM, into a displacement (or, stiffness matrix based) based FEM framework, we can first use hierarchical analysis approach to solve for the fastener loads using ordinary finite element stiffness method, and then use the finite element alternating method to solve for the fracture parameters. Details are shown in the next section.

## **§ 1.2 The FEAM for a Cracked Stiffened Panel**

### **§ 1.2.1 A hierarchical methodology and the FEAM**

A global-intermediate-local hierarchical methodology is presented in this section for the calculation of residual strength of a stiffened fuselage or a wing of an aircraft, containing a Discrete Source Damage (DSD). In this approach, a coarse finite element mesh is first used to model the global behavior of a cracked stiffened structure (wing or fuselage). The traction and/or displacement boundary conditions around a relatively small region around the crack is found from the global model. Then, an intermediate model is used to model the details of the panel, wherein the structural details such as stringers and ribs are modeled completely, to reflect the local effects of these reinforcements. Coarse meshes with unconnected nodes are only used to model the cracks, since the purpose of this intermediate analysis is to obtain the reaction forces, exerted by the stiffeners (via the fasteners), on the skin. Fracture parameters (such as stress intensity factors in a linear elastic analysis) are obtained by analyzing only the isolated skin with a finite element alternating method. A coarse finite element mesh for the skin can be used, because the crack tip fields are captured by the analytical solution and the cracks are not modeled explicitly. The global and intermediate analyses are normally accomplished via a standard finite element (stiffness method) code. The local damage modules, especially the finite element alternating method, discussed in the previous chapter can be used for the local analysis. The flow chart of such a hierarchical analysis approach is shown in Fig. 1.8.

In the global analysis, the stringers are simplified as beams attached to the skin, and ribs are modeled as plates, as illustrated in the Fig. 1.9. Cracks are modeled using a coarse mesh with unconnected nodes at the crack locations, to reflect the loss of stiffness of the structure, so that the redistribution of loads among the skin,

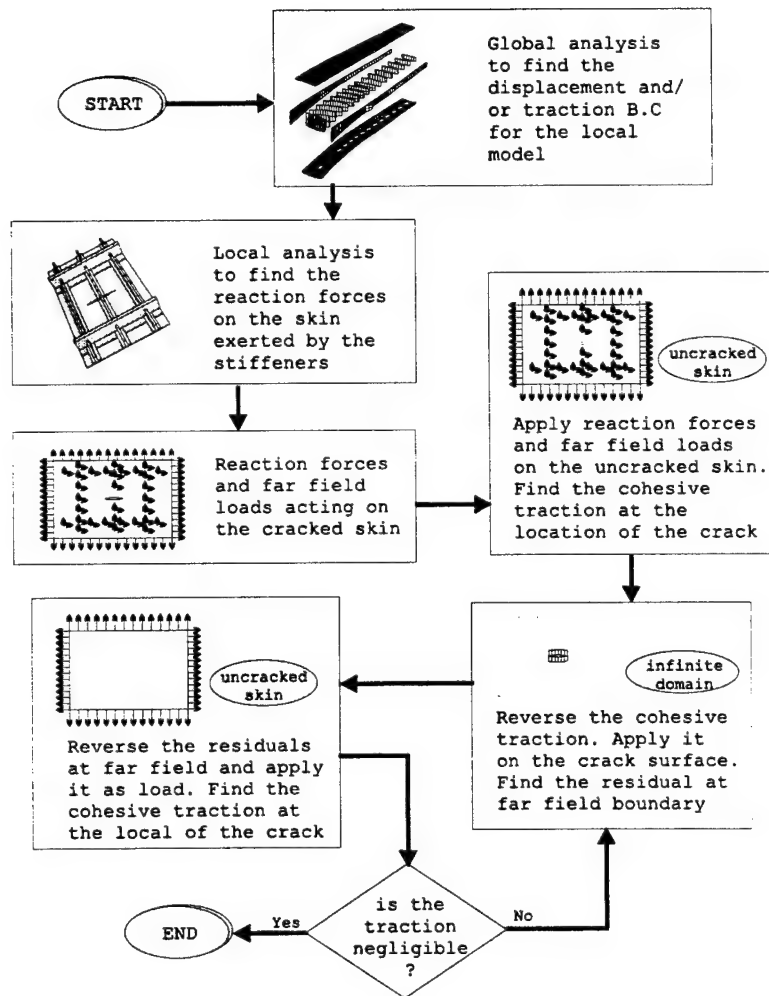


Figure 1.8: Flow chart for the hierarchical damage tolerance analysis

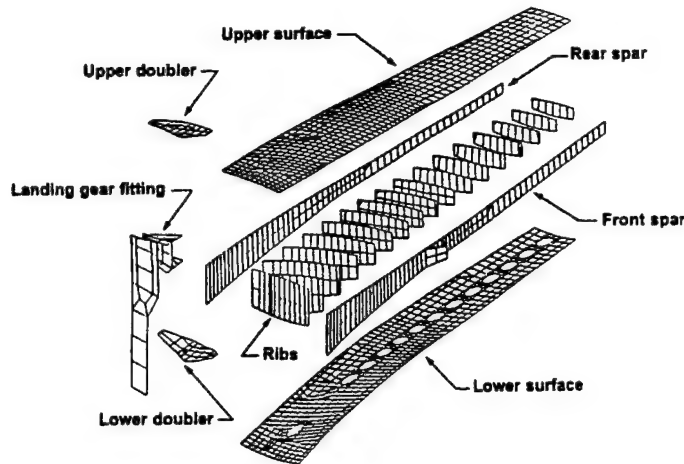


Figure 1.9: A global analysis

stringers and ribs can be captured. *Broken stringers and ribs, if any, are also accounted for.* The details of the crack tip fields are ignored.

The intermediate model, which consists of the skin containing the cracks and several stringers and ribs, can be constructed from the global analysis. The boundary conditions and loads for the panel are obtained from the global analysis. In this model (as illustrated in Fig. 1.10), all the stringers, frames and fasteners are modeled in detail. Cracks are also modeled only with unconnected nodes, without paying attention to the crack tip fields. The intermediate model is used to obtain the forces applied on the skin by the frames and stringers. The effects of the fasteners, that are used to fasten the frames on the skins are also accounted for.

The fracture parameters for the cracked skin (Fig. 1.11), loaded with fastener forces and boundary tractions, can be solved by the Finite Element Alternating Method described in the previous chapter. The superposition principle used by the Finite Element Alternating Method for solving the isolated skin is illustrated in Fig. 1.12. Since finite element alternating method is used, the cracks in the sheet are closed for the local finite element model. The same mesh can be used for different crack lengths. We assume that a small change in crack length does not affect significantly the load distribution among the skin, stringers and ribs. Thus, the isolated skin with the same reaction forces can be used to analyze several cracks of lengths that are slightly different from each other. Similarly, the same global model can be used for several local models with cracks of lengths that are slightly

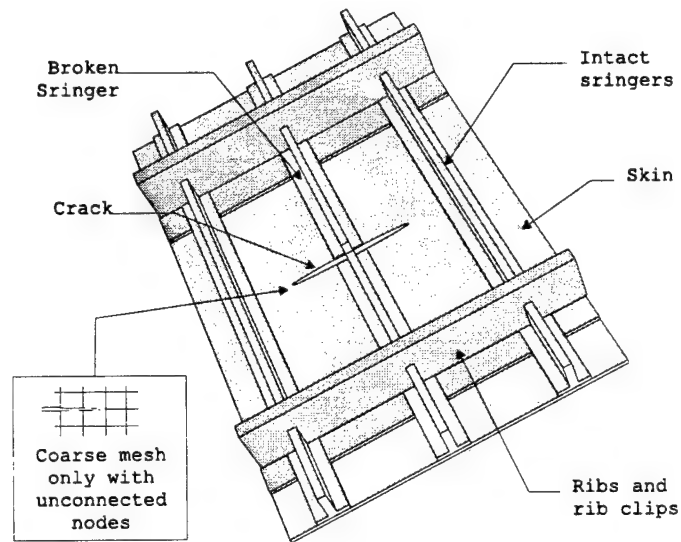


Figure 1.10: A intermediate model

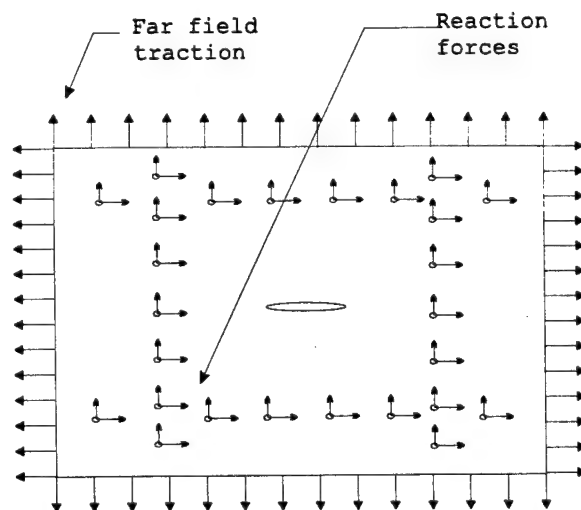


Figure 1.11: The isolated skin with reaction forces from the stiffeners

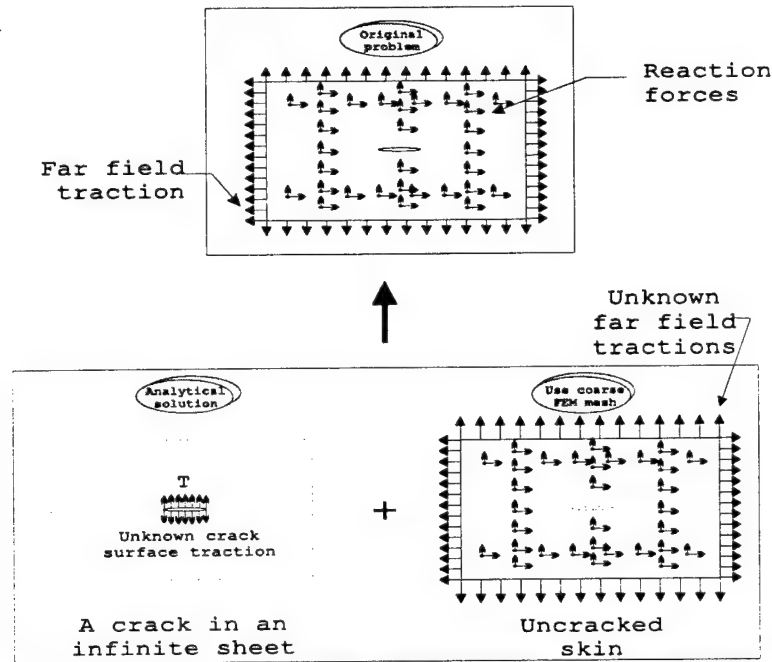


Figure 1.12: Superposition principle for the finite element alternating method

different from each other. Thus, the number of global and intermediate analyses, in a parametric study of cracks of different lengths, can be minimized. In this way, one can dramatically reduce the computational time as well as the data preparation time, as compared to the conventional finite element method. Furthermore, the FEAM is ideally suited for analyzing the multiple-site-damage (MSD) situation, as in the case of a major crack approaching small cracks emanating from fastener holes, as discussed later.

Fracture mechanics parameters can be found accurately because the near-crack-tip fields are captured exactly by the analytical solutions. Coarser meshes can be used in the finite element analysis because the cracks are not modeled explicitly. The finite element method is only used to compute the cohesive tractions at the locations of crack in an otherwise uncracked sheet, which is a smooth distribution. Therefore, a very coarse mesh can be used. Fig. 1.13 shows the typical finite element meshes around the crack tip, when a) the EDI based method is used to evaluate stress intensity factors; or, b) the finite element alternating method is used. In Fig. 1.13, the EDI based method also uses singular quarter-point elements.

In a parametric analysis of various crack sizes to evaluate the residual strength

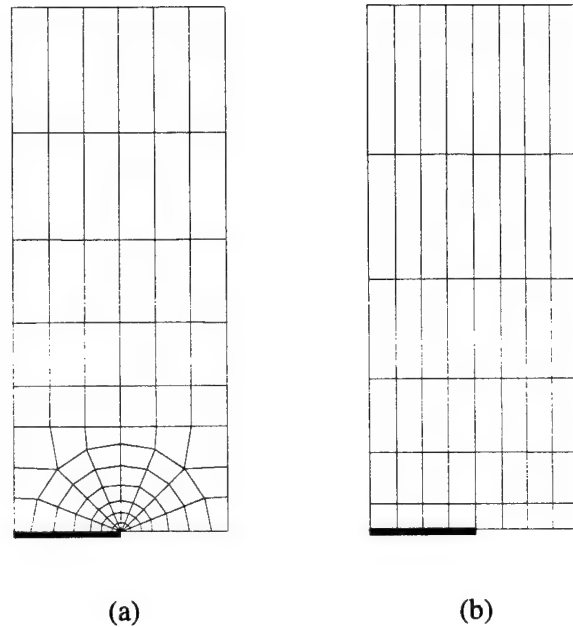


Figure 1.13: The finite element mesh when a) the EDI base method is used; b) the finite element alternating method is used

of a cracked wing structure, the global stiffness matrix of the finite element model is decomposed only once, since the stiffness of the uncracked structure remains the same for all crack sizes. In the other approaches, such as using singular/hybrid type special crack-tip finite elements or using EDI based conservative integrals / interactive integrals, the cracks must be modeled explicitly. Therefore, the global stiffness matrix must be computed and decomposed for each crack size. Thus, the alternating method is very efficient in saving both time in the computational analysis and human effort in the mesh generation.

The details for extracting an isolated skin model for the local analysis are presented in the next section.

### § 1.2.2 *Details of extracting the isolated skin model*

In the intermediate analysis, the skin is discretized using a coarse finite element mesh. This coarse mesh models the broken stiffeners, as well as the broken skin-ligament of the crack; but the crack-tip singularities are not modeled. The axial deformation of the stiffener is modeled by using the conventional “truss-type”( and/or



“beam-type”) elements. Since the fastener shear forces are usually offset from the stiffener neutral axis, an out-of-plane bending is also induced in the stiffeners. The out-of-plane bending deformation of the stiffener, between two fasteners, is given by the elementary beam theory:

$$\delta_b = C \left( \frac{ML}{E_{st}I} \right) = a_b F \quad (1.40)$$

where:

$C$  = axis of the stiffener to the point of action of the fastener shear force,

$I$  = stiffener cross-sectional inertia,

$L$  = distance between two fasteners, or the length of the stiffener “truss” element,

$E_{st}$  = Young's modulus of stiffener material,

$M = F \cdot C$ ,

$F$  is the force in the truss element.

Note that  $\delta_b$  is in the same direction, as the stiffener axial force,  $F$ . From Eq. 1.40, it is seen that:

$$a_b = \left( \frac{C^2 L}{E_{st}I} \right) \quad (1.41)$$

The axial stretch of the stringer is given by:

$$\delta_a = \frac{F}{E_{st}A} \equiv (a_s) F, \quad a_s = \frac{1}{E_{st}A}. \quad (1.42)$$

We use the total axial deformations at the ends of the stringer, at the points where the stringer is attached to the skin, as the generalized degrees of freedom for the stringer. For these degrees of freedom, the stiffness matrix of the stringer element is given by:

$$\mathbf{K}_{St}^e = \begin{bmatrix} \frac{1}{(a_b + a_s)} & \frac{-1}{(a_b + a_s)} \\ \frac{-1}{(a_b + a_s)} & \frac{1}{(a_b + a_s)} \end{bmatrix}. \quad (1.43)$$

The flexibility of the fasteners has been found [Swift (1984)] to be an important factor that influences the stress-intensity factors for a crack in the stiffened skin. If  $Q$  is the shear force acting on the fastener, the shear deformation of the fastener can be represented by the empirical relation [Swift (1984)]

$$\delta_F = \frac{1}{E_{sh}D} \left[ A + C \left( \frac{D}{t_1} + \frac{D}{t_2} \right) \right] F \equiv a_F Q \quad (1.44)$$

where

$E_{sh}$  = modulus of sheet material

$D$  = rivet diameter

$t_1$  and  $t_2$  = thicknesses of joined sheets

$A = 5.0$  for Al rivets and 1.66 for steel fasteners

$C = 0.8$  for Al rivets and 0.86 for steel fasteners.

The "stiffness" of the rivet in shear is thus given by

$$K_F = \frac{E_{sh}D}{\left[ A + C \left( \frac{D}{t_1} + \frac{D}{t_2} \right) \right]} \quad (1.45)$$

Consider, for simplicity (but without any loss of generality), that the skin is discretized into finite elements, with nodes being only at the locations of the fasteners; and likewise, the stringers are discretized into finite elements with nodes being only at the fastener locations. Let the number of fasteners be  $N$ . Let the number of stringer elements be  $N_{st}$ ; and the number of sheet elements be  $N_{sk}$ . Let the generalized displacements of the skin at the nodes of the finite element mesh be denoted as  $q_{sk}$  and those of the stringers at the nodes be denoted by  $q_{st}$ . Then the total strain energy of the stiffened fuselage skin, with flexible fasteners, is given by:

$$W = \sum_{e=1}^{N_{sk}} \frac{1}{2} \mathbf{q}_{sk}^e{}^T \mathbf{K}_{sk}^e \mathbf{q}_{sk}^e + \sum_{e=1}^{N_{st}} \frac{1}{2} \mathbf{q}_{st}^e{}^T \mathbf{K}_{st}^e \mathbf{q}_{st}^e + \sum_{e=1}^N \frac{1}{2} K_F (q_{sk}^e - q_{st}^e)^2 \quad (1.46)$$

where  $\mathbf{q}_{sk}^e$  is the vector of nodal displacements of a skin element; and  $\mathbf{q}_{st}^e$  is the vector of nodal displacements of a stringer (stiffener) element.

Let  $\mathbf{q}_{sk}$  be the master vector of nodal displacements of the skin;  $\mathbf{K}_{sk}$  the assembled nodal stiffness matrix of the skin;  $\mathbf{q}_{st}$  be the master vector of nodal displacements of the stringers; and  $\mathbf{K}_{st}$  the assembled nodal stiffness matrix of the stringers. Let  $\mathbf{K}_F$  be the "assembled" (diagonal) stiffness matrix of the fasteners; i.e.,

$$\mathbf{K}_F = \begin{bmatrix} K_F & 0 & 0 & 0 & \cdots & 0 \\ 0 & K_F & 0 & 0 & \cdots & 0 \\ 0 & & & & & 0 \\ \vdots & & & & & \vdots \\ 0 & 0 & \cdots & \cdots & \cdots & K_F \end{bmatrix}, N \times N \quad (1.47)$$

Then, the total strain energy  $W$  of Eq. 1.46 can be written as:

$$W = \frac{1}{2} \mathbf{q}_{sk}' (\mathbf{K}_{sk} + \mathbf{K}_F) \mathbf{q}_{sk} + \frac{1}{2} \mathbf{q}_{st}' (\mathbf{K}_{st} + \mathbf{K}_F) \mathbf{q}_{st} - \mathbf{q}_{sk}' \mathbf{K}_F \mathbf{q}_{st} \quad (1.48)$$

If the fastener flexibility is ignored, then  $\mathbf{q}_{st} \equiv \mathbf{q}_{sk}$ , and Eq. 1.48 reduces to:

$$W = \frac{1}{2} \mathbf{q}_{sk}' (\mathbf{K}_{sk} + \mathbf{K}_{st}) \mathbf{q}_{sk} \quad (1.49)$$

The potential of the external forces (the hoop stress in the fuselage) may be represented, in general, as:

$$U = (\mathbf{q}_{sk}' \mathbf{Q}_{sk} + \mathbf{q}_{st}' \mathbf{Q}_{st}). \quad (1.50)$$

Let  $\pi = W - U$ . The finite element equations that arise from the vanishing of the variation of  $\delta\pi$  (i.e.,  $\delta\pi = 0$ ) are given by:

$$\begin{cases} (\mathbf{K}_{sk} + \mathbf{K}_F) \mathbf{q}_{sk} - \mathbf{K}_F \mathbf{q}_{st} = \mathbf{Q}_{sk}, \\ (\mathbf{K}_{st} + \mathbf{K}_F) \mathbf{q}_{st} - \mathbf{K}_F \mathbf{q}_{sk} = \mathbf{Q}_{st}. \end{cases} \quad (1.51)$$

for the case of flexible fasteners. Equations 1.51 may be rearranged as:

$$\begin{bmatrix} (\mathbf{K}_{sk} + \mathbf{K}_F) & \mathbf{K}_F \\ -\mathbf{K}_F & (\mathbf{K}_{st} + \mathbf{K}_F) \end{bmatrix} \begin{Bmatrix} \mathbf{q}_{sk} \\ \mathbf{q}_{st} \end{Bmatrix} = \begin{Bmatrix} \mathbf{Q}_{sk} \\ \mathbf{Q}_{st} \end{Bmatrix} \quad (1.52)$$

After the imposition of appropriate boundary conditions,  $\mathbf{q}_{sk}$  and  $\mathbf{q}_{st}$  can be solved for, from Eq. 1.52. Once  $\mathbf{q}_{sk}$  and  $\mathbf{q}_{st}$  are solved for, the reactions of the stiffeners on the skin, at the locations of the fasteners, can be easily calculated as:

$$\mathbf{F}_{stiffener} = \mathbf{K}_F (\mathbf{q}_{st} - \mathbf{q}_{sk}) \equiv \mathbf{Q}_{st} - \mathbf{K}_{st} \mathbf{q}_{st} \quad (1.53)$$

with care being exercised to determine the direction of these reactive forces.

Table 1.1: Properties of stiffener cross-section

Thickness $B_2$ (mm)	Area $A$ (mm <sup>2</sup> )	Inertia $I$ (mm <sup>4</sup> )	Arm length $R$ (mm)
1.6002	121.935	20431.1	13.64
2.5400	163.709	28346.5	13.64
4.0642	231.467	38867.0	13.64
4.8260	265.322	43113.6	13.64

Once the effects of the stringer (with flexible rivets) on the skin are determined, one can consider the free-body diagram of the cracked skin alone (see Fig. 1.11); the skin being subject to the far-field hoop stresses, and the stiffener reaction forces.

### § 1.2.3 Numerical examples

In order to illustrate the application of the above described methodology, some example problems are solved. Consider a crack in a stiffened panel where a stiffener is broken and the crack is located symmetrically with respect to the broken stiffener (see Fig. 1.14). To investigate the effects of stiffener configuration and spacing, four different cross-sectional stiffener areas and four different stiffener-spacings are considered. The data for the stiffeners is given in Tab. 1.1. In order to compare the results, the same panel configuration as in Swift (1984) was employed.

The meshes used in the finite element analysis are shown in Fig. 1.15. Since the geometry and loading are symmetric, a quarter of the panel was modeled. The fastener interval,  $d$ , in Fig. 1.15 was chosen as 1 inch. And the stress intensity factor  $K_I$  is normalized as:

$$K_n = \frac{K_I}{F(\zeta) \sigma \sqrt{\pi a}} \quad (1.54)$$

where  $\sigma$  is the stress applied on the external boundary,  $a$  is the half crack length and  $F(\zeta)$  is the boundary correction factor, given by:

$$F(\zeta) = \frac{1 - 0.5\zeta + 0.370\zeta^2 - 0.044\zeta^3}{\sqrt{1 - \zeta}} \quad (1.55)$$

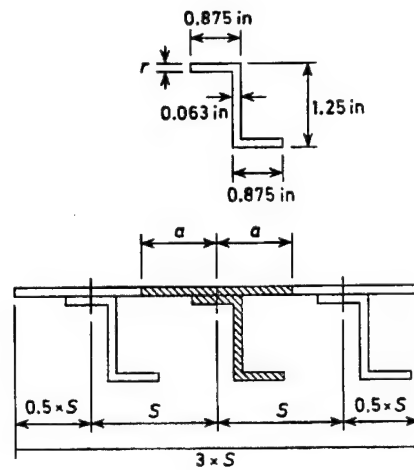


Figure 1.14: Configurations considered in the parametric study

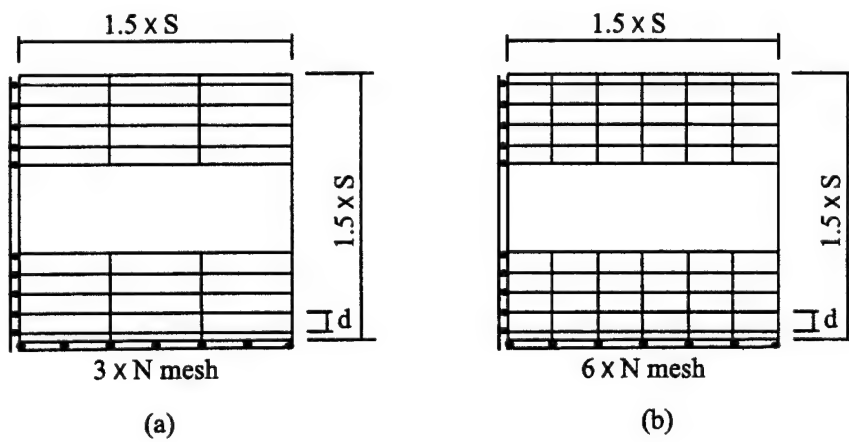


Figure 1.15: Meshes used in the parametric study; S: stiffner spacing, N: number of fasteners, d: Rivet interval

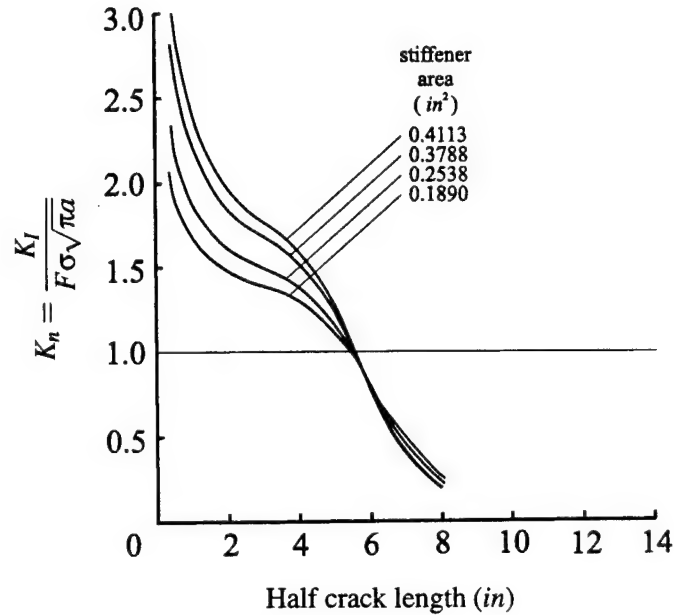


Figure 1.16: Effect of stiffening on crack-tip SIF, spacing 6 inches

where  $\zeta$  is the ratio of the crack length to the width of the sheet. Since  $F(\zeta) \sigma \sqrt{\pi a}$  gives approximately the stress intensity factor for a crack in an unstiffened panel, the normalized stress intensity factor,  $K_n$  indicates the ratio of the stress intensity factor of a stiffened panel to that of an unstiffened panel.

In this parametric study, eight node isoparametric elements were used. The sheet and stiffener materials are assumed to be 6061-T6 where Poisson's ratio is 0.351.

Some results of parametric studies are given in Figs. 1.16 through 1.21. The effects of stiffening are shown in Figs. 1.16 through 1.19. Four different cross-sectional areas of stiffeners were considered for each stiffener spacing. From these results, we can notice that when the crack is very short, the stress intensity factors for the stiffened panel are much larger than those of the unstiffened panel. This is due to the effect of the broken stiffener. As the crack becomes longer, the stress intensity factors decrease and become smaller than those of the unstiffened panel, because of the outer unbroken stiffeners.

In Figs. 1.20 and 1.21, the results of the present parametric study and the results from Swift (1984) are illustrated together. The stress intensity factors from the present finite element alternating method are higher than those from the displacement compatibility method until the crack grows to the outer stiffener. This is

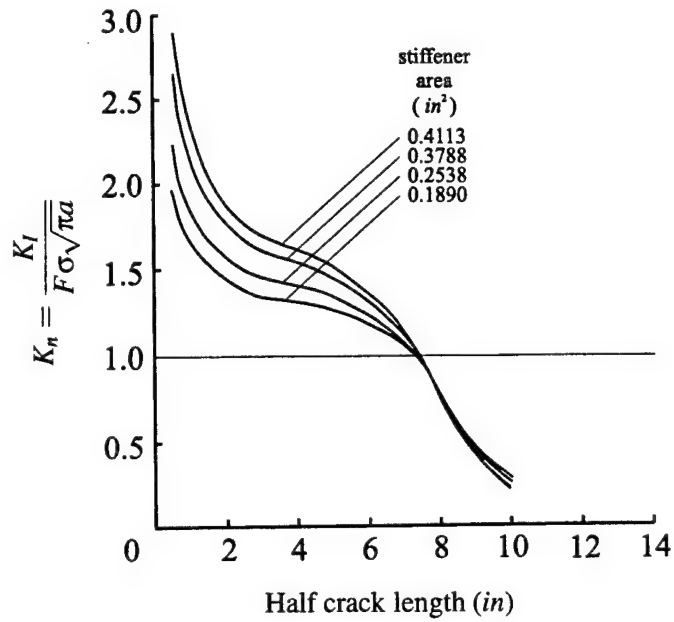


Figure 1.17: Effect of stiffening on crack-tip SIF, spacing 8 inches

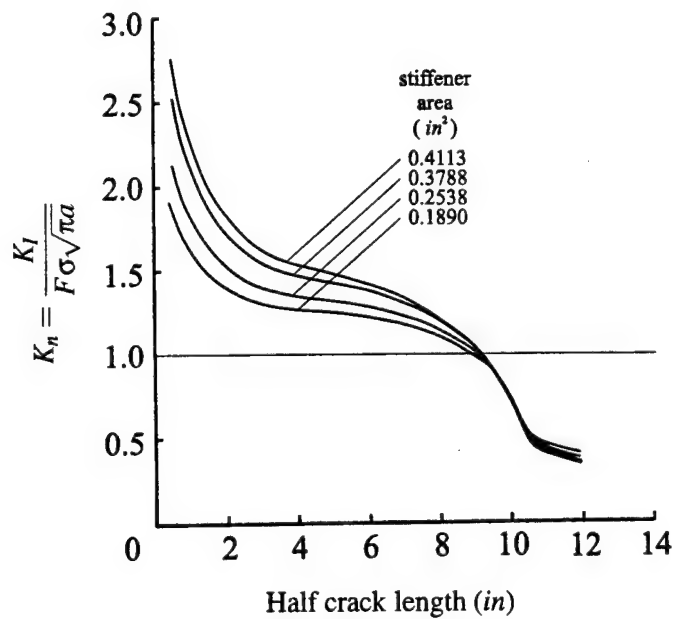


Figure 1.18: Effect of stiffening on crack-tip SIF, spacing 10 inches

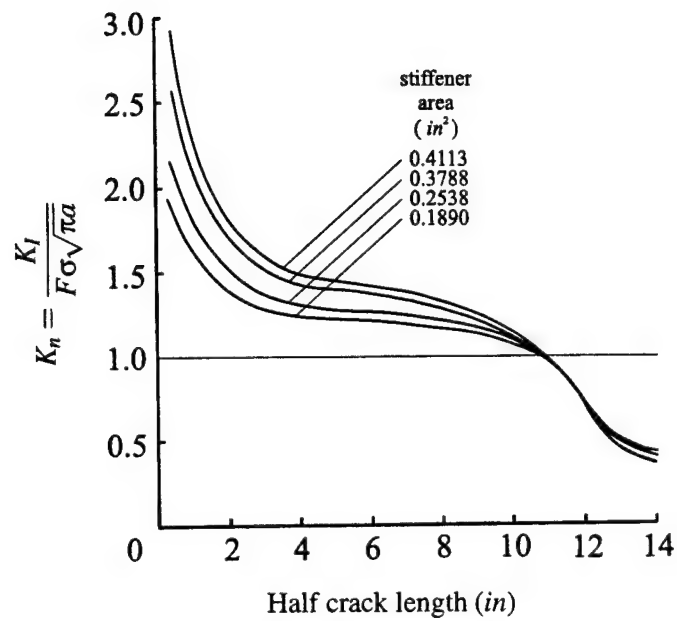


Figure 1.19: Effect of stiffening on crack-tip SIF, spacing 12 inches

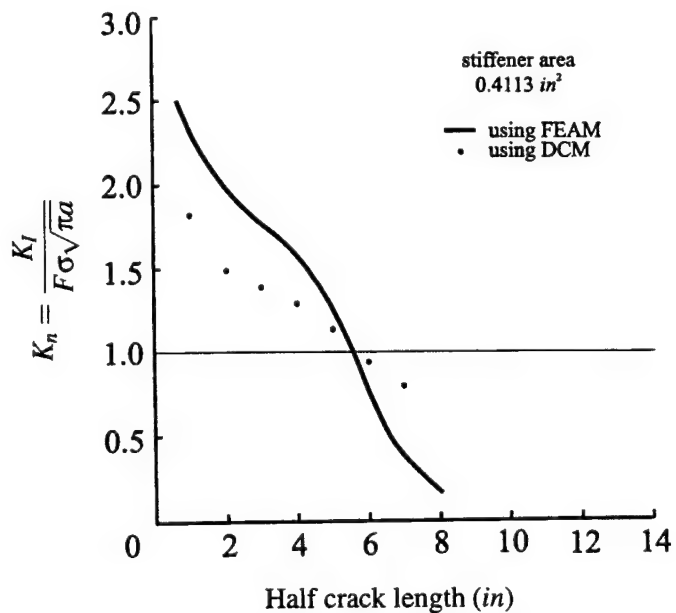


Figure 1.20: SIF by using FEAM and DCM, spacing 6 inches



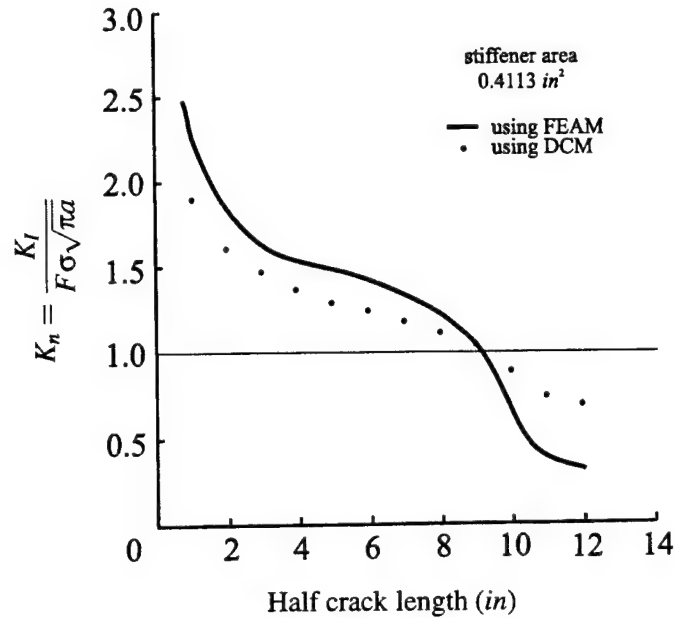


Figure 1.21: SIF by using FEAM and DCM, spacing 10 inches

due to the fact that the finite-size effects are accounted for in the present FEAM, as opposed to the displacement compatibility method wherein the sheet is treated as being infinite.

### § 1.3 Residual Strength of Aircraft Structures with a Single Dominant Flaw (Discrete Source Damage)

#### § 1.3.1 Introduction

Currently, the fleet of aging commercial aircrafts in the U.S. is operating under the concept of damage tolerance [Swift (1985)], which requires that an aircraft should have sufficient residual strength in the presence of damages in the principal structural elements during the interval of service inspections. Such damages include fatigue cracks, propagating at lengths between detectable and critical sizes, and discrete source damage (DSD), induced by foreign objects such as fragments in the case of engine disintegration.

A commercial aircraft is expected to sustain a discrete source damage as large as a two bay crack in the skin [see Fig. 1.22]. In an airliner fuselage, the stiffeners (stringers, frames and tear straps) take a part of the load, but the major fraction is taken by the skin. Large cracks in the skin cause significant redistribution of load

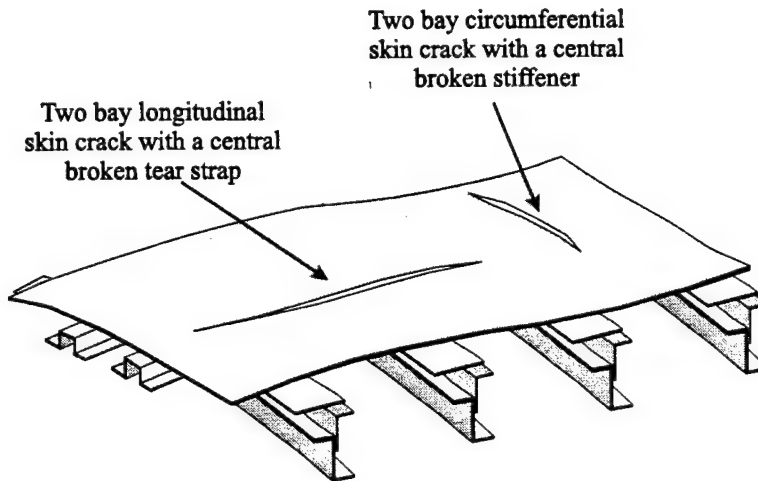


Figure 1.22: Damage tolerance requirement based on two-bay crack

flow, which becomes fairly complex due to the various stiffening elements and the presence of fastener holes and MSD ahead of the dominant crack. When the tip of a lead (dominant) crack approaches an intact stiffener, the stiffener takes over more load and reduces the local stress around the crack tip. Therefore, a residual strength analysis is necessary to understand the load carrying capability of a cracked aircraft structure.

To determine the critical MSD crack size that will reduce the residual strength of an aircraft fuselage to below an acceptable level, we must perform residual strength analysis of the fuselage in the presence of a lead crack and MSD. Non-linear material behavior must be considered in such a study. At the critical load, the plastic zone size ahead of the lead-crack tip in a typical cracked aircraft fuselage is as large as more than a half inch to several inches. However, the typical rivet spacing is only about 1 inch. Therefore, the zone of plastic deformation ahead of the lead crack is not negligible when compared to the size of the MSD cracks<sup>1</sup> and ligaments ahead of the lead crack. In an elastic fracture mechanics model, the deformation and stress are highly localized near the crack tip. Due to the plastic deformation, these stresses must be redistributed along the ligaments to achieve static equilibrium, as suggested in an Irwin model for the estimation of plastic zone size. Such stress redistribution can change significantly the loading condition of the ad-

<sup>1</sup> usually of the order of 0.01 ~ 0.04 in emanating from rivet holes of 0.1 in diameter

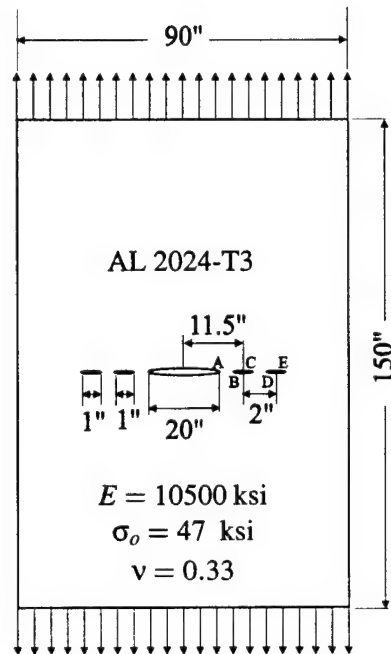


Figure 1.23: A lead crack and MSD in a flat sheet

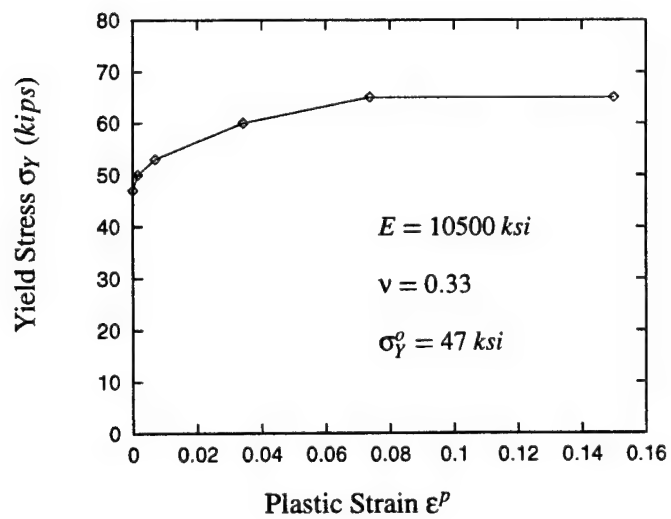


Figure 1.24: Flow curve for AL 2024-T3

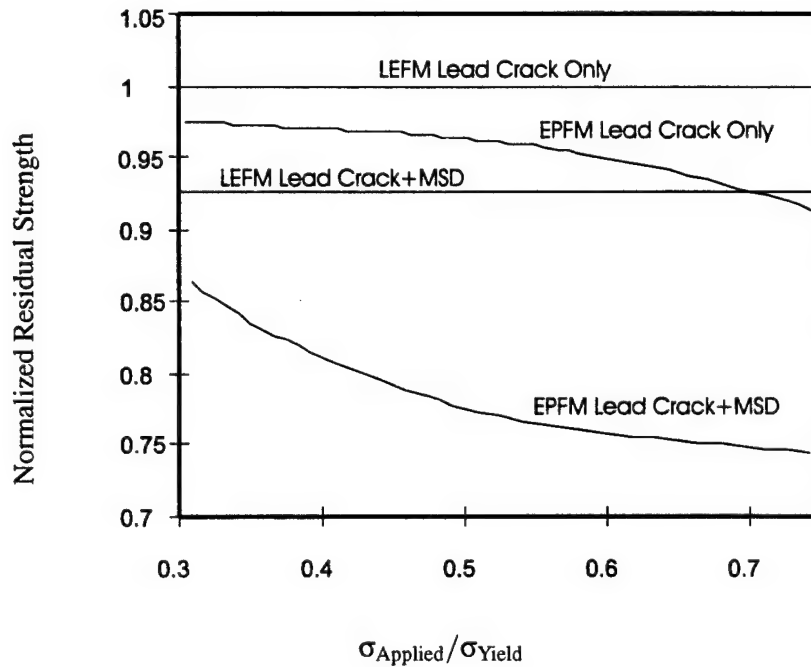


Figure 1.25: Normalized residual strength for i) the lead crack only case, using LEFM; ii) the lead crack only case, using EPFM; iii) the lead crack with MSD case, using LEFM; iv) the lead crack with MSD case, using EPFM.

jacent cracks in the MSD crack situation. On the other hand, the existence of MSD cracks limits the size of the ligaments on which the stress can be redistributed. Furthermore, the stress redistribution is much more complicated in the MSD situation due to the interaction between the MSD cracks and the lead crack. Therefore, a detailed elastic-plastic fracture analysis of the cracked panel is necessary.

Fig. 1.23 shows a typical MSD situation, in which there is a single lead crack located at the center of the flat panel. There are two MSD cracks ahead of each of the lead-crack tips. The length of the ligaments between adjacent cracks is 1-inch. The material is assumed to be AL 2024-T3. A piecewise linear flow curve is used for AL 2024-T3, as shown in Fig. 1.24. The effect of MSD cracks on the residual strength of a cracked panel and the importance of Elastic-Plastic Fracture Mechanics [EPFM] approach can be seen in Fig. 1.25.

Fig. 1.25 is the normalized residual strength plot for the panel shown in Fig. 1.23.

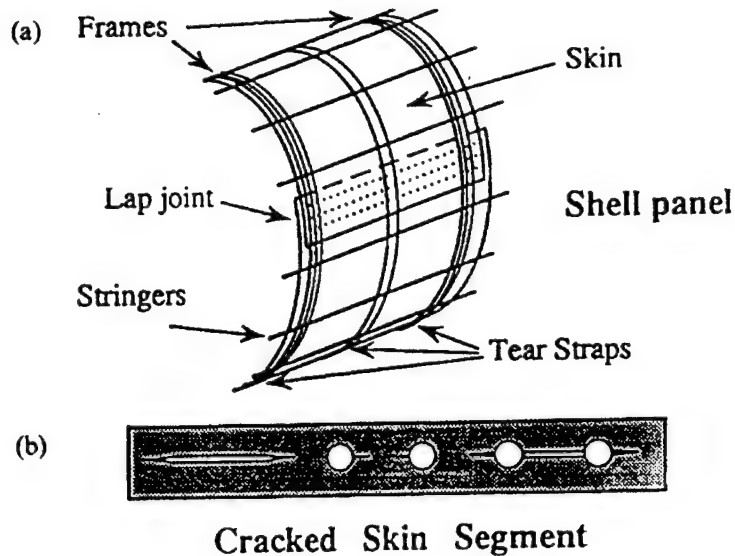


Figure 1.26: Fuselage shell panel configuration (a) Shell panel, (b) Cracked skin segment

The failure strength of the panel is defined as the magnitude of applied far field load at which the crack tip experiences the material fracture toughness  $K_{IC}$  (or the equivalent  $J_{IC}$ ). The residual strength is normalized with respect to the residual strength for the case where there is only a lead crack, obtained using Linear Elastic Fracture Mechanics [LEFM]. It is seen that the LEFM approach over-estimates the residual strength, as compared to the EPFM approach. For the case of a lead crack only in this panel configuration, the amount of over-estimation is very large. However, in the presence of MSD cracks, the LEFM approach can lead to a significant error, especially if the panel operates at a high stress level.

### § 1.3.2 Computational models

The fuselage shell panels under consideration in this section are typical of commercial airliners. They are stiffened along the longitudinal direction by stringers and circumferentially by frames and tear straps [see Fig. 1.1]. Tear straps are generally at frame locations, but can also be present at mid-frame stations depending upon the design philosophies. A typical configuration is shown in Fig. 1.26. Two shell geometries, one of each kind, have been considered. The geometrical details are

listed below.

	Shell 1	Shell 2
Shell radius R	118.5 in	74.0 in
Shell skin thickness t	0.071 in	0.036 in
Distance between frames	20.0 in	20.0 in
Distance between stringers	8.0 in	9.25 in
Distance between tear straps	20.0 in	10.0 in
Width of T-straps	3.0 in	2.0 in
Thickness of T-straps $t_t$	0.025 in	0.036 in
Frame area	0.7171 in <sup>2</sup>	0.160 in <sup>2</sup>
Frame moment of inertia	1.4320 in <sup>4</sup>	0.120 in <sup>4</sup>
Frame neutral axis offset	3.25 in	3.15 in
Stringer area	0.6721 in <sup>2</sup>	0.186 in <sup>2</sup>
Stringer moment of inertia	0.1020 in <sup>4</sup>	0.040 in <sup>4</sup>
Stringer neutral axis offset	0.68 in	0.78 in
Fuselage internal pressure	8.6 psi	9.0 psi
Rivet diameter D	0.1875 in	0.15625 in
Pitch of rivets	1.25 in	1.0 in
Material: skin, frame, stringers	Al 2024-T3	Al 2024-T3
Material: tear straps	Ti 8-1-1	Al2024-T3

The lap joint configuration considered is as follows:

Length of overlap	3.0 in
No. of rivet rows	3
Pitch of rivets	1.0 in
No. of rivets in each bay	20 × 3
Rivet diameter D	0.15625 in
Adhesive layer thickness $t_a$	0.00025 in
Material	Al 2024-T3.

The material properties of Al 2024-T3 and Ti 8-1-1 are taken as follows:

	Al 2024-T3	Ti 8-1-1
Young's modulus E	$10.5 \times 10^3 \text{ ksi}$	$17.5 \times 10^3 \text{ ksi}$
Shear modulus G	$4.2 \times 10^3 \text{ ksi}$	$6.7 \times 10^3 \text{ ksi}$
Poisson's ratio $\nu$	0.32	0.32
Yield strength $\sigma_y$	47.0 ksi	135.0 ksi
Ultimate tensile strength $\sigma_u$	64.0 ksi	145.0 ksi
Crack tip linkup stress $\frac{1}{2}(\sigma_y + \sigma_u)$	55.5 ksi	140.0 ksi
% Elongation	18%	8%

Fracture toughness  $K_{IC}$  is 93.0 ksi  $\sqrt{\text{in}}$ . Adhesive shear modulus is  $G_a = 1.09 \times 10^5 \text{ psi}$ .

Four situations of cracks are considered in § 1.3.3-§ 1.3.6:

1. a single dominant multi-bay crack in shell 1 (§ 1.3.3),
2. a single dominant multi-bay crack at a row of fastener holes in shell 1 (§ 1.3.4),
3. long cracks and MSD at lap splice in shell 2 (§ 1.3.5), and
4. a single dominant multi-bay crack at lap splice in shell 1 (§ 1.3.6).

#### *Global analysis (FEM)*

Conventional linear elastic finite element analysis of the multi-bay stiffened shell panel with cracks, is performed as a part of the global analysis. The FEM model is briefly described below:

The fuselage skin is modeled by four-noded shell elements, with five degrees of freedom per node. The element used is strain-based and was developed by Ashwell and Sabir (1972). Tear straps are also modeled using the same element. The frames and stringers are modeled as two-noded, three degrees of freedom per node, curved/straight beam elements with their shape functions degenerated from those of shell elements. This is done to ensure compatibility within the stiffeners and the sheet. The cracks are incorporated into the problem as unconnected nodes belonging to respective elements. For the purpose of present global analysis, the crack tip singularity is not modeled as the crack will be modeled analytically in the second step, i.e. the local analysis. The fasteners are modeled as two degrees of

freedom connectors between the corresponding nodes and the fastener stiffness is represented by the empirical relation developed by Swift (1984) [see Eq. 1.45, page 25].

Wherever there is a crack, the stiffness along the crack length is relieved as the fastener will not be able to bear the load in that direction. Adhesive is also modeled as a two-noded, two degrees of freedom per node connector between the sheets. The adhesive stiffness is modeled as

$$K_a = \mu_d \frac{A}{\frac{t_a}{G_a} + \frac{3}{8} \left( \frac{t_1}{G} + \frac{t_2}{G} \right)}, \quad (1.56)$$

where  $\mu_d$  is the degradation factor. The values of 0 and 1 represent total degradation and perfect conditions, respectively. A value of 0.1 means 90% degradation.  $A$  represents the bond area being lumped at the nodal connections. Appropriate multi-point constraints have been imposed to prevent crisscrossing of sheet nodes in the lap joint zone. The fuselage internal pressure is applied as a uniformly distributed normal outward load on the shell panel. The four edges of the panel are permitted to undergo only radial displacement in a cylindrical system. A typical problem size for the configurations considered is of the order of 15,000 degrees of freedom and the computer time is of the order of *min* on an HP 9000/700 series workstation.

#### *Elastic local analysis [E-FEAM]*

From the global analysis, the skin segment containing the cracks, holes and fasteners of interest, is isolated with corresponding sheet stresses. The fastener holes are now modeled as circular and the bearing loads (if any, from global analysis) are distributed as sinusoidal variations over the periphery. The stresses due to the misfit of the rivet can also be accounted for at this stage. This problem is solved using the Schwartz-Neumann Finite Element Alternating Method which involves two solutions.

1. An analytical solution to the problem of a row of cracks of arbitrary lengths with crack faces being subjected to arbitrary tractions,
2. Finite element solution for a strip, with/without a row of holes, but without cracks; the strip being subjected to sheet stresses and pin bearing loads. Since the finite element solution is only for the uncracked body and the cracks of arbitrary lengths are accounted for analytically in step 1 above, the computational finite element mesh remains the same as the cracks grow.



The analytical solution to the problem of multiple cracks in an infinite sheet and the alternating technique are presented in detail in Chapter ?? and Chapter ??. Eight-noded isoparametric elements with two degrees of freedom per node are employed in this finite element analysis.

The crack tip stress intensity factors and the stress field are obtained directly from the FEAM analysis. The net section stress for any ligament is obtained by taking an average over the ligament length. To compute the plastic zone size, Irwin's formula does not seem to give a reasonable approximation, due to the complexity of geometry and vicinity of other cracks/loaded-holes. So the plastic zone size is estimated from the computed stress field, obtained from the linear elastic analysis, by doubling the distance from crack tip to the point where the stress falls to yield stress.

Critical pressure for the fuselage is that value of applied pressure differential for which either the crack tip SIF becomes equal to  $K_{IC}$  of  $93.0 \text{ ksi}\sqrt{\text{in.}}$ , or the net ligament stress equals the linkup stress of  $55.5 \text{ ksi}$ . For linear elastic analysis, this can be computed directly from the obtained values of  $K_1$  and average ligament stress  $\sigma_{av}$ .

$$\text{Critical pressure differential} = \text{applied pressure} \times \frac{K_{IC}}{K_1}$$

or

$$\text{Critical pressure differential} = \text{applied pressure} \times \frac{\text{linkup stress}}{\sigma_{av}}$$

### § 1.3.3 *Single dominant multi-bay crack in the skin*

Consider a panel of shell 1, consisting of seven frames (six bays) and six stringers (five bays). There are seven tear straps, one at each frame location. Consider a single dominant crack aligned longitudinally and located centrally, i.e. halfway between two stringers and symmetrical about a frame/strap location. The fuselage stiffened shell must be able to sustain a two-bay-long crack with broken central strap. For this requirement, consider the central tear strap also to be cracked along with the skin. All other stiffening elements are intact.

Analyses have been carried out for various crack lengths up to  $50 \text{ in.}$ , i.e. the crack spreading in four bays. Since there is only one crack and there are no holes in the vicinity of the crack tip, it is difficult to reasonably define an intact ligament length, thus the critical pressure is computed only from the fracture mechanics point of view (Fig. 1.27).

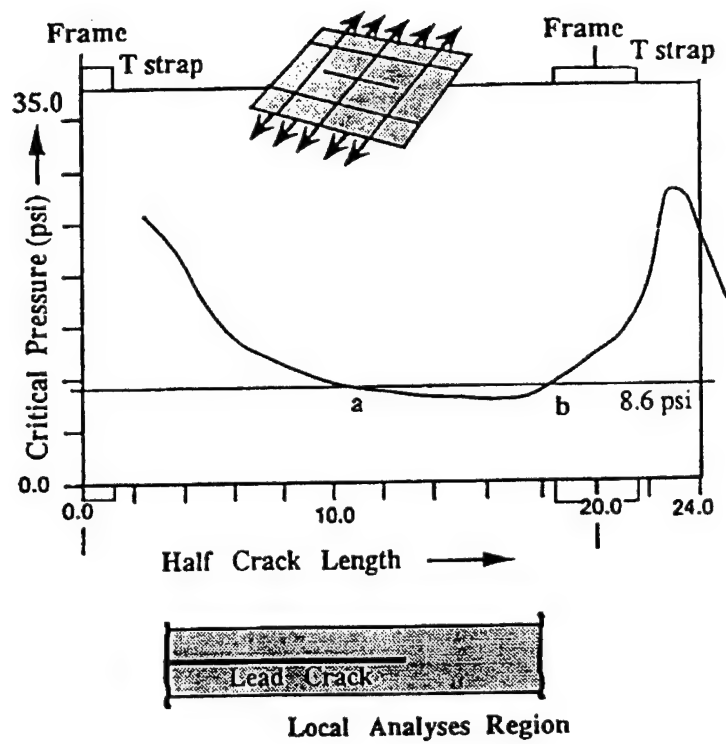


Figure 1.27: Critical pressure diagram for a single dominant mutibay crack in the shell panel

A point on this curve gives information about the cabin pressure required to make the crack tip SIF critical and does not imply that the panel will fail catastrophically. The curve falls below the applied pressure of 8.6 *psi* for crack lengths of 10.8 and 18.2 *in* (points "a" and "b"). The implication of this is as follows. Considering an initial half crack length of, say, 2 *in* and the pressure never exceeding 8.6 *psi*, the crack cannot grow under static loading; it will grow under cyclic loading till it reaches point "a". At this stage, fast fracture will occur and the crack will instantaneously grow up to point "b", where it will be arrested as the SIF falls below the critical value. Further growth of the crack will be again under cyclic loading. The effect of plasticity is not included in this calculation, and stable tearing that follows crack growth initiation is not modeled.

#### § 1.3.4 *Two-bay crack with holes near the crack tip*

Consider a panel of shell 1, consisting of seven frames (six bays) and seven stringers (six bays). There are seven tear straps, one at each frame location. Consider a single dominant crack aligned longitudinally along the fastener holes. The crack is located centrally and is symmetrical about a frame/strap location. The central tear strap is broken. All other stiffening elements are intact. The presence of holes alters the stress flow. The distance between the crack tip and the hole periphery is found to have substantial effect on the crack tip SIF and also, for very small ligaments, the section will yield before the crack becomes unstable. A situation of holes ahead of a two-bay crack is analyzed to study the effects of holes on the critical pressure.

Fig. 1.28 shows the effect of holes ahead of a two-bay crack. For the sake of convenience we will use a term "overhang", defined as the extent of crack length from the closest hole center involved in the same crack. Zero overhang implies a hole at the crack tip and so the SIF has no definition. For extremely small overhang, the SIF value is low and for longer overhangs, the SIF rises sharply. The ligament stress is found to increase steadily with overhang. For any crack length and overhang, the critical pressure is the lower of the two values corresponding to  $K_I = K_{IC}$  and  $\sigma_{av} = \text{linkup stress}$ .

Fig. 1.28 shows the critical pressure from both considerations and interestingly, the structure is critical from the net section failure point of view over most of the region. Thus, small scale yielding assumption breaks down here. The linear elastic fracture parameter can not be used as a failure criteria.

Again, any point on this curve represents the pressure differential required to either make the crack unstable, or cause tensile failure of the ligament. It is seen from this analysis that the presence of holes (even without cracks emanating from

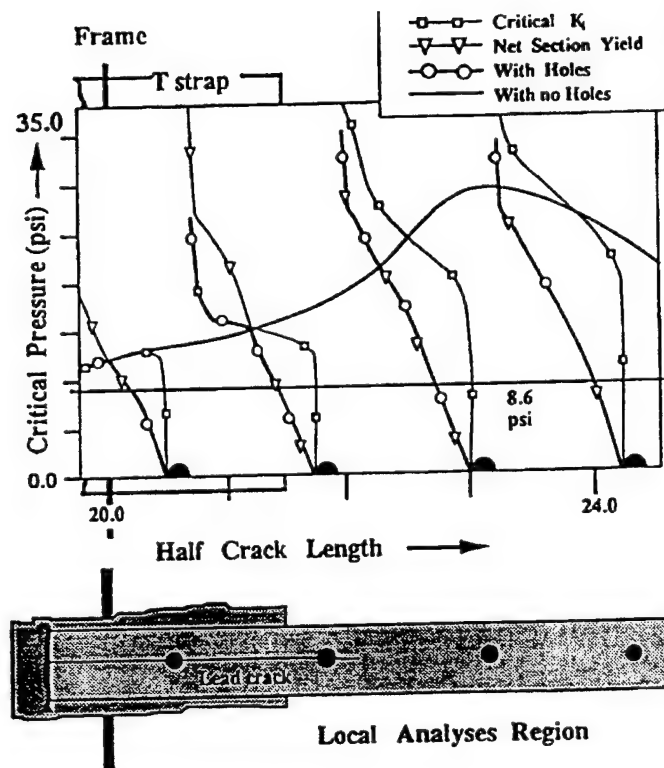


Figure 1.28: Critical pressure diagram for a single dominant 2-bay crack with holes ahead of the crack tip

them) ahead of a lead crack, significantly lowers the residual strength of a stiffened panel; as surmised by Swift (1993a, 1987).

### § 1.3.5 *Long crack and MSD in lap splice*

We now consider the problem of a riveted/bonded longitudinal lap joint in the shell panel. Skin stresses have to flow through this joint. So long as the adhesive is in a good condition, it transfers most of the load across the lap, but the adhesive is found to degrade fairly fast with usage and time, and make the fasteners the major load carriers. The presence of cracks at rivet holes causes further load redistribution. An important aspect of the situation is how one crack effects other cracks in its close vicinity.

Consider the fuselage panel 2 with a longitudinal riveted/bonded lap joint. Let there be cracks at the outer (critical) row of fastener holes. The adhesive is treated to be degraded, so that fasteners share a major part of the hoop load. The fuselage panel considered for analysis, consists of three bays in the longitudinal direction and six bays along the circumferential direction. This panel contains four frames, seven tear straps and seven stringers. Tear straps exist at all frame and mid-frame stations. The cracks are only considered in the central bay. Fig. 1.29 shows 12 cases [B-M] of crack configurations that have been analyzed in this section. Case A is the uncracked situation and forms a reference. These configurations have no relationship with each other and the long crack configurations are not necessarily arrived at through linkup of small crack situations. In all these cases, the stiffening elements (frames, T-straps and stringers) are all intact.

#### *Global load distribution*

The uncracked panel is analyzed as in the first case, to obtain a reference and understand the original load flow path. After the adhesive has virtually degraded (99% for the present problem) the rivets transfer a large part of the hoop load. In this situation 83% goes through the fasteners and only 17% of the load is taken by the frames/straps. Among the three rows of fasteners, the outer two carry 36% each and the rest of the 28% is taken by the central row. In a flat panel lap joint, normally, the center row carries a much lesser portion. The curvature seems to be a cause of more even row-wise load distribution. The maximum sheet hoop stress is found to be 13.4 ksi.

The presence of cracks at rivet holes causes load redistribution at the joint. For various cases considered [A-M] the load changes in straps/frames in the damaged

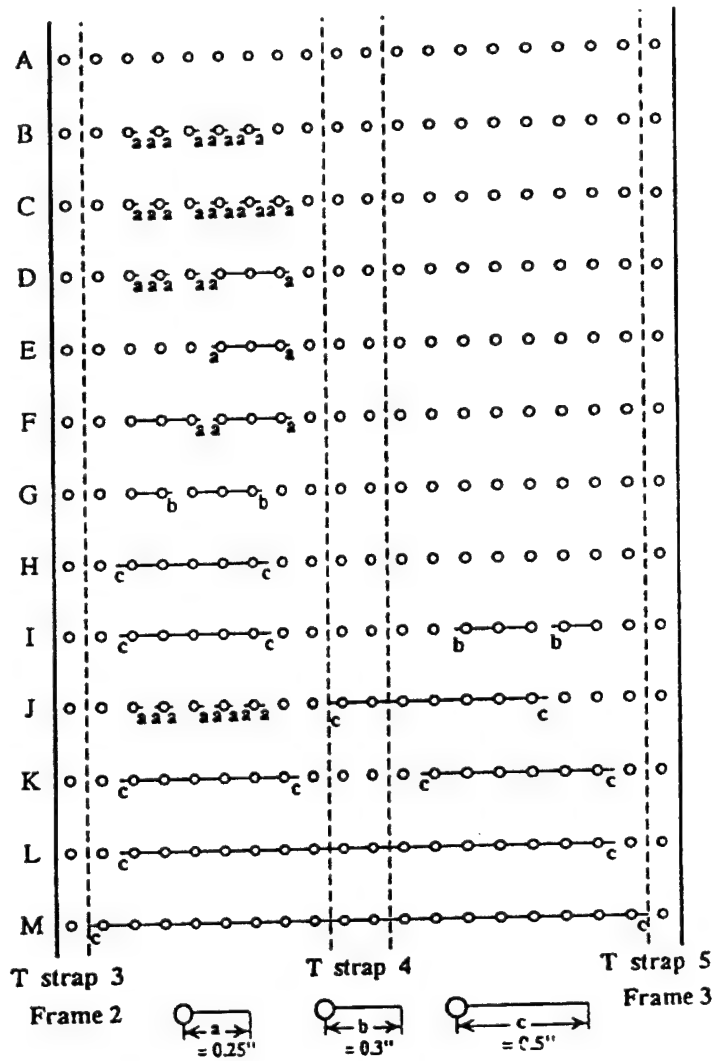


**Figure 1.29: Crack Configurations analysed to study the long crack and MSD interaction at lap splice**

Table 1.2: Load redistribution at frames/T-straps for various cases (lb)

Case	Frame 2	T-strap 3	T-strap 4	T-strap 4	Frame 3
A	1127	24.5	228	24.5	1127
B	1142	34.6	211	24.1	1127
C	1142	34.5	218	23.9	1127
D	1146	34.9	248	21.8	1126
E	1142	32.5	248	22.0	1126
F	1168	47.5	250	20.4	1126
G	1153	40.2	221	22.6	1127
H	1232	86.6	240	16.6	1125
I	1231	84.4	252	32.3	1151
J	1104	-9.4	1510	-4.5	1121
K	1284	100	489	90.0	1271
L	1246	19.9	4163	19.9	1246
M	1535	230	4558	230	1535

Table 1.3: Row-wise rivet load distribution (lb)

Case	Raw 1		Raw 2		Raw 3		Total load
	Load	%	Load	%	Load	%	
A	3394	36.1	2600	27.7	3405	36.2	9398
B	3305	35.2	2682	28.6	3395	36.2	9383
C	3278	34.9	2696	28.7	3402	36.3	9377
D	3280	35.1	2673	28.6	3385	36.3	9339
E	3302	35.3	2661	28.5	3382	36.2	9347
F	3267	35.2	2654	28.6	3366	36.2	9288
G	3361	35.9	2627	28.1	3358	35.9	9347
H	3223	35.2	2615	28.6	3315	36.2	9154
I	3201	35.1	2633	28.9	3272	35.9	9107
J	2778	34.1	2421	29.7	2956	36.2	8156
K	2937	34.7	2485	29.4	3033	35.9	8458
L	1669	34.6	1442	29.9	1718	35.6	4831
M	1101	34.5	952	29.8	1141	35.7	3195

bay are given in Tab. 1.2. It can be observed from this table that MSD, or long cracks, [B-I] do not significantly overload the frames and straps. Even for case I, where one may say that the T-strap load has gone up from 24.5 to 84.4lb, numerically both these values are insignificant as compared to the yield strength of 3384lb ( $2 \times 0.036 \times 47000 = 3384$ ) for the strap. Some amount of overloading for the central T-strap can be seen in cases J and K, where cracks exist across it. From cases K-M, it is evident that if two cracks approach a tear strap from both sides and linkup at a location where there is no frame, the strap will yield.

For all the cases, the row-wise rivet load distribution within the damaged panel is given in Tab. 1.3. It can be observed that as the crack length increases and the load is shed from the rivets, the relative share of the three rows changes marginally. Thus, as the cracked row sheds the load, the other two rows also do so and effectively, the load goes into the skin and the frames/straps. Physically, this appears



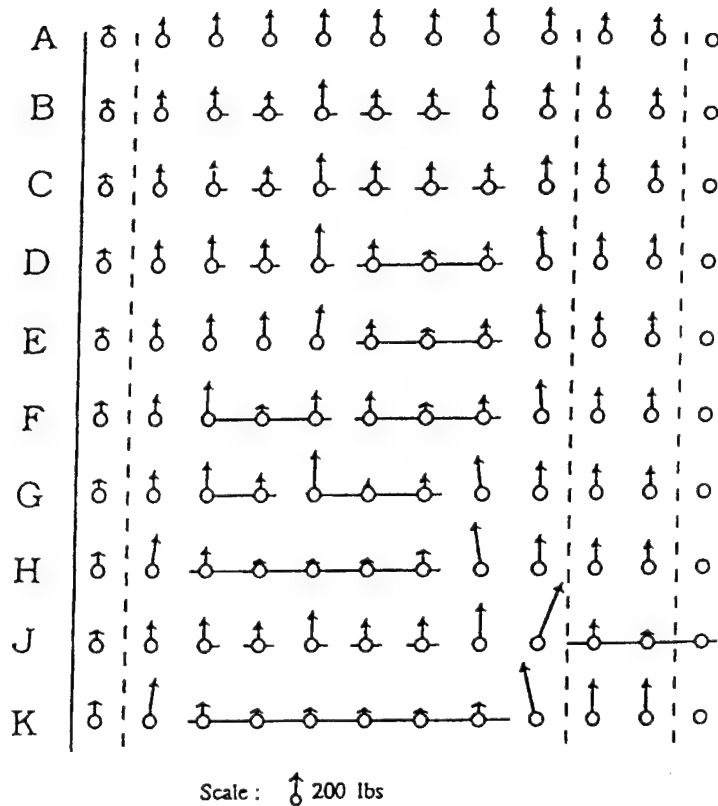


Figure 1.30: Rivet load redistribution pattern due to cracks at fastener holes in lap splice

correct as the rivet rows are 1 *in* apart and with a crack of a few inches in the first row, the second and third rows will hardly get any load to share.

The rivet-wise load redistribution pattern for the critical row for all the cases [A-M] is given in Tab. 1.4. To have an overall qualitative idea of the load redistribution, the loads are also plotted to scale in Fig. 1.30. Rivet numbers 1-10 run from left to right in the damaged bay. A crack diverts the load towards its tips. So, intuitively a crack on one side of the hole should overload the fastener, and cracks on both sides will unload it. Rivets 5 and 6 of cases A and B clarify this point. On a similar logic, the stresses in the ligament between two crack tips will be high and further increase with crack growth. At some stage of loading, the ligament will yield, causing a crack linkup to form a single long crack.

Table 1.4: Rivet load distribution in the critical row (lb)

Rivet	Case												
	A	B	C	D	E	F	G	H	I	J	K	L	M
1	135	141	141	143	141	151	145	176	176	148	203	246	365
2	148	146	146	149	145	171	156	246	246	151	311	388	120
3	164	166	167	172	163	236	195	141	142	170	107	133	35
4	274	123	123	133	186	62	107	40	40	125	33	41	17
5	180	198	200	238	229	150	273	26	26	202	18	20	11
6	182	135	138	126	122	154	60	35	35	140	17	12	9
7	181	132	140	58	57	63	106	101	101	140	29	8	8
8	181	187	131	116	115	121	222	305	305	210	74	3	3
9	179	171	182	217	216	224	183	214	215	269	371	-5	-6
10	168	191	195	208	208	211	196	210	213	75	294	-14	-15
11	168	186	187	191	191	192	188	193	204	18	279	-14	-15
12	179	175	175	176	176	177	176	178	186	8	354	-5	-6
13	181	180	180	180	180	180	180	181	223	11	111	3	3
14	181	181	181	181	181	181	181	181	106	21	35	8	8
15	182	182	182	182	182	182	182	182	60	46	19	12	9
16	180	180	180	180	180	180	180	180	273	175	19	20	11
17	174	174	174	174	174	174	174	174	108	322	33	41	17
18	164	164	164	164	164	164	164	164	196	216	104	133	35
19	148	148	148	148	148	148	148	148	157	171	319	388	120
20	135	135	135	135	135	135	135	135	147	150	196	246	365

Comparing the rivet load patterns for cases H and I, we can see that even long cracks across the tear strap do not affect each other. The rivets involved in long cracks take very little load, thus significantly overloading the neighboring rivets (case H). In these cases, the neighboring rivets are also found to bear some side load as a consequence of inclined load flow path through the skin, at the row of rivets. The side load on rivet 8 of case I is of the order of 55 lb towards rivet 7, and rivet 9 in case J is 48 lb towards rivet 10. Very long cracks (over 10 rivets) are found to even reverse the load direction on some of the centrally located rivets (cases L and M). This happens due to inplane bending, again as a consequence of load flow diversion due to the crack. This analysis is, of course, not correct as the tear strap has yielded. Thus, the cases L and M are not further analyzed. Looking at Tab. 1.4 one can see that case I is essentially the case when the configuration H exists on the left side of the tear strap and the configuration G exists on the right side of the tear strap. In this case, although the strap is overloaded, there is no mutual interaction between the cracks and so it need not be analyzed as an independent case.

*Local analysis results: net section stress and plastic zones*

The finite element alternating technique is employed to cases of interest, viz. B-H, J and K, by isolating the cracked portion (row and bay) from the panel. Crack tip parameters and stress fields are obtained from these analyses. The net section stresses and plastic zones are then computed. Fig. 1.31 shows the maximum net section stresses and the residual strength in terms of cabin pressure based on the linkup stress of 55.5 ksi. Case J is intended to study the effect of a large crack on MSD and so the local analysis is performed only on the MSD region and the indicated maximum stress is not for the complete section, which is likely to be between rivet 9 and 10. The following observations are made from this figure:

Case B and C: The maximum net section stress is not significantly increased by MSD and adequate residual strength still exists in the panel.

Case C and D: Linkup shoots up the maximum net section stress.

Case B and J: A long crack on or across the tear strap marginally increases the net section stress in the MSD zone.

Case D and E: MSD near a long crack increases the ligament stress.

Case F-H and K: One or two long cracks involving five or more rivets push the maximum stress beyond yield stress, thus substantially reducing the residual strength. The sections at the crack tips either yield (F, H, K) or tend to yield (O).

The stress intensity factors and the corresponding residual strength obtained with  $K_{IC} = 93.0 \text{ ksi}\sqrt{\text{in.}}$  are shown in Fig. 1.32. The following observations are

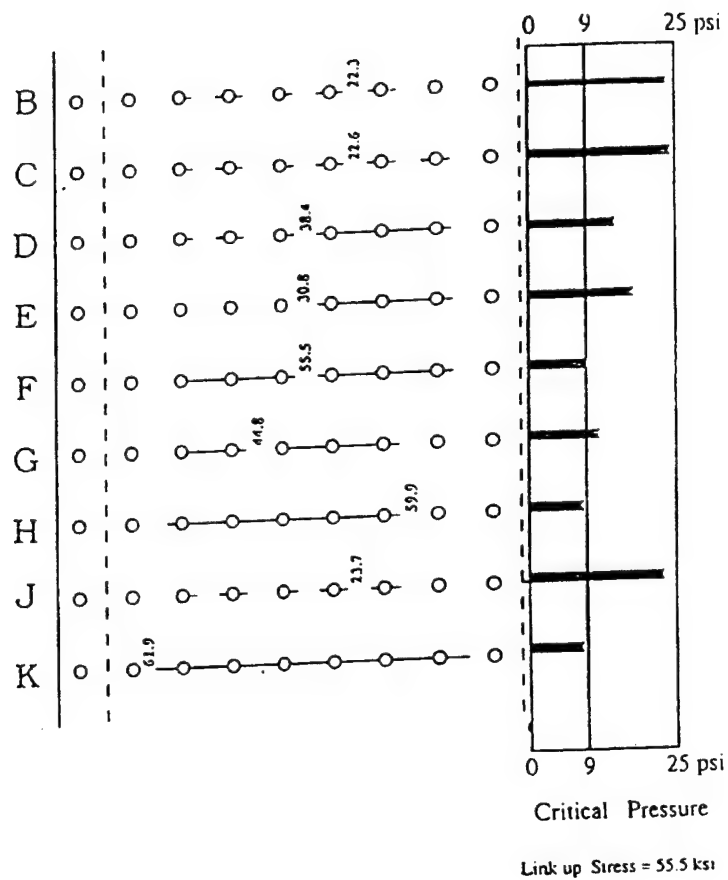


Figure 1.31: Maximum net section stresses and the corresponding critical cabin pressure (psi) based net ligament stress criterion.

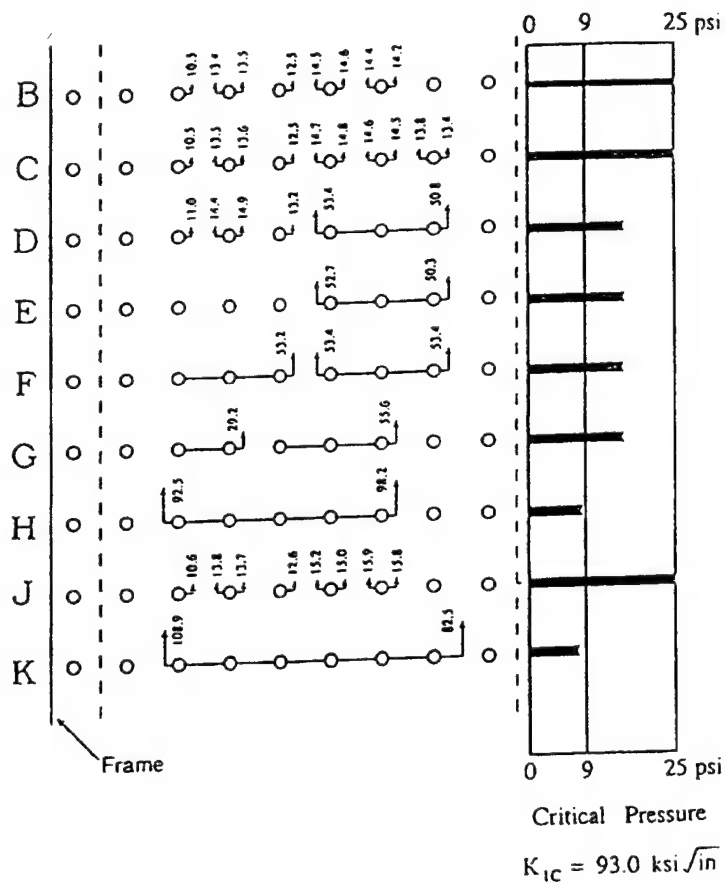


Figure 1.32: Stress intensity factors and the corresponding critical cabin pressure (psi) based on Fracture mechanics criterion.

Table 1.5: Residual Strength for various caes considered (cabin pressure, psi)

Case	Linear Fracture mechanics		Net section stress	
	Max $K_I$	Critical pressure	Max $\sigma_{av}$	Critical pressure
B	14.6	57.33	22.3	22.40
C	14.8	56.55	22.6	22.10
D	53.4	15.67	38.4	13.00
E	52.7	15.88	30.8	16.21
F	53.4	15.67	55.5	9.00
G	55.6	15.05	44.8	11.15
H	98.2	8.52	59.9	8.34
J	15.9	52.64	23.7	21.08
K	108.9	7.68	61.9	8.07

made from this figure:

Case B and C: Short and medium MSD cracks at neighboring rivets have marginal effects, e.g. SIF at rivet 7 goes up from 14.2 to 14.5 due to a crack at rivet 8. Short/medium cracks, one rivet hole apart, do not interact. Adequate residual strength exists in these situations.

Case C and D: Linkup causes significant increase in the crack tip SIF, but has little effect on the SIF at MSD in the neighborhood.

Case D and E: Linked up cracks in close proximity affect each other marginally and do reduce the residual strength.

Case H and K: In moving from H to K, one more fastener hole is involved. Interestingly, the SIF on one end falls and goes up on the other end. This is due to the load redistribution. The residual strength for these cases has just fallen below the applied load of 9.0 *psi*.

The maximum SIF, net section stresses and the corresponding residual strengths are listed in Tab. 1.5.

Looking at Figs. 1.31 and 1.32, and Tab. 1.5 it is quite clear that the net ligament yields before the crack becomes unstable, under static loading conditions. Plastic zone sizes for all the cases have been computed (Fig. 1.33). For MSD cases B, C and J, the plastic zones are insignificantly small. They are found to grow as cracks



Table 1.6: SIFs and the corresponding plastic zones for all crack tips

Case	$K_I$	$r_p$	Case	$K_I$	$r_p$	Case	$K_I$	$r_p$
	10.5	0.0160		11.0	0.0176		10.6	0.0171
	13.4	0.0269		14.4	0.0318		13.8	0.0274
	13.5	0.0271		14.9	0.0331		13.7	0.0274
B	12.5	0.0205	D	13.2	0.0181	J	12.6	0.0214
	14.5	0.0303		53.4	0.2142		15.2	0.0307
	14.6	0.0300		50.8	0.2010		15.0	0.0303
	14.4	0.0299	E	52.7	0.2101		15.9	0.0314
	14.2	0.0296		50.3	0.1986		15.8	0.0316
	10.5	0.0161		53.2	0.2882	K	108.9	0.3395
	13.5	0.0272	F	53.4	0.2089		82.5	0.2873
	13.6	0.0274		53.4	0.2121			
	12.5	0.0208	G	29.2	0.1.90			
C	14.7	0.0313		55.6	0.2237			
	14.8	0.0311	H	92.5	0.2923			
	14.6	0.0304		98.2	0.3210			
	14.5	0.0301						
	13.8	0.0285						
	13.4	0.0279						



link up. Tab. 1.6 gives the various  $K_I$  and  $r_p$  values for all the crack cases analyzed. Plastic zone size becomes significant once  $K_I$  exceeds 50.0, which happens when three or more rivets are involved in a single crack.

### § 1.3.6 *Two-bay cracking at lap splice*

We now consider the aspect of a multi-bay crack with, and without, MSD ahead of it. In this section, we consider a panel of shell 1, consisting of six bays in the longitudinal direction and six bays along the circumferential direction, and a lap joint. This panel contains five frames, five tear straps and seven stringers. Tear straps exist at all frame stations. Let there be a long crack extending equally on two sides of the central broken tear strap. All the other stiffening elements (frames, T-straps and stringers) are considered intact. We are interested in the residual strength for various lead crack lengths and the effect of MSD ahead of the crack tip.

#### *Single dominant crack at fastener holes*

First consider the situation of a single dominant crack only. Global analysis is carried out to obtain the rivet bearing loads and then local FEAM is applied to obtain the crack tip SIF and net section stresses.

In the last section, we saw that the magnitude of crack length from the hole center (overhang) is an important factor in determining the critical pressure. For a single dominant crack, at the outer critical row of fasteners, spreading equally on both sides of a broken tear strap, the critical pressure diagram is shown in Fig. 1.34. Linkup stresses for the lead crack (ahead of which there are fastener holes, but without MSD cracks) correspond to the net section yield between the crack tip and the fastener hole. Up to 40% overhang, the shell panel is  $K_{IC}$  critical and for the later half, it has too little section strength. Interestingly, a two-bay crack is fully section strength critical. Frames/tear straps appear to provide adequate residual strength to the panel.

#### *Single dominant crack and MSD at fastener holes*

We now explore the effect of MSD near fastener holes ahead of the dominant crack in a lap splice. The important parameters are the lead crack length, the lead crack overhang from the nearest fastener hole, and the number and lengths of MSD cracks near fastener holes ahead of the lead crack. The MSD considered for the present purposes is over the three rivets immediately ahead of the lead crack tip, as the far away MSD cracks have insignificant effect on the lead crack tip stress field and

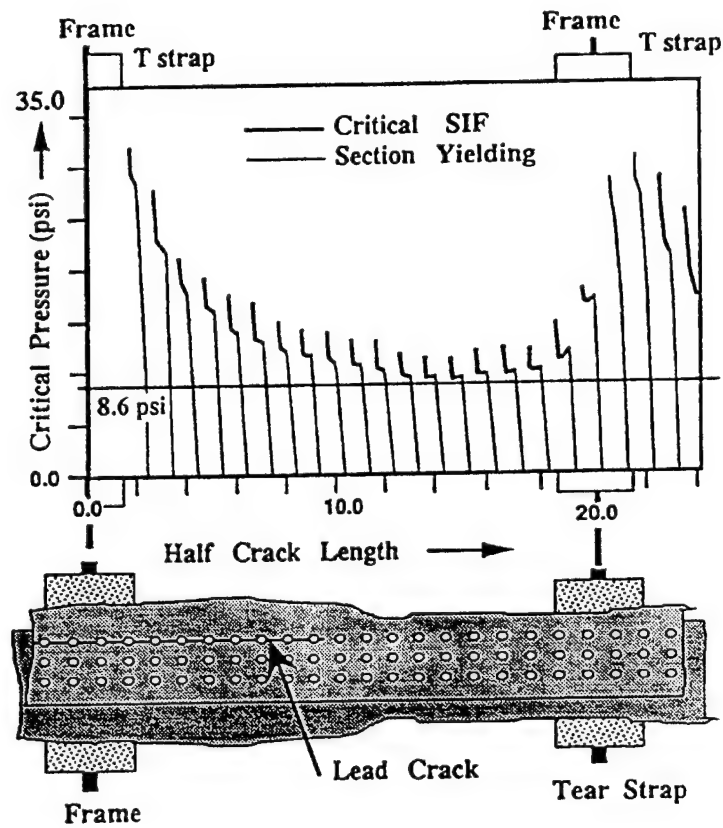


Figure 1.34: Critical pressure diagram for a single dominant multibay crack at outer critical row of fastener holes in a lap splice

also have lower intact ligament stress. In the MSD zone, cracks of equal length are presumed to be present on both sides of the rivet holes. To understand the MSD effects, for various lead crack lengths, starting from a situation where the lead crack spans over only two holes, to a situation of a multi-bay crack involving more than 40 rivets, the following two sets of crack configurations (overhang and MSD length) are analyzed.

1. MSD length of 0.12 *in*, which corresponds to the maximum that can hide under the countersunk head and stays undetected during regular economical nondestructive inspections. Two values of lead crack overhang, viz. 0.25 *in* and 0.50 *in*, are considered.
2. Lead crack overhang of 0.25 *in*, and the MSD lengths of 0.12, 0.25 and 0.35 *in*

The analyses for the configurations of the two sets are performed and the residual strengths are computed, based on linear elastic fracture mechanics, as well as net section stress criteria (Tabs. 1.7, and 1.8).

From Tab. 1.7, it can be seen that the small MSD cracks (0.12 *in*.) have marginal effect on the residual strength of the shell panel, whether it is computed based on linear elastic fracture mechanics or section yielding criteria. Of course, for relatively large overhang values, i.e. 0.75 *in*., the section stress shoots up with the presence of MSD.

We see that the MSD does not significantly alter the lead crack tip SIF, but does raise the net ligament stress when the two crack tips come closer. Thus, the main conclusion is: the use of linear elastic fracture mechanics to study the effect of MSD infested holes ahead of a lead crack is highly questionable. It may be concluded that the effect of plasticity and net section yield dominate the situation when holes with MSD cracks are present ahead of a lead crack. The need for an elastic plastic analysis of the lead crack-MSD interaction is further highlighted in the following section

#### **§ 1.4 Residual Strength of Aircraft Structures under Discrete Source Damage: Use of Elastic-Plastic Fracture Mechanics**

Structural integrity evaluation of aging aircraft structures is extremely important in ensuring the safety of the operation of these structures. A fuselage of an aircraft would typically undergo a cycle of pressurization for every single flight operation.

Table 1.7: Effect of MSD on  $K_I$ ,  $\sigma_{av}$  and residual strength. Set 1, constant MSD crack length of 0.12 in.

Half crack length	LEFM				Net section stress			
	$K_I$		Critical pressure		$\sigma_{av}$		Critical pressure	
	No MSD	MSD	No MSD	MSD	No MSD	MSD	No MSD	MSD
Lead crack overhang=0.25 in.								
1.75	27.5	28.4	28.5	27.6	12.1	12.4	39.4	38.5
3.75	41.2	42.1	19.0	18.6	16.7	17.4	28.6	27.4
5.75	53.8	54.2	14.5	14.4	21.5	22.4	22.2	21.3
7.75	64.4	64.0	12.2	12.2	25.8	26.9	18.5	17.7
9.75	72.7	71.5	10.8	10.9	29.6	31.0	16.1	15.4
11.75	79.4	77.5	9.9	10.1	32.9	34.4	14.5	13.9
13.75	84.8	82.2	9.2	9.5	35.4	37.1	13.5	12.9
15.75	88.0	83.1	8.9	9.4	36.7	38.5	13.0	12.4
17.75	81.9	79.2	9.6	9.9	34.7	36.0	13.8	13.3
18.75	68.8	65.5	11.4	11.9	29.6	30.5	16.1	15.6
19.75	47.6	43.2	16.4	18.1	22.6	23.1	21.1	20.7
20.75	28.6	25.2	27.4	31.1	19.4	19.7	24.6	24.2
21.75	30.7	28.6	25.5	27.4	17.6	18.3	26.7	26.1
22.75	36.4	35.1	21.5	22.3	18.6	19.1	25.7	25.0
Lead crack overhang=0.50 in.								
2.00	27.7	28.3	28.3	27.7	19.4	20.6	24.6	23.2
4.00	41.2	41.8	19.0	18.7	27.1	29.1	17.6	16.4
6.00	53.9	54.1	14.5	14.5	34.9	37.5	13.7	12.7
8.00	64.6	64.2	12.1	12.2	41.8	44.9	11.4	10.6
10.00	73.1	72.0	10.7	10.9	47.8	51.2	10.0	9.3
12.00	80.0	78.3	9.8	10.0	52.8	56.5	9.0	8.4
14.00	85.6	83.2	9.1	9.4	56.7	60.6	8.4	7.9
16.00	88.6	84.3	8.8	9.3	58.6	62.2	8.1	7.7
18.00	81.5	78.9	9.6	9.9	54.2	57.2	8.8	8.3
19.00	67.4	64.2	11.6	12.2	44.8	47.1	10.7	10.1
20.00	47.5	43.6	16.5	17.9	33.2	34.3	14.4	13.9
21.00	31.5	28.4	24.8	27.6	28.2	28.5	16.9	16.7
22.00	32.6	30.8	24.0	25.4	26.8	27.6	17.8	17.3
23.00	37.5	36.4	20.9	21.5	28.6	29.9	16.7	16.0

Table 1.8: Effect of MSD crack length on residual strength. Set 2

Half lead crack length	Residual strength based on							
	LEFM				Net section stress			
	MSD crack length				MSD crack length			
	No MSD	0.12 in	0.25 in	0.35 in	No MSD	0.12 in	0.25 in	0.35 in
1.75	29.0	28.2	28.1	27.9	39.4	38.5	30.2	23.0
3.75	19.4	19.0	18.8	18.5	28.6	27.5	21.4	16.2
5.75	14.9	14.8	14.6	14.3	22.3	21.3	16.6	12.5
7.75	12.4	12.5	12.4	12.1	18.5	17.7	13.8	10.4
9.75	11.0	11.2	11.1	10.9	16.1	15.4	12.0	9.1
11.75	10.1	10.3	10.2	10.1	14.5	13.9	10.8	8.2
13.75	9.4	9.7	9.7	9.5	13.5	12.9	10.0	7.7
15.75	9.1	9.6	9.6	9.4	13.0	12.4	9.7	7.4
17.75	9.8	10.1	10.1	10.0	13.7	13.3	10.4	8.0
18.75	11.6	12.2	12.1	12.1	16.1	15.6	12.3	9.6
19.75	16.8	18.5	18.5	18.4	21.1	20.7	16.5	13.0
20.75	28.0	31.7	31.9	32.1	24.5	24.3	19.6	15.6
21.75	26.1	27.9	27.9	27.9	26.7	26.1	20.8	16.3
22.75	22.1	22.8	22.6	22.4	25.7	25.0	19.8	15.3

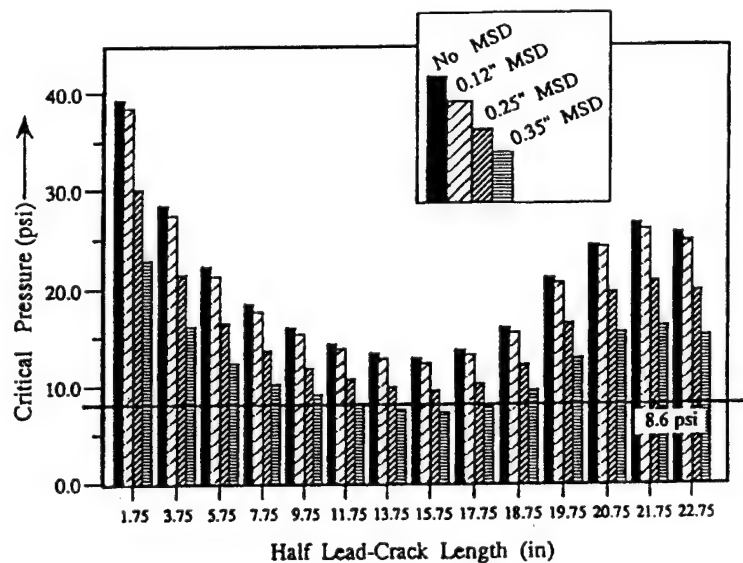


Figure 1.35: Effect of MSD crack length on residual strength, based on net section yield criterion

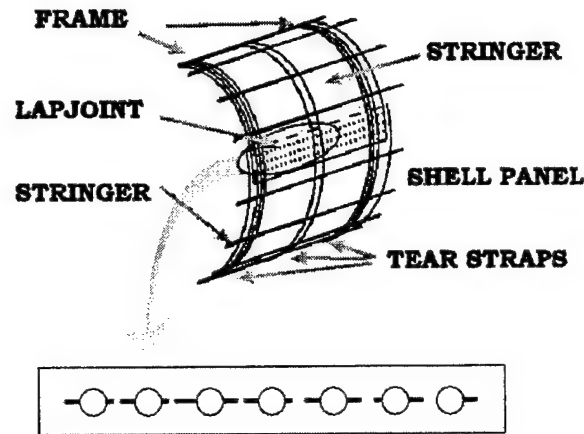


Figure 1.36: Widespread fatigue on fuselage panel

These cycles of pressurization would result in fatigue cracking near the rivet holes of the fuselage panel and may lead to a widespread fatigue damages (WFD). With the formation of widespread fatigue damage on the fuselage panel as shown in Fig. 1.36, the fuselage structure may no longer meet the damage tolerance requirement. Under the current damage tolerance philosophy, the inspection program of a fuselage panel is established on the basis that a single lead crack, propagating between detectable and critical size at limit load, will be detected before failure. This single lead crack is intended to represent a discrete source damage from fatigue, accident or corrosion in service. However, when widespread fatigue damages exist on the fuselage panel, the interaction of the lead crack with WFD has to be studied and the damage tolerance requirement of this structure needs to be changed accordingly, in order to ensure that the structure with WFD would meet the same safety requirements of a structure without WFD. Some preliminary analyses performed by Swift (1993b), based on 2-D solutions, have shown that the residual strength of a fuselage can be degraded below the required levels, when small cracks (with size of the order 0.05 inch) exist ahead of the lead crack. Furthermore, based on experiments of flat panels, Maclin (1991) has found that cracks as small as 0.05 inch ahead of the lead crack can reduce the residual strength by more than 30%.

Given that the cost of computing has declined by several orders of magnitude over the past decade, it is now economically feasible, to perform numerical analysis of a full-scale pressurized fuselage panel to study not just a single two-bay crack but also the interactions of multiple cracks ( say, due to multiple engine fragments) in

a stiffened structures. Furthermore, it is also possible to include nonlinear features such as the elastic-plastic material behavior to accurately calculate the interactions of plastic zones. With the ability to model a full-scale fuselage panel, the effect of location of the two-bay crack can be studied.

As discussed earlier, to ensure the structural airworthiness of aging structures, a study of the interaction between MSD cracks and a two-bay crack, is necessary in order to determine if the residual strength of the fuselage panel is reduced below the required level. In addition, we will also study the interaction of multiple lead cracks to simulate discrete source damage induced by fragments in the event of an engine disintegration.

This section presents a study of the interaction between MSD cracks and a two-bay crack, using Elastic-Plastic Fracture Mechanics (EPFM). The interaction of multiple lead cracks to simulate discrete source damage induced by fragments in the event of an engine disintegration, is also presented.

#### **§ 1.4.1 *Automated evaluation of residual strength in the presence of widespread fatigue damage***

In order to provide the regulatory agencies as well as aircraft manufacturers with the ability to evaluate the effect of WFD on a model-by-model basis, an automated analytical method has been developed to model a full scale fuselage panel with WFD, rather than relying on the approximations based on flat panels. This would allow a fundamental understanding on the behavior of WFD and help engineers in developing structural designs capable of containing WFD. This section describes a software package with a user-friendly Graphical User Interface [GUI], which can efficiently perform the fatigue/fracture analysis of multiple site damage (MSD) in fuselages with various designs of frames and stiffeners. This software has been implemented in Windows NT for personal computers as well as in different Unix based X-window systems for workstations. In order to substantially reduce the cost of computing, the modeling of the MSD cracks in the fuselage is based on the global-intermediate-local hierarchy. The software can automatically generate the finite element mesh of the skins, stiffeners, frames and rivets for each level of modeling using the data provided through the GUI interface. Having generated the mesh, the global and intermediate analyses are carried out using a commercial finite element package, wherein the cracks are modeled explicitly, to obtain the load flow pattern around the damage zone near the MSD cracks. This is followed by a local analysis based on the elastic plastic finite element alternating method (EPFEAM) and the  $T^*$  integral fracture parameter. In the local analysis, there is no need to

model the cracks explicitly. At the end of the analysis, the software will provide the graphical output of the residual life and strength estimates for the fuselage with MSD, in the presence of a discrete source damage.

#### *Functionality of the software program*

In order to capture the interaction of the lead crack with MSD cracks, it is important that the elastic-plastic material behavior of the skin panel be taken into account in the numerical analysis. It is generally found [Wang and Atluri (1996)] that numerical fracture simulations of a panel with multiple cracks based on linear elastic assumption tend to be anti-conservative especially when the cracks are close together. Therefore, one of the most important feature of this software tool is its ability to calculate elastic-plastic fracture parameters for multiple cracks efficiently and accurately using elastic-plastic finite alternating method.

The summary of the functionality of this software tools are listed in Fig. 1.37. In addition to being able to perform the residual strength analysis with MSD interactions, this software tool can also perform the analysis of multiple cracks of similar size. This feature is important in analyzing the damages that can occur when engine fragments of high velocity are to impact on a fuselage panel during an engine failure. During such circumstances, a large region of damage would be formed on the fuselage panel which is usually modeled as a single large crack. However, with this automated tool, the region of damage induced by engine disintegration can be modeled as a lead crack followed by a series of smaller cracks. Furthermore, in order to make the residual strength analysis more accurate, the software tool can account for the nonlinear flexibility behavior of the fasteners as well as the nonlinear geometric behavior of the shell structure. For example, in the residual strength analysis for a large circumferential crack, it has been found that the ability to model the nonlinear flexibility behavior of the fasteners is important in correlating the analysis with experiment [Wang and Atluri (1996)]. Also, it has been generally found that accounting for the nonlinear geometric behavior of the shell structure is important for the residual strength analysis of narrow-body aircraft where the skin panel is relatively thin. Besides the ability to perform residual strength analysis, this automated tool can also perform the fatigue analysis of the fuselage panel using a complete 3-D shell model. In these analyses, the effect of residual stress at the rivet holes due to rivet misfit as well as cold-working are also included.



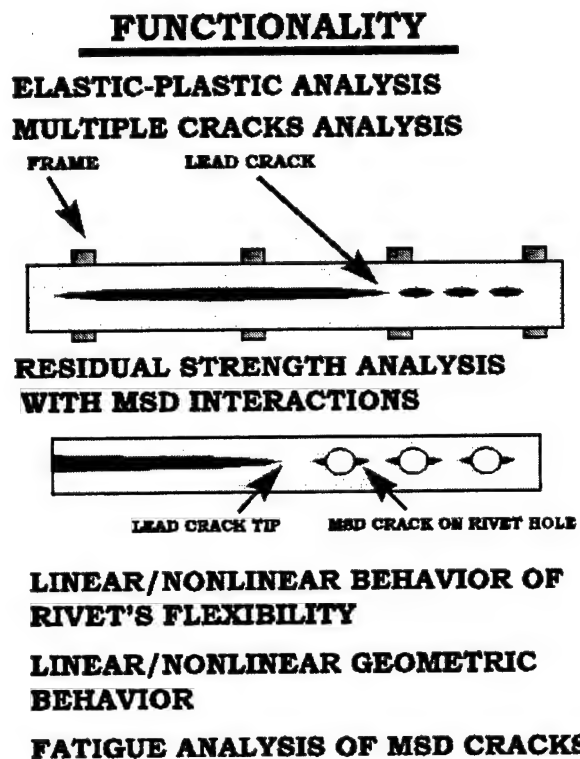


Figure 1.37: List of functionality of the software tool

*Structure of program*

In order to substantially reduce the cost of computing, the modeling of the MSD cracks in the fuselage is based on the global-intermediate-local hierarchy. The software will automatically generate the finite element mesh of the skins, stiffeners, frames and rivets for each level of modeling using the data provided through the GUI interface. In the global analysis, conventional linear elastic finite element analysis of the multibay stiffened shell panel is performed. The fuselage skin is modeled by 8 noded shell elements with 5 degrees of freedom per node while the frame, stringer and tear strap are modeled by 3 noded beam elements. The fasteners on the fuselage panel are modeled using spring elements and multiple point constraints. The linear behavior for the fastener stiffness is represented by the empirical relation developed by Swift (1984) [see Eq. 1.45, page 25]. Whenever there is a crack, the stiffness of the fasteners along the crack length becomes zero as the fasteners will not be able bear load in that direction. A typical global model shown in Fig. 1.39a, has seven frames and twenty stringers with approximately 3,000 elements.

Having performed the global analysis [here the cracks are modeled explicitly, using disconnected finite element nodes] to capture the overall load flow of a large section of a fuselage panel, the displacement boundary conditions of a smaller section is then transferred to an intermediate analysis. This intermediate model will be sufficiently large to contain the entire lead crack of the fuselage panel. In the intermediate analysis, the frames, stringers and fasteners are modeled in greater detail; each of the fasteners would be properly positioned according to the physical model, while the frames and the stringers are modeled with 4 noded shell elements as shown in Fig. 1.39b. In this intermediate analysis, the options of nonlinear fastener behavior as well as nonlinear geometric behavior are carried out. To capture the interaction of the lead crack with much smaller MSD cracks, a local analysis of smaller section of the fuselage skin is carried out. Here, the rivet holes are meshed in detail as shown in Fig. 1.39c and the elastic-plastic material behavior is assumed.

To automate this hierarchical process of global-intermediate-local analysis, this software program can be separated into four major components: (i) main module, (ii) mesh generator, (iii) finite element method, and (iv) finite element alternating method. The main module provides the detail of the geometric data as an input to the mesh generator. The mesh generator not only generates the mesh for the fuselage panel but also allows the proper positioning of the fasteners as well as the meshing of the cracks on the fuselage skin. With the mesh generated for the global and intermediate model, the global and intermediate analyses are performed using

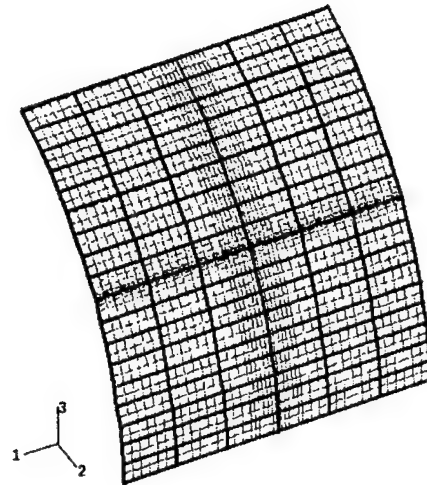
a commercial finite element package. The stress and displacement results are then transferred to the local analysis to be performed by an in-house elastic-plastic finite element alternating method (EPFEAM).

To perform the fatigue crack growth analysis for MSD problem, linear elastic material behavior is assumed. This analysis can be carried out efficiently with FEAM where the MSD cracks do not have to be meshed explicitly. To take into account of the effect of stress ratio, the Forman's crack growth equation is used. The effect of the initial radial pressure induced near a hole in the skin due to a rivet misfit; and the effect of the plastic deformation near the hole due to rivet misfit, are both considered [Wang, Brust, and Atluri (1995a)]. These effects can alter the range of stress intensity factor imposed on a crack-tip during cyclic loading; and thus affect the fatigue crack growth rates. It has been shown that these effects are responsible for a phenomenon whereby the shorter cracks near a row of fastener holes, may grow faster than longer cracks.

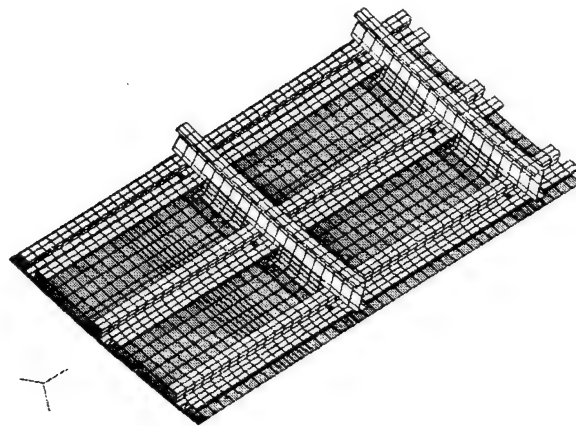
#### *Demonstration of software*

The program begins with the option of performing either a residual strength analysis or a fatigue crack growth analysis. It assumes that the details of the fuselage panel are provided by the OEM or can be easily obtained from a database. For the residual strength analysis, the user can choose the orientation of the cracks either in the longitudinal or circumferential direction as shown in Fig. 1.39. The program can also allow the user to change the center of the lead crack with respect to the frame/stringer position to study the effect of crack location on the residual strength of the fuselage panel. In order to obtain the residual strength curve, the user would be asked to input the initial and final crack length. For longitudinal crack, the user will also be given an option on whether the tear strap is broken; and for circumferential crack, the user will be given an option on whether is stringer is broken. Having completed the software input, the program will automatically generate the appropriate global-intermediate-local models for the analysis.

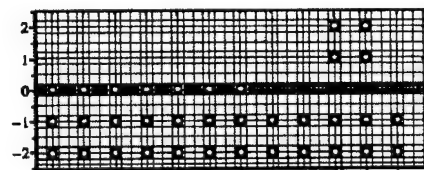
For the fatigue analysis shown in Fig. 1.40, the user can input the MSD crack sizes for each of the fastener holes between two frame sections. These fastener holes are located on the first row of fasteners for the upper panel of a lapjoint. As an additional safety feature, the program accepts a minimum MSD crack size input, in which a MSD crack with a minimum size would be assumed on both sides of all the rivet holes. The program allows two options in which the fatigue growth analysis is carried out. It can calculate the number of fatigue cycles, it takes for (i) a first crack link-up between two rivet holes or (ii) any cracks to reach a maximum



(a) Global model



(b) Intermediate model



(c) Local model

Figure 1.38: Global-intermediate-local hierarchical process

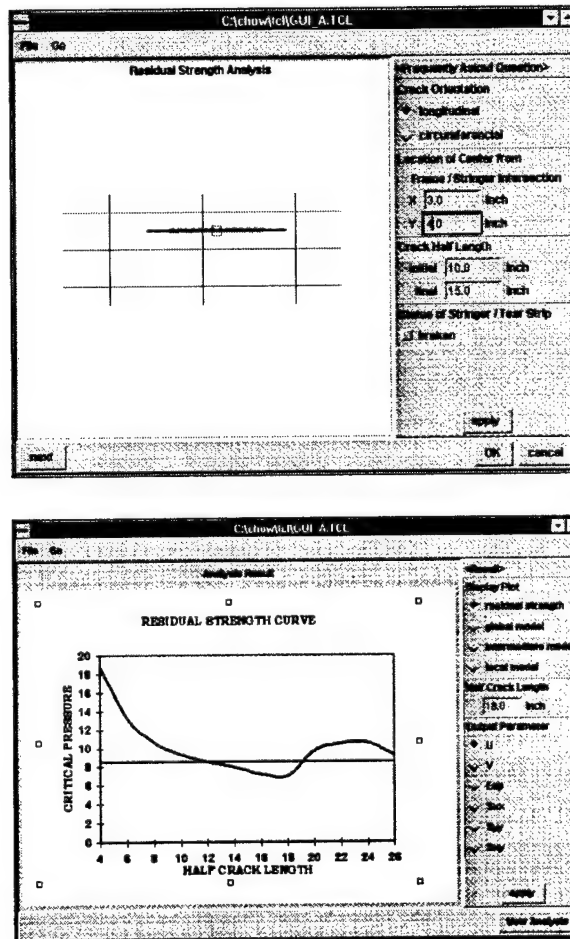


Figure 1.39: GUI for residual strength analysis

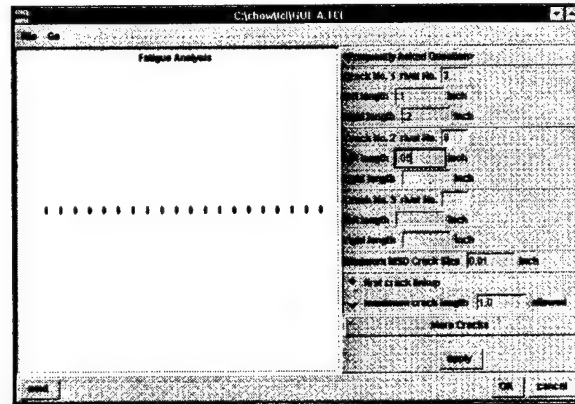


Figure 1.40: GUI for fatigue growth analysis

crack size. At the end of the residual life analysis, the program will output the estimated fatigue life and the final crack size for all the MSD cracks.

#### § 1.4.2 Two-bay longitudinal cracks at various locations

The fuselage shell panel under consideration is a typical wide body commercial aircraft. It is stiffened along the longitudinal direction by stringers and circumferentially by frames and tear straps. The tear strap at the center of the two-bay crack is assumed to be broken. The skins, frames, stringer and rivets are assumed to be made of aluminum while the tear strap is made of titanium. The overall dimensions of the fuselage are given in Fig. 1.41. A critical stress intensity factor of  $90 \text{ ksi}\sqrt{\text{in}}$  is used for the aluminum skin. For elastic-plastic analysis,  $T^*$  integral (with an equivalent critical value of  $0.771 \text{ ksi} \cdot \text{in}$ ) is used as the fracture criterion.

In this study, the residual strength of the fuselage panel has been calculated as a function of the lead crack size. Fig. 1.42 shows that the analysis based on the linear-elastic assumption would overestimate the critical pressure by about 30% when compared with the elastic-plastic solution. Therefore, the linear-elastic solution is significantly anti-conservative.

A two-bay crack has been placed at three different locations to examine the effect that the location of the two-bay crack would have, on the overall residual strength curve as shown in Fig. 1.43. In case (a), the two-bay crack lies in the middle of two stringers; in case (b), the two-bay crack lies in the row of fasteners on top of a stringer; and finally in case (c), the two-bay crack lies on the top of the fastener row of the upper skin section of a lapjoint. It has been found that the

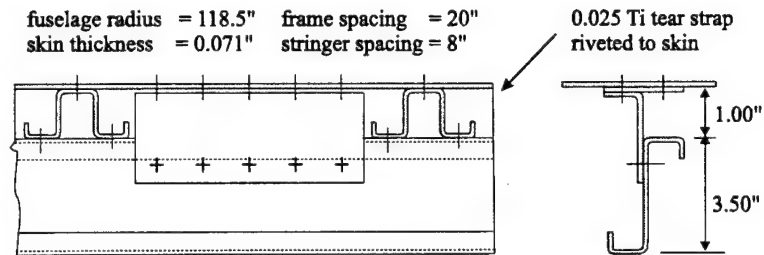


Figure 1.41: The geometric dimension of the fuselage panel

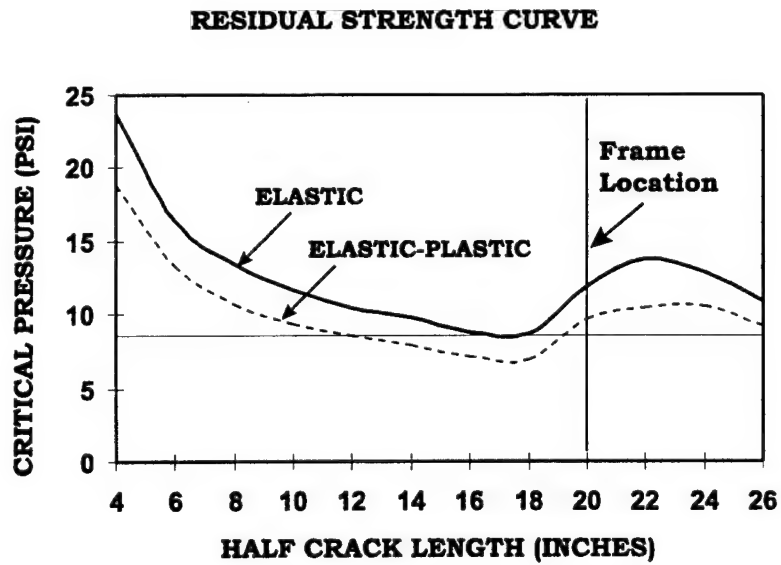


Figure 1.42: Residual strength as a function of crack size

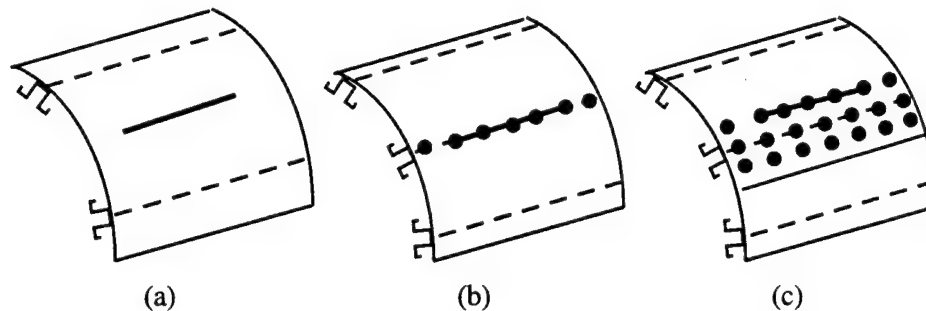


Figure 1.43: Locations of the two-bay crack: (a) in between two stringers (b) on a stringer (c) on a lapjoint

residual strength of a two-bay crack for case (a) is significantly higher than case (b) and case (c) as shown in Fig. 1.44. Furthermore, assuming that the operating pressure on the fuselage is  $8.6 \text{ psi}$ , Fig. 1.44 shows that a two-bay crack for case (a) would be arrested ahead of the frame while the two-bay crack for case (b) would not be arrested until the crack tip passes the frame location. The difference in the residual strength for these three locations can be attributed to the design of the frame structure. As can be seen from Fig. 1.45, when the crack lies between two stringers, there is an additional frame clip which constrains the two-bay crack from opening. However, when the crack lies on the stringer or on the lapjoint, there is no secondary frame to constrain the crack from opening.

### § 1.4.3 Interaction of multiple longitudinal cracks

The first numerical example concerns the interaction of a two-bay crack with a single-bay crack. Both of these cracks lie in the middle between two stringers. The center of the two-bay crack would lie on the frame while the center of the single-bay crack would lie in the middle of the bay. The sizes of these two cracks are varied such that both crack tips have an equal distance,  $d$ , to the frame position as shown in Fig. 1.46.

The result from Fig. 1.46 shows little interaction between these two cracks when the distance between the two crack tips is more than  $4 \text{ in}$  apart even though the size of the lead crack may be as large as  $36 \text{ in}$ . However, when these two crack tips are only two inches apart, the residual strength of the fuselage panel is reduced by more than 20%. These strong interactions between these two cracks can be attributed to the fact that the plastic zones for these two crack tips are interacting with



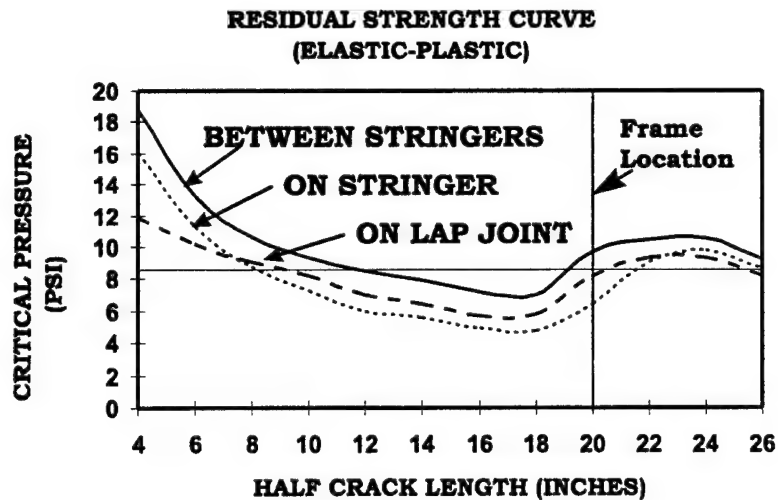
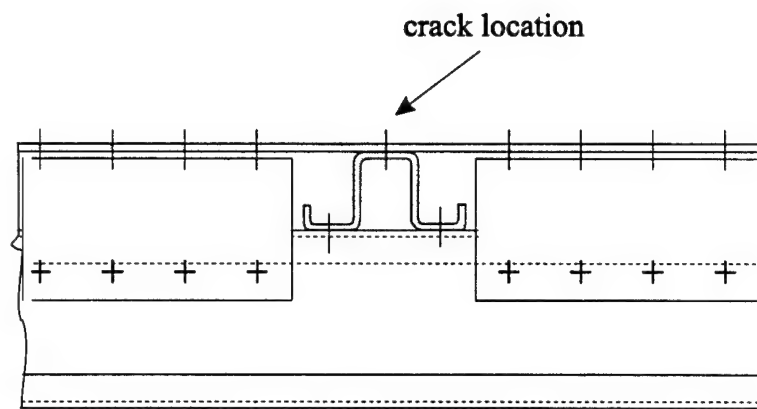


Figure 1.44: Residual strength curve for a two-bay crack at different location

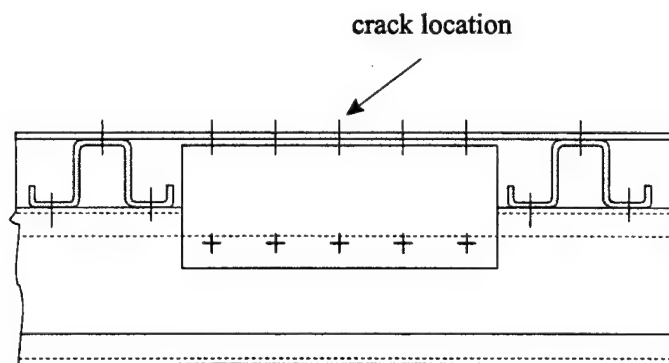
each other.

As shown in Fig. 1.42, the maximum arresting capability of the stiffener occurs when the size of the two-bay crack exceeds the two frame interval. Therefore, to understand how a secondary crack can reduce the maximum arresting capability of the stiffener, the size of the lead crack in this example is chosen to exceed the two frame interval by 4 in. In this example, the secondary crack is 2 in ahead of the lead crack and the size of the secondary crack is varied from 2 in to 8 in, as shown in Fig. 1.47. The result shows that the reduction of critical pressure in the presence of the lead crack varies linearly with the size of the secondary crack, from 10% to 30% (based on elastic-plastic analysis). Furthermore, the result also shows that the larger lead crack has more influence on the smaller secondary crack, than the influence the smaller secondary crack would have on the lead crack. A comparison between linear elastic and elastic-plastic analysis shows that the linear elastic solution would significantly underestimate the severity of the interaction between these two cracks.

In the next example, studies have been carried out to examine the extent of the reduction in residual strength due to three smaller cracks in front of the two-bay crack. The elastic-plastic analysis shows that the residual strength of the lead crack is not only influenced by the size of the smaller cracks but more importantly by the distance of these cracks from the lead crack as shown in Fig. 1.48. Furthermore,



(a) a lead crack on a stiffener



(b) a lead crack in between two stiffeners

Figure 1.45: The effect of frame design on the residual strength of a two-bay crack

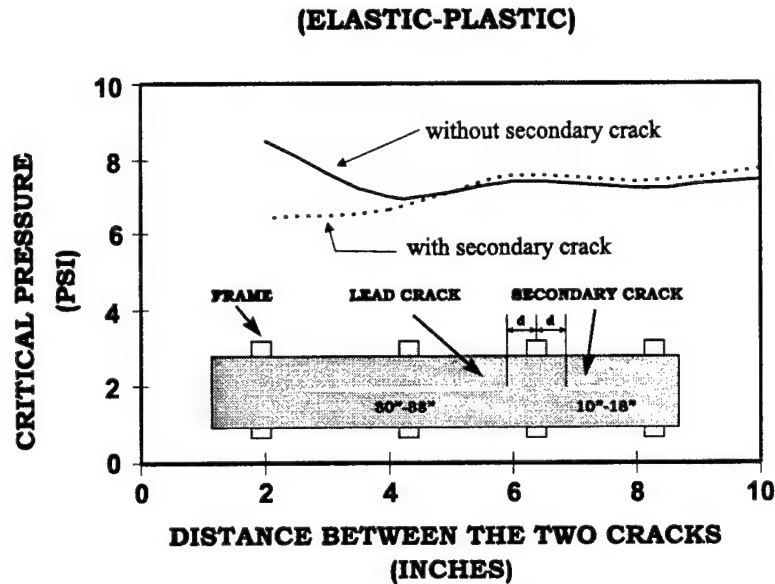


Figure 1.46: Interaction between two large cracks

it has been found that when the same analyses for the 1 in cracks are performed using the linear elastic assumption, the residual strength would be underestimated by a factor of two. Similar studies are also carried out to examine the effect of the interactions of MSD cracks with the two-bay crack. The result given in Fig. 1.49 shows that the residual strength of the lead crack would be reduced by 10% when the size of the MSD cracks is 0.2 in. Again in Fig. 1.49, the linear-elastic assumption greatly underestimates the interaction between the lead crack and the MSD cracks.

#### § 1.4.4 Circumferential cracks

Much research has been devoted to the studies of cracks in the fuselage lap joints. However, circumferential cracks may result in more serious consequences if their growth cannot be arrested by the stiffened structure of an aircraft fuselage. Circumferential cracks received less attention due to the fact that the axial stress due to pressurization is smaller than the hoop stress caused by pressurization. However, the axial skin stress at certain locations on the aircraft fuselage, as illustrated in Fig. 1.50, can be higher than the hoop stress, due to the fuselage down bending and the cabin pressure. The axial stress can be as high as 34 ksi [see Swift (1995)],

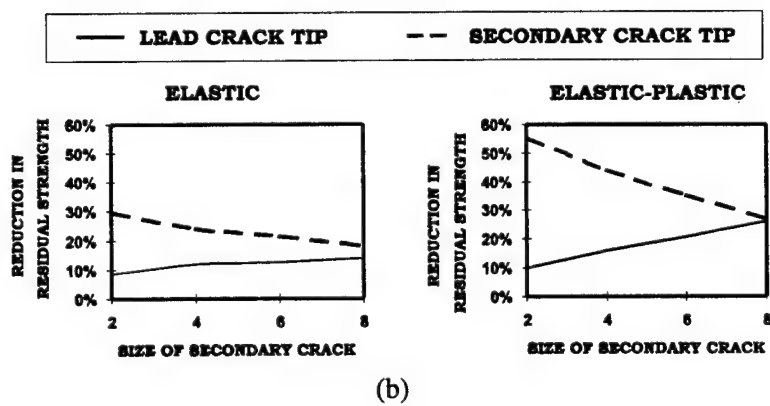
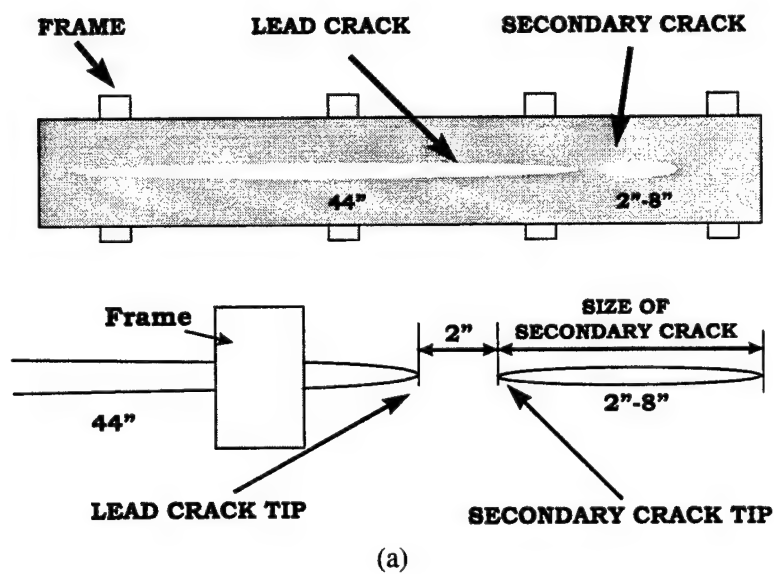


Figure 1.47: Interaction between a lead crack and a secondary crack

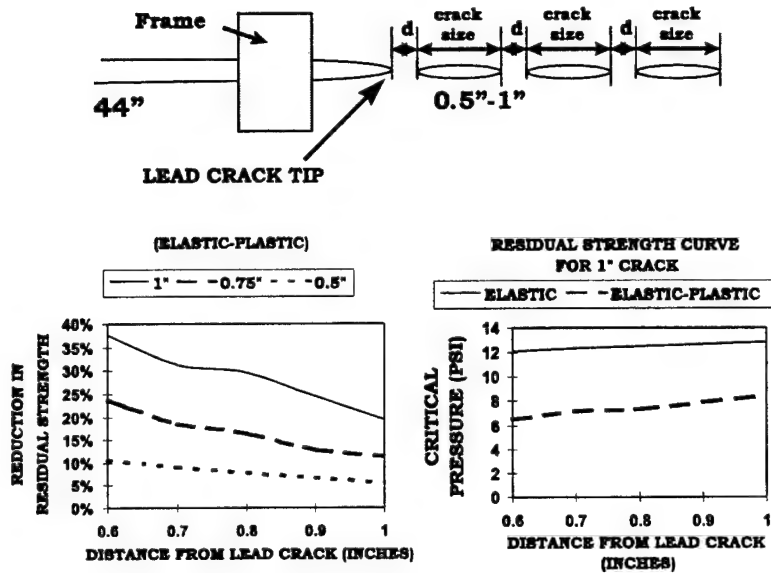


Figure 1.48: Interaction of a lead crack with three smaller cracks

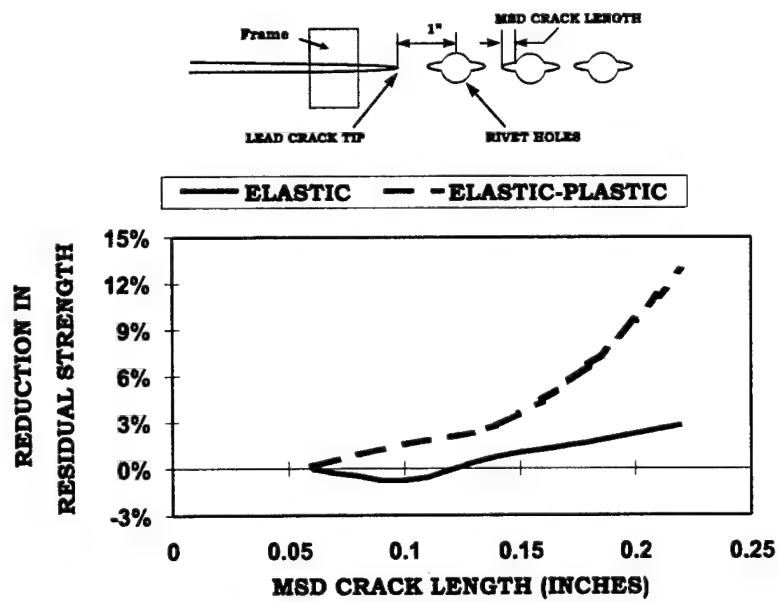


Figure 1.49: Interaction of a lead crack with MSD cracks

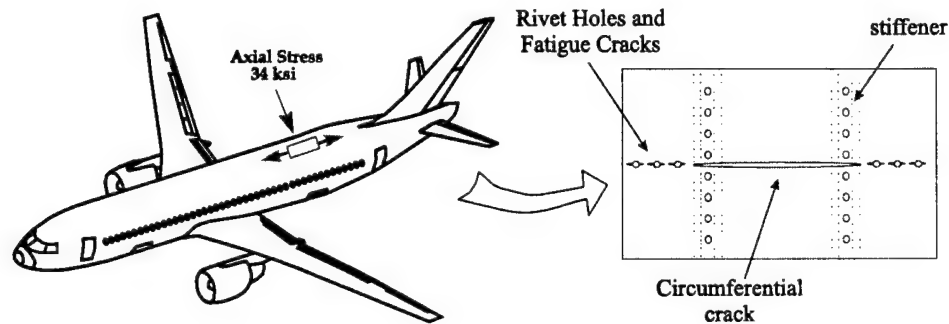


Figure 1.50: A critical location on the aircraft fuselage for circumferential damages

which is about 70% of the initial yield stress. (The initial yield stress of AL 2024-T3 is 47 *ksi*.) Since the panel works at such a high level of gross stress, even a small stress concentration factor can lead to yielding. Therefore, extensive plastic deformation can be expected in the presence of a lead crack; and nonlinear material behavior becomes very important in the study of residual strength in such a case.

Global-intermediate-local modeling strategy is used to perform the detailed analyses of circumferential cracks. The crack configuration in Fig. 1.51 is chosen because there was a component test [Swift (1984)] carried out in such a configuration. At the time of the test it was considered to be the most critical situation for a circumferential crack.

The following is a brief description of the panel under consideration. More details may be found in Swift (1984). The skin is AL 2024-T3 and 0.071 *in* thick. Stringer spacing is 8 *in*. The cross sectional area of each stringer is 0.5471 *in*. In the test the panel failed at the gross stress of 39.7 *ksi*, with the half crack length equal to 9.88 *in*. The fracture toughness of the skin material is 198 *ksi* $\sqrt{\text{in}}$ , as suggested by Swift (1995).

#### *Residual strength analysis*

Fig. 1.52 shows the residual strength curves obtained using Linear Elastic Fracture Mechanics (LEFM) approach and using Elastic-Plastic Fracture Mechanics (EPFM) approach. When the computed residual strength is compared to the load at the failure as predicted in the test, it is seen that the LEFM prediction over-estimates the residual strength of the panel by a large amount. However, the EPFM approach only slightly under-estimated the residual strength of the panel as determined by

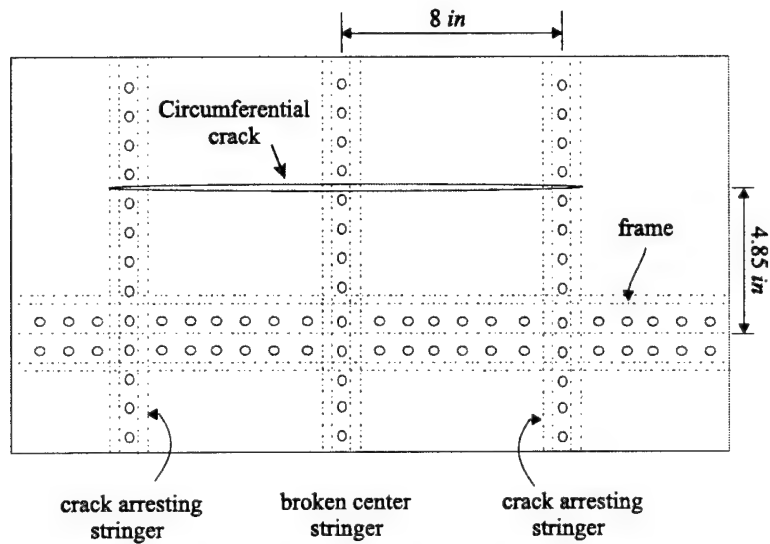


Figure 1.51: The location of circumferential crack in a component test

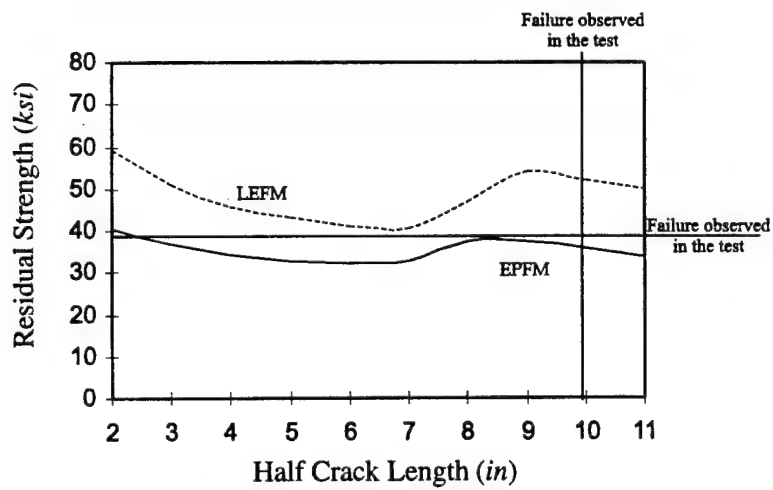


Figure 1.52: Residual strength curve for the circumferential crack

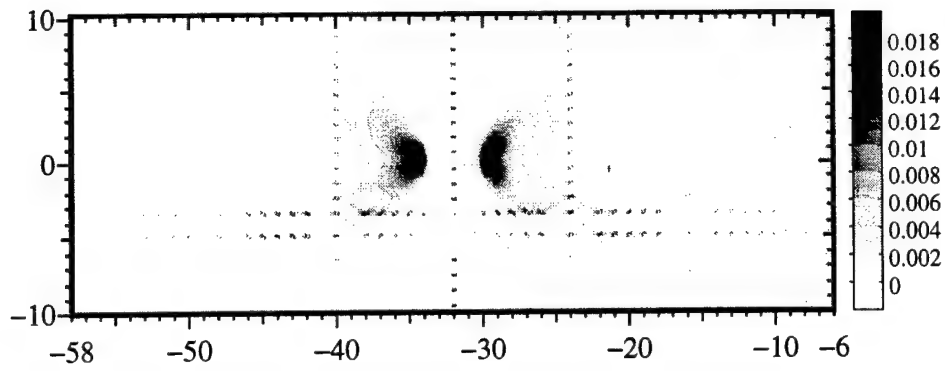
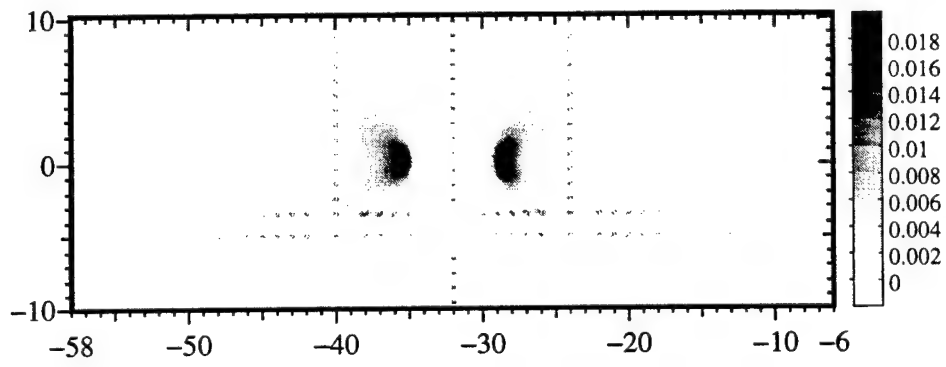
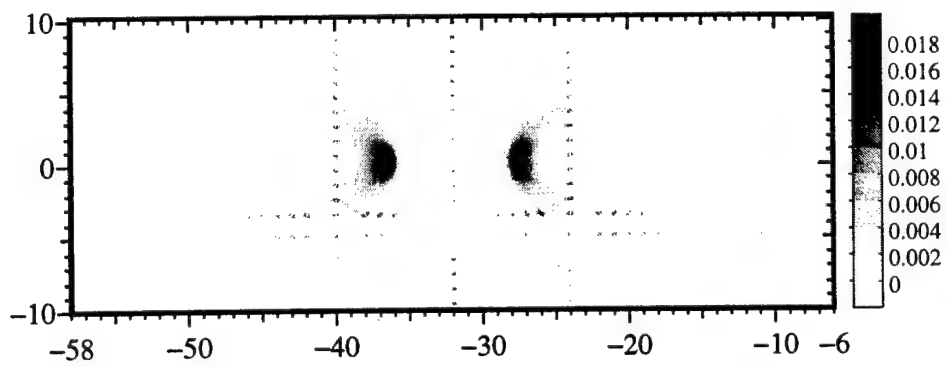
experiment. Here, the residual strength curve is obtained by computing the failure load at different crack sizes. Therefore, the effect of stable tearing of the skin is not considered. In the test, a static loading was applied on the panel to force the crack grow from a half crack length 7.38 in to the final failure. Due to the plastic hardening the panel can take slightly higher load than the load at the crack initiation. Therefore, the load at crack initiation will be slightly smaller than the failure load observed in the test. Thus, we consider the prediction obtained by the EPFM approach to be very good.

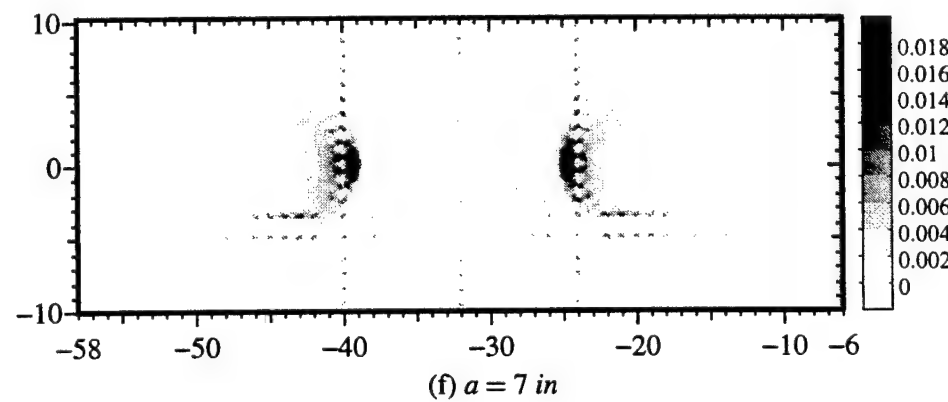
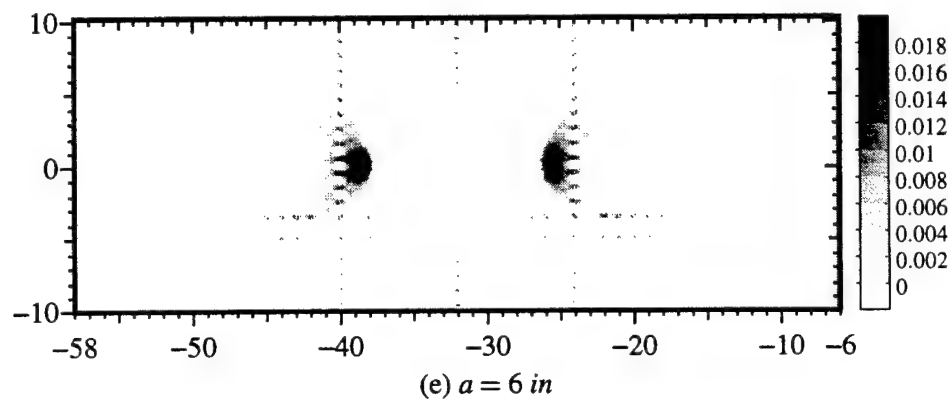
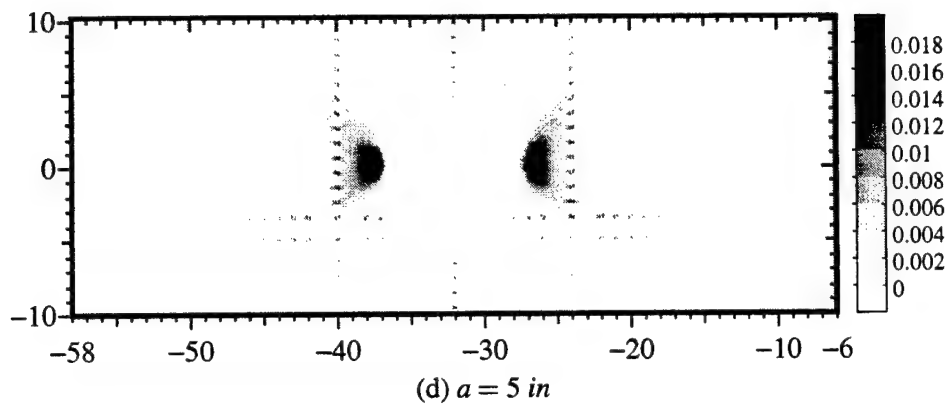
Fig. 1.53 shows the equivalent plastic strain contour plots for cracks of different size at the critical loads. It is seen that the plastic zones are very large, with a radius of more than 5 in. The plastic deformations around the rivet holes can also be recognized by the small dark zones near the locations of the rivet holes. As the crack size increases, the center broken stringer takes less load. This is indicated by the disappearing of plastic deformations near the rivet holes located at the center stringer. More and more load is transferred onto the crack arresting stringers as the crack size increases, as indicated by the plastic deformations near the rivet holes at the crack arresting stringers. As the crack tips approach the crack arresting stringer, the plastic deformations around the crack tips are restricted by the stringers. However, right after the crack tips penetrate the crack arresting stringers, as seen in the contour plot Fig. 1.53(g) ( $a = 8$  in), the size of plastic deformation reaches the maximum. At this point, the residual strength curve reaches a local maximum point (see Fig. 1.52); and the crack arresting stringers are behind the crack tips.

The plastic deformations are nearly symmetric about the crack plane for all crack sizes, though they are disturbed near the location of the frame (located below the crack in the contour plots). This indicates that the effect of the frame is not significant. Fig. 1.54 shows the residual strength curves for the circumferentially cracked panel with frames of different size. In this analysis, the size of the frame was doubled to study the effect of the frame. It is seen that the size of the frame almost makes no difference. In a real structure, the skin of the fuselage will buckle in the presence of a large crack. A frame near the crack can act as an anti-buckling guide. In this hierarchical analysis, no buckling is allowed. Therefore, the anti-buckling effect of the frame is not studied here.

Fig. 1.55 shows the effect of pressurization, in which we compute the residual strength for the case where there is only axial loading and the case where there are both axial loading and hoop direction loading (due to pressurization). Since the pressurization changes mainly the hoop stress, which does not affect mode-I loading of the circumferential crack, little difference in residual strength curves is



(a)  $a = 2$  in(b)  $a = 3$  in(c)  $a = 4$  in



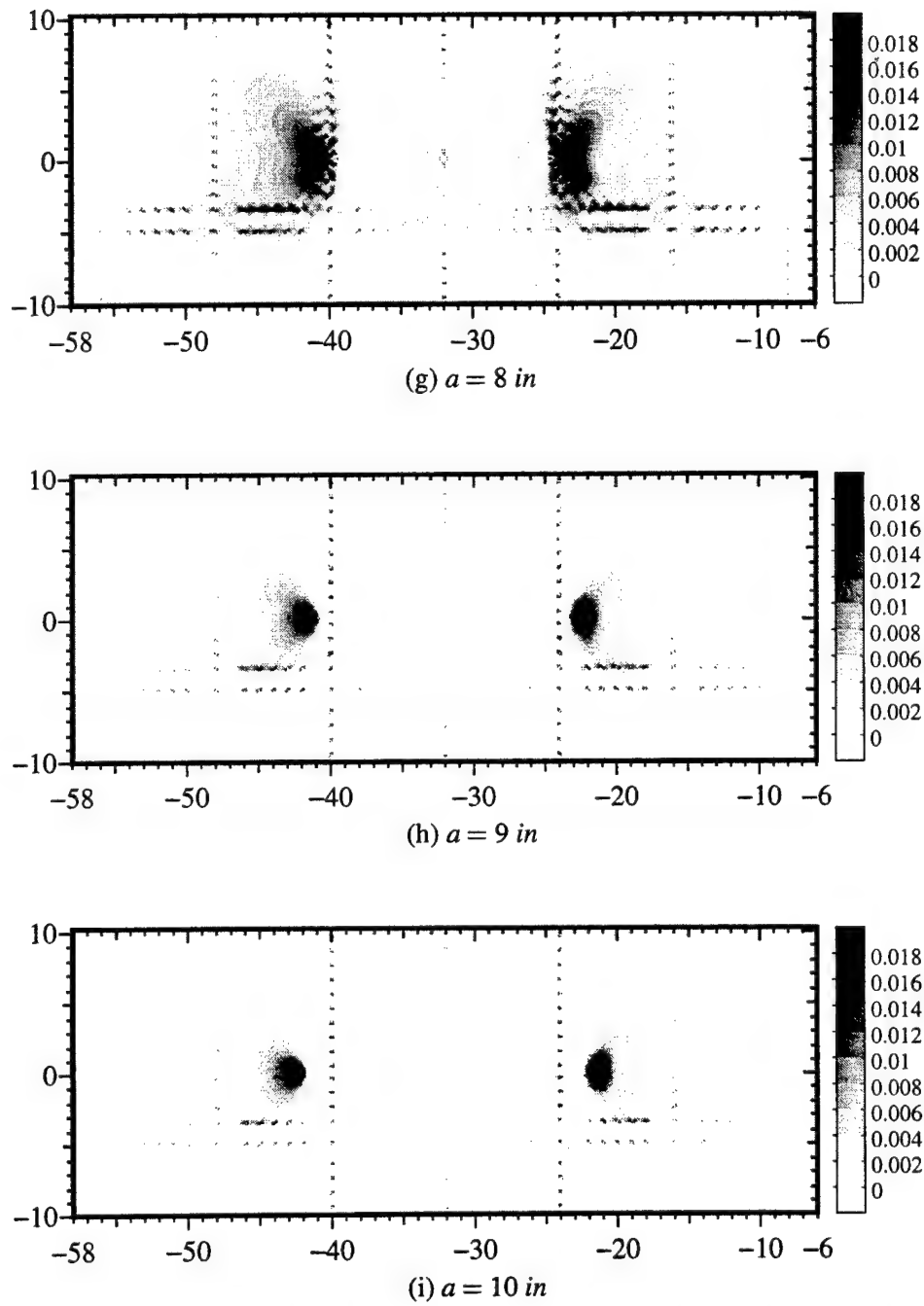


Figure 1.53: Equivalent plastic strain contour plot for lead cracks of different half length

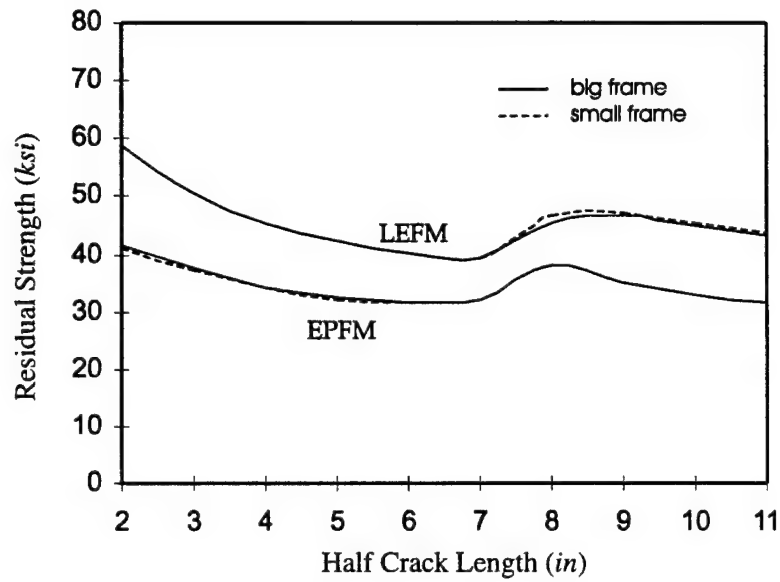


Figure 1.54: The residual strength curves for the circumferentially cracked panel with frames of different size

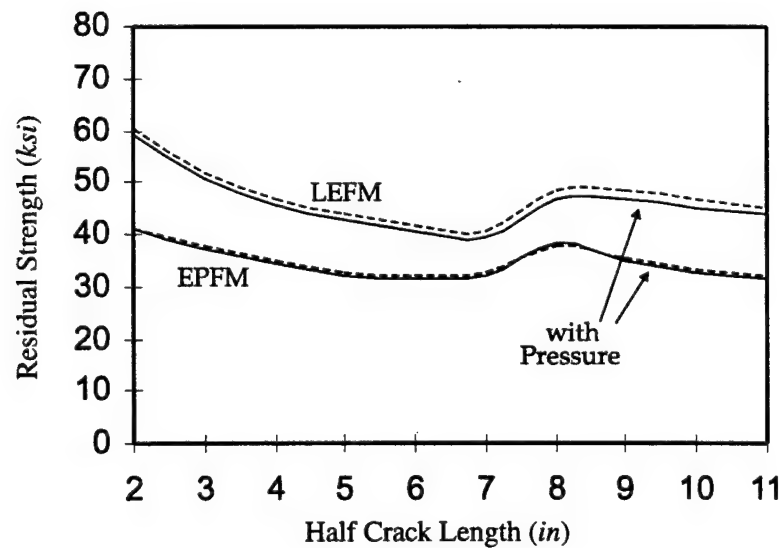


Figure 1.55: The residual strength curves for the circumferentially cracked panel with/without cabin pressure

observed in both the linear elastic fracture analysis and the elastic-plastic fracture analysis.

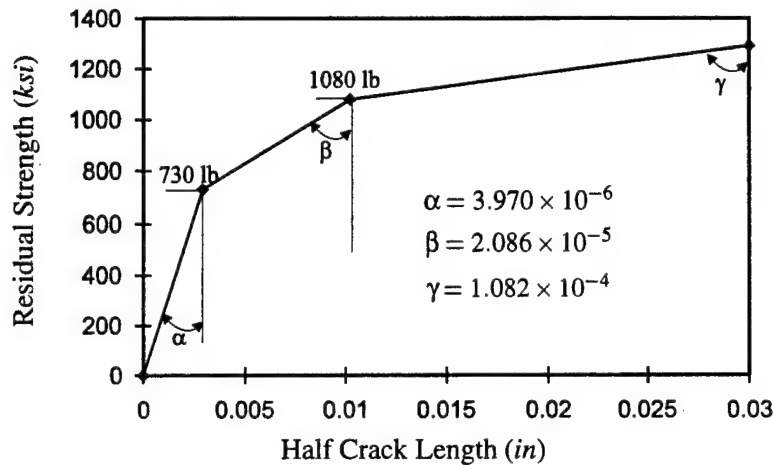


Figure 1.56: Nonlinear rivet flexibility curve

#### *Effects of MSD and nonlinear behavior of rivets*

In the test, it was observed that the panel failure was precipitated by rivet failure in the crack arresting stringers. Since the rivets on the crack arresting stringers transfer the load from the skin to the stringers, the nonlinear behavior of the rivets can have a considerable effect on the crack arresting capability of the panel. To study this effect, we use the empirical flexibility curve [Swift (1995)] to model the nonlinear effect of the rivets on the residual strength of the panel. The empirical flexibility curve is shown in Fig. 1.56. This flexibility curve in Fig. 1.56 was obtained using from an experiment in which a riveted joint was loaded until the rivet failed. Therefore, this flexibility curve includes actually the plastic deformation of the skin. The effect of nonlinear behavior of rivets can be seen in Fig. 1.57. Due to the yielding of rivets, less load is transferred onto the stringer from the skin. This decreases the residual strength of the cracked panel. The reduction is observed in both the LEFM analysis and EPFM analysis. However, the influence of the nonlinear behavior of rivets is smaller in the EPFM analysis, since the yielding of skin around rivet holes were modeled in the EPFM analysis.

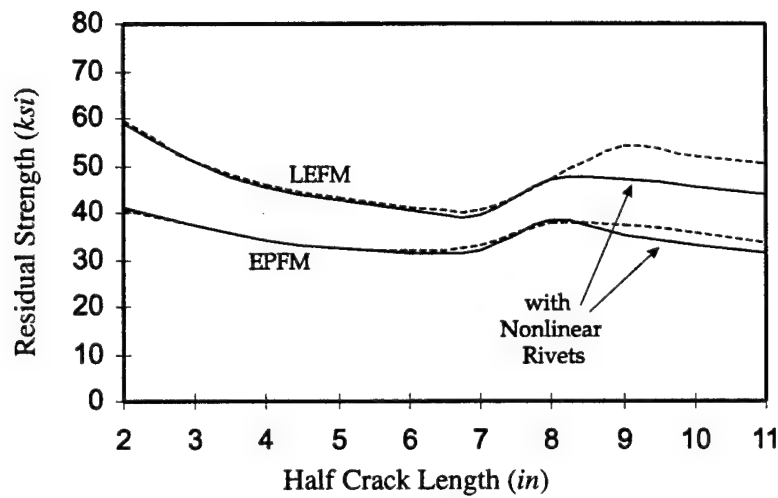


Figure 1.57: Effect of the nonlinear behavior of rivets

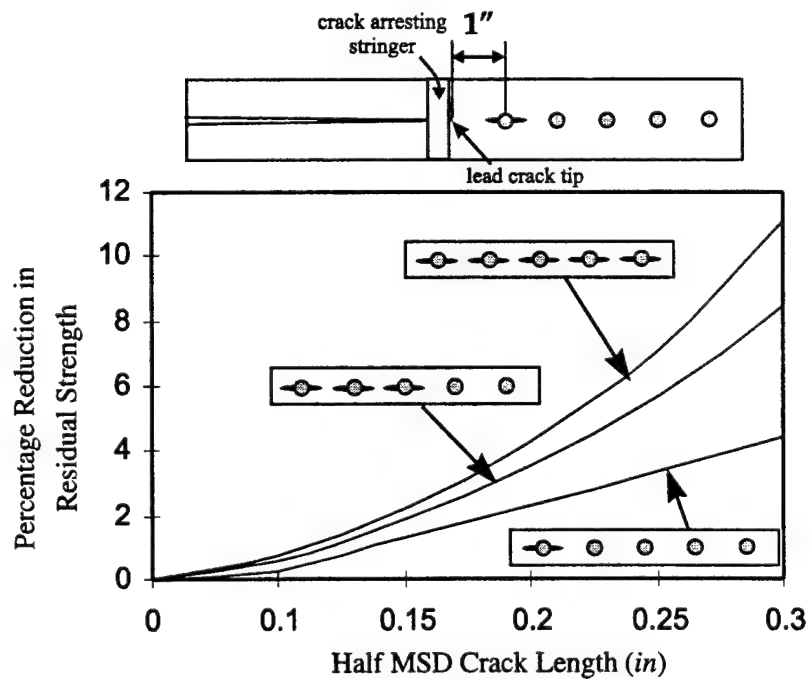


Figure 1.58: Percentage reduction in residual strength due to MSD cracks

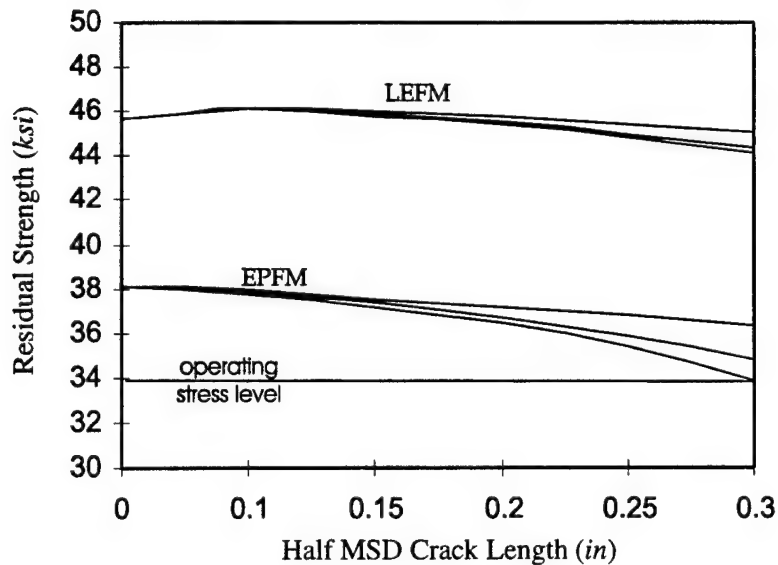


Figure 1.59: Residual strength in the presence of MSD cracks and a lead crack with a half crack length 8 in

Multiple site fatigue damages can reduce the residual strength of an aircraft fuselage in the presence of a large circumferential crack. Fig. 1.58 shows the percentage reduction in residual strength for the case where the lead crack tips just penetrated the crack arresting stringers, and the distance between the first MSD and the tip of the lead crack is one inch. Three different cases were analysed, corresponding to i) there is one MSD crack ahead of a lead-crack tip; ii) there are 3 MSD cracks ahead of a lead-crack tip; iii) there are 5 MSD cracks ahead of a lead-crack tip. Fig. 1.59 shows how the residual strength decrease as the size and the number of MSDs increase. The more the MSD cracks the larger the reduction in residual strength. Although the fatigue damages can reduce significantly the residual strength of the panel, this panel will not degrade to losing the capability to arrest a two-bay circumferential crack at the operating stress level (assumed to be 34 ksi) until the MSD cracks are of significant length. This can be seen in Fig. 1.59.

### *Conclusions*

A circumferential crack at a critical location with high axial stress is analyzed. Very large plastic zones are observed, with a radius of more than 5 in at the critical

loads. Plastic deformation near rivet holes is also very significant. The yielding and failure of the rivets on the crack arresting stringers decrease the crack arresting capability of a circumferentially cracked fuselage; so do the multiple site damages in the skin of the fuselage. Since the LEFM approach significantly over-estimates the residual strength of a cracked panel and under-estimates the influence of MSD, EPFM approach is mandatory for the study of residual strength of a circumferential crack at critical locations

### § 1.5 Widespread Fatigue Damage Threshold

The fatigue damage due to the repetitive loading condition of pressurization is one of the major concerns among the civil aviation industry. There exist two different types of approach in dealing with the multiple site fatigue damage problem. One of them is the Multiple Site Damage Threshold (MSDT) approach; the other is the Widespread Fatigue Damage Threshold (WFDT) approach [Jeong and Tong (1995)]. In the MSDT approach the severity of MSD is measured by the potential of their link-up; while in the WFDT approach it is indicated by the reduction of residual strength of the aircraft.

As shown in the Fig. 1.60(a), the MSDT approach requires the study of fatigue growth and link-up of a number of small fatigue cracks. If the MSD cracks do not link-up during service inspections, it is considered safe. However, small MSD cracks may reduce significantly the residual strength of an aircraft in the presence of a lead crack, as illustrated in the Fig. 1.60(b). For an aircraft designed to operate at a high level of working stress with a small amount of redundant residual strength, very small undetectable fatigue cracks can reduce the residual strength to below an acceptable level. On the other hand, aircraft with sufficient redundant residual strength can have enough residual strength in the presence of detectable fatigue cracks. Therefore, using the MSDT approach alone may lead to a false feeling of safety; and the MSDT approach alone is not sufficient for the evaluation of the severity of multiple site fatigue damage on an aircraft.

From an operational view point, it is important to predict the widespread fatigue damage threshold, i.e. the number of loading cycles that will produce fatigue cracks such that the residual strength of the aircraft is reduced to below an acceptable level. With the knowledge of widespread fatigue damage threshold, aging aircraft operators can schedule service inspections economically without compromising safety requirements. This section presents a methodology to predict the WFD threshold with numerical examples illustrating the typical characteristics of



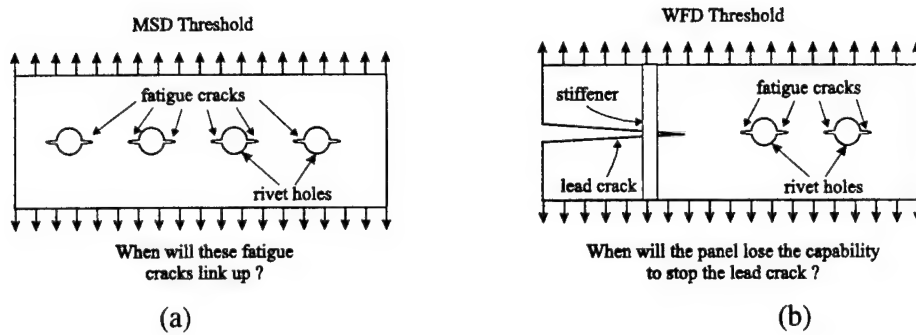


Figure 1.60: MSD threshold approach and WFD threshold approach

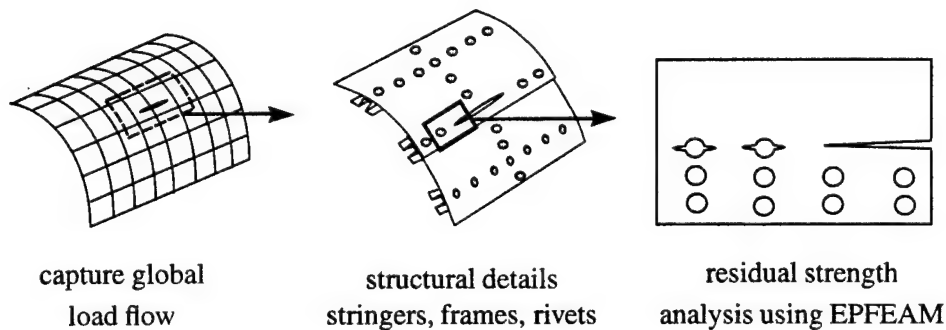


Figure 1.61: A global-intermediate-local hierarchical approach for the residual strength analysis of an aircraft fuselage

an aging aircraft.

### § 1.5.1 Residual strength analyses

Global-intermediate-local hierarchical modeling is an efficient approach for the residual strength analyses of aircraft fuselages, in the presence of a lead crack and MSD. Fig. 1.61 illustrates graphically such a hierarchical approach.

The intermediate model contains a smaller portion of the cracked fuselage, where stringers and frames are modeled in detail, using shell elements. Each rivet is modeled individually using spring elements. The empirical formula suggested by [Swift (1984)] is used to model the flexibility of rivets. Thus, the influence

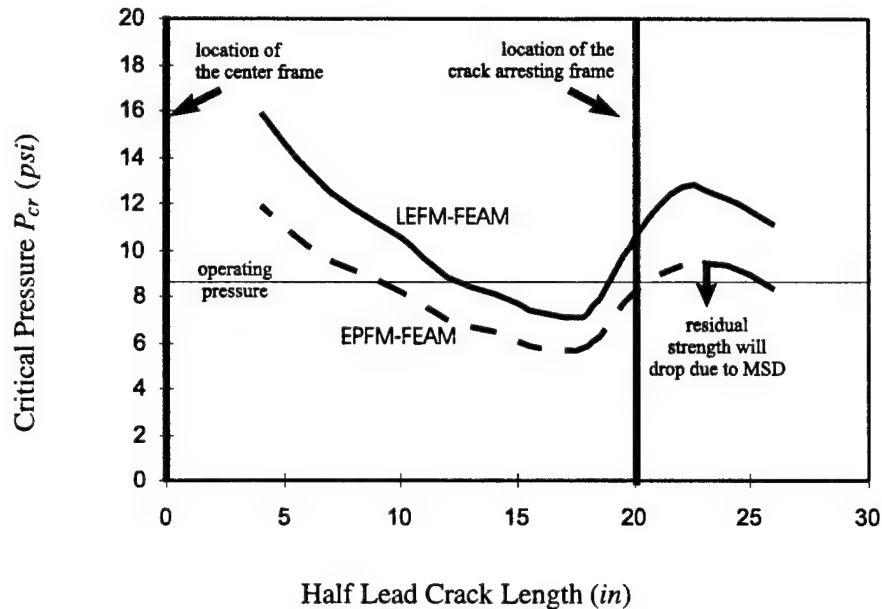


Figure 1.62: Residual strength curve for the lead crack only case

of the detailed structure on the membranous stress in the skin can be determined through this linear elastic intermediate analysis. Again, the lead crack is modeled explicitly; but no mesh refinement around crack tip is made in order to reduce the computational cost.

A rectangular skin model is obtained from the intermediate analysis. In the local model the boundary loading conditions at the four edges, and the rivet pin-loads on the rivet holes are obtained from the intermediate analysis. The skin-only local model is analyzed using Elastic-Plastic Alternating Method, where none of the cracks is modeled explicitly. Analytical solutions for an embedded crack in an infinite domain, subjected to arbitrary crack surface loadings, are used to capture the singular fields near the crack tips.

A typical residual strength plot obtained from such global-intermediate-local analyses is illustrated in Fig. 1.62. In the analysis shown in Fig. 1.62, we assume the aircraft fuselage has a radius of 118 inches. The longitudinal lead crack is located at a lap joint splice. We assume a broken center tear strap while the center frame remains intact. The skin thickness is 0.071 inch. The critical stress intensity factor for the skin is taken as  $K_{Ic} = 90 \text{ ksi}\sqrt{\text{in}}$ . Rivets are of radius 0.095 inch. The

frame spacing is 20 inches; and the stringer spacing is 10 inches.

Fig. 1.62 shows the critical cabin pressure  $P_{cr}$  versus the half crack length  $a$  of the lead crack. The critical pressure is defined as the cabin pressure at which the stress intensity factor (or its equivalent elastic-plastic counter part,  $T^*$ , which is same as  $J$  for stationary cracks) at the lead crack tip reaches the critical value. It is seen that the residual strength reaches a local maximum shortly after the lead crack penetrates the first crack arresting frame. In the numerical modeling, we assume that the crack arresting frame remains intact and the tear strap under the crack arresting frame is broken, when the lead crack penetrates the crack arresting frame. The residual strength curve is obtained by computing the critical pressure for different sizes of the lead crack. Therefore, no stable tearing is considered. It is seen that the linear elastic analysis significantly over-estimates the residual strength of the cracked fuselage.

The local maximum (see Fig. 1.62) is above the operating pressure, which is assumed to be 8.4 *psi*. Therefore, if a large damage, due to link up of fatigue cracks and/or a foreign impact, is induced during the operation, the lead crack will be arrested around the local maximum at the operating pressure, provided that the damage extends to no more than two bays. However, MSD cracks ahead of the lead crack can bring down the local maximum to below the operating pressure. In such a case, the fuselage no longer has the required crack arresting capability. The aircraft with MSD can still operate with sufficient strength, provided no large damage is present in the fuselage. However, it becomes vulnerable to damage, since it no longer has the capability to arrest a two bay damage.

Fig. 1.63 shows how the residual strength at the local maximum point decreases as the number and the size of fatigue cracks ahead of the lead crack tip increase. Here, we assume equal length fatigue cracks emanating from both sides of a rivet hole. The crack lengths are measured from the edges of rivet holes to the tips of fatigue cracks. The distance between the lead crack tip and the center of the first rivet hole is 1 inch. Three different MSD cases are presented. They correspond to fatigue cracks emanating from i) the first rivet hole ahead of the lead crack tip; ii) the first three rivet holes ahead of the lead crack tip; iii) the first five rivet holes ahead of the lead crack tip. From this analysis, we can find the critical size of fatigue cracks that will pose a WFD problem.

Fig. 1.64 shows the reduction of residual strength for the MSD case in which there are only two equal-length fatigue cracks emanating from the first rivet hole ahead of the lead crack tip, as indicated in the figure. The result obtained using Linear Elastic Fracture Mechanics (LEFM) approach and the result obtained using

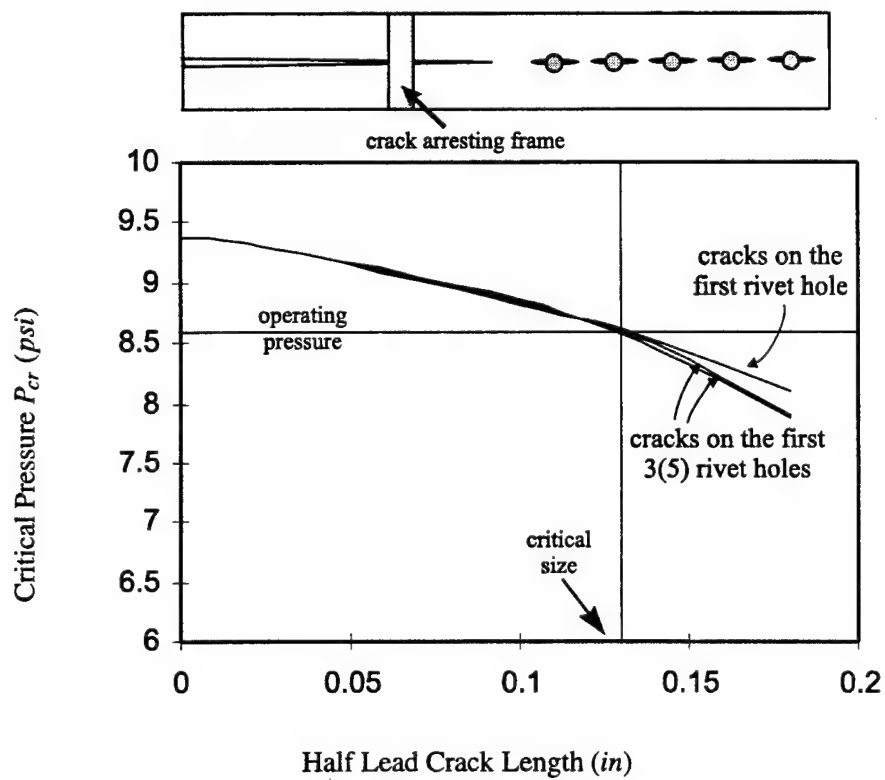


Figure 1.63: Residual strength in the presence of MSD cracks

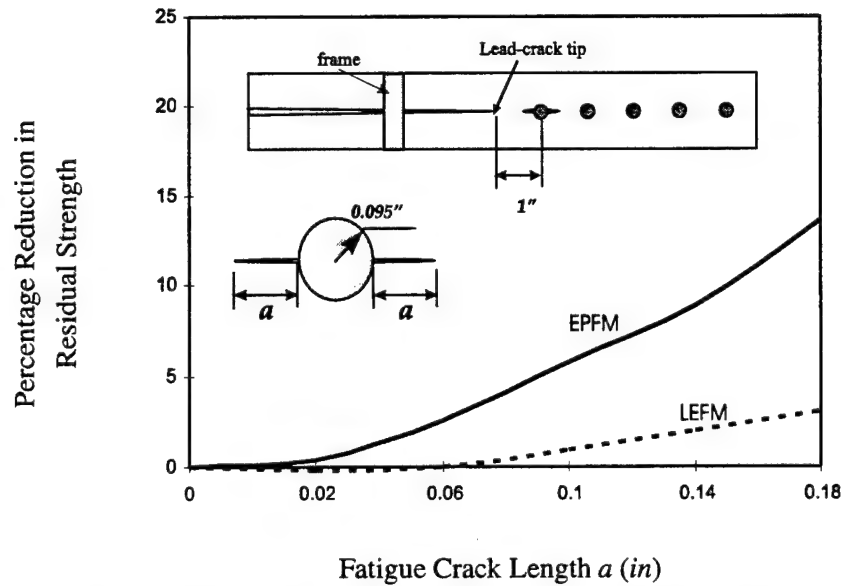


Figure 1.64: Reduction in residual strength for the case of fatigue cracks emanating from the first rivet hole ahead of the lead crack tip

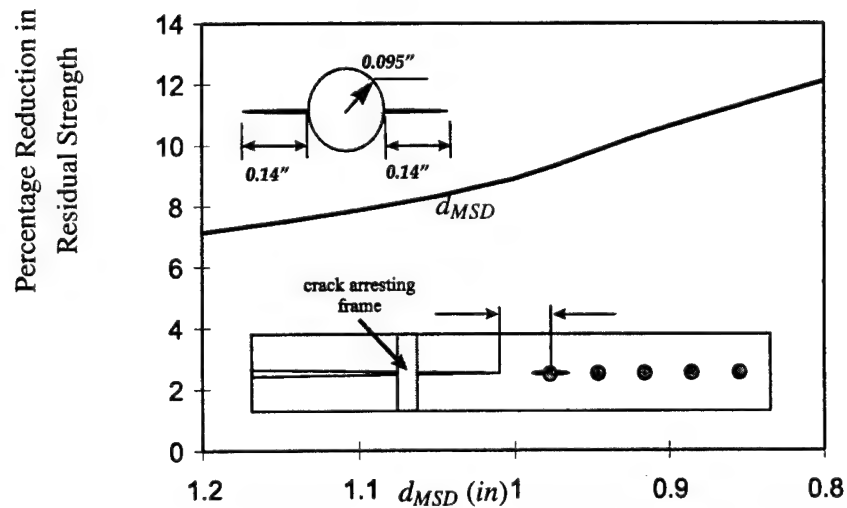


Figure 1.65: The influence of  $d_{MSD}$ , the distance between the lead crack tip and center of the first rivet hole, on the reduction in residual strength

Elastic-Plastic Fracture Mechanics (EPFM) approach are shown in the plot. It is seen that LEFM predicts a very small reduction in residual strength. LEFM overestimates the residual strength for the lead-crack only case by a large amount, as shown in Fig. 1.63. However, LEFM under-estimate the effect of MSD cracks as shown in Fig. 1.64. Thus, using LEFM will lead to the false impression that this structure is too strong to have WFD problems. Therefore, we conclude that EPFM approach is mandatory in the study of WFD problem.

The reduction of residual strength depends also strongly on  $d_{MSD}$ , the distance between the lead crack tip and center of the first rivet hole. The smaller  $d_{MSD}$ , the stronger the influence of MSD cracks. Fig. 1.65 illustrates such an effect. In practical application it is difficult to determine accurately and rationally the spacing  $d_{MSD}$ . The regulatory agency has to decide this requirement. From another point of view, the discrete source damage is random in nature. A probabilistic description seems to be more natural; and a probabilistic analysis is more suitable than a deterministic analysis.

### § 1.5.2 Fatigue crack growth analyses

After the analyses of the effect of MSD on the crack arresting capability of the aircraft fuselage panel, we can perform fatigue crack growth analyses to determine the WFD threshold. The hierarchical modeling strategy described in the previous subsection is also used for the fatigue analysis. The local fatigue analysis uses FEAM and LEFM. Fig. 1.66 shows the results from a simple, straight forward fatigue analysis. Forman's crack growth equation [Forman, Kearney, and Engle (1967)] is used in the analysis. It is

$$\frac{da}{dN} = \frac{C(\Delta K)^n}{(1-R)K_c - \Delta K} \quad (1.57)$$

where  $\Delta K$  is the stress intensity factor range and  $R$  is the stress ratio in cyclic loading. The values of  $K_c$ ,  $C$  and  $n$  were given by Forman *et al.* Forman, Kearney, and Engle (1967) as the following

$$\begin{aligned} K_c &= 83 \text{ ksi}\sqrt{\text{in}} \\ C &= 3 \times 10^{-4} \text{ kcyc ksi}^{-2} \text{ in}^{-2} \\ n &= 3 \end{aligned}$$

However, the initial residual stresses near rivet holes can change the fatigue life of these MSD cracks significantly. Residual stress due to rivet misfitting, cold

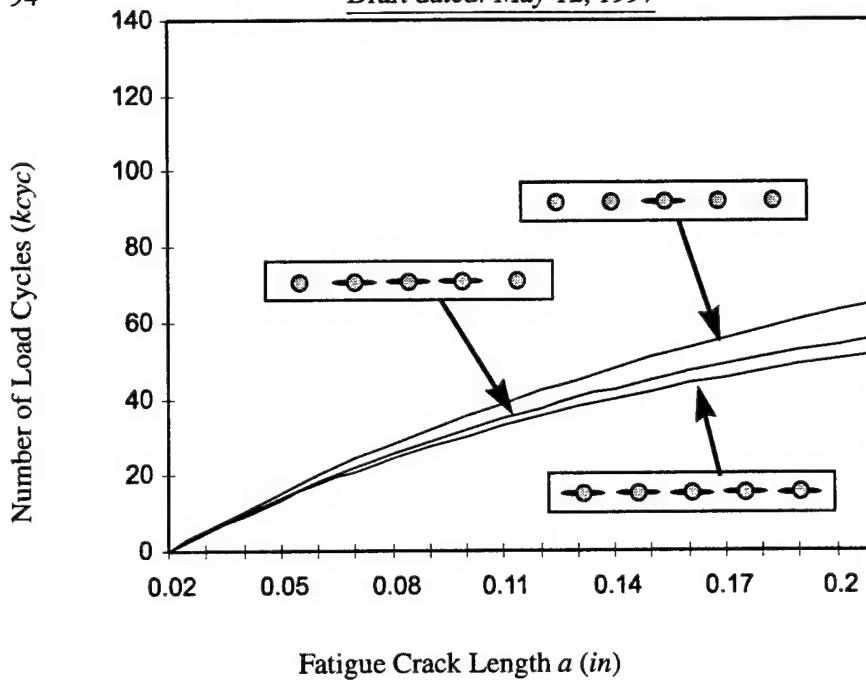


Figure 1.66: Fatigue crack growth, without considering the effect of residual stress

working, and rivet clamping forces, and fretting, etc, can all change the fatigue behavior. For illustration purpose, we demonstrate a case with the consideration of residual stress due to rivet misfitting and cold working. More details of the effect due to cold working and rivet misfitting [Park and Atluri (1993)] are presented in § 1.8.6.

Fig. 1.67 shows the prediction of fatigue growth with the consideration of residual stress. It is seen that in the presence of residual stress the fatigue growth behavior changes significantly. When compared to the case where there is no residual stress, as seen in Fig. 1.68, the small cracks grow faster and large cracks grow slower. Thus, the catch up phenomenon due to such residual stress, i.e., small fatigue cracks may grow faster to catch up with the sizes of larger cracks, may be observed.

This example of numerical analysis is based on a simplified residual stress model. In practice, rivet misfitting and cold working are displacement controlled processes. A more elaborated procedure may be needed to evaluate the effect of misfitting and cold working. Again, due to the random nature of residual stresses, a probabilistic analysis as a follow up to the deterministic analysis is necessary.

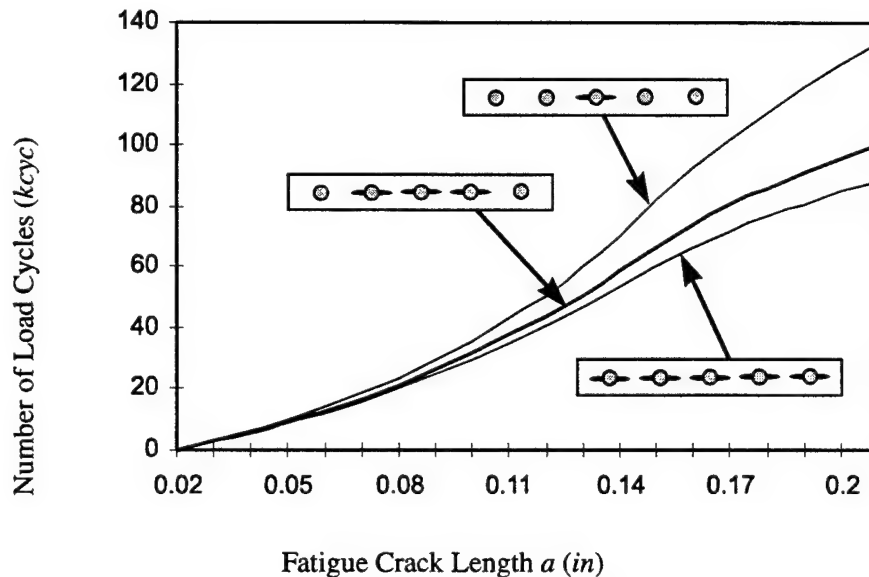


Figure 1.67: Fatigue crack growth, considering the effect of residual stress

### § 1.5.3 Conclusions

It is necessary to use WFDT approach to study the effect of MSD on the crack arresting capability of an aircraft fuselage, in order to enforce truly the damage tolerance concept. With the knowledge of widespread fatigue damage threshold, aging aircraft operators can schedule service inspections economically without compromising safety requirements; and the aircraft designer can optimize aircraft designs for better trade off between production cost, operating cost, maintenance cost and structural strength redundancy. Plasticity is very important in the residual strength analysis of not only the lead crack in the presence of MSD, but also of the lead crack itself. Residual stresses, induced by rivet misfitting, cold working, rivet clamping forces, fretting, etc, can change significantly the behavior of fatigue crack growth on an aircraft fuselage and WFD threshold. Since discrete source damages are random events and the magnitude of residual stresses has also a large scatter, a probabilistic analysis as a follow up of the present deterministic analysis is necessary.



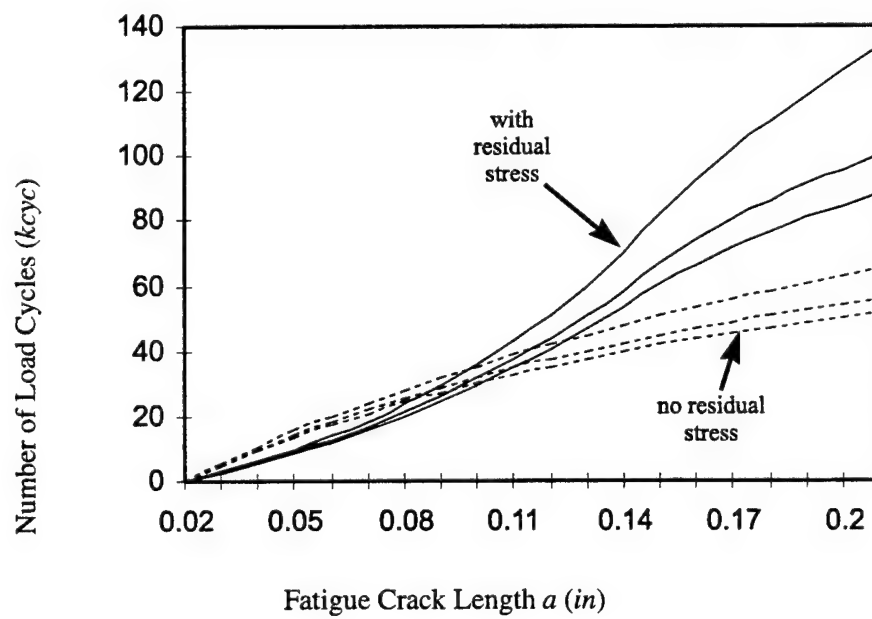


Figure 1.68: Fatigue crack growth, with/without considering the effect of residual stress

### § 1.6 Degradation of Residual Strength in the Presence of MSD: Stable Tearing Analyses

Practical methods for predicting the residual strength of a stiffened aircraft structure with a lead crack in the presence of MSD include the plastic zone technique [Swift (1985)], the crack tip opening angle (CTOA) method [Newman, Dawicke, Sutton, and Bigelow (1993)], and the  $T^*$ -integral method [Pyo, Okada, and Atluri (1994, 1995); Singh, Park, and Atluri (1994a); Brust (1995b,a); Wang, Brust, and Atluri (1995b,a,c)].

The plastic zone method is a simple engineering approximation method. It does not require much computational power, but its result may not be reliable. It predicts that the main crack will link with an MSD crack if their plastic zones overlap. The plastic zones are estimated using an elastic analogy such as an Irwin estimate. Only the main crack and the first MSD ahead of the main crack are considered in the computation of plastic zone. And, the Irwin estimate of the plastic zone size is not very accurate, especially for hardening materials. Further more, crack growth is ignored. Thus, significant errors can occur when the ligaments between the cracks are large enough to permit crack growth before any link up occurs. This actually happened in a series of tests performed at the National Institute of Standards & Technology [deWit, Fields, Low, Harne, and Foecke (1995)].

The CTOA method, which requires a rather detailed finite element analysis to apply, has been shown to be able to predict MSD failures. But, CTOA is a geometric parameter and cannot be used under more general fracture conditions such as cyclic loading and rate dependent fracture. The CTOA for fracture initiation and stable growth is measured in small planar specimens, wherein the crack axis lies in the plane of the specimen and the crack plane is perpendicular to the plane of the specimen. In this case, the CTOA has a reasonably clear physical basis. However, for cracks in cylindrical-shell type fuselage structures, and when such cracks bulge, the CTOA and the plane in which it should be measured are ambiguous. Thus, it is difficult to use CTOA as a fracture parameter in a predictive analysis for a real structure.

$T^*$ -integral is a promising and versatile fracture parameter (as summarized in Chapter ??). Being an energy quantity, it is applicable under severe operating conditions of cyclic loading and rate dependent fracture. Furthermore, it can be defined for cracks in any geometry (including a shell type fuselage structure) and when cracks bulge [see § 1.7].

This section provides validation of the EPFEAM method [presented in Chap-

ter ??] and the use of the  $T^*$ -integral [summarized in Chapter ??] for stable tearing analysis. The validation is made by comparing computational predictions of residual strength using these techniques, to experimental data produced by The National Institute of Standards and Technology (NIST). The experimental data was developed on large panels which contained a large main crack with Multiple Site Damage (MSD) cracks ahead of each tip of the main crack. The predictions provided here are true predictions, i.e. no 'fudging' of either the experimental data or the analysis predictions are made to make the predictions look better.

### § 1.6.1 *Prediction methodology*

The well accepted resistance curve methodology is used in conjunction with the Elastic-Plastic Finite Element Alternating Method (EPFEAM) and  $T^*$ -integral fracture parameter to carry out the computational prediction for the NIST MSD tests. The philosophy of the resistance curve methodology is the following. An experiment on a fracture specimen is analyzed. The values of a fracture mechanics parameter is computed for the fracture process. The computed curve of the fracture mechanics parameter versus the crack growth magnitude is called the resistance curve, which is assumed to be a material property that governs the fracture process. This analysis phase was termed "generation phase" by Kanninen (1978); Kanninen and Popelar (1985), since the purpose of the analysis is to generate information about material properties. Once the resistance curve is available, predictions can be made by forcing the fracture process to follow the resistance curve. Details are presented in the following.

Fig. 1.69 shows the flow chart for a simulative analysis. The test panel is first loaded to the crack initiation load. Then, the crack is extended by a small amount, while the load is changed simultaneously according the load versus crack growth curve obtained in the experiment. After computing a fracture parameter (such as  $T^*$  or CTOA) for all the steps during the crack growth simulation, a resistance curve (fracture parameter versus crack growth) can be obtained.

Generation phase analyses of test data to develop a resistance curve are usually performed when obtaining the curve directly from the test is time consuming, expensive, and impractical. It should be noted that both CTOA [see Newman, Dawicke, Sutton, and Bigelow (1993)] and  $T^*$  [see Okada, Suzuki, Ma, Lam, Pyo, Atluri, Kobayashi, and Tan (1995)] resistance curves can and have been obtained directly from experiments but doing so is not practical nor necessary.

In a predictive analysis, which is termed "application phase", the crack extension is controlled by the  $T^*$ -resistance curve. A flow chart for the application phase

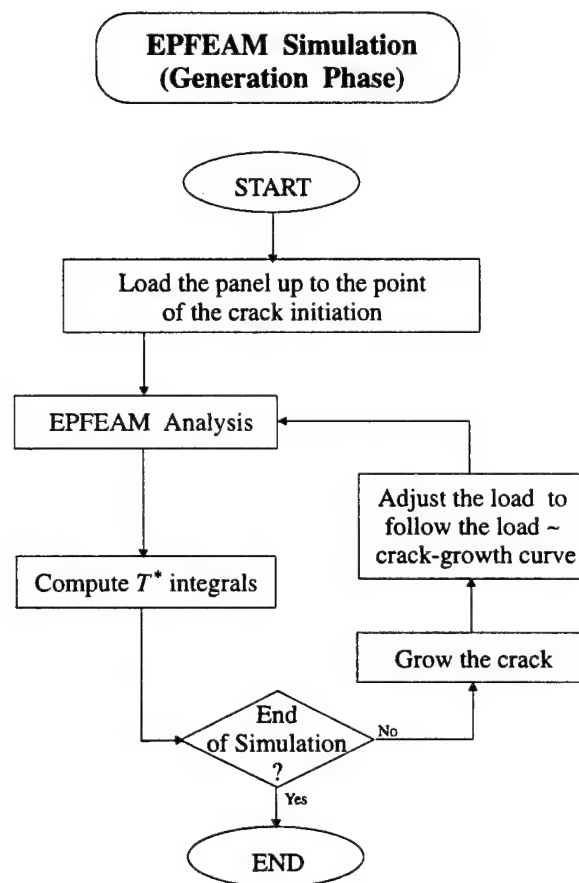


Figure 1.69: EPFEAM crack-growth simulation based on an experimental load versus crack-extension curve

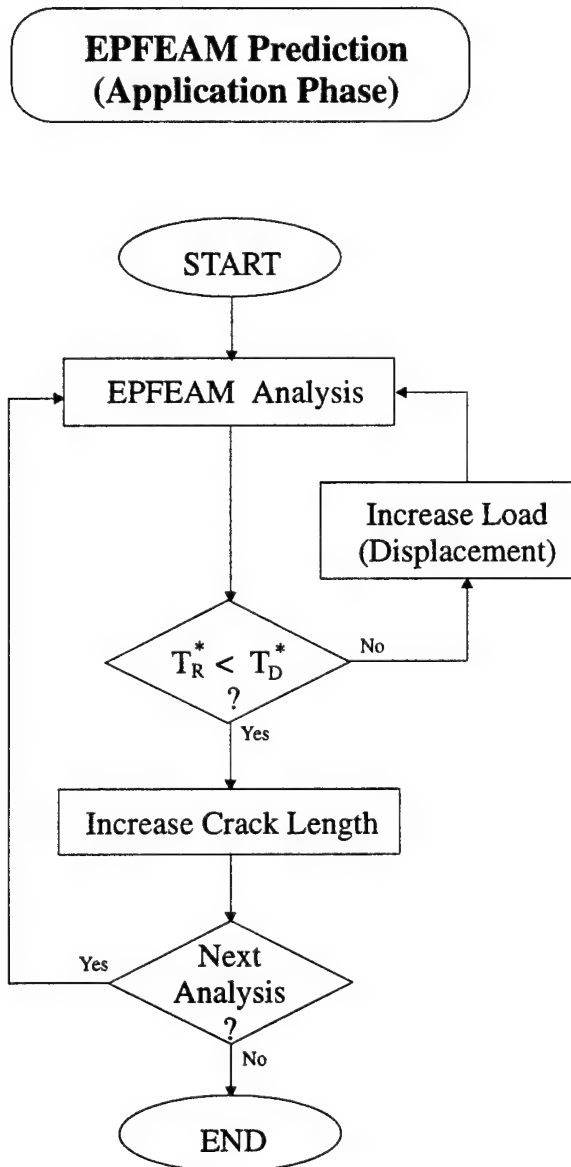


Figure 1.70: Predictive EPFEAM crack-growth algorithm based on a  $T^*$  fracture criterion

Table 1.9: Test matrix for NIST tests

Test No	Main crack		MSD cracks			
	$2a$ (in)	$a$ (in)	$d_{MSD}$ (in)	$s_{MSD}$ (in)	$2a_{MSD}$ (in)	number per side
MSD-1	14.0	7.0				
MSD-2	8.0	4.0				
MSD-3	20.0	10.0				
MSD-4	14.0	7.0	7.5	1.0	0.4	3
MSD-5	5.6	2.8	3.5	1.5	0.6	3
MSD-6	20.0	10.0	<i>(no anti-buckling guides)</i>			
MSD-7	20.0	10.0	10.5	1.5	0.5	5
MSD-8	19.0	9.5	10.5	1.5	0.5	10
MSD-9	10.0	5.0	6.5	1.0	0.4	10
MSD-10 <sup>r</sup>	20.0	10.0	10.5	1.5	0.5	5

<sup>r</sup> repeat of MSD-7

is shown in Fig. 1.70. It is assumed that i) increase the load(displacement) at the far field will increase the  $T^*$  value at crack tip; ii) extend the crack will cause the  $T^*$  value drops; and iii)  $T^*$ -resistance curve does not decrease as the crack extension increases. Under these condition, the simple predictive algorithm in Fig. 1.70 can be used.

In the following sections, the test performed at NIST is first summarized; then, the results for the generation phase and the applications phase are presented.

### § 1.6.2 NIST multiple site damage experiments

A short summary of the Multiple Site Damage (MSD) tests, performed at National Institute of Standards and Technology (NIST), is provided in this section. More details can be found in [deWit, Fields, Low, Harne, and Foecke (1995)].

The series of tests carried out at NIST is summarized in Tab. 1.9. The specimens were made of 2024-T3 aluminum, 90-inches wide, 150-inches high, 0.04-

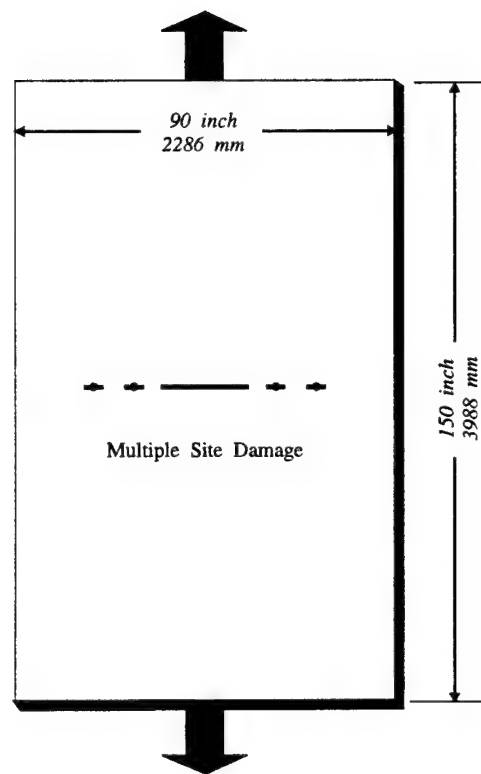


Figure 1.71: A typical NIST 90 MSD test panel

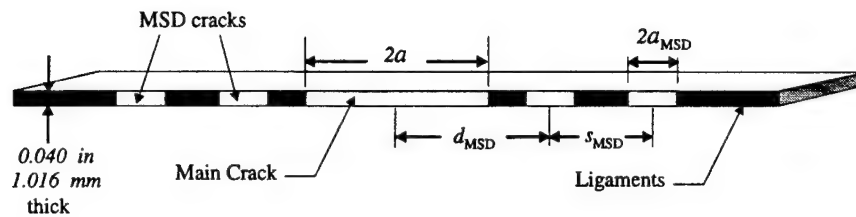


Figure 1.72: Crack locations and MSD spacings on a test panel

inch thick. Fig. 1.71 shows a typical test panel, where there are two MSD cracks in front of each of the main crack tips. The MSD crack definition parameters in Tab. 1.9, such as MSD crack spacing  $s_{MSD}$  etc, are defined graphically in Fig. 1.72. MSD cracks were equally spaced. The specimens were symmetric about their horizontal and vertical center lines. These flat sheet tests were performed to eliminate complications due to curvature and stringers so that good load and displacement control data could be obtained. In this fashion, good basic fracture properties were obtained.

As seen in Tab. 1.9, the first three tests were single center crack panel tests with different initial crack sizes. Tests MSD-4 through MSD-10 were tests of panels with multi-site damages (MSD) in front of the main cracks (except MSD-6 which was a repeat of MSD-3 without the use of anti-buckling guides). The numbers of MSD cracks ahead of each of the main crack-tips can be found in the last column of the Tab. 1.9. It is seen that these MSD tests had various different main crack sizes and different spacing of the MSD cracks.

The cracks were introduced by a series of saw cuts. The crack tips were made by the sharpest jeweler's saw cuts available, having a tip radius of 0.003 inch. To simulate cracks emanating from rivet holes as occurs in aircraft fuselage, the MSD cracks were cut from 0.22-inch holes that were drilled into the sheets before the saw cuts.

These test specimens were the largest structural panels that have been tested in tension. Because of the large size of these specimens, a 400 kips machine with extended grips was used. The grips were specially designed to enforce uniform stress applied to the specimens and were verified with strain gauges at low loads during the beginning of the tests. The measured strains were within  $\pm 10\%$  of the uniform value. It should be noted here that after crack growth and extensive plastic deformation, the uniformity of these stresses will not be achieved. In addition, anti-buckling guides were used, except for the MSD-6, so that the specimens did



not buckle out-of-plane due to the small thickness.

The test procedure consisted of pulling the specimen to fracture under displacement control. The displacement was generally applied at load intervals of 20 to 45 KN. The entire tests typically lasted from 15 to 20 minutes. It was also clear that both tips of the main crack did not grow at the same loads [deWit (1995)], due to the imperfection in the symmetric condition. This must be kept in mind when reviewing the results since crack growth was only recorded at one crack tip.

Fig. 1.73 provides a graphical representation of the crack growth behavior and MSD link-up results as observed from the tests. It is drawn to scale so that the main crack size, MSD crack size and crack spacing can be directly observed. In Fig. 1.73, the right side of the specimens is shown from the center line of the Center Cracked Panels (i.e., centerline of the main large crack) to the edge of the specimen. The half width is seen in Fig. 1.73 to be 45 inches. The ligaments that failed simultaneously, as observed from the experimental results, are illustrated with gray shading. The detailed experimental loads and crack growth response from these tests will be summarized in the next section during the discussion of comparisons between prediction and test results. The experimental failure loads during the link-ups and at the end of the tests are also shown in the next section.

The tests analyzed are: MSD-1 to MSD-5 and MSD-7 to MSD-9. MSD-6 is a single crack test with a crack size identical to the MSD-3 test. This test (MSD-6) was performed without buckling guides to observe the differences between a test with and without buckling guides. Since the computational analyses conducted here were two dimensional, the result is corresponding to the case with an anti-buckling guide. Also test MSD-10 is a repeat of test MSD-7. Hence, all unique tests in Tab. 1.9 have been modeled.

In addition, analyses were also performed on three of the Foster-Miller tests [Broek (1993)] that had a single crack. These aluminum test panels are flat center-cracked panels, only 20 inch wide, 48 inch long, and 0.04 inch thick. They were much smaller when compared to those used at NIST.

### **§ 1.6.3 Resistance curve calculation - generation phase**

A generation phase analysis was performed on the two single crack tests MSD-2 and MSD-3. The resistance curve could be CTOA but in this case we obtained the  $T^*$ -Resistance curve.

The load versus crack growth data from NIST tests MSD-2 and MSD-3 are plotted in Fig. 1.74. It is difficult to identify the crack initiation load from the experiment data, since it is difficult to detect accurately a small amount of crack

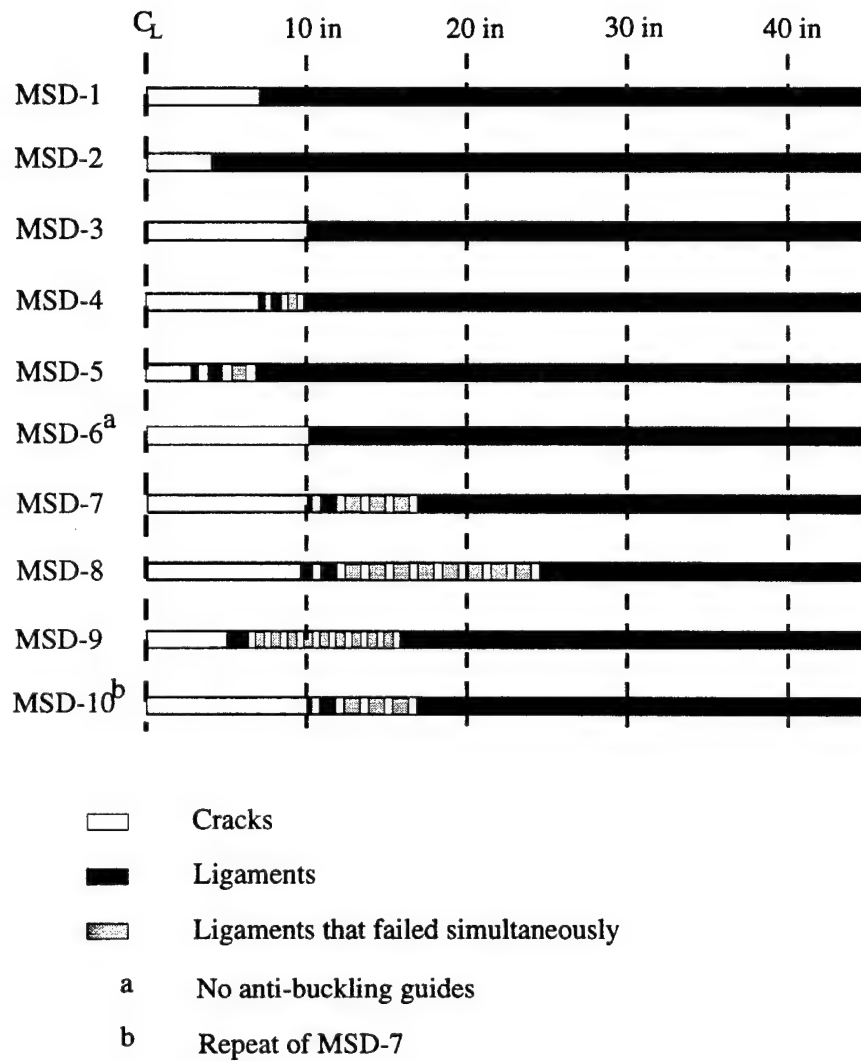


Figure 1.73: Experimental results illustrating the MSD link-up behaviors for each of the NIST 90 MSD tests

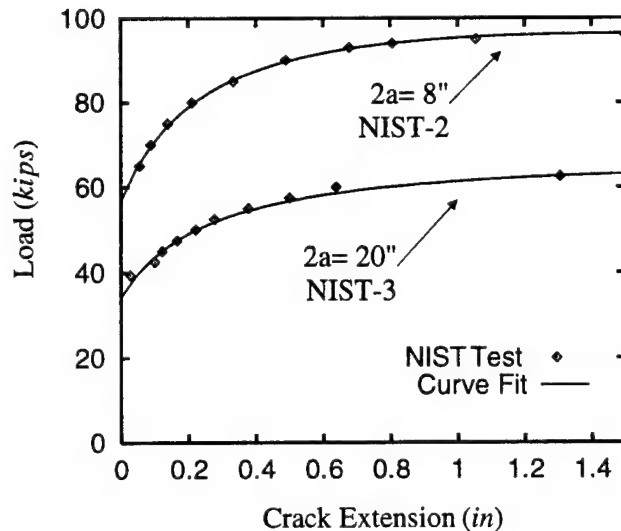


Figure 1.74: Experimental data for NIST 90 MSD-2 and MSD-3

growth. The scattering of measured data points among the different measurement methods, such as the data from the optical microscopy and from the video tape are significant at the crack initiation stage. Curve fitting can help us removing the scattering; and provide us a continuous representation of the test data. These data were fitted with curves, as shown in the Fig. 1.74.

Two generation-phase analyses were performed for each of the two MSD test. In the first analysis, the EPFEAM code was used. In the second analysis, a classical Finite Element Analysis (FEA) was performed. For the classical finite element analysis crack growth was modeled using a node release technique, while for the EPFEAM analysis, the method discussed in Chapter ?? was used. The plane stress assumption was used and eight node isoparametric elements were modeled. Either half or quarter symmetry of the cracked plates were used for analyses (a half model is useful to validate the code). The material properties used for the analyses are illustrated in the Fig. 1.75. The same material properties were also used for the predictive analyses described in the next section.

The calculated  $T^*$ -Resistance curves from this generation phase analysis are illustrated in Fig. 1.76 and Fig. 1.77 for cases MSD-2 and MSD-3, respectively. It is clearly seen that computed  $T^*$  values are basically identical between the two methods, i.e. the EPFEAM and the classical FEM. This is a complete validation of the

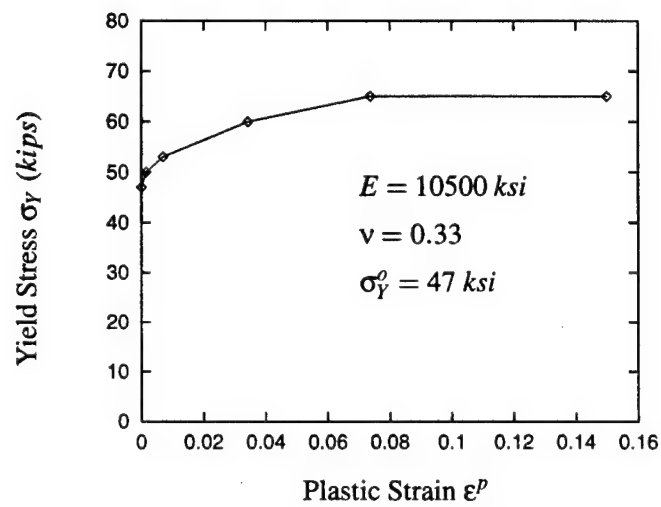


Figure 1.75: Elastic and plastic material properties for aluminum 2024-T3

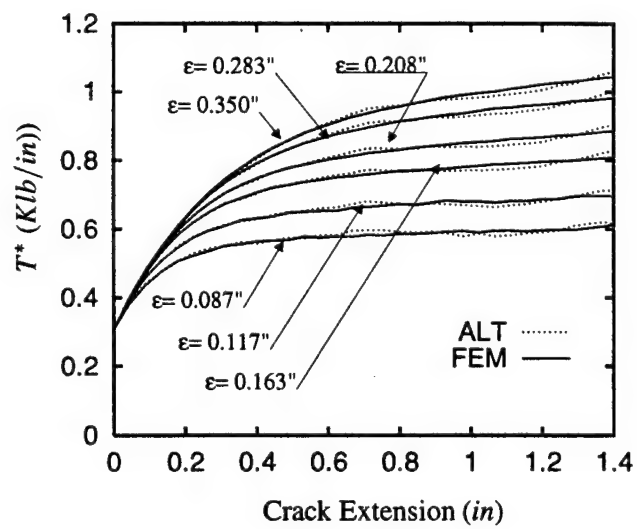


Figure 1.76: The  $T^*$  for NIST 90 MSD-2 using EPFEAM(ALT) and classical FEM

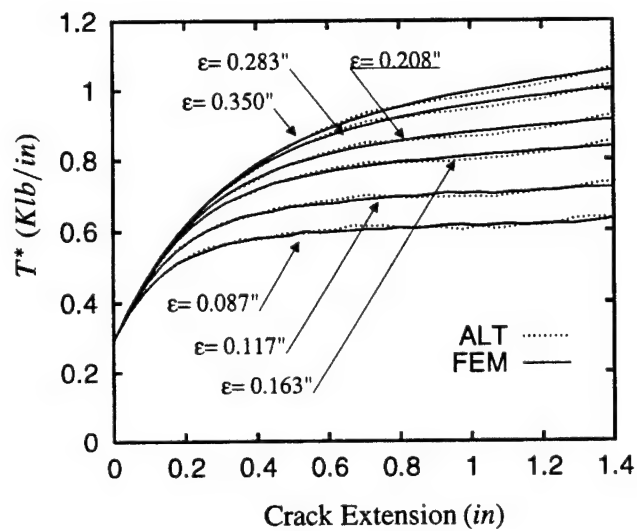


Figure 1.77: The  $T^*$  for NIST 90 MSD-3 using EPFEAM(ALT) and classical FEM

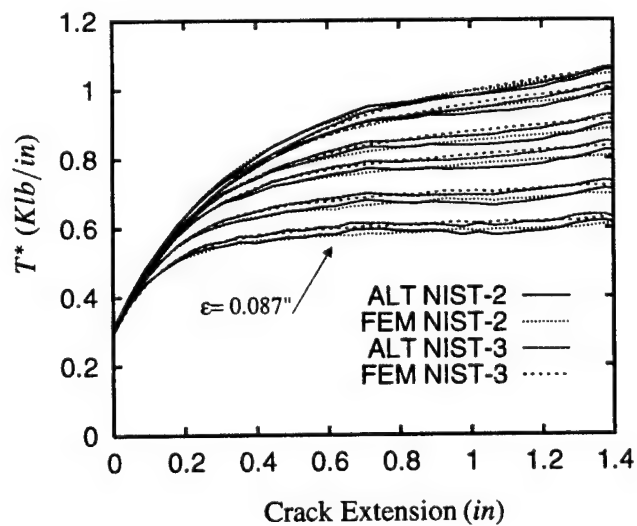


Figure 1.78: The  $T^*$  for NIST 90 MSD-2 and MSD-3 using EPFEAM(ALT) and classical FEM

EPFEAM code since the numerical evaluation of  $T^*$  consists of (see Chapter ??) integrating stress and strain (and their derivatives) type quantities at many locations along many paths surrounding the growing crack tip. Fig. 1.76 and Fig. 1.77 illustrates the evaluation along 6 paths ranging in size from  $\epsilon = 0.087$  inch to  $\epsilon = 0.35$  inch for a complete description of the path definitions for  $T^*$ ). In addition,  $T^*$  was calculated along many other paths with identical good comparison.

The good agreement of computed  $T^*$  along many paths between the the EPFEAM and classical FEA indicates that the full field solution using EPFEAM throughout the entire body is calculated accurately. It has been shown that EPFEAM can capture the asymptotic HRR solution (see, ) for a power hardening material. However, the present comparison is stronger proof of the accuracy of EPFEAM since the HRR field comparison is only near the crack tip and the effect of stress and strain derivative terms are not considered when comparing results to HRR fields.

To compare the  $T^*$ -resistance curves obtained from different tests, Fig. 1.78 places all of the results on Fig. 1.76 and Fig. 1.77 on a single plot. It is seen that the  $T^*$ -resistance curves for the MSD-2, which had an initial crack size  $2a = 8$  inch, and the  $T^*$ -resistance curves for the MSD-3, which had an initial crack size  $2a = 20$  inch, are very close throughout the crack growth history. Ideally, the  $T^*$ -Resistance curves for a given  $\epsilon$  would be identical regardless of the crack size. The differences illustrated in Fig. 1.78 are quite small, well within the scatter band of experimental error, and the lot to lot material variability. Indeed, variations of the J-Resistance curves from specimen to specimen (especially the initiation value,  $J_{IC}$ ) are quite significant [Rahman and Brust (1995)]. Thus, the obtained  $T^*$ -resistance curves can be viewed as a material property that governs the stable crack growth for aluminum 2024-T3.

The resistance curves for  $\epsilon = 0.087$  inch in Fig. 1.78 were fitted with an equation. The result is

$$T^* = 0.706 - 0.0398\Delta a - \frac{0.0697}{0.175 + \Delta a} \quad (1.58)$$

where the unit of  $T^*$  is (Klb/in) and the unit of  $\Delta a$  is in. This curve represents an average of the resistance curves obtained from the tests MSD-2 and MSD-3; and it was used for all other application phase analyses discussed throughout the rest of this dissertation. A discussion of the meaning for the different  $\epsilon$  path size definitions and their physical significance is presented in the Chapter ??.

#### § 1.6.4 *Prediction of single crack tests - application phase (I)*

The predictions are application phase analyses. The tests were analyzed using a displacement control condition and the  $T^*$ -Resistance curve is followed. The analysis is controlled by the driving force value of  $T^*$  being forced to follow the Resistance Curve throughout the crack growth history (see Fig. 1.70). As such, it is a true prediction.

The first prediction shown here is for the single crack test MSD-1. Among the single crack tests (with anti-buckling guides) of NIST, it is the only test that was not analyzed in the generation phase (see Tab. 1.9). The analysis was forced to follow the  $T^*$ -Resistance curve obtained in the generation phase. Recall that the  $T^*$ -Resistance curve was the average of these curves (see Fig. 1.76-1.78) obtained from the test MSD-2 and MSD-3 in the generation phase analyses. The  $T^*$  curve for  $\epsilon = 0.087$  inch was used for all predictions. However, the  $T^*$ -Resistance curve for all of the other values of  $\epsilon$  shown in Fig. 1.78 could have been used and the results would be identical.

Both the load and the crack growth are predicted from the displacement control analyses. Fig. 1.79 shows the analysis prediction compared with the experimental data. The  $T^*$ -Resistance curve equation, which was determined from MSD-2 and MSD-3 for the use in the prediction, is also shown at the top of the Fig. 1.79. Notice that this case is for a crack with a crack length ( $2a = 14$  inch) between those in the MSD-2 ( $2a = 8$  inch) and MSD-3 ( $2a = 20$  inch). As seen in Fig. 1.79, both loads and crack growth predictions compare well with the experimental data.

The "steps" in Fig. 1.79 are due to the nature of the predictive analysis. Consider a crack growth step. An increment of displacement is applied. When the driving force value  $T_D^*$  reaches the material resistance value  $T_R^*$  for the current crack size, the displacement is held constant while an increment of crack growth is permitted. If, after the increment of growth,  $T_D^* > T_R^*$ , the crack must grow more. So again, the displacement is held constant and an increment of crack growth is modeled. As such, the horizontal "steps" in Fig. 1.79 represent the amount of crack growth for a given displacement. Note also that, during a growth step with the displacement held constant, the load, which is predicted, drops slightly. If after an increment of crack growth,  $T_D^* < T_R^*$ , the growth of the crack is stopped. Hence, an additional increment of displacement can be applied. This application phase predictive methodology is illustrated graphically in Fig. 1.70. It is emphasized that the analyses in Fig. 1.79, as well as all analyses shown in the next section (which presents MSD analyses), provide predictions of both load and crack growth using only one  $T^*$ -Resistance Curve.

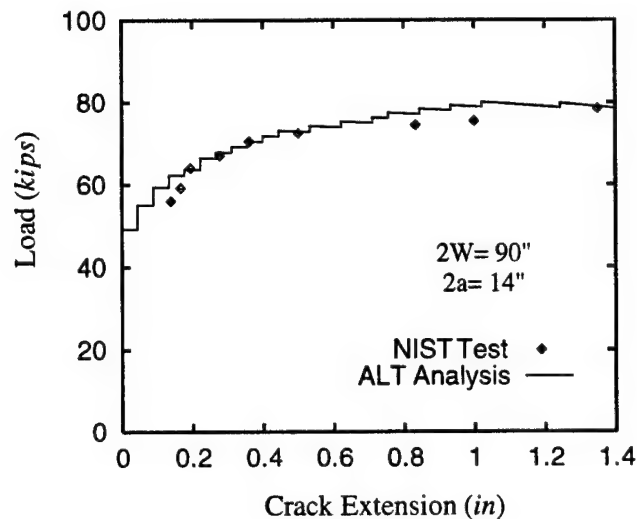


Figure 1.79: Load and crack growth predictions for NIST 90 MSD-1 compared with experimental results

This fashion of predictive analyses allows the numerical test follows the given  $T^*$ -Resistance Curve in an average sense. Small increments of displacements or crack growth are necessary in order to follow closely the  $T^*$ -Resistance Curve. At the expense of computational time, it is possible to design a more sophisticated algorithm to follow closely the  $T^*$ -Resistance Curve and to provide smoother predictions without “steps” in the predicted load versus crack-extension diagram.

Foster-Miller's [Thomson, Hoadley, and McHatton (1993)] flat panel test P1, P2 and P3 are also analyzed to provide additional verification of the predictive capability of the method and the obtained  $T^*$ -resistance curve (Eq. (1.58)). These were tension tests of center-cracked panels, with initial crack size  $2a = 4, 7, 11$  inch for tests P1, P2 and P3 respectively. Fig. 1.80 compares the predictions for three tests with different initial crack sizes. Good comparison is observed. Note that the resistance curve used for these analyses was obtained from the NIST material and not the Foster-Miller material. The mechanical properties of the material were also assumed to be the same (Fig. 1.75).



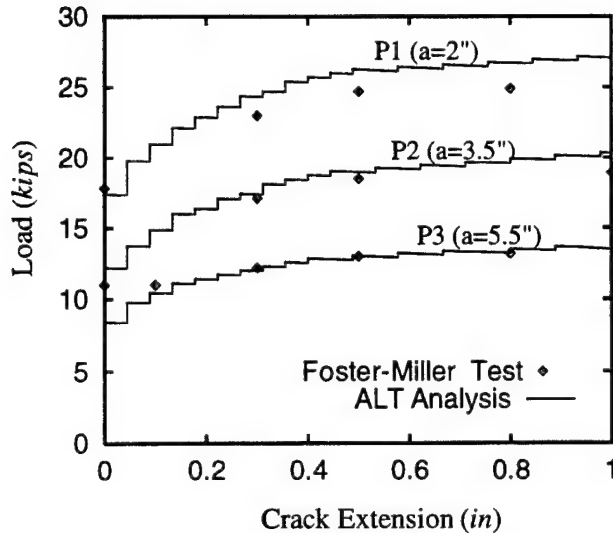


Figure 1.80: Load and crack growth predictions for Foster-Miller single crack panels P1, P2, P3, compared with experimental results

### § 1.6.5 Prediction of MSD tests - application phase (2)

This section describes the results of the analytical predictions of NIST 90 MSD tests using EPFEAM and the  $T^*$ -resistance curve (Eq. (1.58)), which is obtained from the simulation of NIST 90 MSD-2 and MSD-3 in the generation phase.

#### Cases MSD-4 and MSD-5

The experiments labeled MSD-4 and MSD-5 in Tab. 1.9 are seen to contain three MSD cracks on each side of the main crack. The main crack size and the spacing for the MSD cracks are illustrated schematically in Fig. 1.73. Fig. 1.73 is drawn to scale so that the main crack size and spacing can be directly observed. As seen, the main crack for MSD-4 is larger than MSD-5 while the MSD cracks are smaller and spaced closer together.

Fig. 1.81 and Fig. 1.82 illustrates the finite element meshes used for MSD-4 and MSD-5. Half symmetry was used for MSD-4 and MSD-5, i.e. the top half of the specimen was modeled and both the left and right half sections of the cracks were considered. Fig. 1.81 and Fig. 1.82 illustrates a blowup of left main crack and corresponding MSD cracks for these two cases. These mesh details are to scale

and the numbers on the scales represent real distances in inches. Also, the MSD cracks drawn at the bottom of each mesh and their occurrence in the mesh are also illustrated.

Of course, a quarter model rather than a half model could have been used (and was used for cases MSD-7, -8, and -9). However, modeling each crack tip separately provides an excellent check on the computational methodology. More importantly, the versatility of the EPFEAM method combined with the  $T^*$ -integral fracture methodology can be considered. For instance, by introducing an initial perturbation, the effect of uneven crack growth rates for each crack tip can be studied. For instance, the right half main crack tip could be made slightly larger than the left crack, and the effect of uneven right and left side crack tip growth and the corresponding non-symmetric crack growth (which was observed experimentally) can be accounted for very easily. The specimens, which had all cracks machined with a saw, did not have "perfect" crack lengths and the corresponding MSD separation (illustrated in Tab. 1.9) certainly have a statistical scatter associated with their distances. The perturbations associated with the left and right side crack tips growing at different rates can have an important effect on failure loads. This should be kept in mind when observing the following predictions since the left and right cracks did indeed grow at different rates in the experiments. The experiments tracked the left side crack only. Finally, it is important to note that in real aircraft fuselages, the same effect will occur and can have an important effect on residual strength. This is especially true since stringers and frames are present. This "crack tip perturbation" effect is not studied here, but should be considered in future work since it has not been studied to date in the literature.

The application phase predictions for tests MSD-4 and MSD-5 are shown in Fig. 1.83 and Fig. 1.84, respectively. In these figures (and all other similar figures shown subsequently) the abscissa represents crack growth and the ordinate represents load as predicted using the algorithm shown in Fig. 1.70. The predicted results are for the right crack tip. The right and left side cracks grew symmetrically, since no initial crack size or other perturbation sources, such as slight statistical differences in the  $T^*$ -Resistance curves within the specimen, were considered in the analyses here. In Fig. 1.83 or Fig. 1.84 the point of zero crack extension is corresponding to the initial position of the right tip of the main crack. The MSD cracks are drawn to scale in these figures so that the extension of the main crack and MSD link-up points, and corresponding simultaneous ligament failure predictions can be observed.

It is seen that the MSD-4 predictions (Fig. 1.83) are excellent. Both the link-up

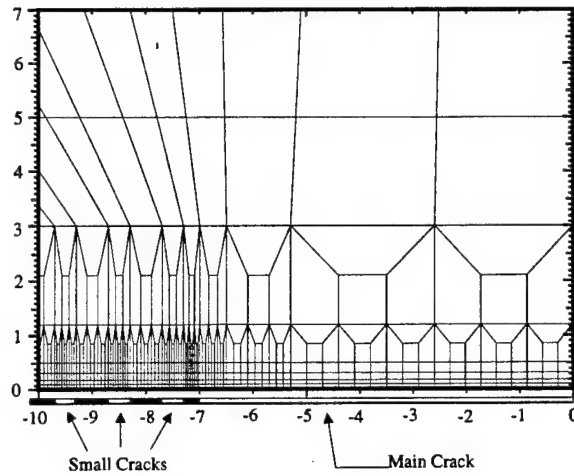


Figure 1.81: FEM mesh, in the vicinity of the left MSD cracks, for NIST 90 MSD-4 in the EPFEAM analysis

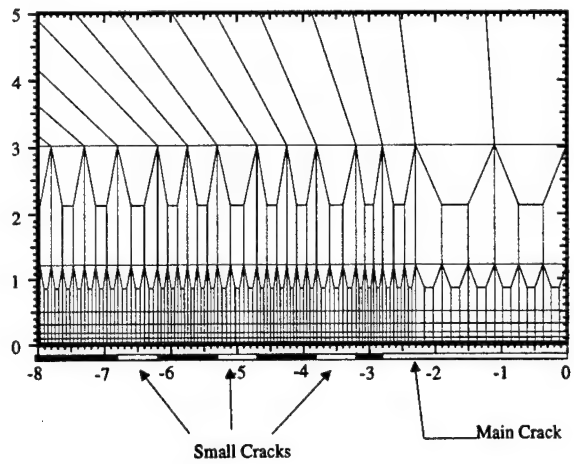


Figure 1.82: FEM mesh, in the vicinity of the left MSD cracks, for NIST 90 MSD-5 in the EPFEAM analysis

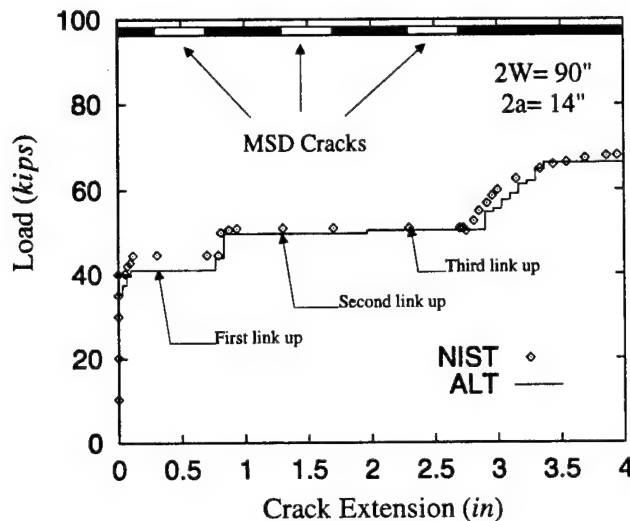


Figure 1.83: Load and crack growth predictions for NIST 90 MSD-4 compared with experimental results

loads, maximum load, and crack growth predictions are almost identical with the experimental values. Fig. 1.84 likewise shows good predictions for MSD-5 except that the failure load is predicted to be identical to the second/third link-up load. Experimentally, a slight increase in load was observed (after the third link-up) at about 4.5 inches of crack growth. However, these predictions are considered excellent given the many sources of statistical variability for these experiments. This variability includes: material lot variability of material properties such as stress-strain response and  $T^*$ -Resistance curves, slight errors in specimen fabrication which led to the experimentally observed crack growth rate differences between the left and right side crack tips, etc. The sources of statistical variability are discussed further in the discussion section.

#### Case MSD-7

The application phase prediction for test MSD-7 is shown in Fig. 1.85. This test had five MSD cracks ahead of both tips of the main crack. The crack spacing and crack sizes are illustrated in Fig. 1.73 and at the top of Fig. 1.85. As seen in Fig. 1.73, all of the MSD cracks joined together after the second link-up (gray shaded regions - Fig. 1.73). Excellent predictions of both link-up loads, link-up instability, and

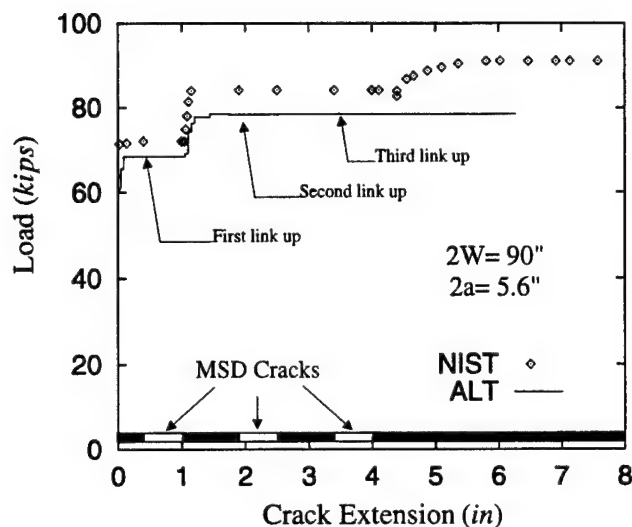


Figure 1.84: Load and crack growth predictions for NIST 90 MSD-5 compared with experimental results

crack growth behavior are seen in Fig. 1.85. Note that MSD-10 test data is also presented here. Having the same crack size, the MSD-7 and MSD-10 tests were identical. Some of the statistical variability in results can be seen here with the test results for MSD-10 higher than those for MSD-7. The analyses for this case, as well as for MSD-8 and MSD-9 (discussed next), used a quarter model, i.e. only the right crack was modeled.

#### Cases MSD-8 and MSD-9

These tests had ten MSD cracks ahead of both main cracks. Fig. 1.73 illustrates the crack configurations, sizes, and MSD separation. It is seen that test MSD-8 had a larger main crack, larger MSD spacing, and larger MSD separation compared with test results for MSD-9.

The application phase predictions for tests MSD-8 and MSD-9 are shown in Fig. 1.86 and Fig. 1.87, respectively. The MSD spacing is illustrated at the bottom of these figures. Again, the initial position of the right main crack tip is corresponding to the point of zero crack extension in Fig. 1.86 and Fig. 1.87, with the MSD spacing ahead of the main cracks. The initiation load prediction for MSD-8 (Figure 14) is quite good. The predicted load at first link-up is slightly higher than the test

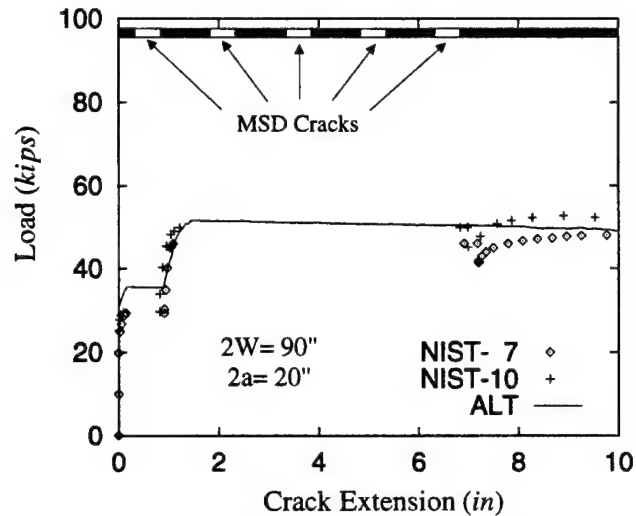


Figure 1.85: Load and crack growth predictions for NIST 90 MSD-7 compared with experimental results

data. In addition, the predicted load at second link-up is higher than the test data. After the second link-up, the MSD cracks all linked together as seen in Fig. 1.86 after about 2.5 inches of crack growth. This link-up instability was predicted by the EPFEAM model quite well.

At this point it is interesting to observe the results after the unstable MSD link-up. This unstable link-up occurs when the main crack links with all of the MSD cracks between crack growth of about 2.5 to 14 inches. The experiments were performed via displacement control (as were the analyses). When the MSD instability occurred between crack growth of 2.5 to 14 inches the crack was observed to 'pop' in an unstable fashion, i.e., the crack propagated in a dynamic unstable fashion as all of the MSD cracks linked together. Since the displacement was held constant while the crack jumped almost 12 inches, the load must drop. This is seen in Fig. 1.86 where the experimental load is about 20 Kips after the crack jump at a crack extension value of about 15 inches. The experimental displacement is then increased until the final load of about 40 Kips is reached. The predictions, which are all quasi-static, cannot account for this dynamic crack jump at present. There are two important events that occurred experimentally here, and which certainly would occur in a real aircraft. These are: (i) The inertial effects of the crack jump

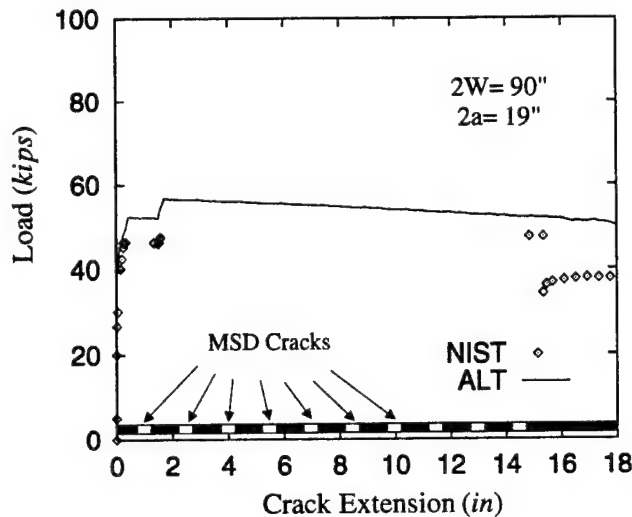


Figure 1.86: Load and crack growth predictions for NIST 90 MSD-8 compared with experimental results

and the greatly increased crack speed and corresponding strain-rates near the growing crack tips reduce the size of the plastic zone and lead to a more 'brittle type' crack growth compared with quasi-static growth, and (ii) because the displacement was held constant during the crack jump, the load decreased, and as a result, an unload-reload cycle occurred. It is well known that such unload/reload effects reduce the load carrying capacity of stable growing cracks. This latter effect can be accounted for with the current model (except it may be necessary to implement a more appropriate cyclic plasticity constitutive law since an isotropic hardening model was used for these analyses). Both the dynamic crack jump effect and the cyclic effect should be considered in future work, since they can reduce significantly the load carrying capacity of a structure. It should be emphasized that both effects are present in real aircraft since, due to the stringers, frames, and tear straps, displacement control MSD 'crack jumps' will occur in service. Note from Fig. 1.86 that the predicted load slowly decreases at the predicted 'crack instability' since we use a quasi-static analysis.

Fig. 1.87 illustrates the prediction for MSD-9. Note that the initial link-up led to a rapid crack jump (Fig. 1.73 and Fig. 1.87). The rapid crack jump was also predicted via the model. The maximum load is somewhat under-predicted

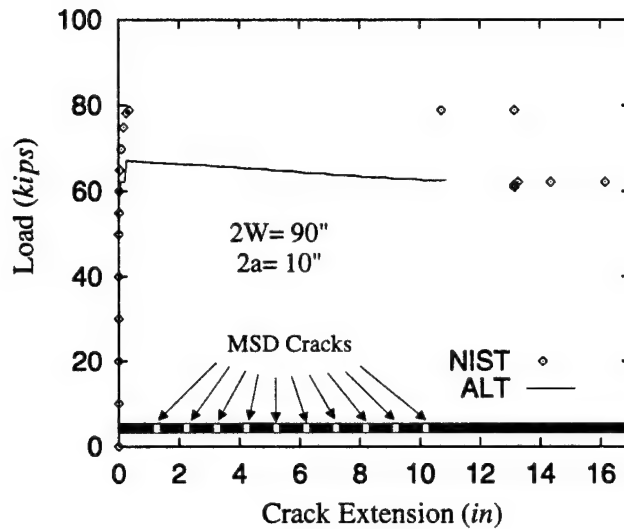


Figure 1.87: Load and crack growth predictions for NIST 90 MSD-9 compared with experimental results

compared with the experimental results. The same effect of the crack jump and unload/reload effect (discussed above regarding Fig. 1.87) is observed here after about 13 inches of crack growth.

#### *Predictions of plastic zones and stresses*

It was seen in the previous section that the load versus crack growth predictions based on the EPFEAM method and the  $T^*$ -integral fracture theory provided good predictions of the phenomena of MSD crack growth, link-up, and unstable fracture. Thus, the tools presented above can be readily used to make residual strength predictions of aircraft fuselage MSD cracking. In this section, some examples of full field solutions of displacements, stresses and strains are presented to show that the tools presented here can also provide detailed information in helping understanding the MSD phenomena. For the purpose of this presentation, results for plastic zones and stresses for case MSD-4 are illustrated. The results for all of the other cases are similar to these.

Fig. 1.88 illustrates the development of the equivalent plastic strains ahead of the main crack and around the MSD cracks, while Fig. 1.89 through Fig. 1.91 shows the evolution of various stress components. The vicinity of the left crack tip



of the main crack and the associated MSD cracks ahead of it is shown in each of these contour plots. The dimensions along the ordinate and abscissa represent real dimensions in inches. Thus, the shapes of plastic zones and stress zones are not distorted.

Recall from Tab. 1.9, Fig. 1.73 and Fig. 1.83 that MSD-4 had a main half crack initial length of 7 inches, with three MSD cracks ahead of each main crack tip. The current position of the left tip of the main crack and the position of the remaining MSD cracks, i.e. those have not been absorbed by the main crack, are indicated at the bottom of each contour plot, using a black-white bar. The black parts indicate the ligaments, while white parts correspond to the cracks.

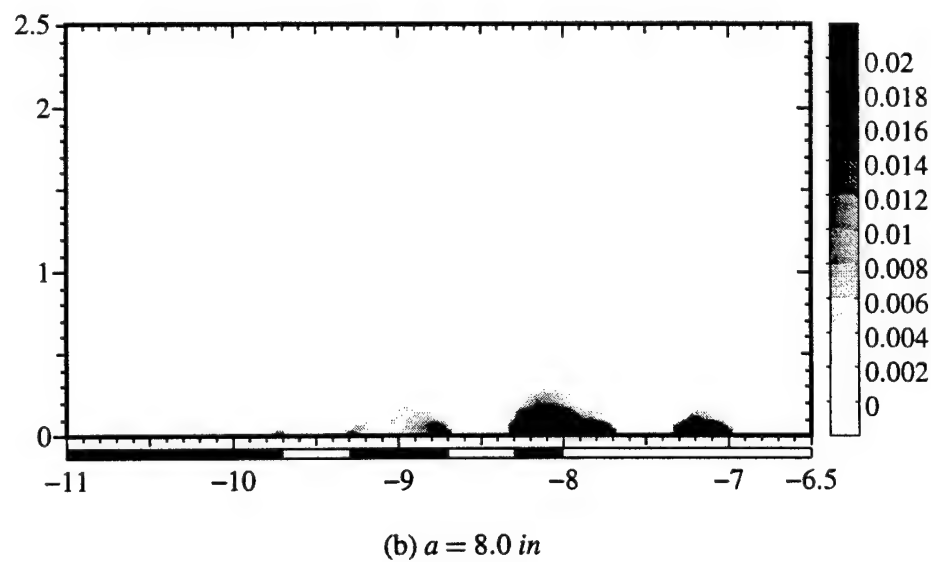
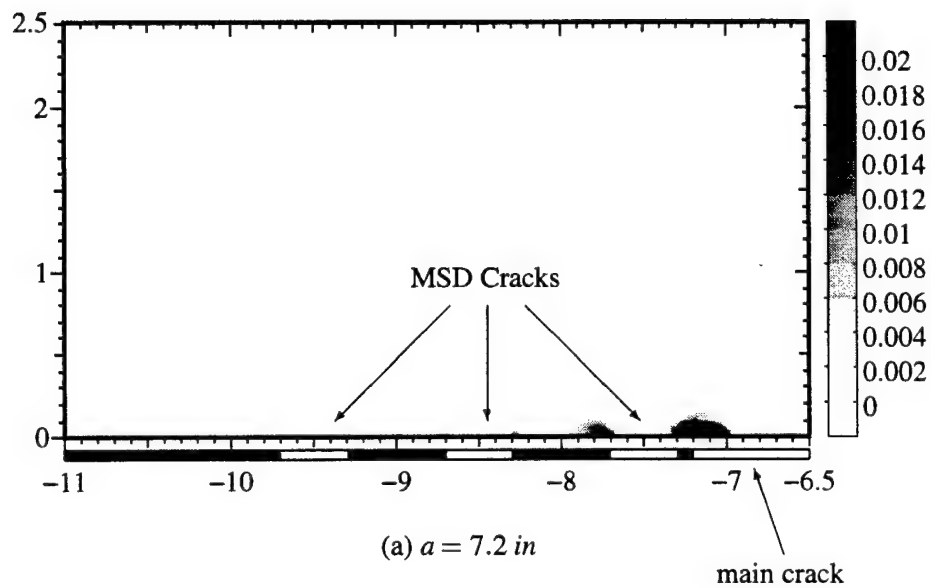
Contour plots are provided at four different locations of crack growth. They are (a) right before the first link up ( $2a = 7.2$  inch); (b) after the first link up ( $2a = 8.0$  inch); (c) after the second link up ( $2a = 9.0$  inch); (d) after all MSD cracks are linked up ( $2a = 9.9$  inch). Detailed discussions about these plots are provided in the following.

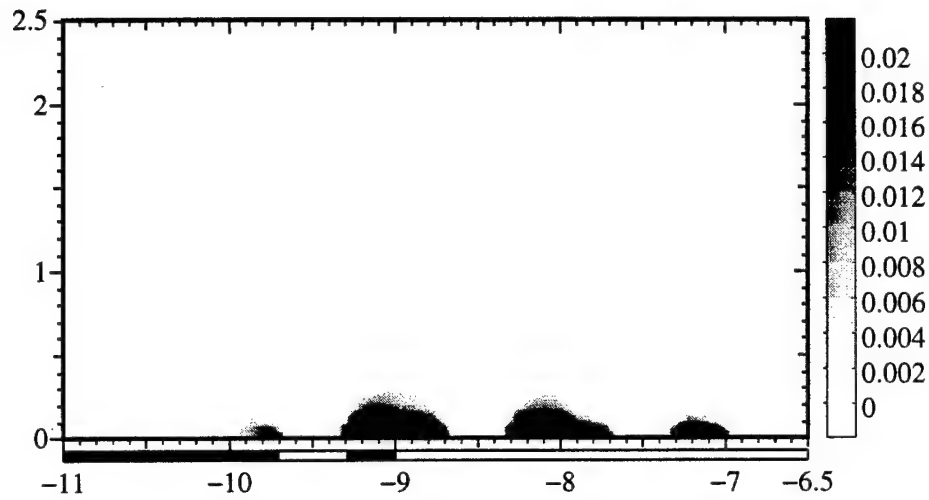
*(1) Plastic zones*

Fig. 1.88 illustrates the development of the equivalent plastic strains ahead of the main crack and around the MSD cracks. The predicted plastic zones can be observed in Fig. 1.88 without distortion since the aspect ratio of the plot is reserved.

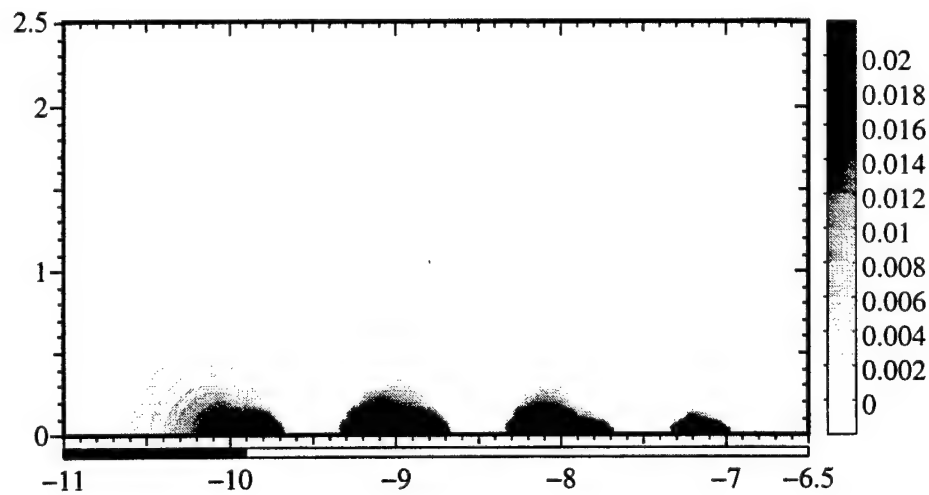
Fig. 1.88(a) illustrates the plastic zone contours near the crack tip regions just after the main crack has begun growing. Fig. 1.88(a) shows the tip of the main crack at -7.2 inches. Observe that the plastic zone size at the main tip, is about the order of the MSD crack lengths. The corresponding load at this point is about 45 Kips as obtained from Fig. 1.83 for 0.2 inches of crack growth. Note that the minimum plastic strain contour plotted here is 0.002 (i.e., the 0.2% offset strain). Note that the presence of the MSD crack ahead of the main crack "stretches" the plastic zone in the crack growth direction as compared with the usual plane stress plastic zone shape for a single crack and that the entire net section between the first MSD crack and the main crack is plastic. Observe also from Fig. 1.88(a) that the plastic zone at the left tip of the first MSD crack is becoming larger, and that the net section between the left tip of the first MSD crack and the right tip of the second MSD crack is approaching full plasticity. Note also that there are small zones of plasticity already developing at the tips of all cracks at this point just after main crack initiation.

Fig. 1.89(b) illustrates the plastic zone when the main crack is 8 inches long. This represents a point after the main crack and first MSD crack have linked and the current main crack is half way through the ligament between the first and second





(c)  $a = 9.0$  in



(d)  $a = 9.9$  in

Figure 1.88: Equivalent plastic strain contour plot( $\epsilon^P$ ) at different locations of crack growth

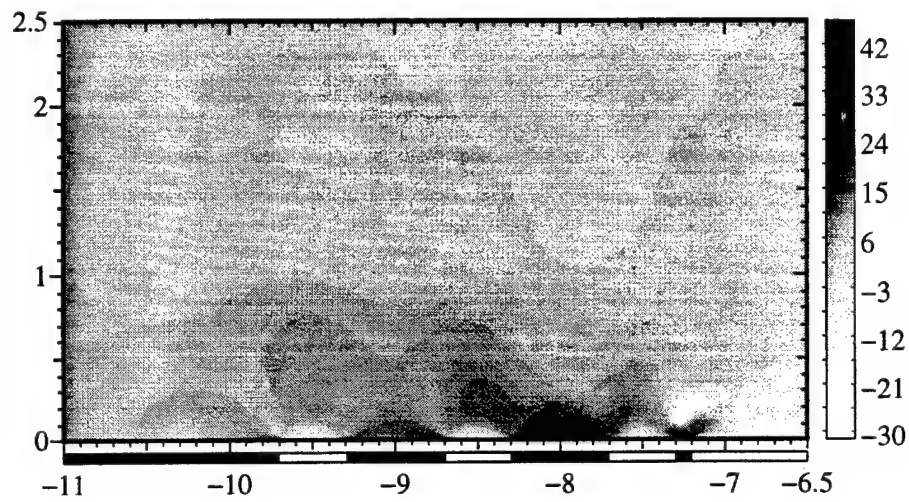
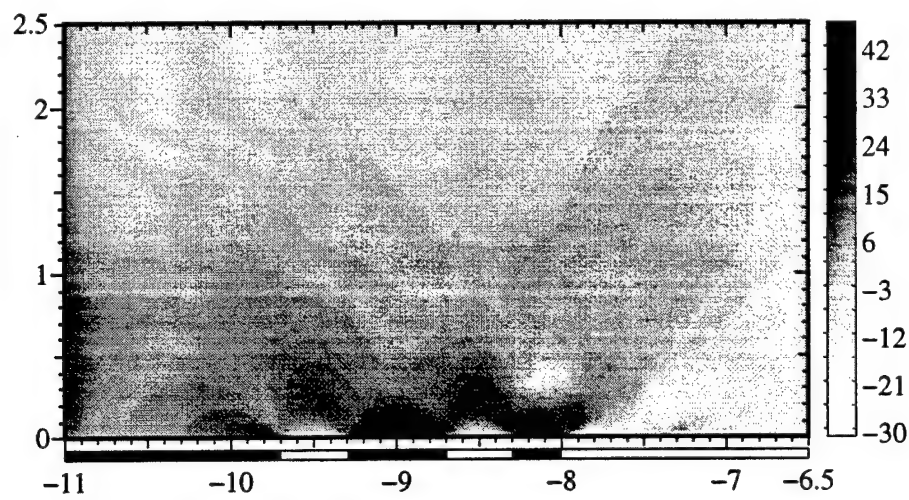
MSD cracks. The residual plasticity at the ligament between the main crack and the first MSD crack (which is now a region of the current main crack tip since the main crack has grown through the first MSD crack ligament) is seen to be very similar to that seen in Fig. 1.89(a). It is also important to observe that the net ligament between the current main crack tip (at 8-inches) and the second MSD crack is fully plastic. Moreover, the ligament between the second and third MSD crack is fully plastic. From Fig. 1.83 the load is about 49 Kips for crack growth of 1-inch and the link-up between the current main crack and the second MSD crack occurs at a crack growth of 1.3 inches. This indicates that the load carrying capacity of the ligaments between the MSD crack is about reached. But this does not mean that the loading carrying capacity of the panel is reached, since the main ligament that is the part after the MSD cracks may still be able to carry load. It is seen that the plastic zone at the left tip of the third MSD crack is still very small.

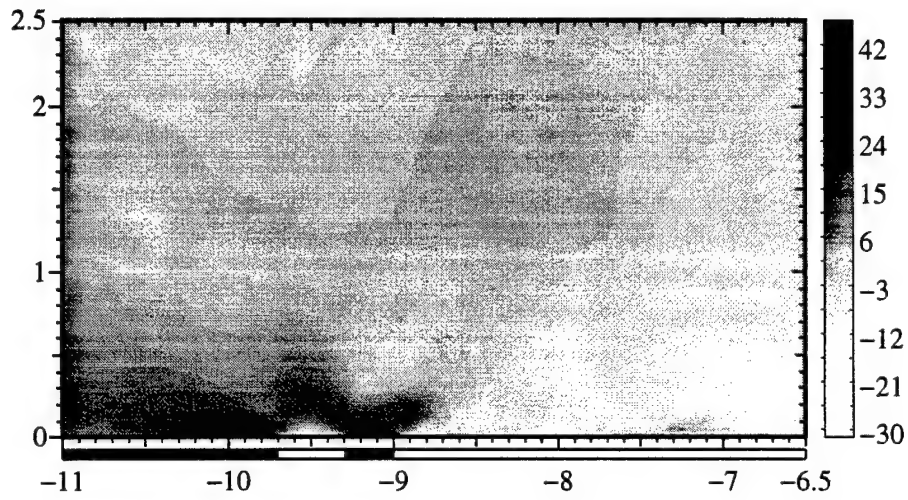
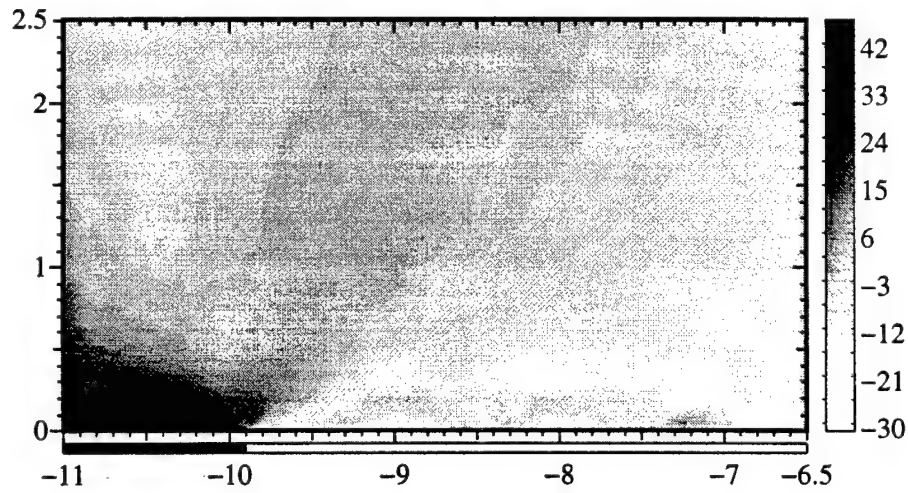
Fig. 1.88(c) shows the plastic zone profiles when the main crack is 9 inches long, i.e., total crack growth of 2 inches has occurred. At this point the main crack has linked with both the first and second MSD cracks and is currently halfway through the ligament between the second and last MSD crack. As seen from Fig. 1.83, the current load is about 50 Kips at this point. Again, the plastic zones along the main crack faces at the locations where the first two MSD crack ligaments were located are similar in size and shape to the zone sizes before linkage occurred [see Fig. 1.88(a) and (b)]. Note that the ligament ahead of the left side of the last MSD crack is beginning to attain a significant plastic zone.

Finally, Fig. 1.88(d) shows the plastic zone profiles after all MSD cracks have linked and the current main crack has grown 0.2 inches ahead of the left tip of the last MSD crack. At this point the main crack has grown a total of 2.9 inches and the load (from Figure 11) is currently about 54 Kips. As seen in Fig. 1.83, at this point there is still a significant amount of residual strength left in this specimen.

## (2) Stresses

Fig. 1.89 illustrates  $\sigma_x$  at four different crack growth lengths for MSD-4. The x-component of stress is along the crack growth direction. The x-coordinate of -7 represents the initial position of the left tip of the main crack. The three MSD crack lengths and locations appear at the bottom of Fig. 1.89. For Fig. 1.89(a) the main crack has grown 0.2 inches through the ligament between the main and first MSD crack and at that point the ligament is only 0.1 inches long. This ligament can be identified by the red color (high  $\sigma_x$  in tension) above the  $x = -7.2$  and  $-7.3$  in Fig. 1.89(a). In addition, the ligament between the first and second MSD cracks experiences a large stress state. Also, observe the "cyclical" stress pattern

(a)  $a = 7.2$  in(b)  $a = 8.0$  in

(c)  $a = 9.0$  in(d)  $a = 9.9$  inFigure 1.89: Stress contour plot( $\sigma_x$ ) at different locations of crack growth

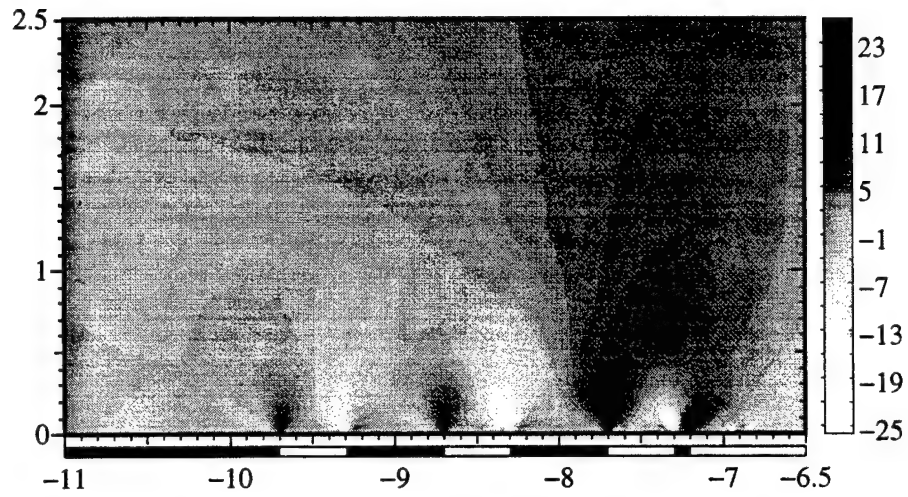
that develops along the crack extension direction caused by MSD. Fig. 1.89(b) shows the  $\sigma_x$  stresses after the main (half) crack has grown to 8.0 inches. Likewise, Fig. 1.89(c) and (d) show this stress component for main (half) crack lengths of  $a$  9.0 and 9.9 inches, respectively.

By observing the progression of  $\sigma_x$  as the main crack grows in Fig. 1.89 (a) through (d), the following trends are noted.

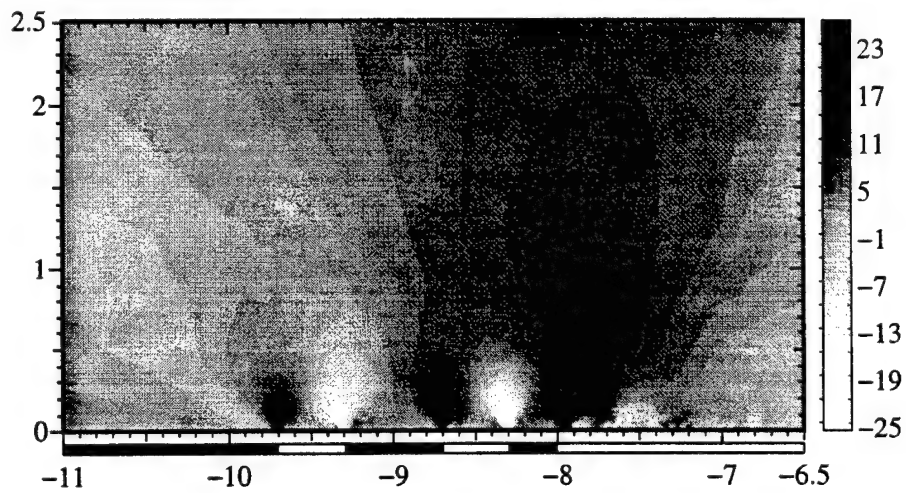
1. A large zone of compressive stress develops above the main crack. Despite the fact that these figures show a blowup of the region in front of the left crack tip, it should be clear that this compressive zone is large and extends above and along the entire main crack. Indeed, these stresses are the reason that buckling guides are required for the experiments.
2. A compressive 'wake' zone of larger magnitude stresses above the MSD crack ligaments is seen, after these ligaments are absorbed by the main crack. This may be seen from the dark blue color above the ligaments between the second and third MSD cracks (i.e. above the -8.0 and -9.0 coordinates). This large wake compression zone is well known to exist for the single crack growth problem [see Brust, Nishioka, Atluri, and Nakagaki (1985); Brust, McGowan, and Atluri (1986) for instance] and can result in significant residual stresses after removal of the load. This zone contributes to the 'unload/reload' phenomena where a cycle of unloading followed by reloading reduces the load carrying capacity of the cracked structure [Brust, McGowan, and Atluri (1986)].

Fig. 1.90(a) through (d) show the shear stress component ( $\sigma_{xy}$ ) at these same four crack growth locations as discussed for Fig. 1.88 and Fig. 1.89. The locations of the current main crack tip as well as the MSD cracks can be observed by focusing on the large (pairs of dark red and dark blue contours) stresses. It is interesting to observe that the zone size of the large shear stresses at the main crack tip is rather small when MSD is present [Fig. 1.90(a) through (c)] while it is much larger when all cracks have linked up and only one large crack remains [Fig. 1.90(d)]. However, the zone size of the large shear stresses for the MSD cracks [Fig. 1.90(a) through (c)] is quite large compared to the MSD crack lengths.

Fig. 1.91(a) through (d) show the same type of contour plots for  $\sigma_y$ , where the  $y$  coordinate direction is perpendicular to the crack. Again, the crack tip locations may be easily identified by the large (red) stress contours and the net section ligament stresses are quite large. The traction free condition at crack surfaces results



(a)  $a = 7.2$  in



(b)  $a = 8.0$  in



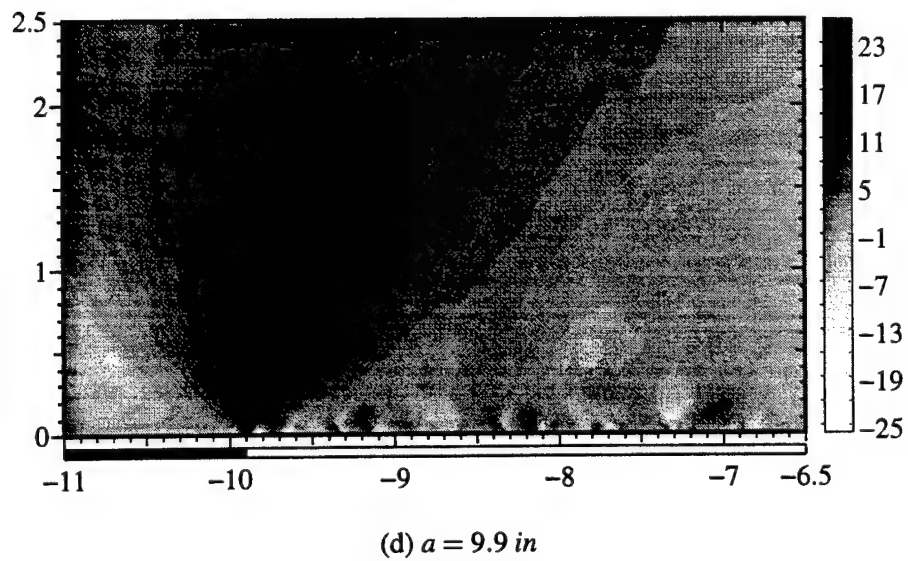
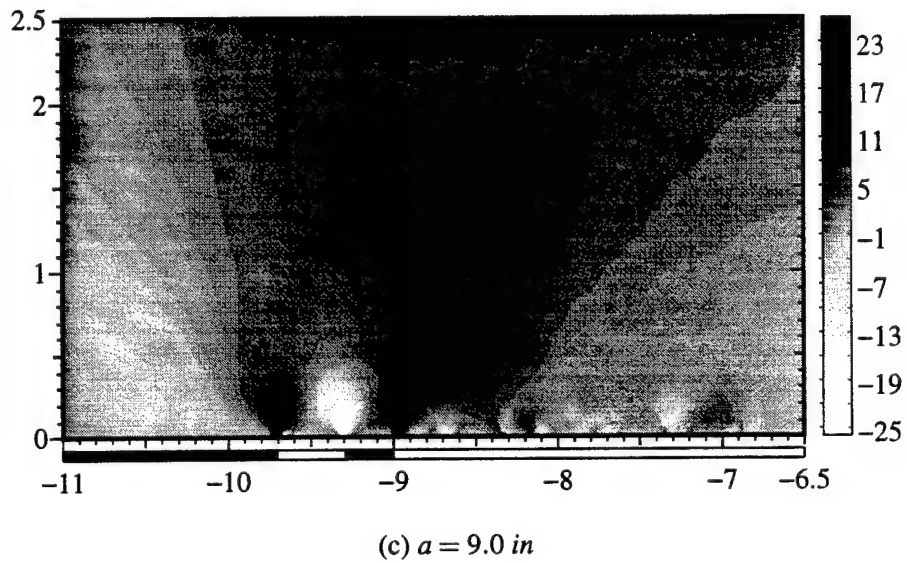
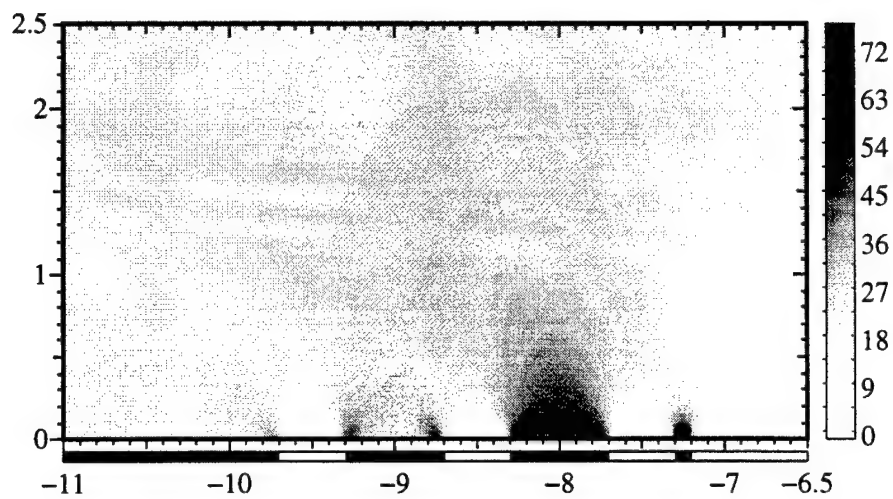
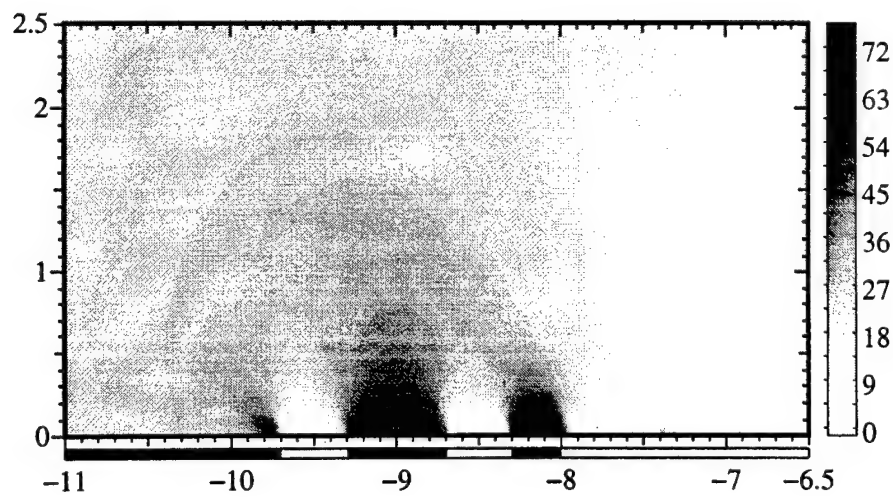


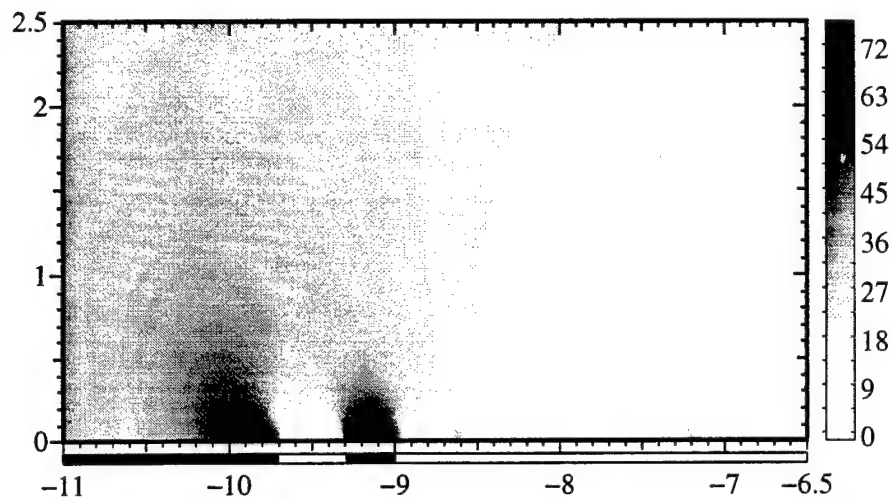
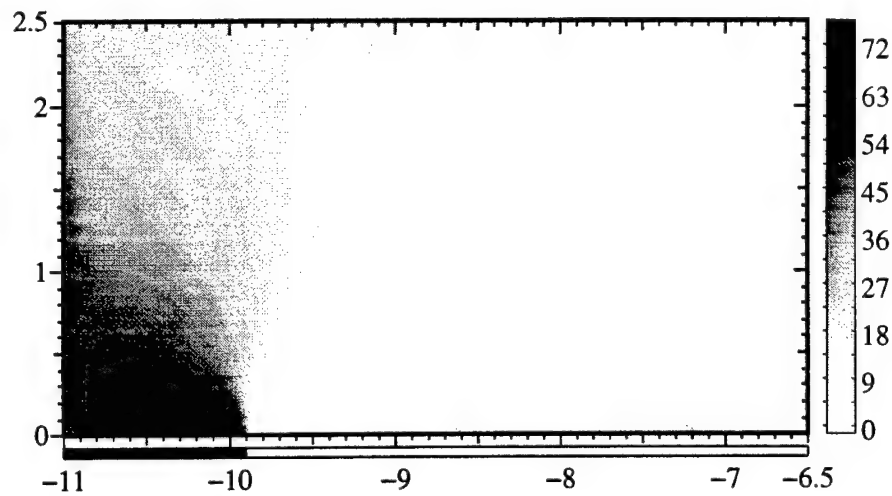
Figure 1.90: Stress contour plot( $\sigma_{xy}$ ) at different locations of crack growth



(a)  $a = 7.2 \text{ in}$



(b)  $a = 8.0 \text{ in}$

(c)  $a = 9.0 \text{ in}$ (d)  $a = 9.9 \text{ in}$ Figure 1.91: Stress contour plot( $\sigma_y$ ) at different locations of crack growth

in the dark blue zones (low  $\sigma_y$  stress) above the cracks, especially the large zone above the main crack. These plots provide a graphical check on the accuracy of the EPFEAM algorithm, since the traction free condition is achieved by erasing the traction at the locations of cracks with analytical solutions.

### § 1.6.6 Conclusions

This section presented the computational predictions and corresponding comparisons with test data developed at National Institute of Standards and Technology (NIST) on large panels with MSD. NIST performed ten experiments on wide panels, of which eight were unique and two were repeats. All eight unique tests were analyzed using the Elastic-Plastic Finite Element Alternating Method (EPFEAM). In addition, three tests performed by Foster-Miller were analyzed. Of the eight NIST tests, three were single crack tests and five had MSD cracks ahead of a main crack. The three Foster-Miller tests considered here were single center crack panel tests.

The predictions were performed as follows:

- First, the tensile stress-strain properties are obtained for the material (2024-T3 aluminum). This curve is used to define the elastic and plastic material properties.
- Second, a  $T^*$  material resistance curve was obtained by modeling two of the single crack NIST tests. In such a generation phase analysis, the experimental load versus crack growth record from a single crack test is modeled and the result is the  $T^*$ -Resistance curve. This curve is then assumed to be an intrinsic material property that is only a function of crack growth and is used to predict the failure of all other tests.
- Finally, all the analyses are performed using the Elastic Plastic Finite Element Alternating Method (EPFEAM) using the stress strain properties of the first step. The driving force value of  $T^*$  (i.e.,  $T_D^*$ ) is forced to follow the  $T^*$ -Resistance curve (i.e.,  $T_R^*$ ) from the second step. Since the analyses were performed via displacement control, the predictions consisted of loads and crack growth. These were then directly compared with experimental data.

It is emphasized that these predictions are simple to obtain with this newly developed methodology. Moreover, all predictions were made using the simple three step procedure described above and no "fudging" of any results was made.

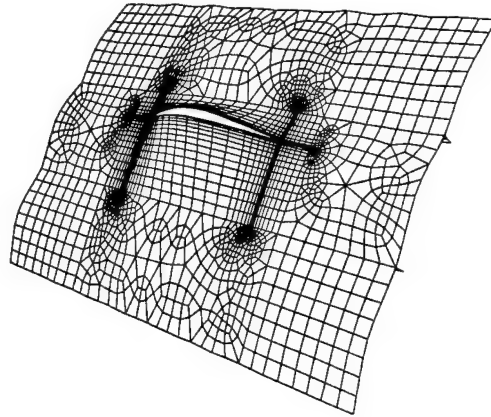


Figure 1.92: Bulging of a longitudinal crack

Many of the predictions compared exactly with the experimental data and at worst, a difference of 15% between analysis and experiment was obtained. These results are considered excellent given the material and test statistical variability.

## **§ 1.7 Crack-Bulging in a Pressurized Aircraft Fuselage: Large Deformation Analyses**

### **§ 1.7.1 Introduction**

Large longitudinal cracks in a fuselage may control the residual strength of the structure. Such cracks tend to bulge or “pillow”, developing a double-curvature near the crack tip (see Fig. 1.92). For a bulged crack of sufficient length, the longitudinal stress in the immediate vicinity of the crack tip may equal or exceed a certain critical value. As a consequence, the crack may change its growth direction from longitudinal to circumferential, a phenomenon known as flapping. Flapping is a favorable phenomenon in that it prevents the explosive decompression of the aircraft by relieving the internal pressure and thereby stopping the crack growth. Thus, a knowledge of the stress field around the tip of such a crack is essential for the economic design of new aircraft and the structural integrity evaluation of aging aircraft. Computational tools are needed to achieve this goal. The computational problems associated with large longitudinal cracks in pressurised fuselages are thus twofold: (1) obtain the values of a suitable fracture parameter that quantifies the severity of the conditions near the crack tip; and, (2) obtain a quantitative

criterion for flapping [Atluri and Tong (1991)].

The stress field near the crack tip is affected by various factors viz. the large deformation, presence of stiffeners and other structural elements, and plasticity near the crack tip. Previous work has ignored the plasticity effects and utilized the stress intensity factor as the fracture parameter. The bulging of the crack edges leads to an increase in the mode-I stress intensity factor from that of an equivalent flat sheet and can be expressed in terms of a "bulge factor". Swift (1987) obtained an empirical formula for the bulge factor by comparison of fatigue test results of full-scale DC-10 fuselage panels with those of flat panels. Swift's factor was found to be valid for cracks that were sufficiently far away from the stiffeners. Lemaitre, Turbat, and Loubet (1977) were the first to perform large deformation analysis of these problems and obtained the energy release rate. Riks (1987) performed a geometrically nonlinear analysis to obtain energy release rates which were used to determine bulge factors. In addition, he found that the bulging displacement at the center of the crack is a nonlinear function of the pressure and that the bulge factor decreases with increasing internal pressure, thereby demonstrating the importance of a geometrically nonlinear analysis. Ansell (1988) performed a geometrically nonlinear analysis and reported deformation patterns similar to those reported by Riks. He also performed a large number of experiments, and parametric studies, and proposed an empirical formula for the bulge factor. Chen (1990) and Chen and Schijve (1991) have also developed empirical formulae for bulge factors. Their analysis was performed on a simplified model of the zone of bulge, using an energy balance approach and an expression for the out-of-plane displacement based on experimental observations. Rankin, Brogan, and Riks (1993) have developed a computational procedure to evaluate the energy release rates of cracks in pressurised fuselages based on geometrically nonlinear shell finite elements. They used a "crack-closure integral" approach to determine the energy release rate.

Other workers have computed stress intensity factors or energy release rates directly for particular configurations. Miller, Kaelber, and Worden (1992) computed stress intensity factors for cracks in narrow-body and wide-body configurations using a geometrically nonlinear finite element analysis and found good comparison of fatigue life predictions made using these stress intensity factors with results of full-scale pressurised panel tests. Potyondy (1993) developed a methodology for simulating curvilinear crack growth in thin, stiffened, pressurised shells and a modified crack closure integral for computing various components of the energy release rate from the results of a geometrically nonlinear shell finite element analysis. He obtained good comparison of crack trajectory and fatigue life with results of a full-

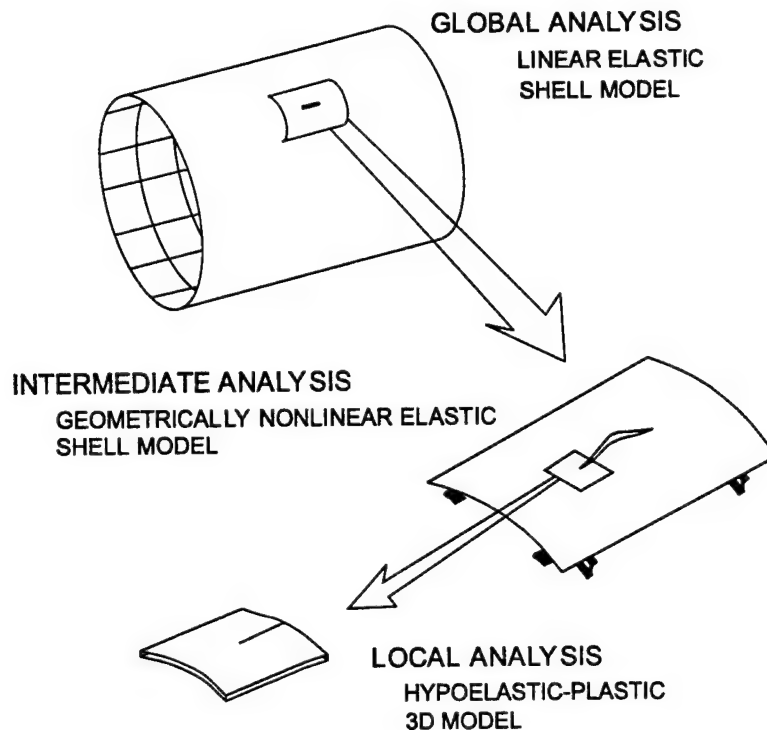


Figure 1.93: Hierarchical modeling strategy.

scale pressurised panel test.

It is worth noting again that the plasticity at the crack tip has been ignored completely in all previous work. The present work describes a computational methodology which incorporates the plasticity effects and allows one to compute a suitable nonlinear fracture parameter, the  $T^*$ -integral, that is valid in the presence of the large deformations and plasticity occurring near the crack tip. The methodology consists of a hierarchical modeling of the cracked fuselage involving three stages of analysis. The global analysis is a linear shell finite element analysis of a large portion of the fuselage; the intermediate analysis is a geometrically nonlinear shell finite element analysis of a smaller portion (the section in which bulge effects are predominant); and, the local analysis is a hypoelastic-plastic three-dimensional solid finite element analysis of the fuselage skin.

Table 1.10: Load and geometric properties of the fuselage model

Internal Pressure	8.0 psi
Radius	74.0 inches
Longitudinal Stiffener (Stringer)	Height - 1.0 inches Thickness - 0.342 inches
Circumferential Stiffener (Frame)	Height - 2.0 inches Thickness - 0.171 inches
Stringer Spacing	9.3 inches
Frame Spacing	20.0 inches

### § 1.7.2 *Computational models*

The three models in the hierarchical strategy are illustrated in Fig. 1.93. The first stage (global model) is a linear elastic shell finite element analysis in which the stiffeners are modeled using beam elements. A linear model suffices, since global buckling and related instability phenomena are not investigated. Symmetry boundary conditions approximating a closed cylinder are imposed on the global model. The portion of the fuselage containing the crack, where the nonlinear bulging is prominent, is contained within the geometrically nonlinear shell finite element model which forms the second stage (intermediate model) of the analysis. Stiffeners are modeled using shell elements. Displacements and rotations from the global model are imposed on the panel boundary. The third stage (local model) is a 3D solid finite element analysis of a portion of the cracked skin. The portion is chosen so that the plastic zone is contained well within its boundary. Displacements and rotations from the intermediate model are imposed on the portion's boundary after transformation from the shell space to 3D. A hypoelastic-plastic constitutive model is used with an objective stress update. The nonlinear fracture parameters are evaluated from the local model.

The present methodology was exercised on a number of example problems. The bulging of cracks is affected by many factors such as the presence of stiffeners, fastener flexibility, and skin thickness. In the present examples, fastener flexibility is not modeled; the skin is assumed to be attached rigidly to the stiffeners. (Note



Table 1.11: Example problems

Name	Stiffened	Crack Length (inches)	Offset (inches)	Skin Thickness (inches)
Case 1	No	10.0	-	0.036
Case 2	No	15.0	-	0.036
Case 3	Yes	10.0	0.0	0.036
Case 4	Yes	15.0	0.0	0.036
Case 5	Yes	10.0	2.08	0.036
Case 6	Yes	15.0	2.08	0.036
Case 7	Yes	10.0	0.0	0.072
Case 8	Yes	10.0	2.08	0.072

that fastener flexibility could be modeled by incorporating it into the global and intermediate models.) The example fuselage model is representative of the narrow-body fuselage configuration studied by Rankin, Brogan, and Riks (1993) (cf. Fig. 1.95 and Tab. 1.10). The effects of stiffening elements, crack length, crack location, and skin thickness are examined for the eight cases shown in Tab. 1.11. The offset value in Tab. 1.11 is the distance by which the crack has been offset from the midbay towards the stringer (in the positive  $X_2$  direction of Fig. 1.94).

The Young's modulus of the skin and the stiffeners are 10,500 *ksi* and 10,700 *ksi*, respectively. The Poission's ratio for both skin and stiffeners is taken to be 0.33. For the local analysis of the skin, a piecewise approximation of the uni-axial stress strain curve of Al2024-T3, given in MIL-HDBK-5E (1987), is adopted for the flow rule [see Fig. 1.75].

The global model consisted of 5 frame bays and 7 stringer bays with symmetry boundary conditions approximating a closed cylinder. Each of the eight finite element models contained approximately 12,000 degrees of freedom. The intermediate model consisted of 2 frame bays and 3 stringer bays (a slightly larger intermediate model was required for Case 2 since the bulge out zone was considerably larger), with an average of approximately 15,000 degrees of freedom. The local analysis was performed on a rectangular portion of the skin with a side length of 5-

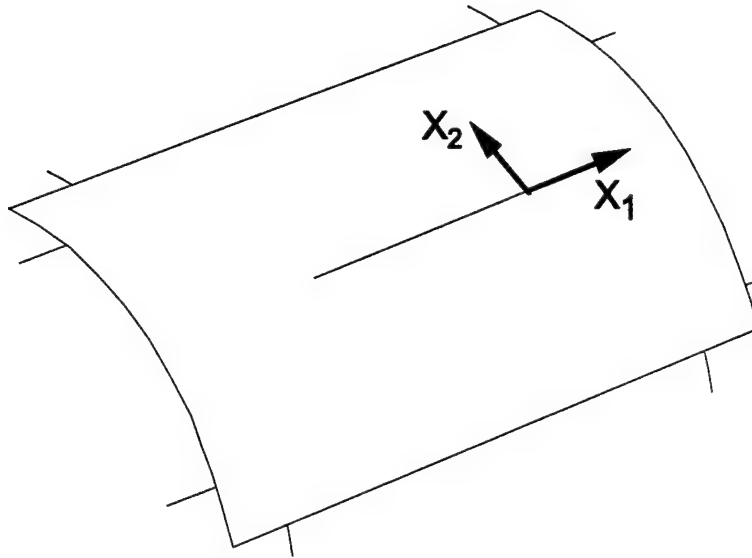


Figure 1.94: Crack tip coordinate system.

6 inches with approximately 8,000 degrees of freedom. For the computation of the  $T^*$ -integral, the  $s$ -function was chosen to be constant through the thickness, with sixteen elements about the crack tip used in the computation. The total analysis time did not exceed eight hours (global: 0.4-0.5 hours; intermediate: 1.5-2.0 hours; local: 3-5 hours) on a HP-735 workstation. Deformed meshes of the various stages of the analysis for Case 6 are shown in Figs. 1.96, 1.97, and 1.98. As expected, the global model significantly overestimates the bulging deformation which is modeled more accurately in the intermediate and local models.

### § 1.7.3 Numerical results

The computed values of  $T^*$  are presented in Figs. 1.99, 1.100, 1.101, and 1.102. In most cases, plasticity began to develop after a load factor of 0.25, and at large load factors (greater than 0.5) the variation of  $T^*$  is nearly linear. Stiffening produces a large reduction in  $T_1^*$  (cf. Fig. 1.99). Offsetting the crack by one quarter of bay length has no significant effect on  $T_1^*$  (cf. Fig. 1.100). Doubling the skin thickness while maintaining the same loading, reduces  $T_1^*$  by more than half (cf. Fig. 1.101). The computed value of  $T_2^*$  is negligible for the cases in which the crack is centered between the stringers and becomes nearly 40% of the  $T_1^*$  value for the offset crack

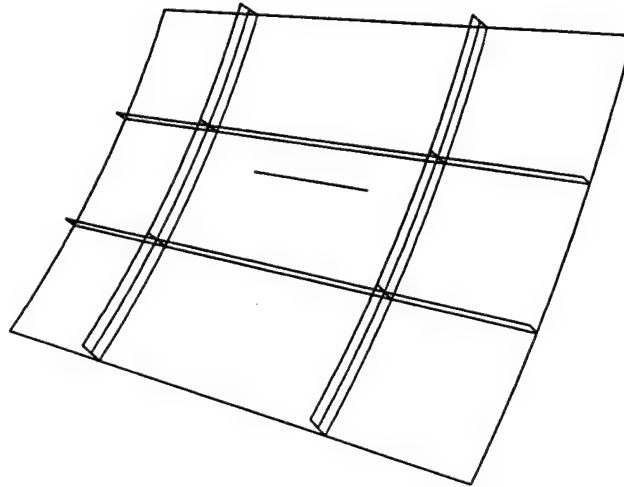


Figure 1.95: Example fuselage model.

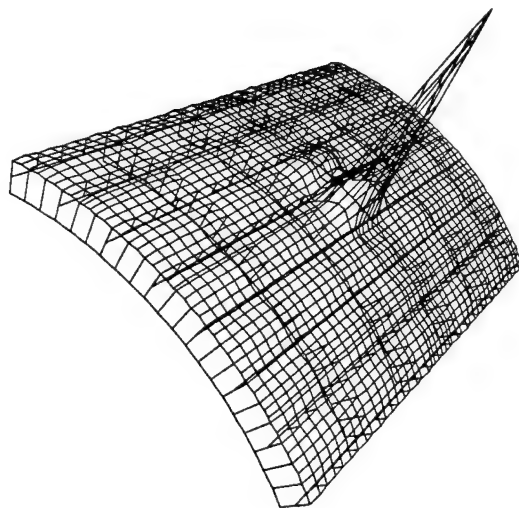


Figure 1.96: Deformed global model, Case 6 (magnification 5.0).

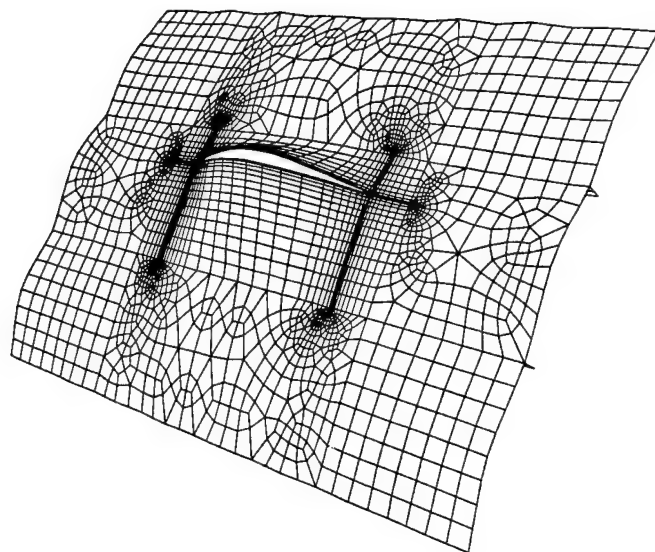


Figure 1.97: Deformed intermediate model, Case 6 (magnification 5.0).

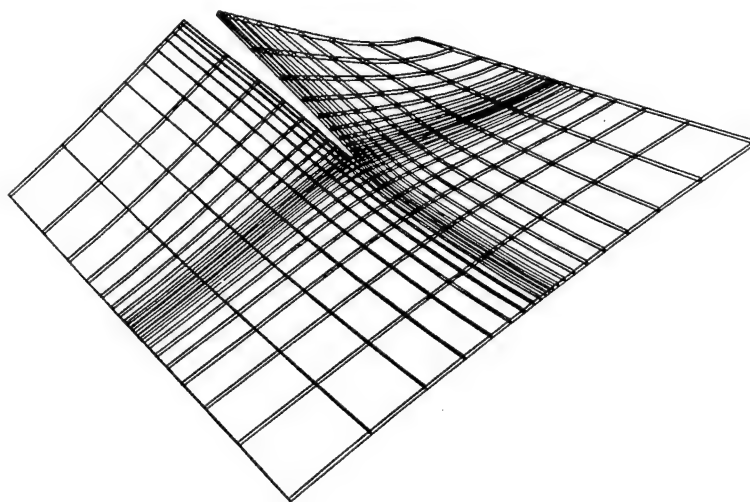


Figure 1.98: Deformed local model, Case 6 (magnification 5.0).

(cf. Fig. 1.102).

In an industrial setting, a nonlinear analysis may not be feasible, and often only a linear stiffened shell analysis is performed. The present methodology can be used to develop correction factors which account for both the geometric nonlinearity and the plasticity. The correction factors are defined as

$$\text{Correction Factor} = \frac{T_1^*}{T_{1l}^*}, \quad (1.59)$$

where  $T_{1l}^*$  denotes the value of  $T_1^*$  obtained from a linear elastic analysis. Note that  $T_{1l}^*$  is identical to the energy release rate  $G_I$ , and is related to the various stress intensity factors via well-known relations [Hui and Zehnder (1993)].

The computed correction factors are presented in Figs. 1.103 and 1.104. They were obtained by performing a geometrically linear elastic analysis of the intermediate model and computing  $G_I$  using the extension of the modified crack closure technique described in Potyondy (1993). The correction factors decrease as the load is increased because of the growing discrepancy between the bulging displacements of the linear and nonlinear models. As the nonlinear effects increase with increasing load factor, the correction factor decreases. The trend in the correction factors for the thicker shell differs from that of the thinner cases (cf. Fig. 1.104). The nonlinear effects do not develop as rapidly for the thicker and thus stiffer shell causing these correction factors to remain near unity for small load levels.

As stated previously, the present work is the first attempt to evaluate quantitatively the effect of plasticity occurring at the tips of a bulging crack. In the presence of plasticity, the stress intensity factors are no longer theoretically valid fracture parameters, and the  $T^*$ -integral may be used. For a monotonically loaded elastic-plastic structure,  $T^*$  has the meaning of an energy-flux to the crack tip. For an elastic-plastic structure with growing cracks,  $T_e^*$  has the meaning of an energy flux to the process-zone of size  $\epsilon$  near the crack tip. It is valid for the behaviour occurring in all three hierarchical models (global: linear elastic; intermediate: geometrically nonlinear elastic; and local: both geometrically and materially nonlinear). The effect of both the geometric nonlinearity *and* the plasticity is quantified in Figs. 1.103 and 1.104 by the correction factor of Eq. 1.59. The effect of the plasticity alone upon  $T^*$  is quantified in Fig. 1.105 by plotting the ratio of  $T_1^*$  to  $T_{1l}^*$ , where  $T_1^*$  is computed both with and without plasticity. The plot in Fig. 1.105 demonstrates that the plasticity results in a reduction of  $T_1^*$ . (Geometric nonlinearity is present for both cases. The cases with no plasticity were computed using the energy release rate of the geometrically nonlinear solution using the technique described in Potyondy (1993). This approach was verified for Case 1 where the

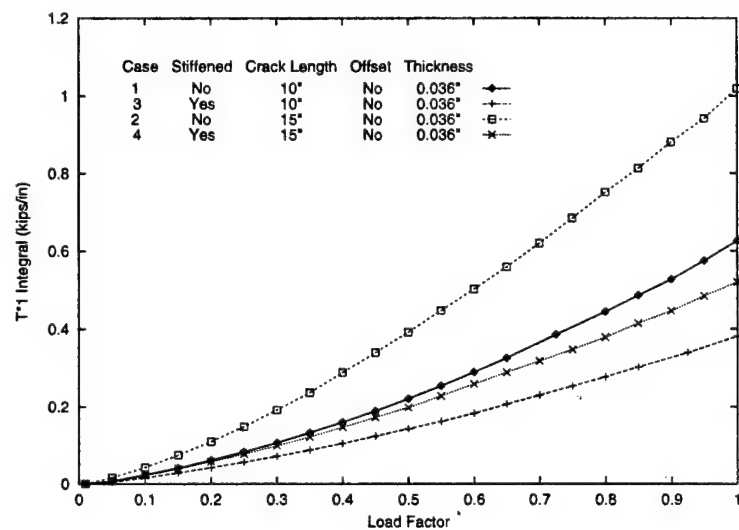


Figure 1.99:  $T_1^*$ -Integral, effect of stiffeners.

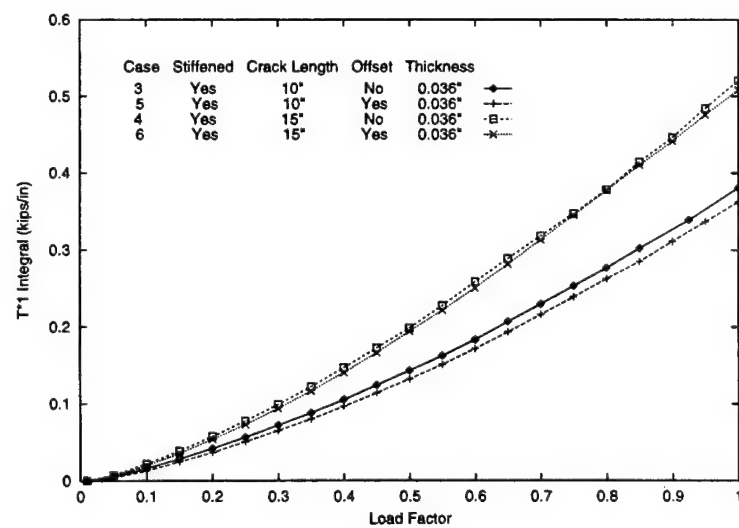
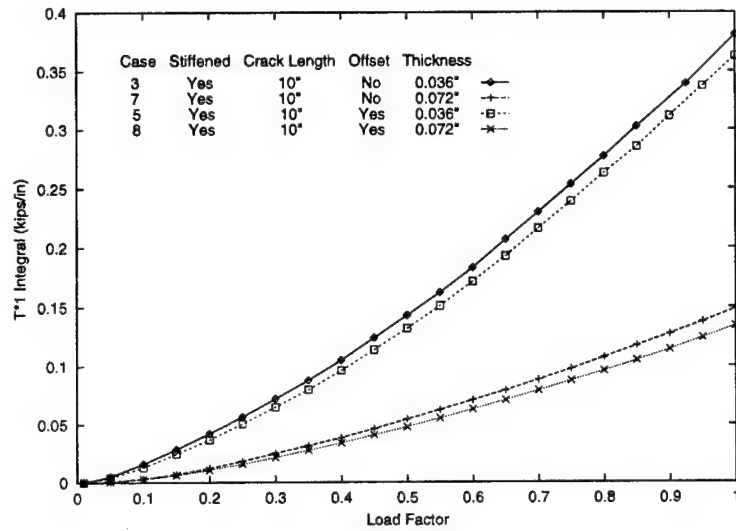
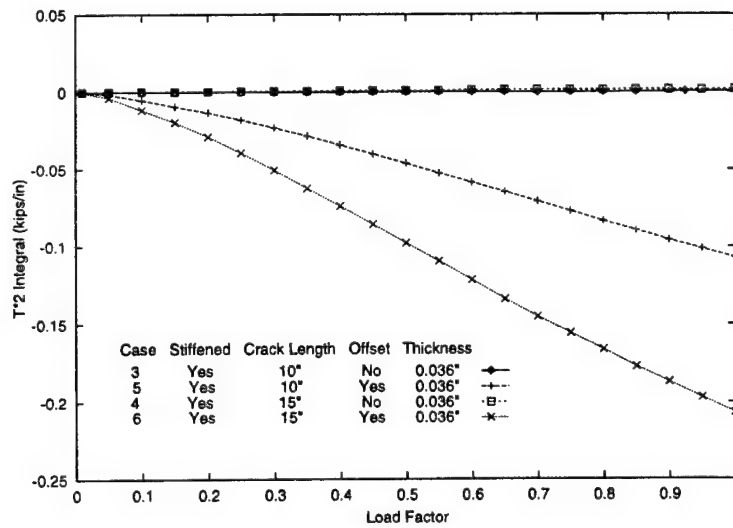


Figure 1.100:  $T_1^*$ -Integral, effect of offset.

Figure 1.101:  $T_1^*$ -Integral, effect of skin gauge.Figure 1.102:  $T_2^*$ -Integral

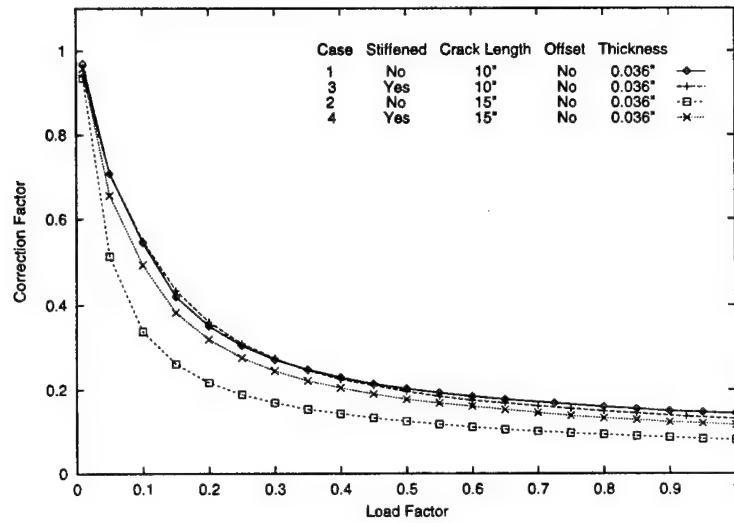


Figure 1.103: Correction factors, Cases 1-4.

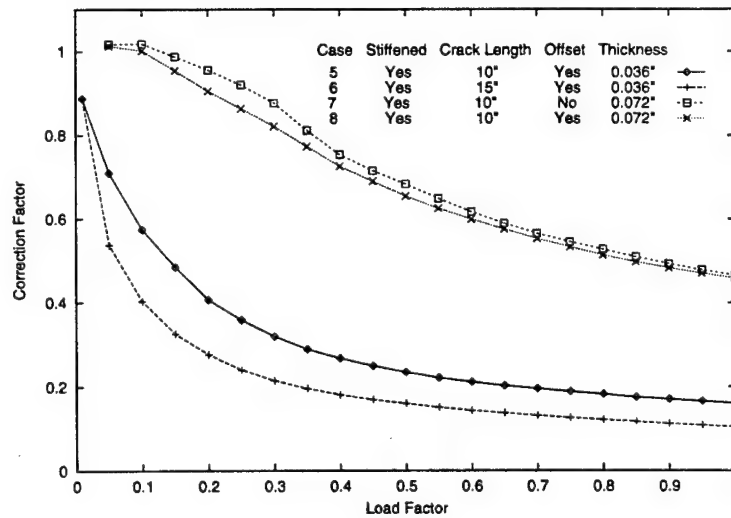


Figure 1.104: Correction factors, Cases 5-8.



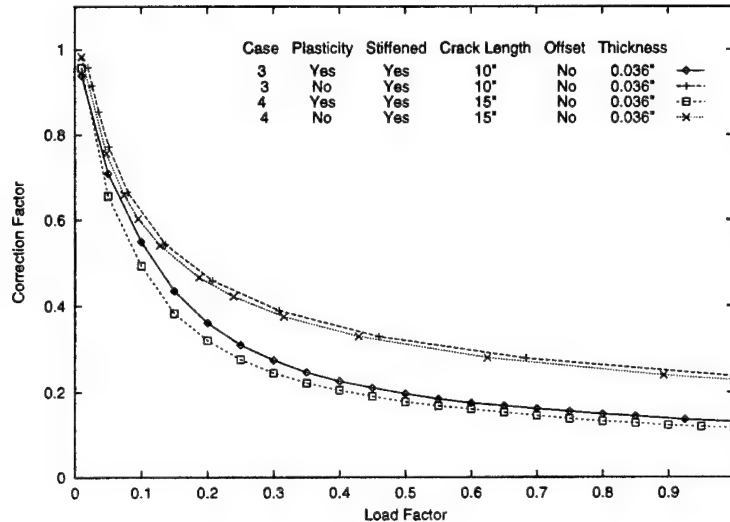


Figure 1.105: Correction factors both with and without plasticity.

energy release rate computed using this method (1.090 *kips/inch*) was compared to the value of  $T_1^*$  (1.010 *kips/inch*) computed by turning off the plasticity in the local model and using the EDI method. An additional verification was obtained by comparing the energy release rates for Cases 3 and 4 to energy release rates obtained by Rankin, Brogan, and Riks (1993). For Case 3, the energy release rate was 2.7% less than Rankin's value, and for case 4, it was 7.9% less.)

Additional qualitative information about the plasticity occurring at the crack tip is presented in Figs. 1.106 and 1.107 where the size and shape of the plastic zone at the shell midsurface under the full applied loading is shown. The plastic strains at the eight Gauss points of the 20-noded brick elements were averaged through the thickness to obtain a value on the midsurface which was then depicted as a color contoured image such that a positive plastic strain indicates the presence of plasticity. For all eight example cases, the plastic zone shape is that expected for a plane stress crack, and the diameter is between 0.7 and 0.9 inches (approximately 14 and 12 percent of the half crack length). The effect of offsetting the crack toward the stringer causes the plastic zone to become skewed in the direction away from the nearest stringer (cf. Fig. 1.107). The longitudinal and hoop stresses on the shell midsurface (defined in terms of the deformed shell coordinates) are presented in Figs. 1.108 and 1.109 for the offset crack of Case 6. Offsetting the crack signif-

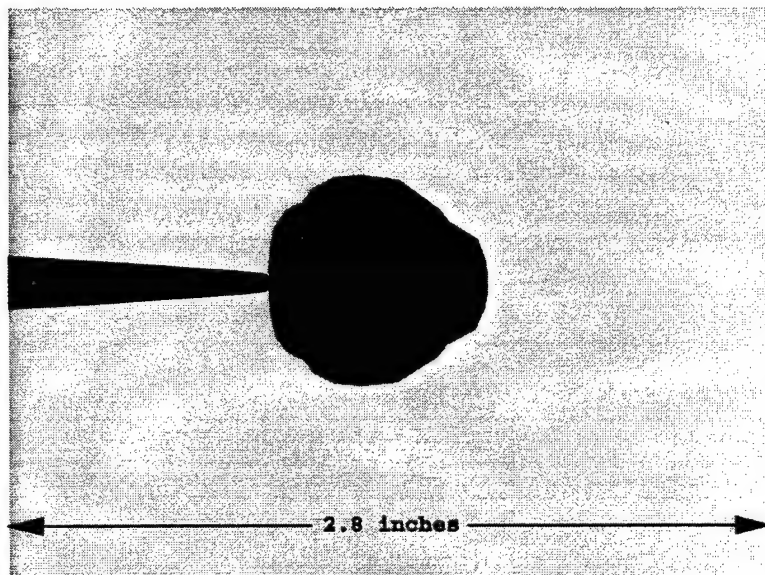


Figure 1.106: Plastic zone, Case 4 (drawn on deformed shape with magnification 5.0).

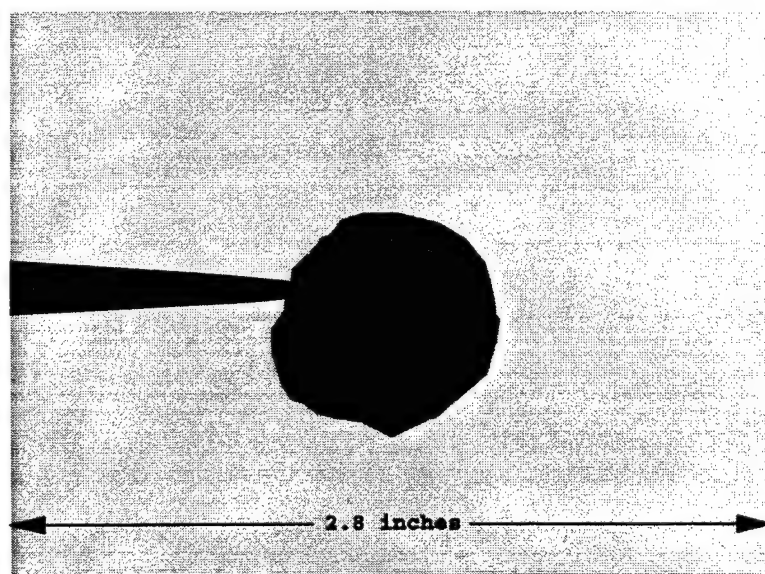


Figure 1.107: Plastic zone, Case 6 (drawn on deformed shape with magnification 5.0).

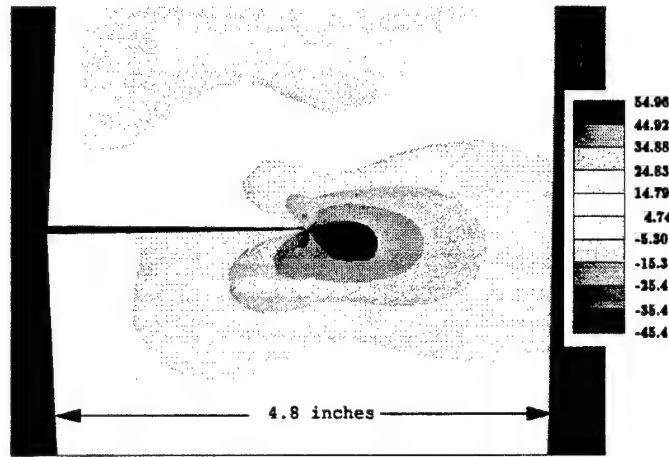


Figure 1.108: Longitudinal stress contour, values in *ksi*, Case 6 (drawn on deformed shape with magnification 1.0).

icantly effects the symmetry of the longitudinal stress but has little effect on the symmetry of the hoop stress. The longitudinal stress is skewed in the same way as the plastic zone (compare Figs. 1.107 and 1.108).

The phenomenon of flapping is an important issue in the design and structural evaluation of aircraft. A survey of various crack path stability criteria and their application to flapping is provided by Zaal (1992). None of the existing criteria account for plasticity directly. We do not develop an explicit criteria for flapping here; rather, the following discussion will suggest a possible mechanism for flapping and explore its application to the example cases.

Flapping results from the large nonlinear deformation which causes an increase in the longitudinal stress parallel to the crack. It is postulated that for a crack of sufficient length, the longitudinal stress acting on a plane perpendicular to the crack and straight above the tip will reach a critical value causing the material on this plane to separate and thereby allowing the crack to flap. The variation of the longitudinal stress (normalised by the yield stress,  $\sigma_y = 47.0 \text{ ksi}$ ) acting on the line where this plane intersects the shell midsurface is presented in Figs. 1.110, 1.111, 1.112, and 1.113. These values were obtained by transforming the Gauss point stresses from the global coordinates to the deformed shell coordinates, then extrapolating and averaging these values at the row of nodes directly above and below the crack tip. As one would expect, the longer crack has higher values (cf. Fig. 1.110). Al-

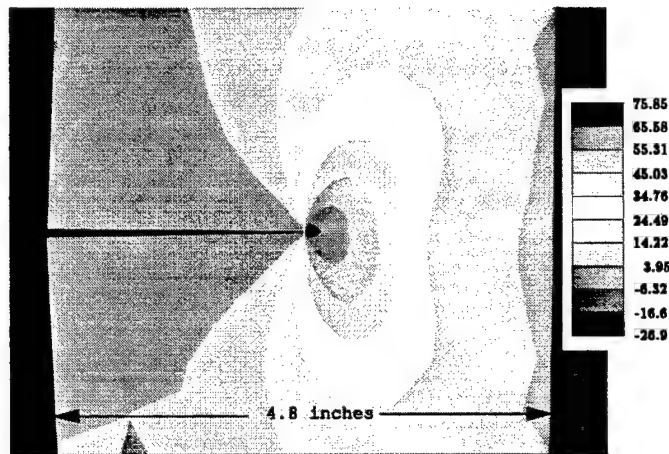


Figure 1.109: Hoop stress contour, values in *ksi*, Case 6 (drawn on deformed shape with magnification 1.0).

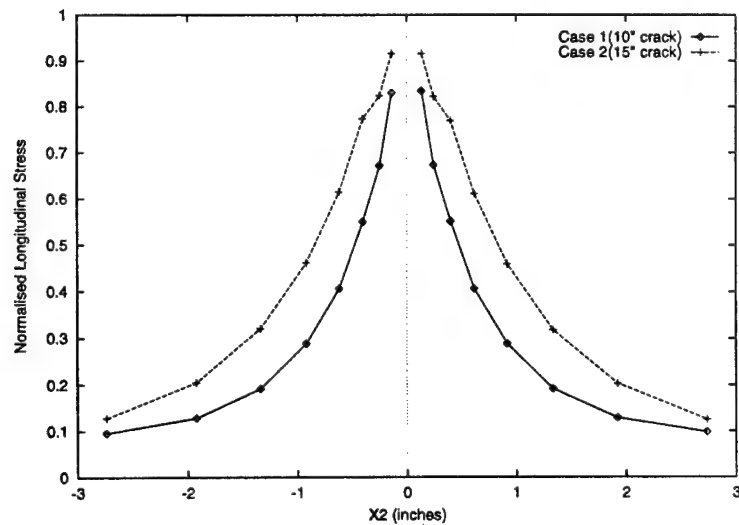


Figure 1.110: Normalised longitudinal stress (unstiffened cases).

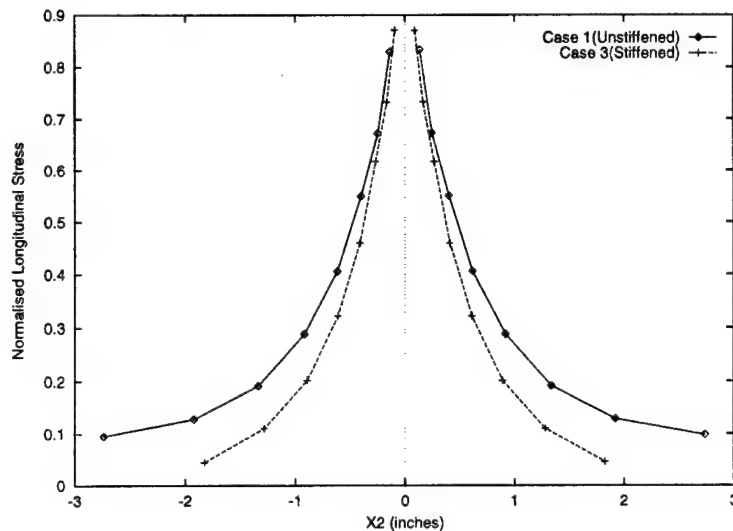


Figure 1.111: Normalised longitudinal stress (10 inch crack).

though the values of the stiffened cases are smaller than those of the unstiffened cases away from the crack, they grow faster as the crack tip is approached (cf. Figs. 1.111 and 1.112). Offsetting the crack causes the distribution of values to become unsymmetric, with greater values on the side away from the nearest stringer (cf. Fig. 1.113). An examination of the longitudinal stress contour in Fig. 1.108 indicates that the longitudinal stress does not attain a maximum directly above the crack tip but rather at some finite distance away from the crack tip.

## § 1.8 Fatigue Life Estimation & Linkup of MSD Cracks Due to Fatigue: Generic Methodology and Illustrative Examples

### § 1.8.1 Introduction

In this section, a simple and efficient computational method to study the fatigue growth of MSD cracks is presented. This method can be implemented on a modern personal computer. It relies on the Schwartz-Neumann alternating method presented in Chapter ???. The key ingredient in this method, viz., the analytical solution for the problem of multiple collinear cracks in an infinite sheet, the crack-faces being subject to arbitrary tractions, has been discussed in Chapter ??.

The effect of the initial radial pressure induced near a hole in the skin due to a

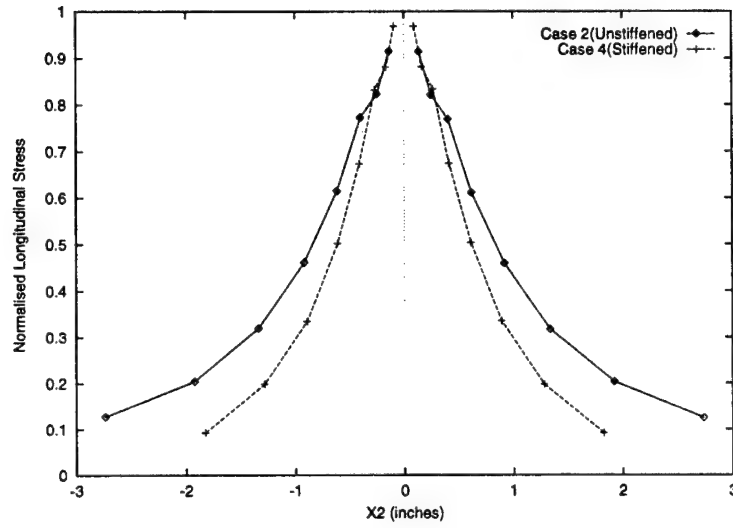


Figure 1.112: Normalised longitudinal stress (15 inch crack).

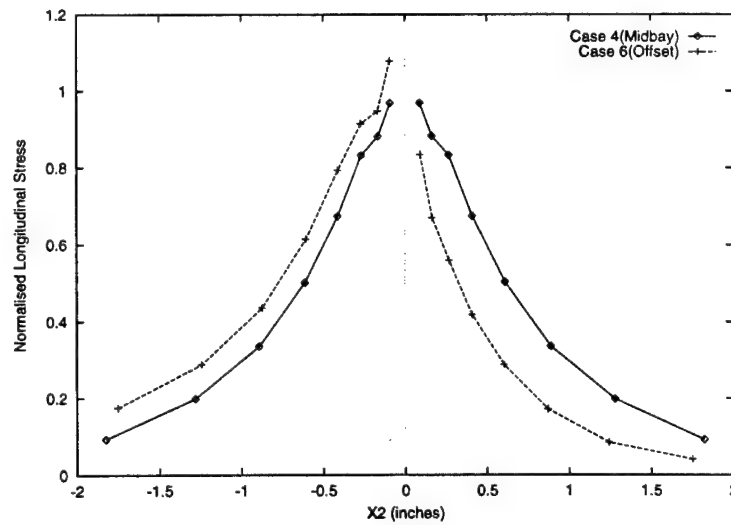


Figure 1.113: Normalised longitudinal stress (midbay vs offset).

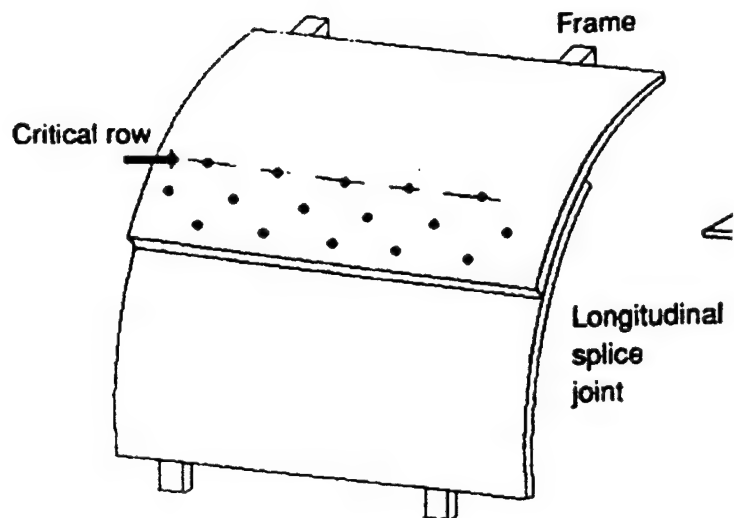


Figure 1.114: A schematic representation of multiple cracks emanating from the upper-row of fastener holes in a bonded lap-joint in a fuselage

rivet misfit; and the effect of the plastic deformation near the hole due to rivet misfit, are both considered. These effects alter the range of stress-intensity-factor imposed on a crack-tip during cyclic loading; and thus affect the fatigue crack growth rates. It is shown that these effects are responsible for a phenomenon whereby the shorter cracks near a row of fastener holes, may, in certain specific situations, grow faster than longer cracks.

As the cracks grow under fatigue, the situation eventually arises when the uncracked ligament between two crack-tips may fully yield; leading to a crack-link up. This link up of MSD cracks, especially if they are ahead of a single dominant crack, may result in unarrested fast fracture.

#### **§ 1.8.2 Multiple-site-damage near a row of fastener-holes in a bonded fuselage-lap-joint: A Model Problem**

The problem is schematically represented in Fig. 1.114. It is assumed that an arbitrary number of cracks, of arbitrary lengths, emanate from the fastener holes in the upper-row. In the initial phases of fatigue, corner surface cracks may emanate from

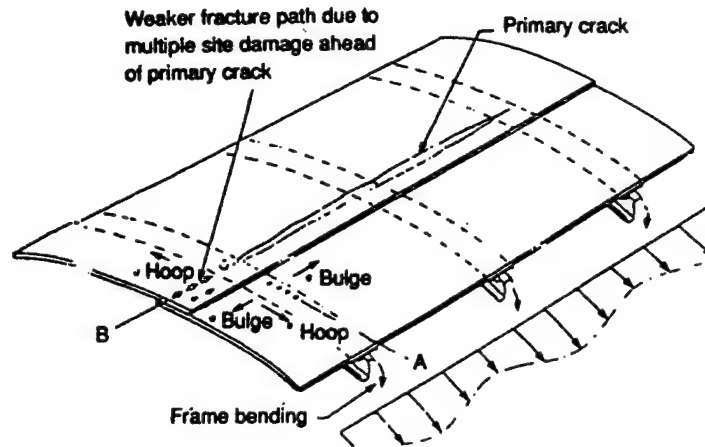


Figure 1.115: MSD ahead of a single dominant crack in a fuselage

the counter-sunk rivet holes in the skin. At later stages, these surface cracks evolve into through-the-skin cracks. The central issues to be analyzed are:

1. If cracks of unequal lengths emanate from the fastener holes, is there a mechanism by which the shorter cracks may grow faster than the longer cracks, thus involving a "catch-up phenomenon"?
2. Can a simple analytical methodology be developed to predict the fatigue growth of these MSD cracks and their link-up, especially when MSD-cracks are present ahead of a single dominant crack as in Fig. 1.115?

The primary aim of this section is to attempt to answer these questions.

1. The hoop stress in the fuselage may vary in the longitudinal direction, between frames, as shown in Fig. 1.116. These hoop stresses and longitudinal stresses, on a position of the lap joint are obtained from a global analysis of the fuselage as depicted in Fig. 1.116.
2. The rivet flexibility, as shown in Figs. 1.117a and 1.117b, must be accounted for.
3. The fuselage lap splices are assumed to be adhesively bounded.
4. The contact stresses between the rivet and the hole, due to the external load carried by the rivets, are accounted for.



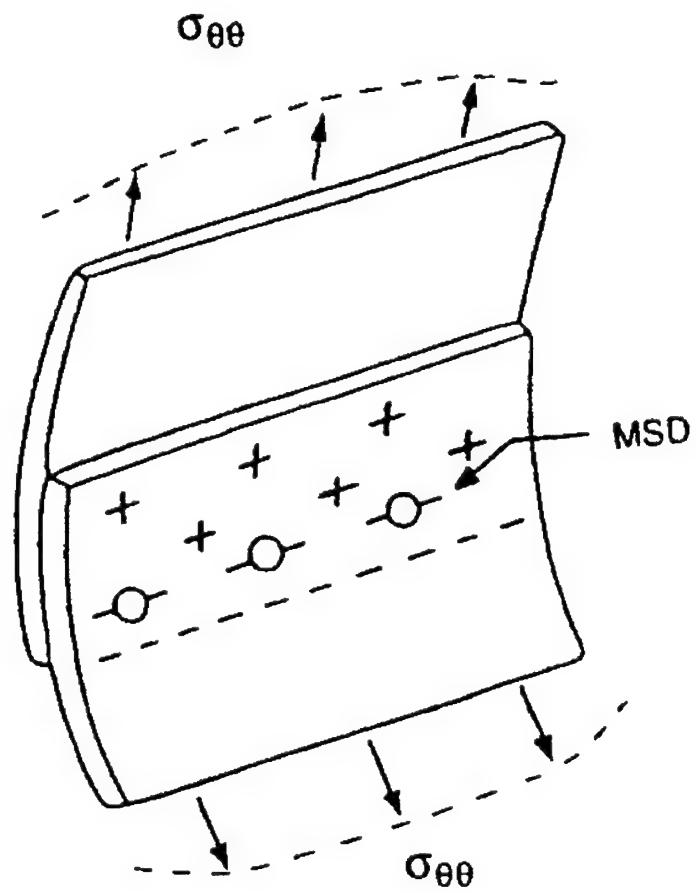


Figure 1.116: A schematic of a bonded, riveted lap-joint in a fuselage

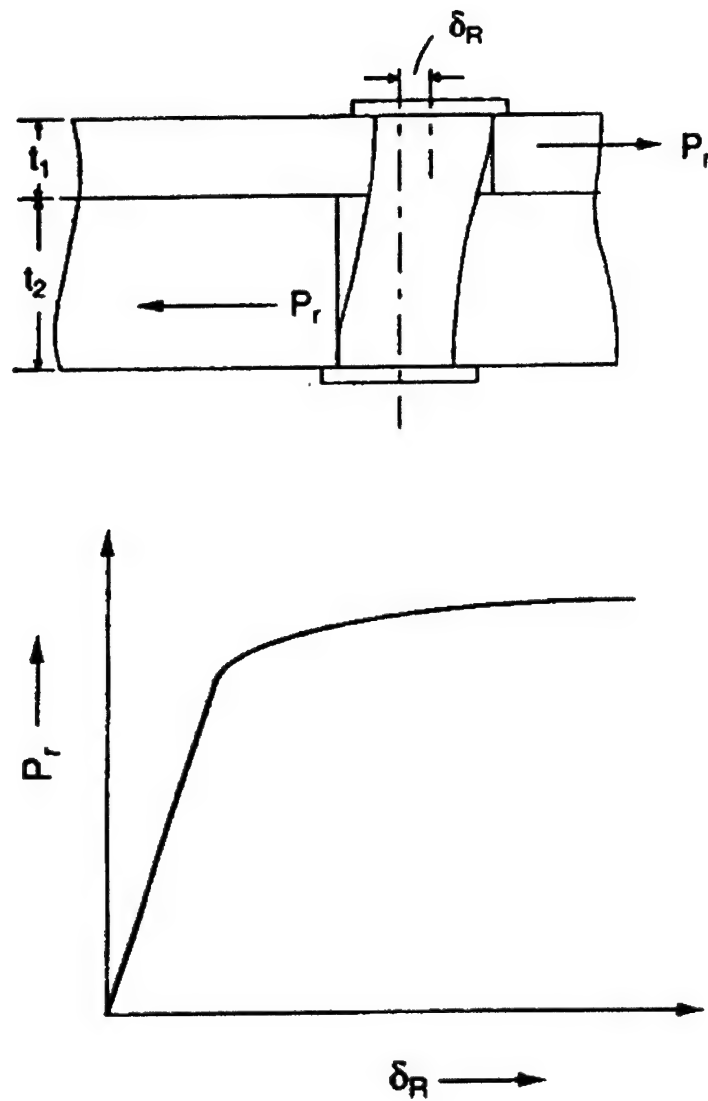


Figure 1.117: A schematic representation of a flexible fastener

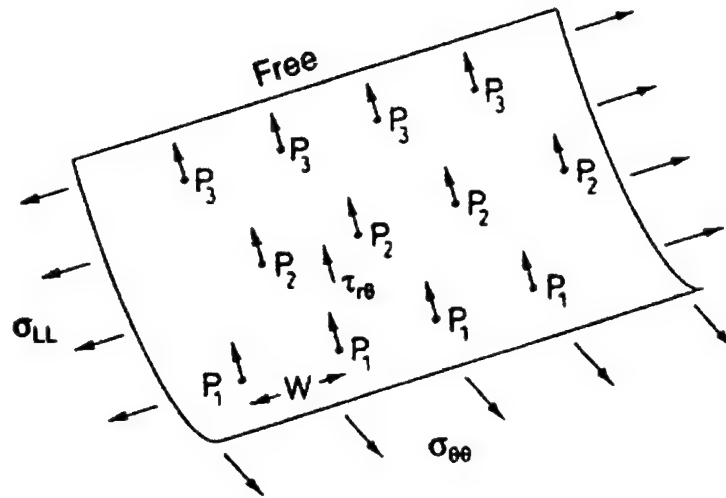


Figure 1.118: A free-body diagram of the inner skin in a fuselage lap-joint

5. The residual stresses in the skin, due to the misfit of an oversized rivet in the fastener hole, are accounted for.
6. Even though mode II crack behavior is present for cracks near pin-loaded fastener holes the mode II component is assumed to be small in comparison to the mode I component.

The key steps in the solution procedure presented in this section are:

1. To isolate the free-body diagram of each skin (the inner and the outer) as shown in Fig. 1.118. For instance, the inner skin shown in Fig. 1.118 is subject to hoop stress  $\sigma_{\theta\theta}$ , longitudinal stress  $\sigma_{LL}$ , fastener-reaction loads  $P_i$  in the  $i$ th row of fasteners, and adhesive shear stresses  $\tau_{r\theta}$ .
2. A finite-element stiffness analysis, with a very coarse mesh as in Fig. 1.119 (wherein the fasteners and fastener-holes are modeled as points) is used to analyze the load transfer through the rivets and the adhesive. The cracks near the fastener holes are modeled with unconnected finite elements, even though the crack-tip stresses are not modeled at this stage.

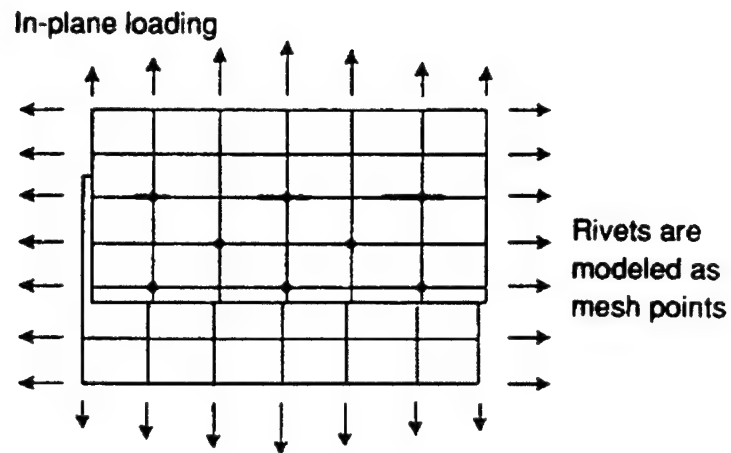


Figure 1.119: Coarse grid for a load-transfer analysis to determine rivet forces on the cracked sheet

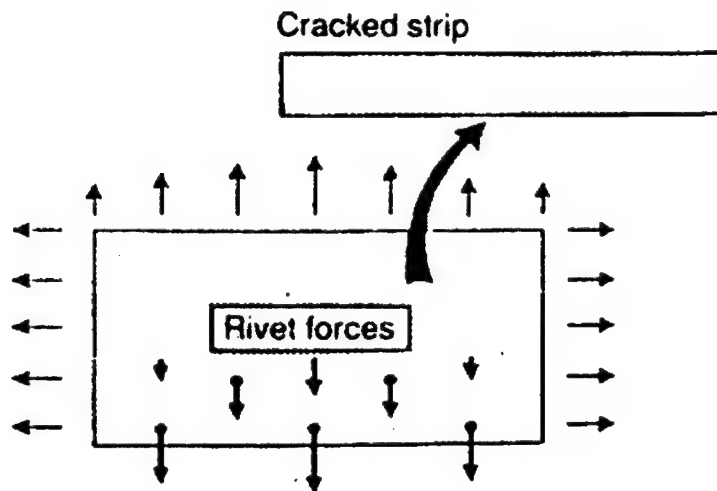


Figure 1.120: The isolated sketch of a strip containing a row of fastener holes with MSD

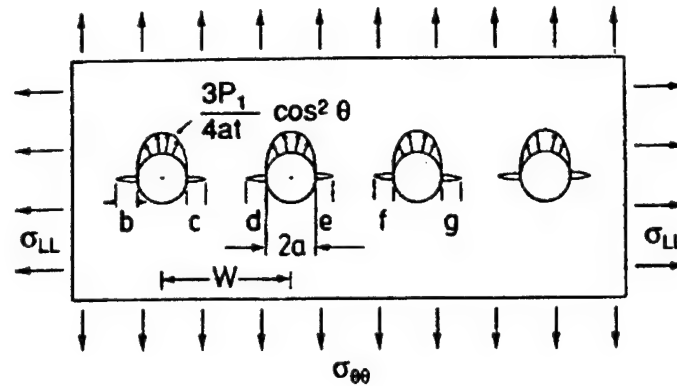
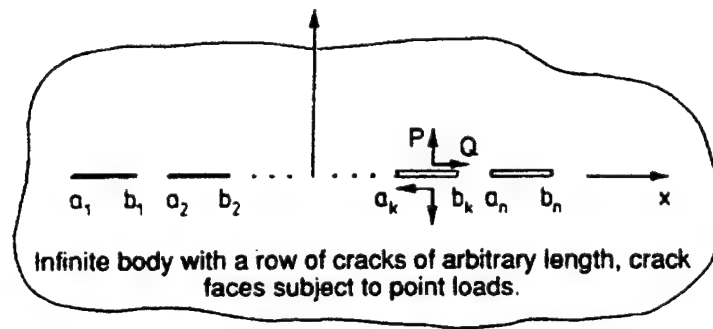
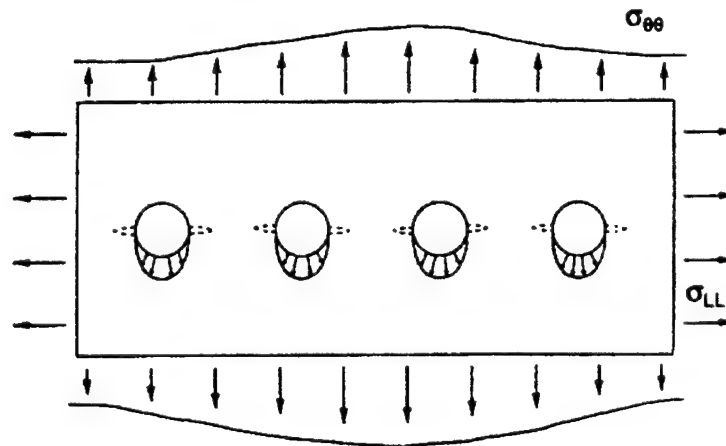


Figure 1.121: A strip with a row of fastener holes and MSD, subject to far field stresses and rivet contact stresses

3. From the analysis in Step (2) above, the inner (or outer) skin is isolated as in Fig. 1.120. From this, the row of fastener holes with cracks is isolated, as in Fig. 1.121.
4. Fig. 1.121 represents a strip of the fuselage with a row of fastener holes with MSD. The strip is subject to hoop stress  $\sigma_{\theta\theta}$  at one longitudinal edge and a hoop stress  $(\sigma_{\theta\theta} - P_1/W_t)$  at the other edge. Here,  $P_1$  is the load carried by each fastener in this row,  $W$  is the rivet-spacing, and  $t$  is the skin thickness. The longitudinal stress is  $\sigma_{LL}$ .
5. The fastener-load  $P_1$  is distributed along the periphery of the hole, by using the analytical solution for the contact problem between the rivet and the hole. In the present section, however, for simplicity, the fastener load  $P_1$  is distributed as shown in Fig. 1.121.
6. The problem in Fig. 1.121 is solved by using the Schwartz-Neumann alternating method as sketched in Fig. 1.122. This involves two solutions as follows:
  - (a) An analytical solution for a row of cracks, each of arbitrary length, in an infinite sheet; the crack-faces are subject to arbitrary self-equilibrating point forces as shown in Fig. 1.122A.



(A) The analytical solution needed in the alternating method



(B) Finite element solution needed in the alternating method

Schwartz-Neumann Alternating Method  
Alternation between solutions A & B

Figure 1.122: The two basic solutions needed in the alternating method

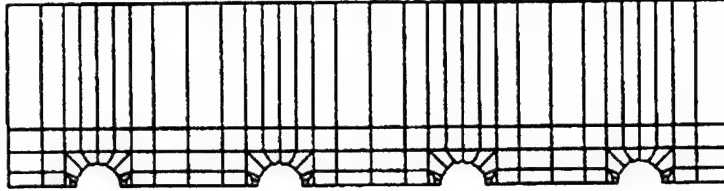


Figure 1.123: Finite element mesh of uncracked body

- (b) A numerical (finite element or boundary element) solution for a strip with a row of holes, but without cracks, subjected to the loading system as shown in Fig. 1.122B.
- (c) The finite element model for the uncracked strip with holes is shown in Fig. 1.123. Since the cracks are not numerically modeled, this finite element model remains the same irrespective of the lengths of the cracks. Thus, as cracks grow during the fatigue-crack-growth process, the finite element mesh remains the same. Thus, the entire fatigue-crack-growth analysis of the MSD problem, including the analysis of link-up, can be performed on a personal computer.

The details of this alternating method for fatigue-crack growth of MSD cracks are further elaborated upon below.

### § 1.8.3 *Analysis of load transfer through fastener and adhesive bonding in a fuselage lap-splice joint*

The methodology to account for the effect of the flexibility of the fastener on the load transfer through the fasteners has been discussed in detail in Park, Ogiso, and Atluri (1992). Here we discuss briefly the additional effect of the adhesive bonding of the skins on the load transfer between the two skins in the lap joint, to analyse the problem developed in Fig. 1.119.

The total strain-energy of the lap-joint, with flexible fasteners and flexible adhesive bonding, in linear-elastic deformation, is given by:

$$W = \sum_{ele=N_{Sk}^u} \frac{1}{2} ({}^u q_{Sk}^t) ({}^u K_{Sk}^e) ({}^u q_{Sk}^e) + \sum_{N_{Sk}^l} \frac{1}{2} ({}^l q_{Sk}^t) (K_{Sk}^e) ({}^l q_{Sk}^e)$$

$$+ \sum_{N_{Sk}} \frac{1}{2} \int_{el} \frac{(u^u - l^l u)^2}{F} dA + \sum_N \frac{1}{2} K_F (u^u q_{Sk} - l^l q_{Sk})^2$$

where  $u^u q_{Sk}$  is the vector of nodal displacements of the upper-skin;  $l^l q_{Sk}$  is the vector of nodal displacements of the lower skin;  $K_{Sk}^e$  is the stiffness matrix of the skin element,  $K_F$  is the stiffness of the fastener, and  $F$  is the flexibility of the adhesive layer (as discussed in Park, Ogiso, and Atluri (1992));  $u^u$  and  $l^l u$  are the vectors of inplane displacement in the upper and lower skins respectively.

Following the details as given in Park, Ogiso, and Atluri (1992), the global stiffness equations for the present case can be derived as:

$$\begin{bmatrix} (u^u K_{Sk} + l^l K_{Sk} + K_F + K_a) & -(K_F + K_a) \\ -(K_F + K_a) & (u^u K_{Sk} + l^l K_{Sk} + K_F + K_a) \end{bmatrix} \begin{Bmatrix} u^u q_{Sk} \\ l^l q_{Sk} \end{Bmatrix} = \begin{Bmatrix} u^u Q_{Sk} \\ l^l Q_{Sk} \end{Bmatrix} \quad (1.60)$$

From Eq. 1.60, the fastener and adhesive layer forces on the skin can be determined to be:

$$P_{Fa} = (K_F + K_a) (u^u q_{Sk} - l^l q_{Sk}) \quad (1.61)$$

The effect of cracks, near the upper row of fastener holes on the loads carried by the rivets is accounted for, in the present analysis. The cracks are modeled simply by unconnected finite elements, while the crack-tip singularities themselves are not modeled by any special finite elements. If there are no cracks in the upper row of fastener holes, this row of fasteners in a lap joint can be expected to carry more load than the middle row. In the presence of cracks, however, load shedding from this row may be expected to occur.

The solution for  $P_{Fa}$  enables one to draw the free-body diagrams for one of the skins as in Fig. 1.119. Thus, one is in a position to consider the problem shown in Fig. 1.121.

As mentioned before, the problem in Fig. 1.121 is solved by using the Schwartz-Neumann alternating method, which relies on the two solution steps outlined in Fig. 1.122. These two solution steps are discussed below:

#### § 1.8.4 The finite element alternating method for MSD near a row of fastener holes

A general and detailed description of the finite element alternating method (FEAM) has been given in Chapter III. In order to analyze the present problem of MSD near



a row of fasteners, the conventional FEAM is modified as follows.

1. Consider the problem of a section of the fuselage panel, with a row of fastener holes with MSD cracking. Let the number of fastener holes be arbitrary. Let the lengths of the cracks emanating from each hole be arbitrary.
2. Using the analytical solution for the problem of an infinite sheet containing a single hole, but no crack, and subjected to far-field stresses as well as the sine pin-loading [Muskhelishvili (1953)], obtain the residual tractions at the boundaries of the finite sheet, the other hole-surfaces, and at all the locations of the cracks. However, for fastener holes that are far removed from the presently considered hole, the residual tractions from the present solution are nearly zero.
3. To create the traction-free crack-surfaces, erase the stresses, as found in Step (2), on the crack-surfaces, using the analytical solution for an infinite sheet containing multiple collinear cracks, as obtained in Chapter II. Determine the SIF at each of the crack-tips of each of the cracks. Let the  $x$  coordinate of the center of the  $i$ th hole be  $x_i^h$ . Let the  $x$  coordinates of the tips of the left and right cracks emanating from the  $i$ th hole be  $x_i^l$  and  $x_i^r$  respectively. Then the integration to obtain the SIFs from the Green's functions is performed in the range of  $x_i^l < x < (x_i^h - R)$  and  $(x_i^h + R) < x < x_i^r$ . Suitable Gaussian type integration formulae are used in the presence of a  $1/\sqrt{t}$  type singularity.
4. Corresponding to the solution in Step (3) determine the residual tractions at the surfaces of all the holes, as well as at the other boundaries of the finite strip of the lap-splice joint.
5. In order to satisfy the given traction boundary conditions at the outer boundaries of the finite strip as well as at the surfaces of all the fastener holes, reverse the residual tractions at these surfaces, as calculated from both Steps (2) and (4). Using the finite element method, calculate the equivalent nodal forces at the finite element nodes on these surfaces. A typical finite element mesh is shown in Fig. 1.123.
6. Using the finite element method, obtain the stresses at the location of the crack, corresponding to the nodal forces as calculated in Step (5).

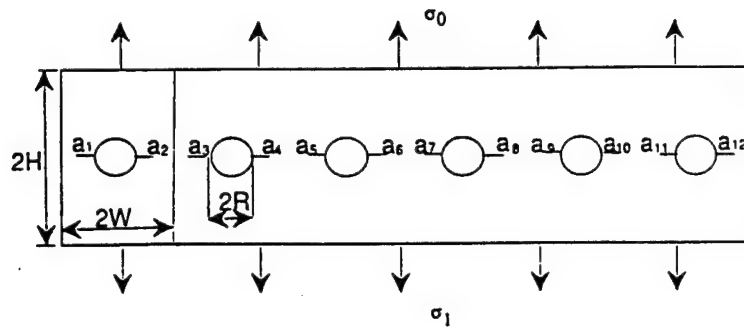


Figure 1.124: MSD (multiple cracks of unequal lengths) near a row of fastener holes

7. Erase the residual stresses on all crack-surfaces, as computed in Step (6), by repeating Step (3).
8. Continue this iteration until the increments in SIF resulting from Step (7) are vanishingly small.
9. By summing all the appropriate contributions, compute the total SIF for each of this tips of each of the cracks.

### § 1.8.5 Multiple site damage near a row of fastener holes

#### *Problem description*

Consider a typical multiple site damage problem illustrated in Fig. 1.124. Twelve cracks of different lengths emanate from six equally spaced fastener holes. Let the lengths of the cracks (as measured from the holes surfaces) be  $a_1, a_2, \dots$  and  $a_{12}$  respectively. A cyclic hoop stress, varying from zero and  $\sigma_1 = 82.74 \text{ MPa}$  (12 ksi) is assumed to exist in the fuselage skin (see Fig. 1.114). We assume that three rows of rivets carry this applied load in the fuselage lap joint (see Fig. 1.114) and that MSD exists in the top row of rivets. While a load-transfer analysis for each of the rows of the rivets, per se, is not included here, it is clear that the top row of rivets will carry more load than the middle row if there are no cracks near the top-row of fastener holes. However, as cracks develop and grow near this top row of holes, the load carried by the fasteners in this row will be reduced. We focus our attention on only the strip of the fuselage containing the top row of rivet holes and the MSD

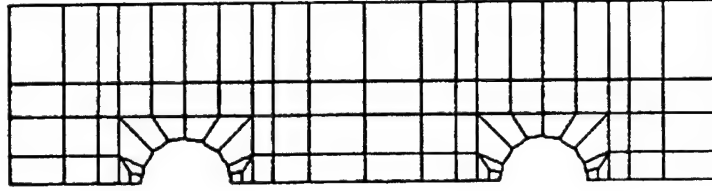


Figure 1.125: Finite element mesh

cracking. We assume that the upper surface of the strip containing the top row of rivet holes be subject to a cyclic load of  $\sigma_0$  and the bottom surface to a cyclic load of  $\sigma_1$ . Thus, cyclic load varying between zero to  $\sigma_0 = 55.16 \text{ MPa}$  (8 ksi) is assumed to be applied on the lower surface of the strip. At the maximum applied loading state, the contact stresses due to the fastener, on the hole surface are described as:

$$\sigma_r = -\frac{4W}{\pi R} (\sigma_1 - \sigma_0) |\sin \theta| \quad -\pi < \theta < 0, \quad (1.62)$$

Here  $W$  is the half of the distance between the holes, and  $R$  is the radius of the holes. In this problem  $W = H = 12.7 \text{ mm}$  (0.5in) and  $R = 2.045 \text{ mm}$  (0.0805 in) are used.

Since the loads applied on the strip are not symmetric in the  $y$  direction, mode II SIF as well as mode I SIF exists. However, we assume that the magnitude of mode II SIF is small compared with mode I SIF. Thus, only the mode I SIF is considered in this study. The mode I SIF can be obtained by superposition of two symmetric problems. One is the problem when only uniform normal stresses are applied on the outer boundaries and the other is when only the symmetric pin loads are applied on the hole surface.

The finite element model used in this problem is shown in Fig. 1.125, where one third of total mesh is shown. Here 264 8-node isoparametric elements and 981 nodes are used to analyze the problem with six holes. And the material is assumed as 2024-T3 aluminum alloy with Young's modulus  $E = 78500 \text{ MPa}$  and Poisson's ratio  $\nu = 0.32$ .

*Fatigue crack growth*

The fatigue growth of the twelve cracks shown in Fig. 1.124 is obtained as a function of loading cycles. In order to take into account the stress ratio effect, Forman's crack growth equation [Forman, Kearney, and Engle (1967)] is used. This equation is given by:

$$\frac{da}{dN} = \frac{C (\Delta K)^n}{(1-R) K_c - \Delta K} \quad (1.63)$$

Here  $\Delta K$  is the stress intensity factor range and  $R$  is the stress ratio in cyclic loading. For 2024-T3 aluminum alloy, the values of  $K_c = 83,000 \text{ psi}\sqrt{\text{in}}$ ,  $C = 3 \times 10^{-3}$  in and  $n = 3$  are used as given in Forman, Kearney, and Engle (1967).

In this study, the crack length increments are calculated at each 500 cycle interval, a constant rate of crack growth is assumed during the interval.

*Multiple "symmetric" cracks near a row of fastener holes*

Consider the fatigue crack growth of multiple symmetric cracks emanating from fastener holes. Here "symmetric cracks" implies that the lengths of the two cracks emanating from the same hole are equal, but the cracks emanating from different holes can have different lengths. Initial crack lengths are assumed as follows:

$$\begin{aligned} a_1 &= a_2 = a_9 = a_{10} = a_{11} = a_{12} = 0.03 \text{ in} = 0.762 \text{ mm} \\ a_3 &= a_4 = 0.04 \text{ in} = 1.016 \text{ mm} \\ a_5 &= a_6 = 0.06 \text{ in} = 1.524 \text{ mm} \\ a_7 &= a_8 = 0.05 \text{ in} = 1.270 \text{ mm} \end{aligned} \quad (1.64)$$

Fig. 1.126 shows the fatigue growth of each crack. First, we examine the cracks excluding  $a_1, a_2, a_{11}$  and  $a_{12}$ . It can be noticed that the longer crack always grows faster than the shorter crack. Thus, the difference in length between the longer crack and the shorter crack always keeps increasing with an increasing number of loading cycles. In some specific case, the SIF of the shorter crack subject to only the pin loading can be greater than that of the longer crack. However, in this problem, the ratio of pin loading to the total external loading is such that there is no possibility that the SIF of the shorter crack is larger than that of the longer crack. We also find that the crack growth curves of the two cracks with the same length, coincide with each other. In the later loading cycles, however, the separation between crack growth curves increases gradually, due to the interaction effect of adjacent cracks.

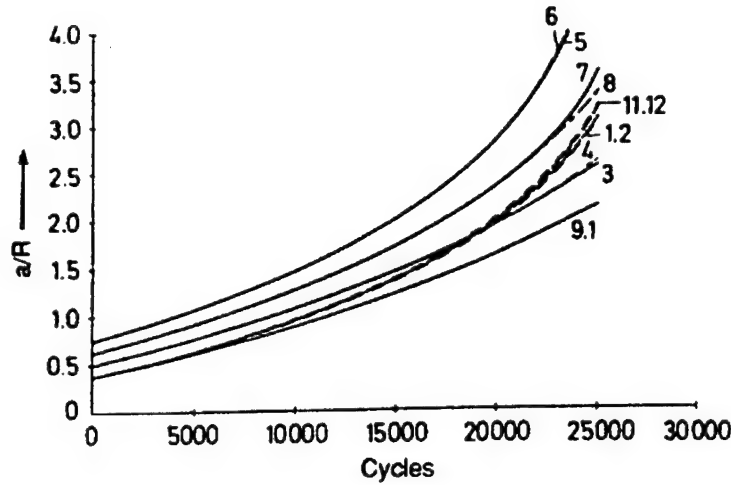


Figure 1.126: Fatigue growth of equal-length multiple cracks near a row of fastener holes, without considering the effects of residual stresses

From Fig. 1.126, we notice that the growth rates of  $a_1, a_2, a_{11}$  and  $a_{12}$  are greater than those of the interior cracks with the same length. As expected, positive axial stress,  $\sigma_x$  may produce negative  $\sigma_y$  stress along the  $x$  axis near the hole, and this negative  $\sigma_y$  stress will reduce the SIF values of the cracks near the holes.

*Multiple “unsymmetric” cracks near a row of fastener holes*

Here the term “unsymmetric” implies that the lengths of the two cracks emanating from the same fastener hole are unequal. Initial crack lengths are assumed as follows:

$$\begin{aligned}
 a_1 &= a_2 = a_6 = a_{10} = a_{11} = a_{12} = 0.03 \text{ in} = 0.762 \text{ mm} \\
 a_3 &= a_8 = 0.04 \text{ in} = 1.016 \text{ mm} \\
 a_4 &= a_9 = 0.06 \text{ in} = 1.524 \text{ mm} \\
 a_5 &= a_7 = 0.05 \text{ in} = 1.270 \text{ mm}.
 \end{aligned}
 \tag{1.65}$$

Fig. 1.127 shows the fatigue growth of each crack. We can observe the “catch-up” phenomenon for the two cracks emanating from the same hole. For example, consider  $a_3$  and  $a_4$ . Initially  $a_3 = 1.06 \text{ mm}$  and  $a_4 = 1.524 \text{ mm}$ , so the difference in the crack lengths is  $0.408 \text{ mm}$ . After 25,000 loading cycles,  $a_3$  becomes

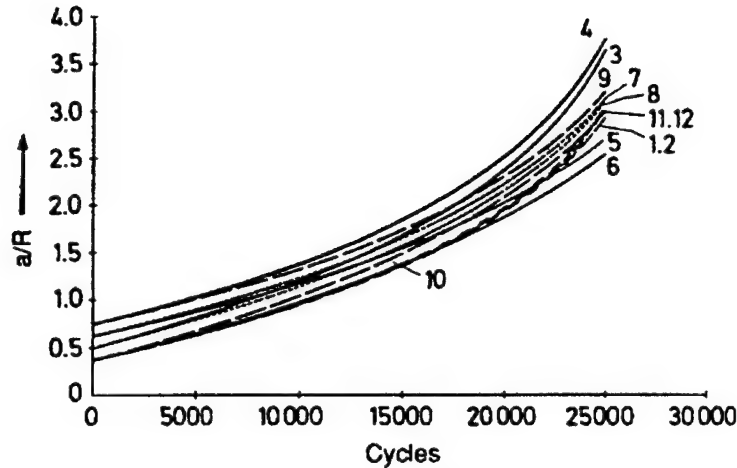


Figure 1.127: Fatigue growth of unequal length multiple cracks near a row of fastener holes, without considering the effects of residual stresses

9.455 mm and  $a_4$  becomes 9.690 mm. So the difference is reduced to 0.235 mm from 0.408 mm. This is because the SIF of  $a_3$  is greater than that of  $a_4$  during the whole loading cycles. The same phenomenon can be observed also in the other cracks emanating from the same hole.

#### § 1.8.6 Effect of residual stresses in the fastener hole

In a riveting process, since the fastener hole surface is expanded by plastic deformation, there are residual stresses near the fastener hole. In this section we employ a simplified model to account for these residual stresses. Assuming that the rivet is rigid, and that its radius is larger than that of the hole by an amount  $v_0$ , the residual stress due to the riveting process is considered to be equivalent to a constant residual radial pressure on the hole surfaces. Thus the likely partial separation between the rivet and the hole surface is not considered, and the effect of friction is not included.

When the applied far-field loads are such that, the radial displacement at the hole surface is greater than  $v_0$ , the radial pressure on the hole surface will reduce to zero, as there is not longer a misfit between the hole and the rivet. Thus, the actual radial pressure on the hole surface, due to the rivet misfit, is taken to depend on the applied far-field load, and hence on the displacement  $v$  (in the  $y$  direction) at the

upper most point in the  $y$  direction (see Fig. 1.124) of each hole. This is done as follows.

For a single hole in an infinite sheet [Muskhelishvili (1953)], if a rivet of radius  $(R + v_0)$  is inserted into a hole with a radius  $R$ , the relation between the radial pressure on the hole surface and its radial displacement  $v_0$  is given by:

$$p_0 = (2\mu) \frac{v_0}{R} = k_0 \frac{v_0}{R} \quad (1.66)$$

Eq. 1.66 assumes that there is no crack present near the hole;  $k_0$  is the "stiffness" of the hole in an infinite sheet for purposes of the initial stresses.

We assume that the rivet misfit is equal to  $v_0$  for all the fastener holes in a row; and that the initial radial pressure on each hole in a row of fastener holes, without cracks and without any far field loading, is equal in magnitude to  $p_0$  as in Eq. 1.66.

Assuming once again that the rivets are rigid, and a rivet radius misfit of  $v_0$ , when cracks are present near the holes, the initial radial pressure on the hole will be a function of the crack-length, in the absence of any other far-field loading. Thus,

$$p_i = k_i \left( \frac{v_0}{R} \right) \quad (1.67)$$

or

$$k_i = \left( \frac{v_0 p_i}{R} \right). \quad (1.68)$$

These initial radial pressures  $p_i$  may be solved for, using the finite-element-alternating method described earlier.

The stiffness  $k_i$  in Eq. 1.67 would depend on the lengths of the cracks emanating from the  $i$ th hole.

Corresponding to the initial radial pressure  $p_i$  at each hole, and in the absence of external loading, let the  $K$  factor at the  $r$ th crack emanating from each hole be given by  $K_{ir}^0$ . We now assume that once the stiffness  $k_i$  of the  $i$ th hole is determined from Eq. 1.68, the residual radial pressure on the  $i$ th hole is determined solely by the maximum  $y$  displacement  $v_i$  at the  $i$ th hole, in the presence of MSD near the holes. Let the applied far-field stress be  $\sigma_1$ , and let the maximum  $v$  displacement at the  $i$ th hole due to  $\sigma_1$  alone be designated as  $v_{i1}$ . Clearly  $v_{i1}$ , which is determined from the alternating method described earlier, is a function of the lengths of the cracks emanating from the  $i$ th hole. If  $v_{i1}$  is greater than  $v_0$ , there is no longer a radial pressure exerted by the fastener on the hole due to fastener-misfit. Thus, the

radial pressure exerted due to initial fastener-misfit, is given during the course of far-field loading, by:

$$p_{i1} = \begin{cases} k_i |v_{i1} - v_0|/R & \text{when } v_{i1} < v_{i0} \\ 0 & \text{when } v_{i1} \geq v_{i0} \end{cases} \quad (1.69)$$

where  $k_i$  is given by Eq. 1.68.

If, for a specified applied loading  $\sigma_1$ ,  $p_{i1} \neq 0$ , the effect of the non-zero  $p_{i1}$  on the SIF for the crack near the  $i$ th hole must be computed.

It is clear from the discussion in this section, even at zero far-field applied load, there is a non-zero SIF at each of the crack-tips; and for a non-zero far-field applied stress  $\sigma_1$ , the stress-intensity factors at each crack-tip must be computed by accounting for not only  $\sigma_1$  but also the radial pressure  $p_{i1}$  at each hole, as determined from Eqs. 1.69. Thus, it is clear that the stress-intensity range  $\Delta K$  that affects the fatigue crack-growth rate, is affected by the initial stresses due to fastener misfit.

#### *An example of a residual stress effect*

Residual stresses can affect fatigue crack growth by two factors: one by reducing the SIF range  $\Delta K$ , and the other, by increasing the stress-ratio  $R$ .

We illustrate these effects now by considering the case when radial cracks of equal lengths, of magnitude  $a_i$ , emanate from either side of the  $i$ th hole. Let the cyclic load be a far-field zero-to-tension load, say 0 to  $\sigma_1$  at the upper edge; and 0 to  $\sigma_0$  at the lower edge.

$K_i$ : Be the SIF at the crack at the  $i$ th hole, due to far-field [ $\sigma_1$  and  $\sigma_0$  at the upper and lower edges] alone.

$K_{i0}$ : Be the SIF at the crack at the  $i$ th hole, due to the initial (at zero far-field tension) radial pressure due to fastener misfit.

$K_{i1}$ : Be the SIF at the crack at the  $i$ th hole, due to the residual pressure  $p_{i1}$  as defined in Eqs. (1.68,1.69) when the applied far-field stress is ( $\sigma_1$  and  $\sigma_0$ ).

Consider the case when  $p_0 = 3\sigma_1$ , where  $\sigma_1$  is the higher of the far-field tensions as shown in Fig. 1.124. [Recall that for the results presented in Figs. 1.126 and 1.127,  $\sigma_1 = 12$  psi and  $\sigma_0 = 8$  psi].

Fig. 1.128 shows the values of  $K_i$ ,  $K_{i0}$  and  $K_{i1}$ , (for the cracks emanating from the 3rd hole as in Fig. 1.124) as a function of the length of the crack, ( $a/R$ ). It is seen that  $K_{i1}$  decreases rapidly after its maximum value and becomes zero at  $a/R = 1.46$ , while  $K_{i0}$  decreases gradually from its maximum value.  $K_i$ , on the other hand, as expected, becomes a monotonically increasing function of ( $a/R$ ).



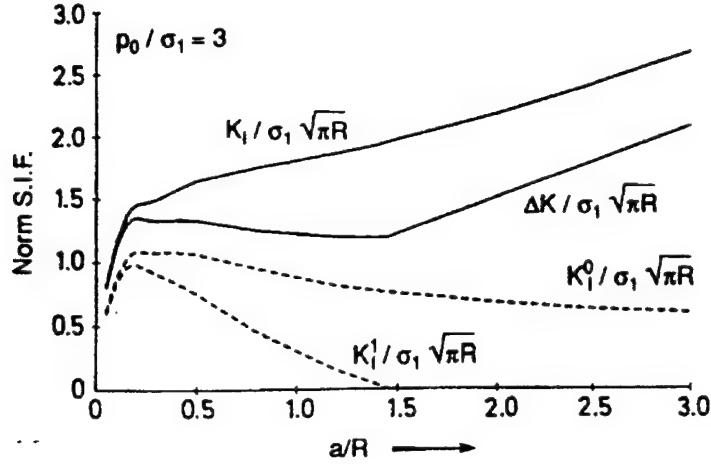


Figure 1.128: Variation of SIF and stress-intensity range as functions of  $(a/R)$ , with the effect of residual stresses being considered ( $p_0/\sigma_1 = 3$ )

The actual SIF at the maximum applied load  $\sigma_1$ , is seen to be  $(K_i + K_{i1})$  at the  $i$ th crack, and that at the minimum (i.e. zero) applied load is seen to be  $K_{i0}$ . Thus the SIF range is  $(K_i + K_{i1} - K_{i0})$ . If  $K_{i1}$  decreases more rapidly than the increase of  $(K_i - K_{i0})$ ,  $\Delta K$  will decrease with crack growth. From Fig. 1.128, it can be noticed that  $\Delta K$  decreases in the range of  $0.2 < (a/R) < 1.46$ . For crack lengths when  $K_{i1} = 0$ ,  $\Delta K$  increases rapidly. Thus, if cracks of different lengths are present in the range  $0.2 < (a/R) < 1.46$ , then the “catch-up” phenomenon can happen.

Fig. 1.129 shows another set of results for  $K_i$ ,  $K_{i0}$ , and  $K_{i1}$ , when  $p_0 = 4\sigma_1$ . The magnitudes of  $K_{i0}$  and  $K_{i1}$  have increased as compared to those in Fig. 1.128, but the trends are similar. In this case, the value of  $(a/R)$  where  $K_{i1}$  becomes zero is larger than that in Fig. 1.128. Thus, the range of  $(a/R)$  values for which the “catch-up” phenomenon is possible, is widened.

Fig. 1.130 shows the variation of stress ratio,  $R$ , with  $(a/R)$  when  $p_0/\sigma_1 = 3$  and 4. As the residual stress increases, so does the stress ratio. As the crack extends, the stress ratio increases to a maximum value, and then decreases gradually.

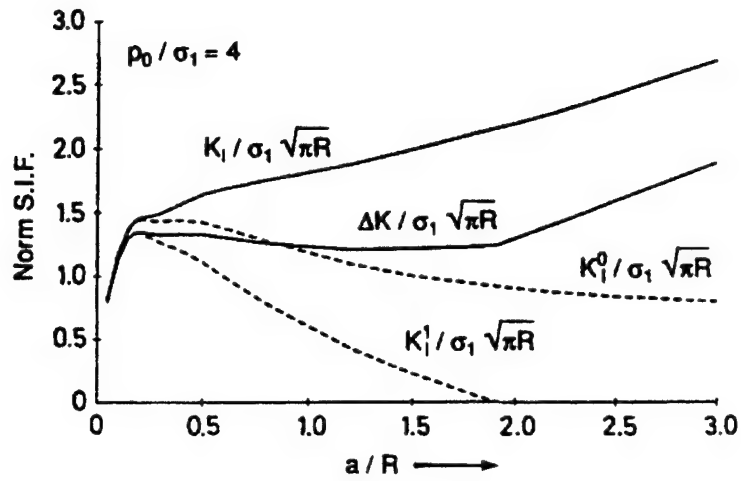


Figure 1.129: Variation of SIF and stress-intensity range as functions of  $(a/R)$ , with the effect of residual stresses being considered

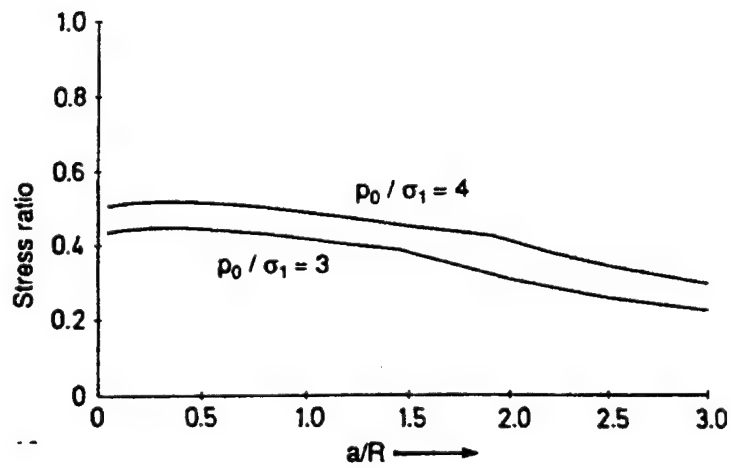


Figure 1.130: Variation of stress ratio as a function of  $a/R$

*Effect of plastic deformation due to cold-working*

The rivet misfit (or cold-working) generally induces a plastic deformation near the hole<sup>2</sup>. In this section, the effect of this plastic deformation on the fatigue crack growth is estimated. In order to simplify the analysis, it is assumed that the plastic deformation is caused solely by cold-working of the fastener-hole; and that the applied far-field hoop stress does not produce any plastic deformation. The material is regarded to be elastic-perfectly-plastic.

When the radial pressure,  $p_0$  applied on the hole surface is small, the material deforms elastically; and the stress-field near the hole can be expressed as:

$$\sigma_{rr} = -p_0 \left( \frac{R}{r} \right)^2, \quad (1.70)$$

$$\sigma_{\theta\theta} = p_0 \left( \frac{R}{r} \right)^2 \quad (1.71)$$

where  $r$  is the distance from the center of a hole of radius  $R$ .

As the pressure  $p_0$  is increased, the material near the hole begins to deform plastically. Let the region,  $R \leq r \leq r_y$  deform plastically and let the region outside this deform elastically. The stress field inside and outside the plastically deforming region can be obtained easily by solving the corresponding field equations, with the simple Tresca yield condition. For the region  $R \leq r \leq r_y$ , the stresses are given by:

$$\sigma_{rr} = -p_0 + \sigma_{ys} \ln \left( \frac{r}{R} \right) \quad R \leq r \leq r_y, \quad (1.72)$$

$$\sigma_{\theta\theta} = (\sigma_{ys} - p_0) + \sigma_{ys} \ln \left( \frac{r}{R} \right) \quad R \leq r \leq r_y \quad (1.73)$$

and

$$\sigma_{rr} = -\frac{\sigma_{ys}}{2} \left( \frac{r_y}{r} \right)^2 \quad r > r_y, \quad (1.74)$$

$$\sigma_{\theta\theta} = \frac{\sigma_{ys}}{2} \left( \frac{r_y}{r} \right)^2 \quad r > r_y. \quad (1.75)$$

Here  $\sigma_{ys}$  is the yield-strength of the material and  $r_y$  is the radius of the plastic-region, which is related to  $p_0$  as:

---

<sup>2</sup>The effect of rivet clamping force may also be significant. It is not considered here. For an experimental evaluation and a simple analysis of this effect, see Müller (1995)

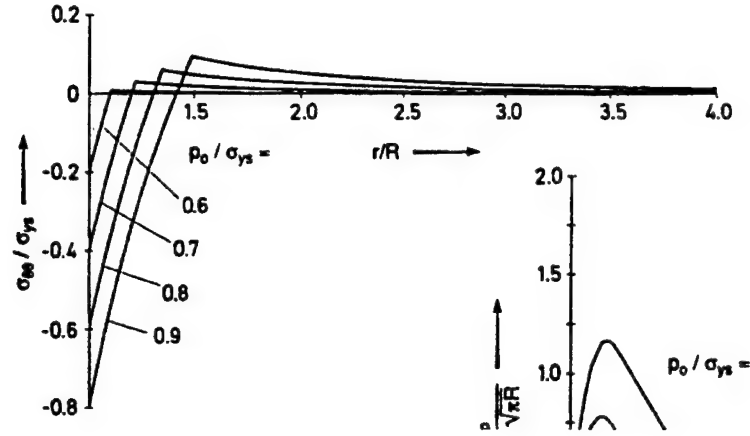


Figure 1.131: Residual stress along a radial line from the center of the hole, due to cold-working induced plasticity

$$p_0 = \sigma_{ys} \left[ \frac{1}{2} + \ln \left( \frac{r_y}{R} \right) \right] \quad (1.76)$$

The residual stress-field can be obtained by subtracting the elastic stress field of Eqs. 1.70 and 1.71 from the stress fields of Eqs. 1.72 to 1.75. Fig. 1.131 shows the distribution of this residual stress field along the radial direction from the hole-surface, for various values of initial pressure,  $(p_0/\sigma_{ys})$ .

Let a crack exist in the compressive residual stress-field near the fastener-hole surface. Then this crack will not open until the SIF due to the applied far-field load reaches a certain threshold value. Let this value be  $K_{op}$ . If a far-field cyclic loading is applied on the cracked sheet, and the SIF due to the applied minimum load is less than  $K_{op}$ , the compressive residual stress field will thus decrease the effective SIF range, and reduce the crack-growth rate. We examine the effect of the residual stress field by obtaining  $K_{op}$  values for various values of the lengths of a crack in relation to the radius of the plastic zone near the hole due to cold-working. We consider again the case of the MSD situation depicted in Fig. 1.124. It is assumed that each hole has the same residual stress field as in Fig. 1.132. The yield stress of the material is taken to be:  $\sigma_{ys} = 414 \text{ MPa (60 ksi)}$ .

Let the value of  $K_{op}$  for the  $i$ th hole be designated as  $K_{iop}$ . Fig. 1.132 shows the values of  $K_{iop}$  for  $i = 3$ , for various values of  $p_0$ , as a function of the crack-length  $(a/R)$ . It is seen that, initially,  $K_{op}$  increases rapidly as the crack-length increases

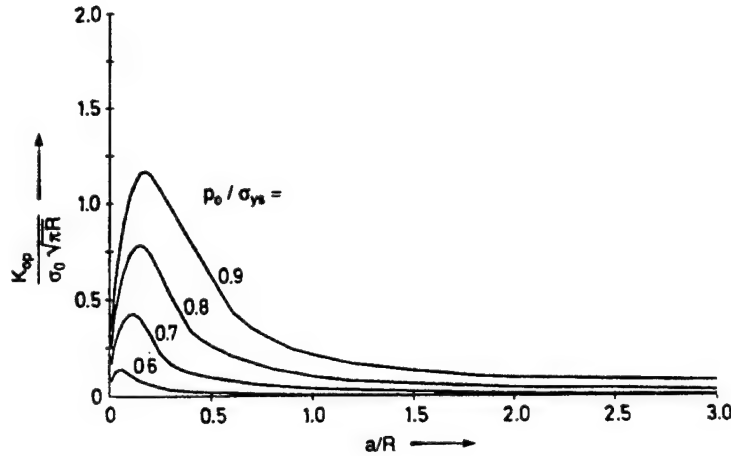


Figure 1.132: Variation of the  $K_{ep}$  needed to open the crack, for cracks of various length as compared to the radius of the plastic zone due to cold working

upto a certain value of  $(a/R)$ , and decreases very rapidly.

As discussed in earlier in this section, when there is a rivet misfit, because of the presence of the initial radial pressure  $p_i$ , the SIF at the  $i$ th crack at zero applied far-field loading is not zero, but of magnitude  $K_{io}$ . However, in that analysis, the effect of plastic deformation near the hole surface was not considered. However, the effect of plastic deformation alone is characterized by the value of  $K_{iop}$  that is needed to open the crack. Thus, in accounting for the effect of rivet misfit, the values of  $K_{iop}$  and must be superposed, in order to determine the value of SIF at zero far-field load. However, if we compare the  $K_{iop}$  values in Fig. 1.133 with the  $K_{io}$  values of Fig. 1.128 [ $(p/\sigma_{ys}) = 0.6$  is equivalent to  $p_0 = 3\sigma_0$ ] and of Fig. 1.129 [ $(p/\sigma_{ys}) = 0.8$  is equivalent to  $p_0 = 4\sigma_0$ ], it can be noted that the  $K_{iop}$  values are much smaller than the  $K_{io}$  values. It means that the effect of the plastic deformation near the hole surface due to a rivet misfit is not significant in reducing the effective stress intensity range, as compared to the effect of the initial radial pressure on the hole surface, but treating the problem within the theory of elasticity.

#### *MSD fatigue growth under residual stress effect*

The effect of residual stress on the fatigue crack growth of symmetric multiple cracks is examined. In order to compare with the case of no residual stress, the

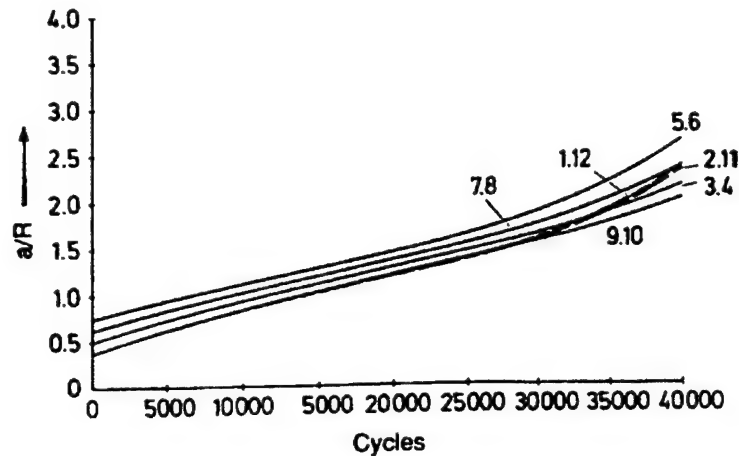


Figure 1.133: Fatigue growth of multiple cracks of equal length, emanating from a row of fastener holes; with the effect of the residual stresses being accounted for

same crack lengths as given in Eq. 1.64 are used. Fig. 1.133 shows the fatigue crack growth when  $p_0 = 3\sigma_1$ , and  $\sigma_1 = 12 \text{ psi}$ , and  $\sigma_0 = 8 \text{ psi}$  as in Fig. 1.124. From Fig. 1.133, we can notice that the growth rate of each crack is much reduced as compared with the case without residual stress (see Fig. 1.126). Thus, the residual stress may have a beneficial effect on the fatigue crack growth. We can see also that the shorter crack grows faster than the longer crack, until the longer crack grows to  $a/R = 1.46$ . Thus, the difference between the growth rates of the longest crack and the shortest crack decreases until about 30,000 cycles. It is an example of the "catch-up" phenomenon.

Next we consider the effect of residual stress on multiple unsymmetric cracks near holes. In order to compare with the case of no residual stress, the same crack lengths as given in Eq. 1.65 are used. It can be also noticed from Fig. 1.134 that the fatigue crack growth rate of each crack is much reduced as compared with the case of no residual stress. Also the "catch-up" phenomenon is observed as in multiple symmetric crack case.

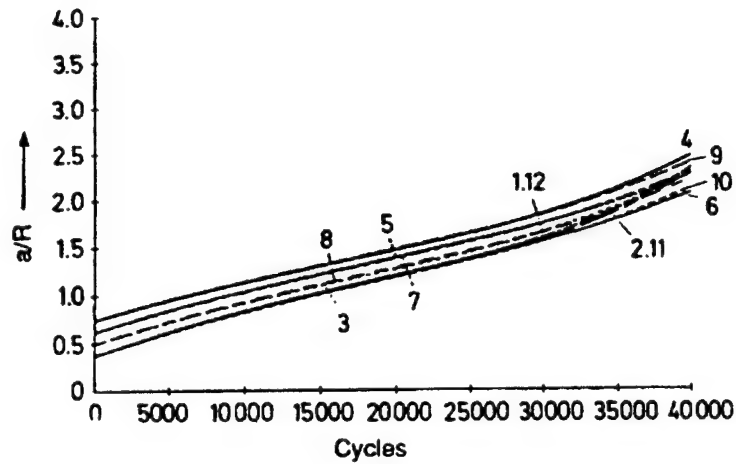
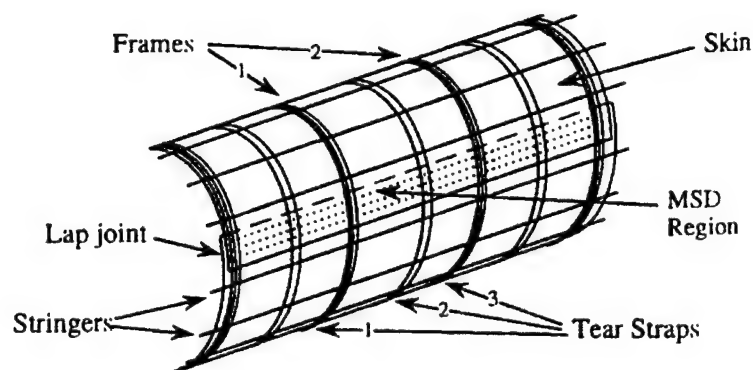


Figure 1.134: Fatigue growth of multiple cracks of unequal length, emanating from a row of fastener holes; with the effect of the residual stresses being accounted for

### § 1.9 Growth of Multiple Cracks and Their Linkup in a Fuselage Lap Joint: A Realistic Aircraft Structure

A multi-bay shell panel of a typical narrow body fuselage, with all of its structural features and a lap splice, is modeled. An arbitrary Initial crack configuration, at the outer critical row of fasteners, is chosen as a starting point. The fatigue loading applied is the cyclic pressurization of the fuselage. The pressurization induces a hoop stress that is transferred across the shell skins mainly through the lap joint and partly through the circumferential stiffening elements, i.e., frames and tear straps. In a perfectly bonded lap, the adhesive transfers most of the load through shear, but with aging the bond may deteriorate and the load is transferred primarily through the countersunk rivets. The cracks grow up to a certain length under the fastener heads and make the detection difficult. When the cracks start showing up from under the head of the fastener, they are long enough, have a reasonably high growth rate, and can soon become catastrophic, through linkup.



Shell Panel for Global Analysis



Cracked Skin Segment for Local analysis

Figure 1.135: Shell panel configuration



### § 1.9.1 Problem definition

#### Shell panel

Consider a typical narrow body fuselage shell stiffened longitudinally by stringers and circumferentially by frames and tear straps. Tear straps are present at all frame locations and midframe stations. Refer to Fig. 1.135 for a typical configuration. The geometrical details are as follows:

Shell radius $R$	74.0 in. (187.96 cm)
Shell skin thickness $t$	0.036 in. (0.0915 cm)
Distance between frames	20.0 in. (50.8 cm)
Distance between stringers	9.25 in. (23.495 cm)
Distance between tear straps	10.0 in. (25.4 cm)
Width of tear straps	2.0 in. (5.08 cm)
Thickness of tear straps $t_t$	0.036 in. (0.0915 cm)
Frame area	0.160 in. <sup>2</sup> (1.032 cm <sup>2</sup> )
Frame moment of inertia	0.120 in. <sup>4</sup> (5.0 cm <sup>4</sup> )
Frame neutral axis offset	3.15 in. (8.0 cm)
Stringer area	0.186 in. <sup>2</sup> (1.2 cm <sup>2</sup> )
Stringer moment of inertia	0.040 in. <sup>4</sup> (1.67 cm <sup>4</sup> )
Stringer neutral axis offset	0.78 in. (1.98 cm)
Fuselage internal pressure	9.0 psi (62 kPa)
Rivet diameter $D$	0.15625 in. (0.397 cm)
Pitch of rivets	1.0 in. (2.54 cm)
Material	Al 2024 – T3

Consider a longitudinal lap joint with the following particulars:

Length of overlap	3.0in.(7.62cm)
Number of rivet rows	3
Pitch of rivets	1.0in.(2.54cm)
Number of rivets in each bay	20 × 3
Rivet diameter $D$	0.15625in.(0.397cm)
Adhesive layer thickness $t_a$	0.0025in.(0.00635cm)
Material	Al 2024-T3

The material properties of Al 2024-T3 are taken as follows:

Young's modulus $E$	$10.5 \times 10^3 \text{ ksi (72.3 GPa)}$
Shear modulus $G$	$4.2 \times 10^3 \text{ ksi (28.9 GPa)}$
Poisson's ratio $\nu$	0.32
Yield strength $\sigma_y$	47.0ksi(323MPa)
Ultimate tensile strength $\sigma_u$	64.0ksi(440MPa)
Crack tip linkup stress (1/2) ( $\sigma_x + \sigma_y$ )	55.5ksi(381MPa)
Elongation	18
Fracture toughness $K_{IC}$	93.0ksi $\sqrt{\text{in}}$ (102MPa $\sqrt{\text{m}}$ )

The adhesive shear modulus is:

$$G_a = 109\text{ksi}(751\text{MPa}).$$

Consider a panel of this shell, consisting of five frames (nine tear straps), seven stringers, and a longitudinal lap joint. Initially all of the stiffening elements are presumed to be intact. As the cracks grow and link up to form a dominant crack, these stiffeners get overloaded and may fail. The adhesive is treated to be degraded to 1% of its original strength due to aging, so that the fasteners transfer all of the load through the joint. Consider the problem of multiple cracks of finite lengths emanating from the outer critical row of fastener holes in two adjacent bays, across a frame (called frame 1). Fig. 1.136 shows the initial crack configuration of six cracks (with two tips each) numbered 1L to 6R (L for left and R for right) emanating from six fastener holes. All of the MSD cracks in a bay are considered in the same half of the bay, i.e., between two tear straps, numbered T-strap 1 and 2 in this case. The crack lengths of 0.10 in. (0.254 cm) are chosen to typically represent

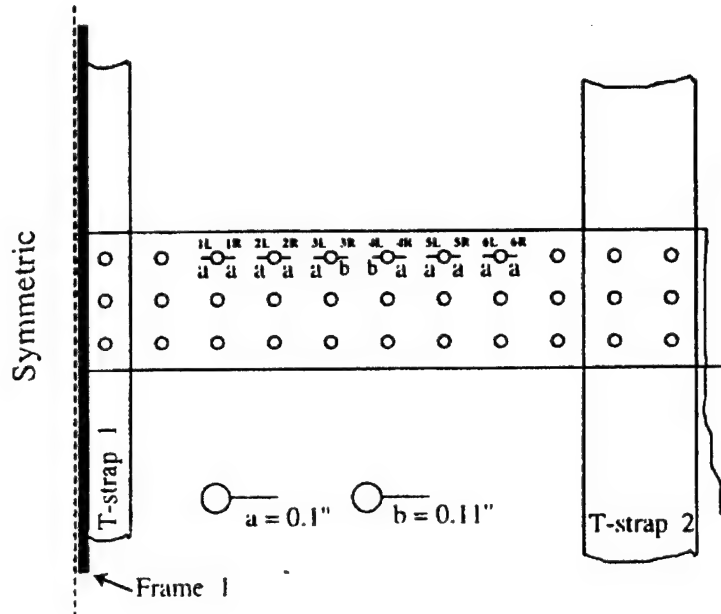


Figure 1.136: Initial crack configuration in the shell panel

a situation where the cracks are hidden well under the countersunk head of the fastener. The cracks lengths are measured from the center of the hole and thus include the fastener radius. At the central ligament, the cracks 3R and 4L have been specifically chosen to be a length of 0.11 in. (0.279 cm) so as to insure the first linkup at this location. The configuration is chosen to be symmetric about the frame for ease of analysis. Thus we need to analyze only one-half of the damaged panel, i.e., three frames and five straps. The fatigue loading applied is the cyclic pressurization of the shell from 0.0 to 9.0 psi (62 KPa). Under this loading, the MSD cracks are expected to link up to form two long cracks, one in each bay, which will framer link up at the frame location to form a single dominant two-bay crack. Fatigue growth of the initial set of cracks is considered up to the formation of a full two-bay-long crack.

Whenever there is a crack linkup, and if there is no crack emanating at the other end of the hole, it can be treated as having arrested, and fatigue growth has no meaning beyond this point. However, in reality there could be small cracks and they will grow, and so to perform fatigue analysis, very small cracks are presumed to exist at all other fastener holes but are considered in the analysis only when the

dominant crack tip comes close enough.

#### *Coupon configuration*

Laboratory test of MSD fatigue crack growth at a lap joint in a flat coupon, performed at the Aeronautical Research Laboratory, Melbourne, Australia, has been simulated to verify the analysis procedure. The configuration for the coupon is shown in Fig. 1.137. The sheet thickness is 0.04 in. (0.1 cm) in the present case. The width of 8 in. (20.32 cm) represents the portion of the skin between the tear straps. The lap splice configuration is identical to that in the shell panel joint, with a fastener diameter of 5/32 in. (0.3968 cm). The initial crack configuration considered is shown in Fig. 1.138. In the experiments the cracks were generated using an electrical spark erosion technique. The cracks were taken tube 0.047244 in. (0.12 cm) long so that the defect was obscured by the fastener head and represents a possible undetectable flaw. This would correspond to a crack tip distance of 0.124 in. (0.315 cm) from the hole center. In the experiment the local bending was minimized by testing the specimens bonded back to back and separated by a honeycomb core 0.492 in. (1.25 cm) thick. The fatigue loading on the sheet is uniaxial tension varying between 0.67 and 13.4 ksi (4.61 – 92 MPa), corresponding to a stress ratio of 0.95. The sheet material is Al 2024-T3.

#### *§ 1.9.2 Analytical approach*

The analytical approach employed for the present study consists of a repetitive global-local analysis. A global finite element analysis is first carried out on the initial crack configuration to determine the fastener loads and the sheet stresses some distance away in the meridional direction from the longitudinal crack axis. A local analysis on the isolated, loaded, and cracked skin segment is then carried out to obtain the crack tip parameters using the Schwartz-Neumann finite element alternating method (FEAM). With the evaluated crack tip parameters, the crack is allowed to grow as per the Paris equation. The local analysis is performed for crack increments small enough not to alter the load flow through the panel. Whenever the crack growth is significant to effect the load flow pattern or the crack linkup occurs, a fresh global analysis is performed to update the fastener loads and the sheet stresses.

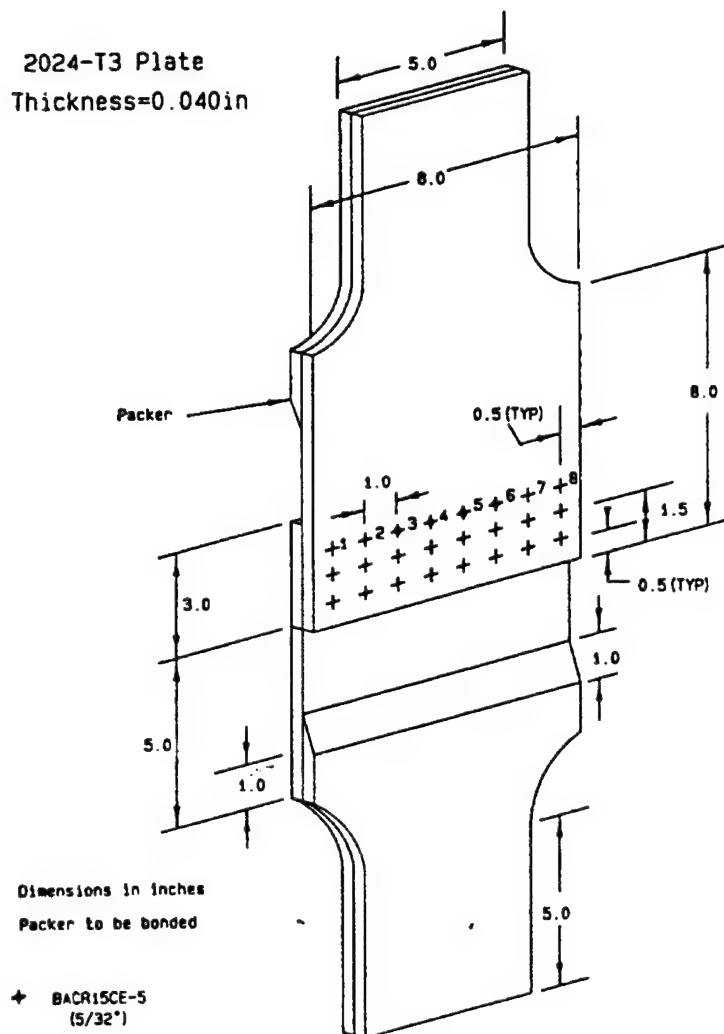


Figure 1.137: Flat coupon lap joint configuration

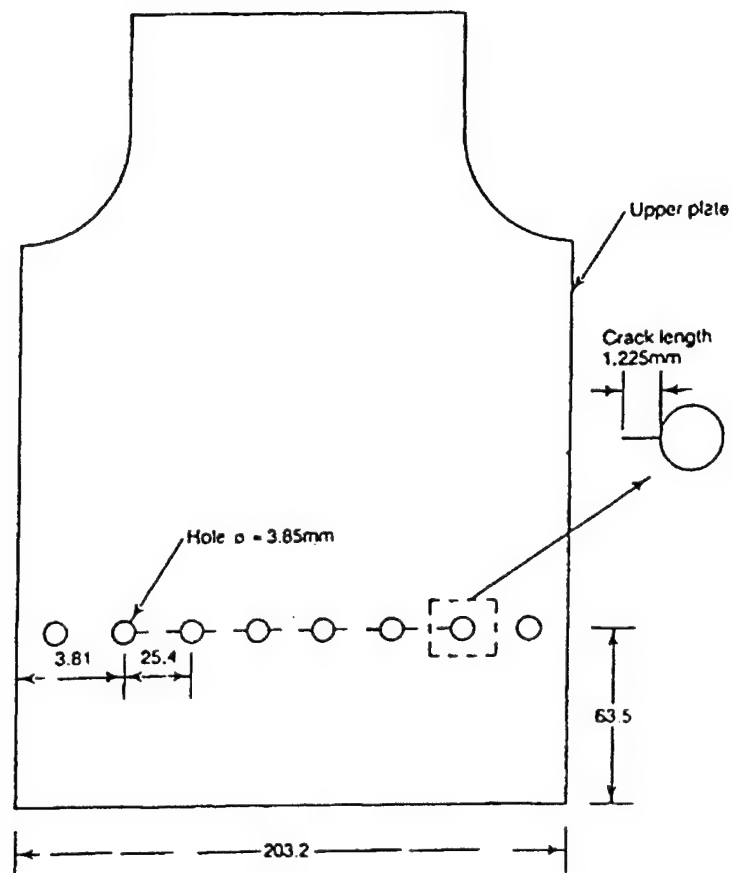


Figure 1.138: Initial crack configuration in the coupon

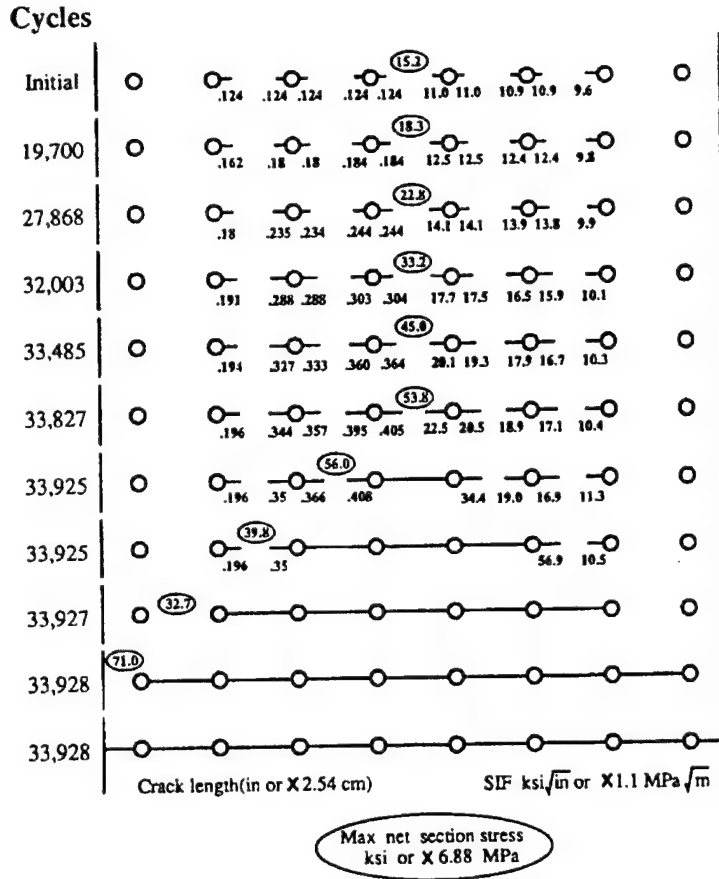


Figure 1.139: Comprehensive picture of MSD crack growth in the coupon

### § 1.9.3 Results and observations

#### Coupon problem

The fatigue growth analysis of MSD in a lap joint in a flat coupon of Fig. 1.137 with an initial crack configuration of Fig. 1.138 is carried out as per the procedure discussed in the preceding sections. The local and the global analyses are performed at crack length increments of 0.015 in. (0.0381 cm) and 0.060 in. (0.1524 cm), respectively. The comprehensive picture of the fatigue damage is shown in Fig. 1.139. Each stage marked by the number of fatigue cycles represents a state when the fresh global analysis was carried out to up date the load distribution. Since the problem

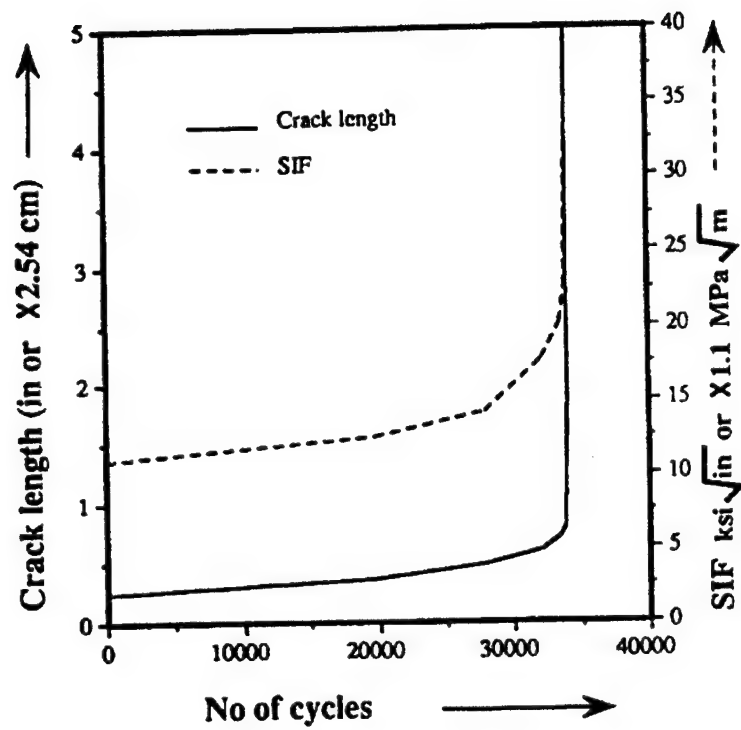


Figure 1.140: SIF and crack length variation with number of cycles



is symmetric, only one-half of the domain is analyzed. In Fig. 1.139, the left-hand side represents the crack lengths and the right-hand side gives the corresponding SIFs. The numbers within the ellipse denote the location and the magnitude of the maximum net ligament stress. The variations of SIF and the length of longest crack with number of cycles is presented in Fig. 1.140. The crack growth rate increases substantially at around 25,000 cycles. The first linkup occurs at 33,925 cycles, and then the cracks snap through all of the other ligaments almost instantaneously. This is both due to load redistribution as well as a substantial increase in crack tip SIF after the first linkup. The stress intensity factors increase with crack length and shoot up at linkup, thus increasing the crack growth rate to over 1/4 in./cycle. The load redistribution at first linkup shows that the next neighboring ligament has yielded. After the second linkup, the dominant crack tip SIF is high enough to snap through the third ligament within two cycles. Now, at the linkup of all cracks, there exists a central crack of 5 in. (12.7 cm). If there are no cracks in the next outer ligaments, the cracks can be treated as being arrested. However, if there is even a small crack, it can grow to the outermost hole in just a cycle, and then the outermost ligament yields, causing a complete failure of the panel. The significant observation is that the fatigue life of the coupon was only up to first linkup.

The load flow through the fasteners in the damaged row of fasteners at various stages is given in Tab. 1.12. Tab. 1.13 gives the row-wise load distribution at all of the stages. Interestingly, after first linkup, the damaged row takes up more load. The explanation may be as follows: As the cracks grow, the stiffness of the fasteners comes down, and they shed the load to the intact ligament, which now carries more stress. But at linkup the ligament can no longer take any load, and the entire load is diverted to the end rivets, which get heavily loaded.

The experimental effort considered 10 specimens of this coupon. Out of these, five specimens were subjected to fatigue loading until failure, which occurred almost instantaneously after the first linkup. The five specimens demonstrated a fatigue life of 25,000, 105,700, 67,000, 41,400, and 57,370 cycles, respectively, loading to a mean life of 59,300 cycles. The analytical results give a life of about 34,000 cycles. Our analysis has given a conservative estimate that could be due to two main reasons. First, the plasticity effects on fatigue crack growth, such as the crack closure effects, have not been modeled in the analysis. Crack closure due to crack tip plasticity is known to reduce the effective stress intensity factor range over which fatigue crack growth occurs and thus to result in a prediction of slower growth. Previous investigations of static residual strength of damaged panels<sup>1</sup> did bring out the importance of plasticity in establishing the linkup criterion under sta-

Table 1.12: Rivetwise load (in pounds or  $\times 4.45\text{N}$ ) distribution in the outer row at various stages of the panel fatigue failure

	Rivet No.							
Cycles	1	2	3	4	5	6	7	8
Initial	172	172	172	172				
19,700	182	184	147	152				
27,868	182	185	140	144				
32,003	183	186	135	139				
33.485	185	188	129	133	Symmetric			
33,827	187	191	126	128				
33,925	188	193	125	124				
	First linkup							
33,925	196	205	133	98				
33,927	235	262	113	43				
33,928	290	352	51	29				
33,928	612	78	36	21				

Table 1.13: Row-wise load (in pounds or  $\times 4.45$  N) distribution at various stages of the panel fatigue failure

Cycles	Row 1	Row 2	Row 3
Initial	1370	1118	1370
19,700	1328	1157	1372
27,868	1306	1167	1384
32,003	1286	1177	1395
33,485	1272	1184	1401
33,827	1265	1188	1405
33,925	1261	1190	1407
First linkup			
33,925	1268	1188	1405
33,927	1314	1155	1388
33,928	1447	1065	1330
33,928	1494	1020	1296

Table 1.14: Crack lengths and the crack tip SIF at various stages of fatigue

Cycles	MSD crack lengths, $a$ , in. or $\times 2.54\text{cm}$											
	1L	1R	2L	2R	3L	3R	4L	4R	5L	5R	6L	6R
Initial	0.100	0.100	0.100	0.100	0.100	0.100	0.100	0.100	0.100	0.100	0.100	0.100
7,003	0.116	0.116	0.132	0.132	0.154	0.159	0.164	0.160	0.145	0.144	0.131	0.131
10,166	0.123	0.124	0.152	0.154	0.203	0.207	0.222	0.220	0.178	0.178	0.148	0.148
11,685	0.127	0.128	0.165	0.167	0.245	0.249	0.282	0.280	0.205	0.204	0.160	0.159
12,210	0.129	0.129	0.170	0.172	0.264	0.269	0.342	0.338	0.216	0.214	0.164	0.164
12,435	0.129	0.130	0.173	0.175	0.277	0.286	0.403	0.392	0.222	0.219	0.166	0.166
12,548	0.130	0.130	0.174	0.176	0.285	0.299	0.465	0.442	0.225	0.222	0.168	0.168
12,594	0.130	0.131	0.175	0.177	0.289			0.475	0.266	0.223	0.168	0.168
12,595	0.130	0.131	0.175	0.177	0.306			0.491	0.227	0.223	0.168	0.168
12,597	0.130	0.131	0.175	0.177	0.347					0.223	0.168	0.168
12,598	0.130	0.131	0.175	0.177	0.457					0.317	0.168	0.168
12,599	0.130	0.131	0.175							0.479	0.168	0.168
12,599	0.130	0.131	0.175			Linkup						0.168
12,600	0.130											0.168
Cycles	MSD crack tip SIF ( $\text{ksi}\sqrt{\text{in}}$ or $\times 1.1 \text{ Mpa}\sqrt{\text{m}}$ )											
	1L	1R	2L	2R	3L	3R	4L	4R	5L	5R	6L	6R
Initial	9.3	9.4	10.6	10.6	11.8	11.8	12.0	12.1	11.4	11.3	10.5	10.5
7,003	9.3	9.4	11.2	11.3	13.4	13.4	14.0	14.0	12.5	12.5	11.0	11.0
10,166	9.4	9.5	11.7	11.7	14.6	14.6	15.9	15.9	13.2	13.2	11.5	11.5
11,685	9.5	9.5	11.9	12.0	14.9	15.3	19.1	19.0	13.6	13.4	11.6	11.6
12,210	9.5	9.6	12.1	12.2	16.1	16.9	22.0	21.6	13.8	13.4	11.8	11.8
12,435	9.6	9.7	12.2	12.3	16.5	18.4	24.9	23.8	14.2	13.4	11.9	11.9
12,548	9.6	9.7	12.3	12.4	17.0	20.1	28.3	26.2	14.6	13.3	12.0	11.9
12,594	10.1	10.3	11.9	11.5	40.8			40.6	14.5	12.9	12.7	12.6
12,595	10.2	10.3	11.6	11.1	43.1			42.7	15.1	12.7	12.8	12.6
12,597	10.8	10.9	11.7	11.0	55.8					54.5	11.4	12.4
12,598	11.0	11.2	10.8	11.2	59.6					59.5	10.6	11.6
12,599	11.2	10.2	71.4							73.5	10.8	10.4
12,599	11.6	10.6	80.4			Linkup						79.1
12,600	78.8											64.6

ble growth due to static monotonic loading. Another factor could be that the crack tip in the experiment is initially blunt as it was generated due to spark erosion. Considering these points, the analysis seems to give a reasonably good estimate of fatigue life, with only a few hours of computational effort. By incorporating plasticity into the local analysis, we will be able to have better estimates.

### Shell panel problem

The shell panel of Fig. 1.135 is now analyzed with the initial crack configuration of Fig. 1.136. The local and the global analyses are performed at crack length increments of 0.01 in. (0.0254 cm) and 0.04 in. (0.1016 cm) respectively. The fatigue damage is pictorially presented in Fig. 1.141. The corresponding crack

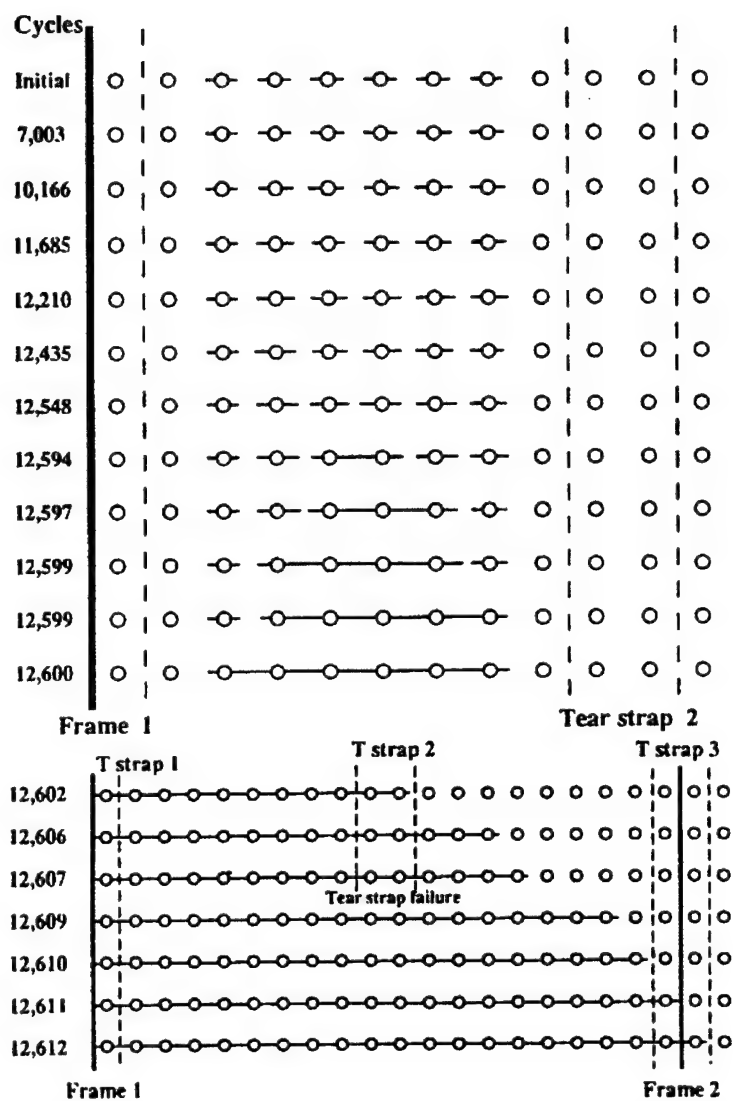


Figure 1.141: Pictorial representation of fatigue damage in the shell panel

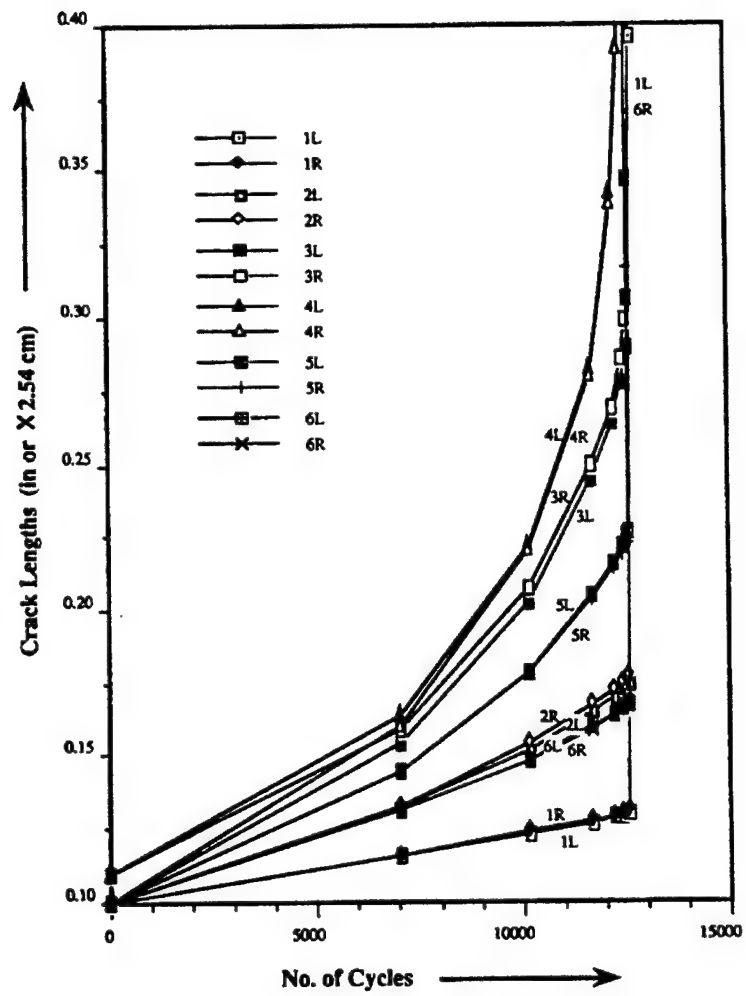


Figure 1.142: Fatigue crack growth of the 12 cracks in the shell panel

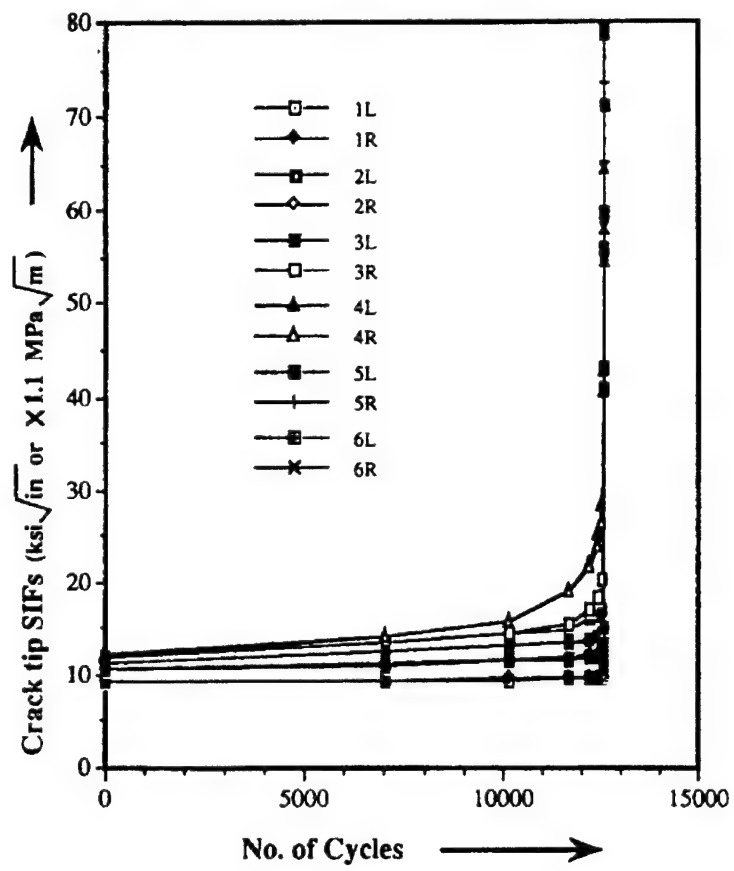


Figure 1.143: Crack tip SIFs of the 12 cracks in the shell panel

lengths and the SIFs are pinned in Fig. 1.142 and 1.143, respectively, and their numerical values are listed in Tab. 1.14. Once again the same striking feature can be clearly seen; the "sudden death" of the panel. The first linkup occurs at 12,594 cycles, and then within 6 cycles, in each bay, all of the cracks link up to form a long crack. Within the next two cycles, the two long cracks across the frame coalesce to form a single dominant tow-boat crack of over 20 in. (50.8 cm) in length. This dominant crack, due to its length and the associated tip SIF, has a growth rate of almost an inch/cycle. Even when the growth rate is less than an inch/cycle, it is large enough to reduce the length of the intact ligament, which fails under direct stress. Thus, with every cycle, the crack grows to the next fastener hole. At 12,607 cycles, when the crack spans over 15 holes in each bay, the mid-bay tear straps yield. From this stage onward, these are treated as having failed and modeled as not to take any more load (this is a conservative approach, as they might continue to bear some load). Because of this failure, the crack tip SIF suddenly shoots up and so does the crack growth rate. The tear straps do not appear to arrest the crack growth. By 12,611 cycles, there exists a full two-bay-long crack spanning from frame to frame. Thus, from the first linkup up to the formation of a two-bay crack, all it took was just 17 cycles. The analysis is stopped at this stage.

From Fig. 1.142, the crack closest to the frame has the lowest growth rate. The initially longer cracks (0.11 in.) are the fastest to grow and the first ones to link up (as intended at the time of initial crack configuration selection). Fig. 1.143 shows the shootup of SIF after the first linkup. The presence of a frame does reduce the SIF (increasing the static residual strength) and does slow down the crack growth, but the effect adds virtually nothing to the countable cycles of residual life. These observations are, of course, within the limitations of applicability of the Paris equation to low cycle fatigue.

Fig. 1.144 and Tab. 1.15 present the load flow pattern in the frames and the tear straps as the cracks grow. Yielding of the mid-bay strap can be seen to overload the intact frame/straps. Tear strap 3 shows a negative load for a small range; this could be due to the local in-plane bending moments being generated out of substantial load diversion.

Both the coupon and the shell panel with MSD are found to have fatigue lives only up to the first linkup. This is because after the first linkup the crack has a dominant length with high stress intensity factors. This is an important piece of information for the analyst involved in fatigue life estimation of similar structural components with widespread damage.

In a lap joint, the growth of multiple cracks emanating from a row of fastener



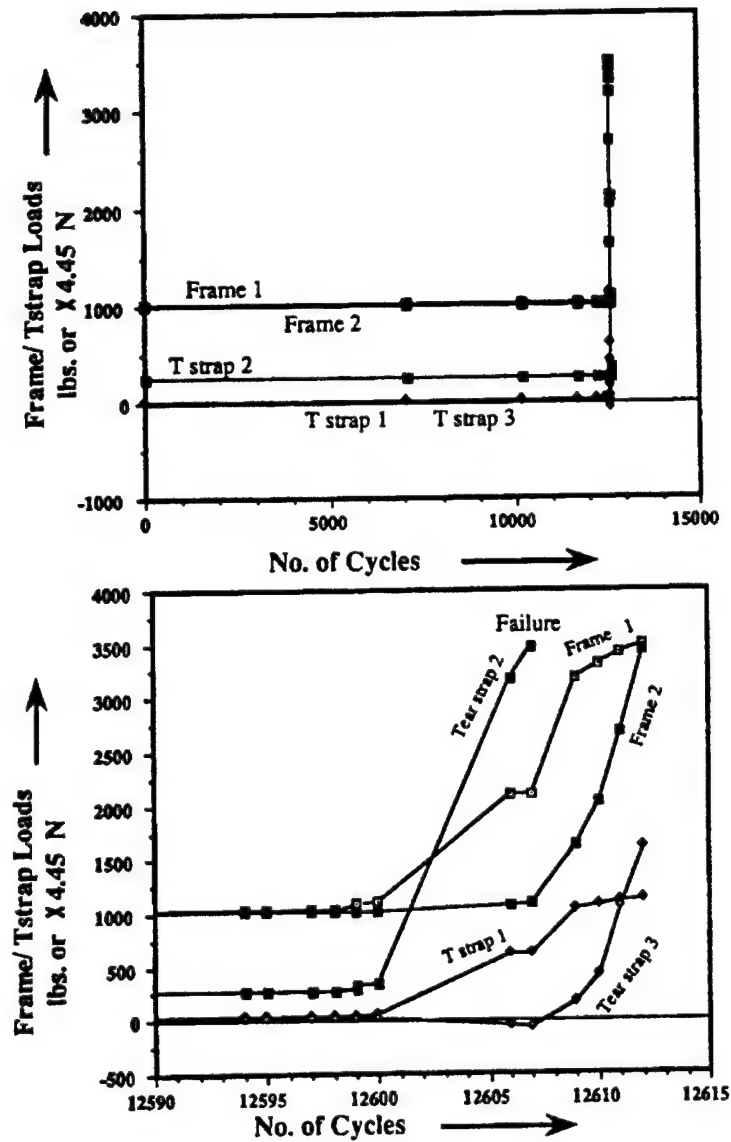


Figure 1.144: Frame and the tear strap loads during fatigue

Table 1.15: Frame and tear strap loads at various stages of fatigue

Cycles	Frame and tear strap loads, lb or $\times 4.45N$				
	Frame 1	Tear strap 1	Tear strap 2	Tear strap 3	Frame 2
Initial	1019	31	264	30	1010
7,003	1019	31	264	30	1010
10,166	1020	31	265	30	1010
11,685	1021	32	265	30	1010
12,210	1021	32	266	30	1010
12,435	1021	32	266	30	1010
12,548	1022	32	267	30	1010
12,594	1028	34	269	29	1010
12,595	1029	34	269	29	1010
12,597	1037	36	278	29	1011
12,598	1040	37	282	28	1011
12,599	1067	46	291	27	1011
12,599	1082	50	327	26	1011
12,600	1110	57	357	25	1012
12,606	2106	612	3178	-54	1080
12,607	2110	613	3474	-60	1083
12,609	3185	1031	Fail	166	1636
12,610	3314	1071		428	2038
12,611	3430	1105		1055	2681
12,612	3490	1121		1609	3434

holes has been investigated under cyclic loading. A flat plate coupon and a stiffened shell structure, typical of an air-liner fuselage, were analyzed. The most important feature that emerges is that the fatigue life of the lap splice with widespread cracking is only up to the first linkup. Beyond this, the crack lengths, the corresponding stress intensity factors, and the crack growth rates become prohibitively high. A good linkup criterion is thus very important for residual life estimation of a structural component with multisite damage that is subject to fatigue loading. The second feature is that the frames or tear straps are hardly capable of arresting the growth of dominant cracks under fatigue loading.

#### **§ 1.10 Prediction of Fatigue Crack Growth and Linkup for a Full Scale Curved Stiffened Panel**

The fatigue life of an undamaged structure subjected to a repeated external load can be divided into two periods. The first period is the fatigue crack initiation period. Depending on the design, material, manufacture and operating environment of structure, detectable fatigue cracks may be found near the regions of high stress level, such as the edges of rivet holes, after years of service. This period of fatigue life can be obtained from the service record of aging flight vehicles. The second period is the fatigue crack growth period, during which the initial fatigue cracks (MSD) grow and propagate, resulting a local failure. Estimating the second period is significant for aging flight vehicles in economy and safety. In this section, the focus is on the estimation of second period of fatigue life. A numerical analysis is carried out to predict the number of cycles to failure for a full scale curved test panel. Numerical results are compared with the experiment measurements obtained by Foster-Miller, Inc. [Samavedam, Hoadley, and Thomson (1992)]

##### **§ 1.10.1 Foster-Miller curved panel test**

The Full Scale Fuselage Panel 12 tested for fatigue in Foster-Miller, Inc. [Samavedam, Hoadley, and Thomson (1992)] is considered as an example. The geometrical details are listed below. Both skin and tear strap were made of Al 2024 T3.

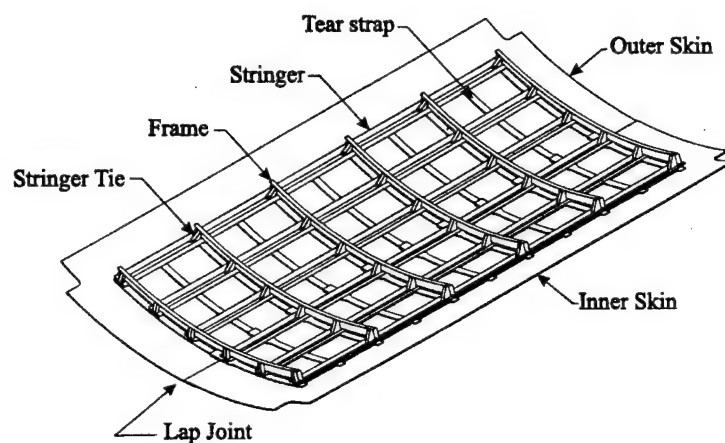


Figure 1.145: Full Scale Fuselage Panel

length	120 in
radius	75 in
width	68 in
number of frames	6
number of tear straps	11
number of stringers	6
frame spacing	20 in
tear strap spacing	10 in
stringer spacing	9.6 in
skin thickness	0.04 in
Tear strap thickness	0.04 in

This test fuselage panel was designed to represent critical construction features of the aging commercial aircraft. The panel has a 2.7 in wide lap joint. All through-skin rivets are low profile, shear head 100° countersunk rivets, with a diameter of  $5/32$  in. The minimum diameter of rivet bucktail of panel lap is  $1.26 d$ , where  $d$  is the rivet diameter. The maximum diameter of rivet bucktail of panel lap is  $1.48 d$ . The three dimensional fuselage test panel 12 is shown in Fig. 1.145. The fatigue

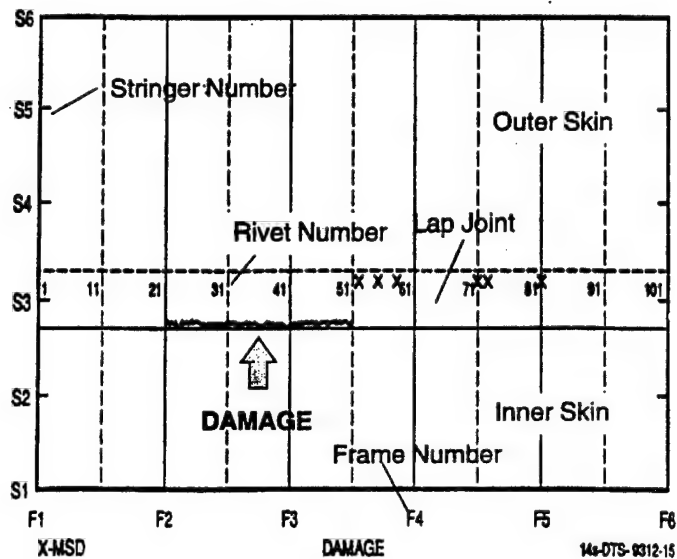


Figure 1.146: Fatigue Damage

load is cyclic pressure. The pressure was applied at 0.2 *Hz* over a pressure range of 8.5 *psi* with a loading ratio of 0.11.

At 75,000 loading cycles, the cracks were found on the underside of the panel along the lower rivet line at lap joint 27, 28, 29 in inner skin. The rivet number and fatigue damage are denoted in Fig. 1.146. The test report shows that the cracks between the rivet hole 27 and 28 link-up after 114938 cycles of loading.

### § 1.10.2 Computational models

#### *Global analysis*

The fuselage panel consists of outer skin, inner skin, 22 peaces of tear strap, 106 fillers, 6 stringers, 6 frames, 24 stringer ties and rivets. The longitudinal length of global model is  $L = 112 \text{ in}$ , the circumferential width is  $B = 53 \text{ in}$  ( circular angle  $a = 40.49^\circ$ , skin radius  $R = 75 \text{ in}$  ). The outer and inner skins are modeled by 3-dimensional 4-node doubly curved shell element. The tear straps and fillers also are modeled by 3-dimensional 4-node doubly curved shell element. The stringers and frames are modeled by the 3-dimensional 2-node linear beam element. The

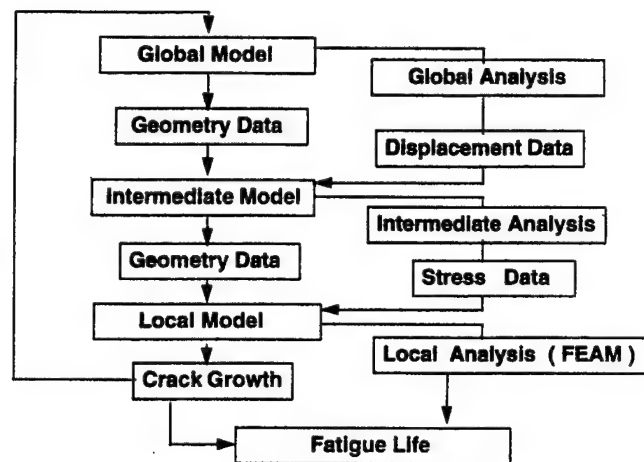


Figure 1.147: Fatigue Life Estimation Procedure

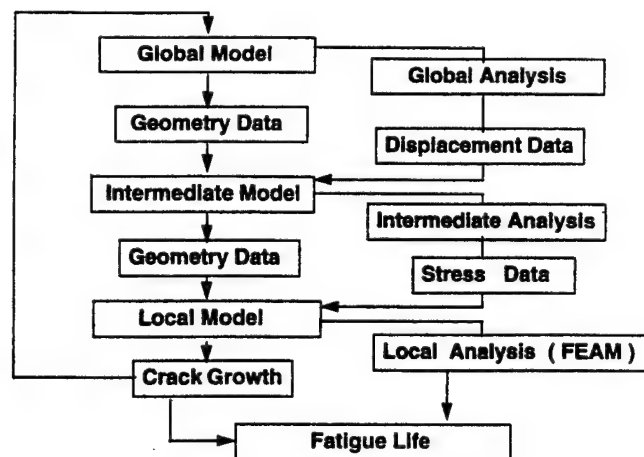


Figure 1.148: Global Model, Intermediate Model and Local Model

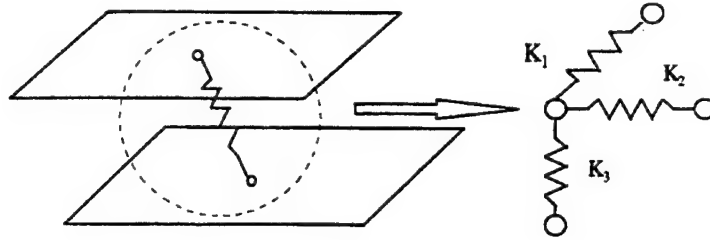


Figure 1.149: Spring Model

rivets between the tear straps and the frames, between the tear straps and strangers, between the filler and stranger, and between the stringer and the frames are modeled by beam element, but the rotations of two ends of this beam are constrained to be the same. The boundary conditions are fixed except the rotation about the longitudinal axis on the longitudinal boundary and the rotation about the circumferential axis on the circumferential boundary. The cracks are considered in the global model. The crack size in the global model increases by moving the crack tip node. The mesh in the crack area is refined to satisfy the requirement of elements. The pressure load on the skin is 8.5 psi. The total number of nodes is 10798. The total number of elements is 14161. The global analysis is carried out by using a commercial finite element analysis code, taking about 714 sec CPU time on HP 735 workstation.

The rivets between the outer skin and inner skin at lap joints, between the skin and tear strap, and between skin and filler are modeled by the spring model. The spring model consists of three spring elements. They are shown in Fig. 1.149. The stiffness of the rivet in the transverse plane of rivet is presented by the spring element stiffness  $K_1$ ,  $K_2$ . They are given by following equation [Swift (1984)]

$$K_{1,2} = \frac{E_{sh}D}{A + C(D/t_1 + D/t_2)} \quad (1.77)$$

The  $K_3$  is the stiffness of rivet in the direction of rivet axis.

$$K_3 = \frac{ED^2\pi}{2(t_1 + t_2)} \quad (1.78)$$

where  $E_{sh}$  ( $E$ ) are the Young's modules of skin (rivet);  $D$  is the rivet diameter,  $t_1$  and  $t_2$  are the thicknesses of the jointed sheets;  $A = 5.0$  and  $C = 0.08$  for aluminum rivet.

*Intermediate analysis*

Intermediate model contains structural detail around the area of MSD. The longitudinal length of intermediate model is  $L = 35 \text{ in}$ , circumferential width  $B = 16.7 \text{ in}$  (circular angle  $\theta = 12.77^\circ$ , skin radius  $R = 75 \text{ in}$ ). Intermediate model consists of outer skin, inner skin, 8 tear straps, 4 fillers, 1 stringer, 2 frames, 2 stringer ties and rivets. The outer skin, inner skin, tear straps, fillers, stringers, frames and stringer ties are modeled by 3-dimensional 4-node doubly curved shell element. At the crack area, the fine mesh have been used. The shell elements near to the cracks are about  $0.13 \text{ in} \times 0.1125 \text{ in}$ . All rivets are modeled by the spring model. The boundary condition is the displacement, which is provided by the global analysis. The displacement of nodes on the boundary of intermediate model is produced by an interface code. The displacement of nodes on the boundary of intermediate model is determined by the displacement obtained from the global analysis. The external load is the pressure 8.5 psi on the skin. The crack growth can be modeled by moving the node at crack tip. The number of nodes of intermediate model is 6180. The total number of elements is 6685. A single intermediate analysis takes about 207 sec at HP 735 workstation.

*Local analysis*

Finite element alternating method is used to analyze a two-dimensional model of a small area near MSD to obtain the stress intensity factors at the crack tips. The local model is a piece of inner skin, which contains the rivets holes 26, 27, 28, 29, 30. The local model consists of the 8 - node plane finite elements. Traction boundary conditions are obtained from the intermediate analysis.

The length of local model is  $L = 5 \text{ in}$ , height is  $H = 0.9 \text{ in}$  and thickness is  $T = 0.04 \text{ in}$ . The rivet reaction forces are applied on the surface of rivet hole and normal stresses are on the boundary of local model. It is illustrated in Fig. 1.150. The finite element mesh for the local model has only 1605 nodes and 480 elements.

**§ 1.10.3 Fatigue crack growth analysis**

The numerical solutions for the normalized Stress Intensity Factor histories of the cracks at right side of rivet hole 27 and at left side of rivet hole 28 are shown in Fig. 1.151. To estimate the fatigue life, the Paris' model is used. The Paris' Model is:

$$\frac{da}{dN} = \left( \frac{\Delta K}{C} \right)^n \quad (1.79)$$



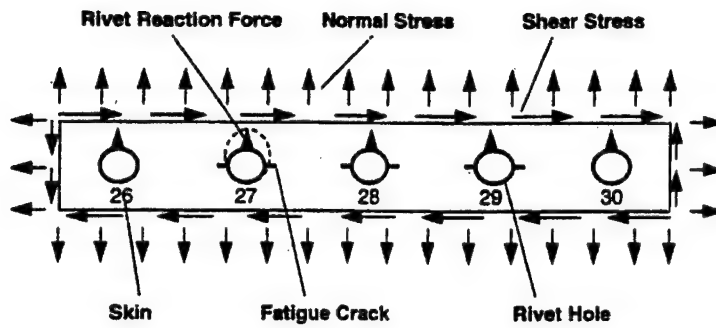


Figure 1.150: Force on Local Model

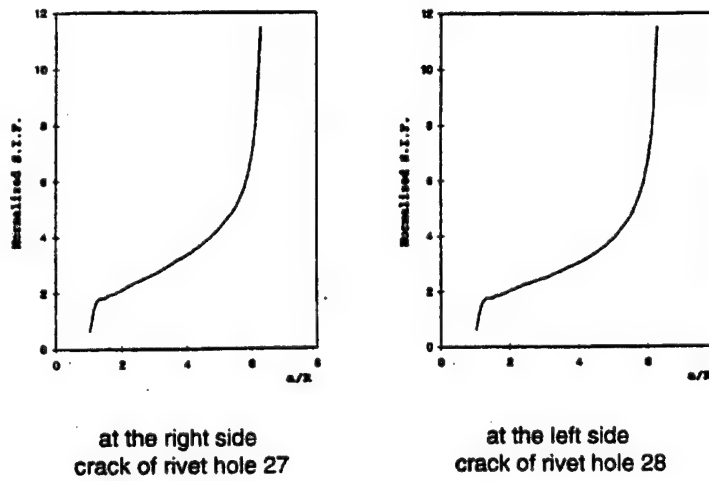


Figure 1.151: Stress Intensity Factor History of Cracks

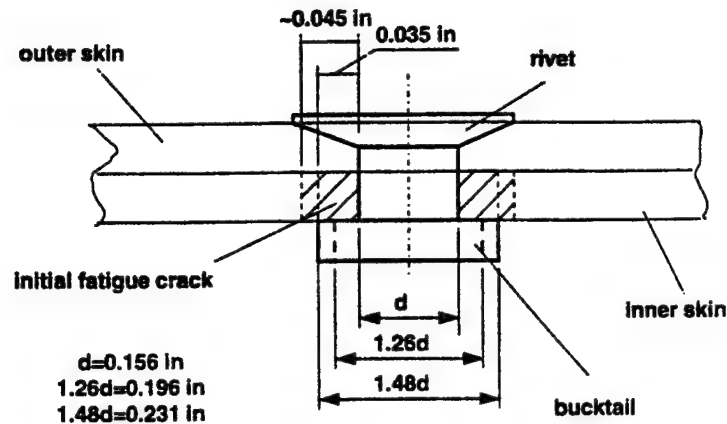


Figure 1.152: Initial Fatigue Crack in the inner skin

where  $a$  is the crack length;  $n = 6.0$ ,  $C = 0.364 \times 10^{-11}$ ; and  $N$  is the number of external load cycles.

When the crack length grows from initial fatigue crack length  $a_o$  to the link-up crack length  $a_f$ , the fatigue life can be calculated by the following equation or approximately

$$N = \int_{a_o}^{a_f} \frac{C^n}{(\Delta K)^n} da \quad (1.80)$$

or approximately

$$N = \sum_{j=1}^m \frac{C^n \Delta a_j}{(\Delta K_j)^n} \quad (1.81)$$

where  $\Delta a_j$  is the increment of crack length from initial fatigue crack length  $a_o$  to the link-up crack length  $a_f$

$$a_f - a_o = \Delta a_1 + \Delta a_2 + \cdots + \Delta a_m \quad (1.82)$$

#### § 1.10.4 Results and discussions

Before the test, the full scale fuselage panel 12 did not contain any crack. After 75,000 cycles of external loading, the rivet holes 27, 28, 29 at lower row in the inner skin were inspected for microcracks. The test report did not present crack length.

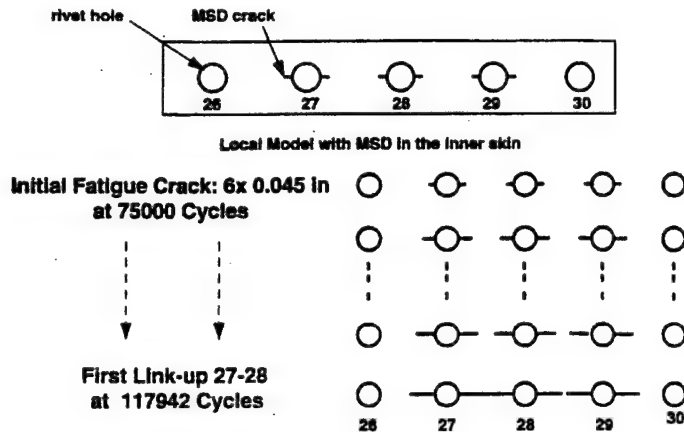


Figure 1.153: The Estimated Fatigue Life with Initial Fatigue Cracks 0.045 in

But the inspected microcrack length can be estimated from the rivet bucktail size. In the test report, the rivet bucktail diameters were manufactured to recommended 1.4d specification. The rivet bucktail diameters have been controlled in the range between the minimum 1.26d and the maximum 1.48d in fatigue test panel 12, where d is the rivet diameter ( $= 5/32 \text{ in}$ ). The microcrack length, i.e. initial fatigue crack detectable length are estimated about 0.045 in to 0.05 in ( see the Fig. 1.152). At 98782 cycles of loading, cracks at rivets 36-38, 48-50 were inspected.

The test report shows that the cracks between the rivet hole 27 and 28 is link-up at 114938 cycles of loading. The computational estimated loading cycles from the initial fatigue cracks 0.045 in ( 75000 cycle ) to local failure, 27-28 link-up are 42942 cycles by using the methodology presented in this analysis. Since cracks at rivets 36-38, 48-50 were inspected at 98782 cycles of loading, the cracks at rivets hole 36-38, 48-50 are considered when the crack length at rivets hole 26-28 are 0.06 in . The fatigue life of fuselage panel is 117942 cycles. The difference from the test result is 2.6%. ( Fig. 1.153 ). If the initial fatigue crack length are considered to be 0.05 in , the estimated fatigue life is 113389 cycles. The difference from the test result is 1.3 %. (Fig. 1.154) Thus, the estimated fatigue life excellently agrees with the test result. It shows that the fatigue life estimation methods based on FEAM and computer codes are effective.

Another case, in which the cracks length at rivets 26-28, 36-38, 48-50 started

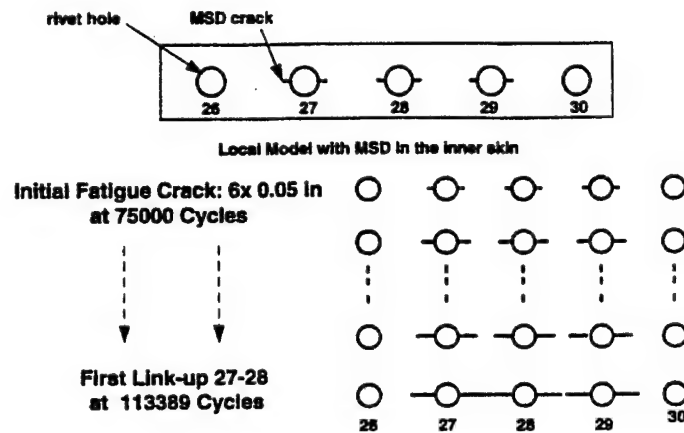


Figure 1.154: The Estimated Fatigue Life with Initial Fatigue Cracks 0.050 in

at 0.045 in is considered in this analysis. In this case, the estimated fatigue life is 108339 cycles. The fatigue life reduce 8% from the above estimated fatigue life 117945 cycles. This result shows that more initial fatigue cracks will reduce the fatigue life of structure.

### § 1.11 Residual Life and Strength Estimates of Aircraft Structural Components with *MSD/MED*

The Industry Committee on Widespread Fatigue Damage has identified about 15 different aircraft structural details that are susceptible to widespread fatigue damage. These include:

1. Longitudinal skin joints, frames, and tear straps (*MSD, MED*)
2. Circumferential joints and stringers (*MSD, MED*)
3. Stringer cutouts in frames at successive locations in the fuselage (*MED*)
4. Aft pressure dome outer ring and dome web splices (*MSD, MED*)
5. Other pressure bulkhead attachments to the skin, (i.e. web attachment to stiffener and pressure decks)
6. Stringer to frame attachments (*MED*)

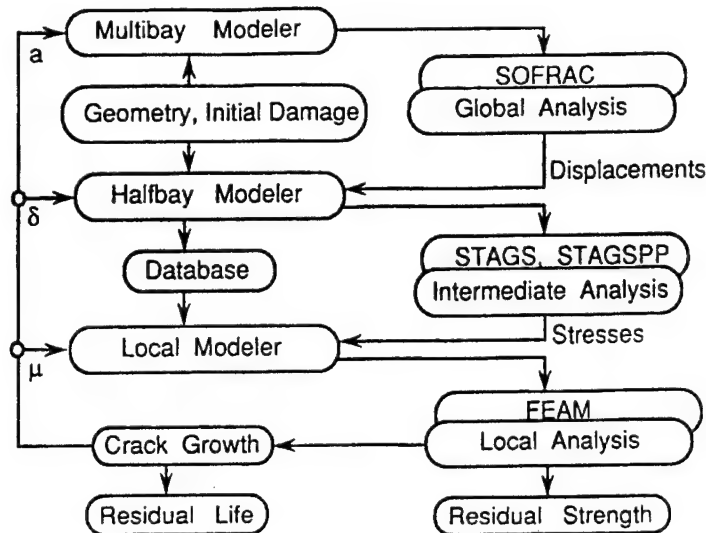


Figure 1.155: Computational procedure for analysis of MSD in Structures

7. Window surround structure
8. Over wing fuselage attachments (*MED*)
9. Latches and hinges of nonplug doors
10. Skin at runout of large doubler (*MSD*) in the fuselage, wing or empennage
11. Chordwise splices (*MSD*, *MED*)
12. Rib to skin attachments
13. Stringer runout at tank end ribs
14. Spar cap/web (*MSD* multiple cross-section).

This section presents the generic computational framework for the analysis of the above mentioned structural components with wide-spread fatigue damage. As a typical illustration of the developed generic methodology, this section presents an investigation of *MSD* and *MED* at a stringer – frame junction of a pressurized fuselage stiffened shell panel.

### § 1.11.1 *Computational framework*

#### *Analysis of Multi-Site Damage*

For the analysis of structural components with *MSD*, Fig. 1.155 describes the computational procedure. Starting from the geometric and the initial damage database, the Multibay modeler generates the global model that is fed into the FEM code SOFRAC for global analysis. The Halfbay modeler generates the finite element model based on same initial geometric and damage information, with boundary conditions as prescribed displacements, extracted from the solution of SOFRAC. At this stage, another set of files is also written, containing information necessary to post process the output of STAGSPP and generate the local model. The local modeler picks up the necessary information from the output of Halfbay Modeler and STAGSPP, generate the local model and feeds into the FEAM. The FEAM code is capable of handling multiple cracks of arbitrary lengths. This local analysis gives the cracktip parameters for multiple cracks, which are now used to estimate the residual strength and crack growth rates. The cracks was grown at this stage with net ligament yield as the linkup criterion (Research is now being completed to use  $T^*$  as the link-up criterion). For very small crack growth, local analysis is performed with updated damage information. If the crack growth is large or a crack linkup occurs, the damage is updated at the intermediate analysis level. For substantial crack growths, the global analysis is redone. This procedure simulates the crack growth and provides with information about residual life. Experience has shown that for every 5 stages of local analysis, intermediate analysis needs to be done and for every 5 stages at intermediate analysis (25 local analyses), there is a requirement for a fresh global analysis.

#### *Analysis of Multi-Element Damage*

The modular nature of the subprocedures and their interfacing through regular ASCII files, lends itself to various possibilities. One of them is the handling of structural components with *MED*. The Halfbay Modeler generates database for multiple local analyses, each local zone covering a damage which can be a single crack or an *MSD*. The Local Modeler generates multiple models and these are now be analyzed independently, using. FEAM. The cracks are grown in each of these analyses independently. Whenever required, the Halfbay Modeler can integrate the current damage configuration and perform fresh intermediate analysis. Fig. 1.156 explains this procedure pictorially. The methodology at and above the level of intermediate analysis in the hierarchy remains same as before. Since the FEAM local

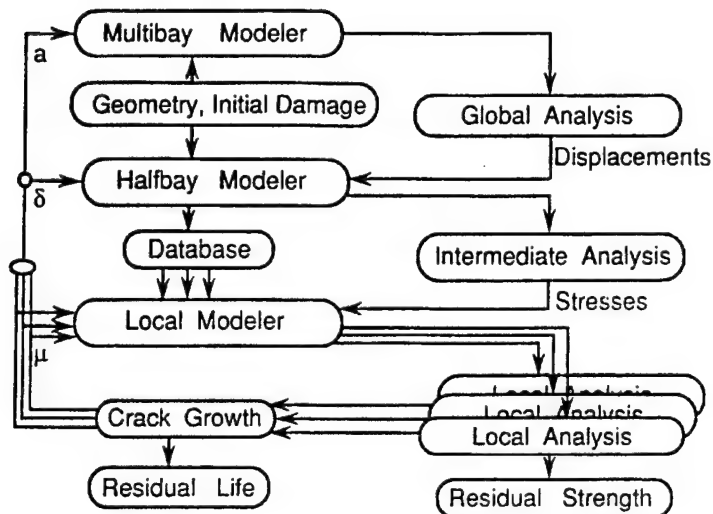


Figure 1.156: Computational procedure for analysis of MED in Structures

analyses can handle multiple cracks, this procedure has the power to resolve situations where *MSD* exists in neighboring elements, viz., *MSD* as a subset of *MED*.

#### *Analysis of problems with bending*

For the analysis at the local level, if there is a significant bending involved, the Halfbay Modeler can generate two sets of information, one for inplane and one for bending problems. The local modeler will generate two models which will go independently into two different Finite Element Alternating codes. The crack tip parameters for the two loading situations will then be integrated to evaluate the residual strength and the crack growth rates. This methodology, presented in Fig. 1.157, depends upon FEAM for cracked plate bending problems.

The power of all these procedures emerges from the fact that a wide range of problems with widespread fatigue damage can be handled. Multiple cracks can grow irrespective of where they are in the substructure. The efficiency has been achieved by automating the procedures to an extent where more than half a dozen modules work from a single set of initially generated input files.

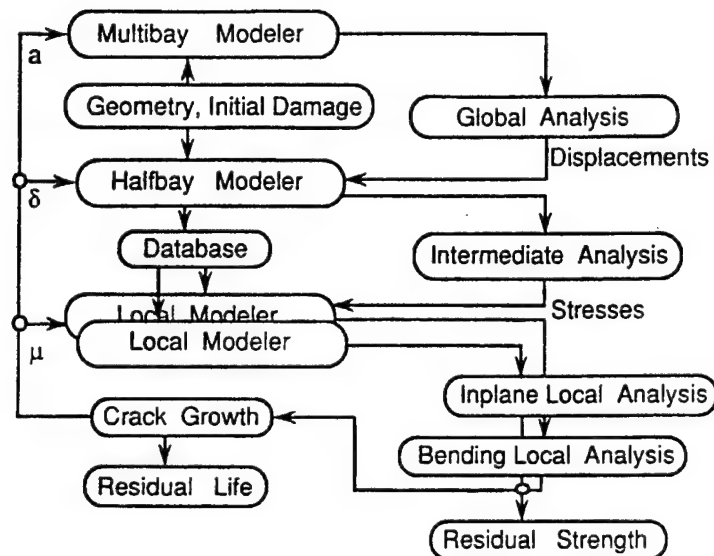


Figure 1.157: Computational procedure for analysis of MSD/MED with significant bending

### § 1.11.2 An example computation: MSD/MED at a frame stringer junction

We now employ the above described methodologies to analyze a situation of *MSD* and *MED* at the frame stringer junction in a typical narrow body fuselage panel, to demonstrate the potential of the developed computational procedure.

Consider an airliner fuselage formed by 0.036" thick, Al 2024-T3 shell, of radius 74" and stiffened by 'Z' section frames 20" apart, 2" × 0.036" tear straps at each frame location and 'Z' section stringers 9.25" apart, all of them attached with fasteners, 5/32" in diameter spaced at 1". The stringers run through the cutout in the 'L' section shear clips which attach the frames to the skin through the tear strap. The internal pressure in the fuselage is 9.0psi.

For the purpose of global analysis, we consider a multibay panel of 5 frames and 9 stringers. A typical deformed finite element model from SOFRAC, (approx 15,000 degrees of freedom, magnification = 5), is shown in Fig. 1.158. On an HP workstation 7000 900 series, the CPU time for the problem of this size is about 10 minutes.

For an intermediate analysis, a section of this consisting of a single frame, shear clip & tear strap and 3 stringers is modeled. Fig. 1.159 shows an exploded view of a



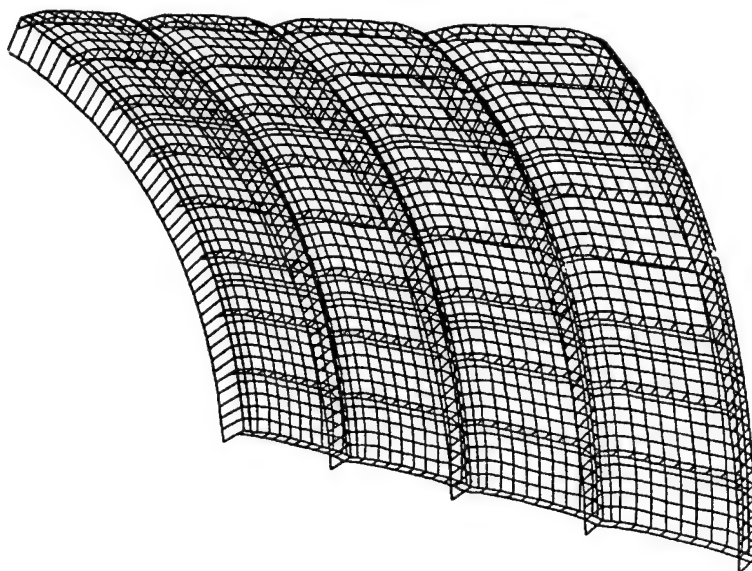


Figure 1.158: Deformed View of the Global Modal of  $4 \times 8$  Bays of Fuselage Panel

typical deformed FE model (approx 20,000 dof, magnification = 5). This problem takes about 15 minutes on an HP workstation.

The local model consists of a flat rectangular cracked sheet and depends upon the type of damage being analyzed. It takes approximately 3 minutes per crack tip for the local analysis to be complete. The damage is considered in various forms and is categorized in the following three sets.

#### *Multi-Site Damage in the skin*

Consider the situation of an *MSD* cracking in the skin at the row of fasteners joining the skin and the central stringer. Let the initial crack configuration-consist of 5 cracks of length 0.125" on both sides of the fasteners, along the row of fasteners, at a location directly below the central frame. This location is marked by 'A' in Fig. 1.159. This situation was run through the procedure of Fig. 1.155 and it was found that the first linkup of cracks occurs at 8,920 fuselage pressurization cycles. The same *MSD* situation was analyzed with the tear strap fully cracked at the same location. The type of the damage considered in the tear strap is apparent from the Fig. 1.159. The effect of broken strap is to reduce the life to only 2,518 cycles (about 28%). This analysis is presented graphically in Fig. 1.160 The analysis is

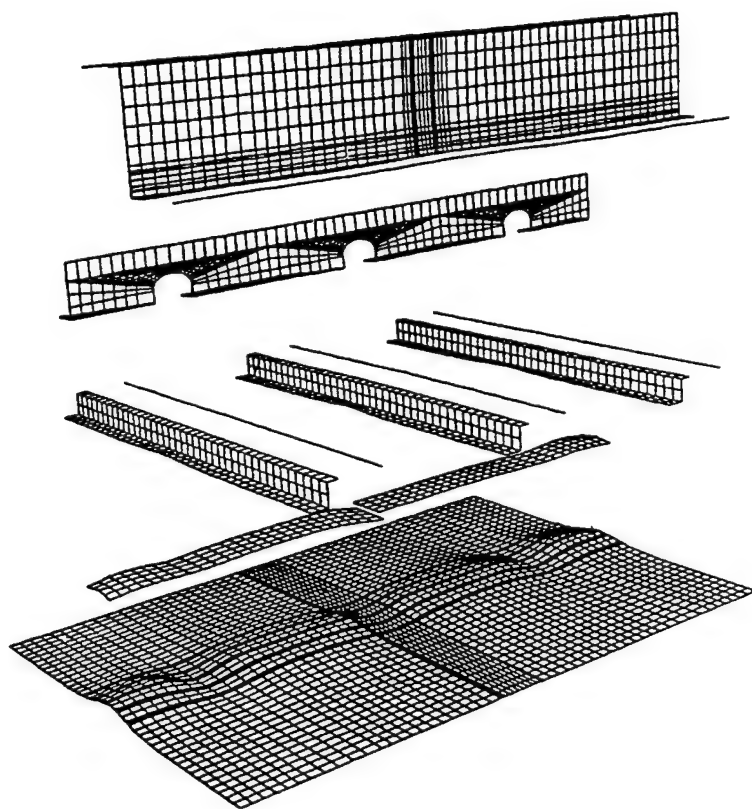


Figure 1.159: Exploded Deformed View of the Intermediate Model of  $1 \times 3$  bays of fuselage panel

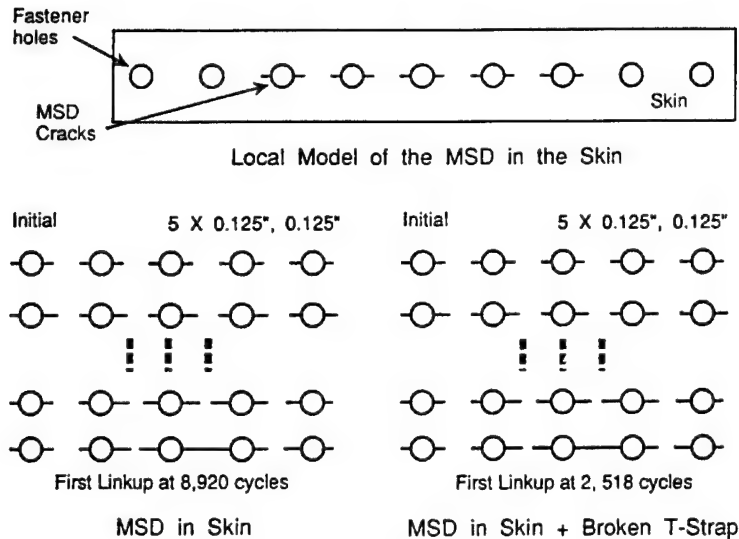


Figure 1.160: Analysis of MSD in the Skin

carried out only upto first linkup as it has been observed [Park, Singh, Pyo, and Atluri (1994)] that the first linkup is virtually the end of the life of a panel with *MSD*. A lot of other damage scenarios with *MSD* can also be analyzed in a similar manner.

#### *A crack in the frame*

Consider the situation of a single crack in the frame, emanating from a fastener, running normal to the row of fasteners joining the frame and the shear clip, located directly above the cutout in the clip through which the central stringer runs. This location is marked by 'B' in Fig. 1.159. Initially, let the crack lengths be 0.122" & 0.228" respectively towards & away from the shear clip. The crack lengths are measured from the hole center to the crack tip, and have been chosen arbitrarily. The fatigue analysis is done, as per the procedure described in Fig. 1.155, upto a situation where the plastic zone size ahead of the lower crack tip (towards the shear clip) touches the flange of the frame. This corresponds to a crack length of about 0.372". The scenario is presented in Fig. 1.161.

The above described growth of the crack is found to take 451,811 cycles of fuselage pressurization. But the situations gets suddenly worse if any of the other

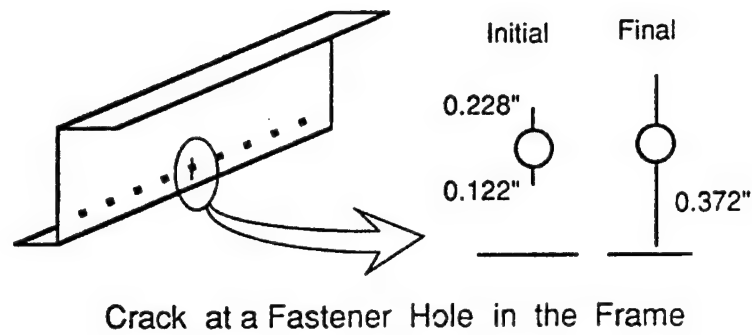


Figure 1.161: Analysis of a Single Crack in the Frame

Table 1.16: Effect of damaged elements on crack growth in frame

Tear strap	Shear Clip	Skin	Cycles
intact	intact	intact	451,811
broken	intact	intact	4,476
intact	broken	intact	2,172
broken	broken	intact	284
broken	broken	MSD	268
broken	broken	5" crack	84

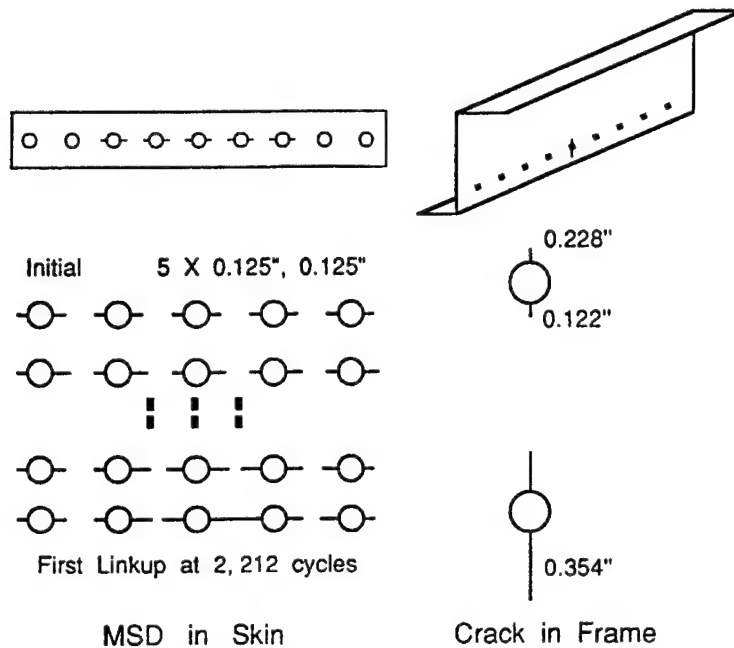


Figure 1.162: Analysis of MED in the Skin and the Frame

stiffening elements are damaged. The same crack grows about 100 times faster with a broken tear strap, about 200 times faster with a broken shear clip, about 1600 times faster with both strap and clip broken. Cracking in the skin further speeds up the crack growth. This is presented in Tab. 1.16. Although, in actual case, the *MSD* or the lead crack in the skin will grow as the crack in the frame grows, but that is not modeled in this particular example, and is looked at in the following subsection.

#### *Multi-Site Damage in the skin and a crack in the frame*

Consider now a situation of Multi-Element Damage with a crack in the frame, *MSD* in the skin and a broken tear strap. The initial crack configuration corresponds to the combination of initial *MSD* situation with a fully cracked tear strap and the initial crack configuration in the frame analyzed in the previous two subsections. The *MSD* cracking in the skin and the crack in the frame are grown by running two independent models at the local level, as described in Fig. 1.156. The first

linkup of *MSD* in the skin occurs at 2,212 cycles. The analysis is stopped at this stage. Comparing this with results of Fig. 1.160, the crack in the frame speeds up the *MSD* crack growth by about 12%. In the mean time the lower crack in the frame had grown to a length of 0.354", as shown in Fig. 1.162. For the problem in the previous subsection, the crack in the frame had grown to this length in 2,390 cycles. This implies that the *MSD* in the skin speeds up the crack in the frame by about 8%. Thus both *MSD* in the skin and the crack in the frame are found to speed up each others growth.

The above set of examples were analyzed in less than 24 computer-man hours. This shows the power and efficiency of the developed procedures.

## § 1.12 Fatigue Growth of Surface Flaws

### § 1.12.1 Introduction

The finite element alternating method, which has proved to be an extremely efficient scheme for the accurate calculation of stress intensity factors, is augmented here by an algorithm to calculate the fatigue life, under cyclic loading, of three dimensional structural components. The advantage here is that mesh generation and computational time are considerably reduced since this finite element approach only entails an analysis of the uncracked body. These simplifications make it possible to implement a three dimensional fatigue crack growth algorithm into the alternating method. This approach has been applied here to various fatigue problems in complex aircraft components. Solutions were initially developed for constant amplitude loading and then extended to the more difficult case of variable amplitude loading.

The presence of cracks in complex three dimensional components is always a cause of concern to engineers. This is primarily due to the fact that accurate calculation of stress intensity factors, using the finite element method or some other numerical technique, has been a non-trivial task. Conventional three dimensional finite element fracture mechanics techniques require the construction of an extremely fine mesh in the vicinity of the curved crack front with a large number of elements in this region. This is likely to be very time consuming both from a mesh generation stand-point and also with regard to the computational time. Analysis difficulties are compounded in many instances due to the sub-critical crack growth that can take place under conditions of cyclic loading. The effort required to integrate a fatigue analysis directly with conventional finite element stress intensity factor calculations is prohibitive due to difficulties inherent in ensuring that the mesh must coincide

with the crack front during the growth process.

The finite element alternating method (FEAM), which has been described in Chapters II and III is an innovative computational scheme for stress intensity factor calculation that offers significant savings in time without sacrificing any accuracy. The major advantage of the alternating method is that it overcomes many of the limitations inherent in other numerical techniques. The FEAM has been implemented into a software package called SAFEFLAW<sup>3</sup>. Both two dimensional and three dimensional versions of SAFEFLAW have been developed. This section is exclusively confined to three dimensional applications. The alternating method has been successfully exploited to analyze a wide variety of engineering components including semi-elliptical surface cracks in pressure vessels and off-shore structures and quarter elliptical corner cracks in aircraft components. Motivated by a number of practical problems in the aircraft industry, several enhancements have recently been made to the FEAM. These applications involve part elliptical cracks emanating from countersunk rivet holes and quarter elliptical cracks emanating from holes in wing components. In addition, a fatigue crack growth algorithm has now been integrated with the FEAM and provision is made to consider both constant amplitude and variable amplitude loading. These enhancements are described in this section.

The aging of the commercial airline fleet is increasing the anxiety in all segments of the industry, particularly as there is a desire to operate the aircraft beyond their original design lives. Crack formation and growth in the vicinity of rivet holes in the fuselage has been identified as a serious problem. Fig. 1.163 schematically illustrates plan and elevation views of the fuselage skin in the vicinity of a countersunk rivet. The elevation section X-X shows that cracks can form in three possible initiation sites around the rivet hole, labeled A, B and C. Due to the cyclic loading on the aircraft fuselage, one or more of these cracks can grow over a period of time until the crack extends through the skin. This crack can then grow, again under cyclic loading, along the fuselage in the direction of the adjoining rivet. In some instances, this phenomenon has been observed to occur at several locations along a row of rivets and is referred to as multiple site damage. The subsequent link up of these cracks can lead to catastrophic consequences [Hendricks (1991)].

Clearly it is important to examine the fatigue crack growth of flaws emanating from the countersunk rivet hole. One of the primary objectives is to investigate the

---

<sup>3</sup>This is a trade mark of a commercial software package developed by Knowledge System, Inc. of Forsyth, GA. Further information on this software can be obtained at the email address: ksi@mylink.net

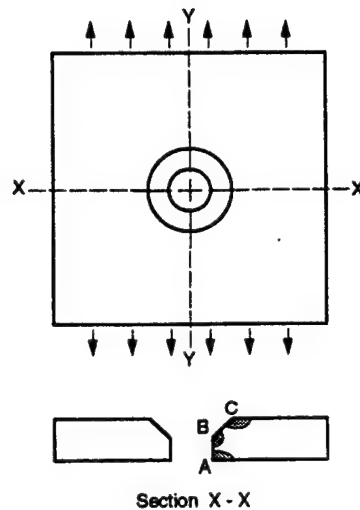


Figure 1.163: Schematic of countersunk rivet configuration

early stages of this crack growth; i.e. prior to the crack propagating through the wall of the fuselage. Thus, stress intensity factor computations and estimates of the fatigue life must be made for the cracks shown in Fig. 1.163. The crack surfaces in this instance can be assumed to be flat and have part elliptical shapes. For example, the crack at location A in Fig. 1.163 is a quarter elliptical corner crack. The sizes of the cracks at locations B and C will depend on the countersunk rivet angle,  $\alpha$ . Typically, this angle is  $40^\circ - 50^\circ$ .

A second application motivating the present work stems from the presence of cracks in the vicinity of weep holes in the wing region of the USAF C-141B aircraft. The relevant geometry is illustrated in Fig. 1.164. The cross section here is essentially an inverted T shape consisting of the lower wing skin and a riser. In some instances under flight loads, quarter-elliptical cracks were found to emanate from a small hole (called a weep hole) in the riser. The cracks were either on the top or bottom of the hole as indicated by locations D and E of Fig. 1.164 and are subject to cyclic loading. Prior to the crack breaking through the wall of the riser, the crack growth can be viewed as three dimensional. However, soon after breakthrough, the crack front becomes relatively straight and can be idealized using a two dimensional approach. The analysis work described here is focused on the three dimensional phase of the growth. Test specimens, consisting of the Fig. 1.164 geometry with appropriate end connections, were subjected to variable amplitude



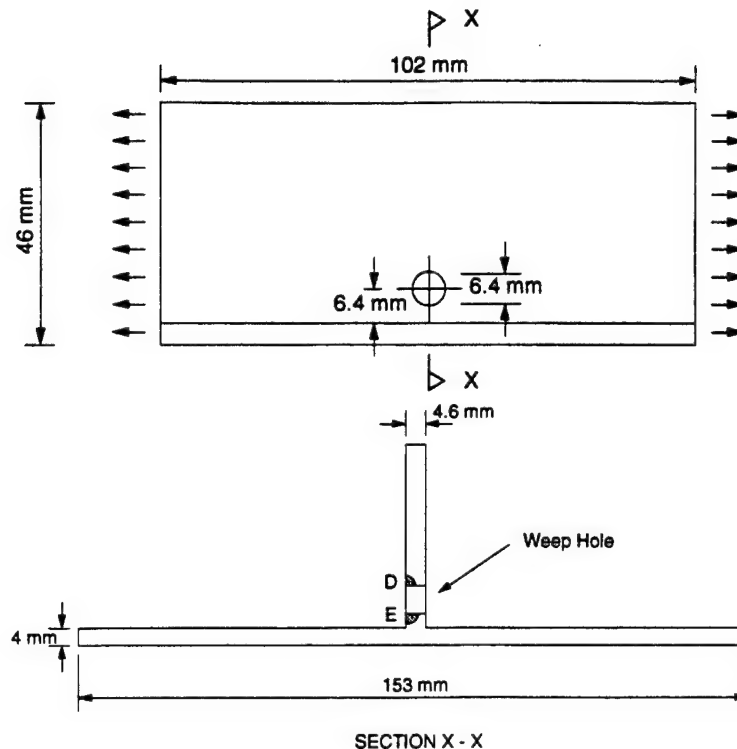


Figure 1.164: Schematic of weep hole configuration

loading normal to the crack front. Comparisons between these experimental data and the numerical analysis model are presented in this section.

The most significant feature that contributes to the simplicity and efficiency of the FEAM approach is that the finite element analysis is for the uncracked component. Thus, a relatively coarse mesh will suffice since the crack is not modeled explicitly and there is no need to have special crack tip elements. The only requirement for the mesh in this region is that an accurate representation of the uncracked stress distribution is obtained at the location of the crack. In addition, it is not necessary for the edges of the elements to conform to the curved surface of the crack front. Straight sided elements can therefore be used in this region, greatly simplifying the mesh generation effort. Because of this, the same mesh can frequently be used for cracks of different size (a big advantage in fatigue simulations) and even for cracks at different locations in a given component. These factors greatly reduce pre-processing time and computational time when compared with other numerical

techniques. For example, comparable accuracy was achieved for a rivet hole crack problem between a 90 element FEAM solution and an analysis with conventional elements containing 1430 elements [Park, Ogiso, and Atluri (1992)].

### § 1.12.2 *Cracks emanating from rivet holes*

Fig. 1.163 illustrates the geometrical complexities associated with cracks of arbitrary shape emanating from countersunk rivet holes. This section describes the modifications to the alternating method that were necessary to analyze part elliptical cracks of arbitrary shape.

#### *Implementation*

The analytical solution for an elliptical crack in an infinite solid requires the residual stresses to be defined over a complete ellipse. The crack configurations in Fig. 1.163 are only part ellipses. Consequently, to utilize the infinite body solution, it is necessary to establish a stress distribution over the entire ellipse, including the fictitious portion that lies outside the physical component. The validity of such an approach has already been established for semi-elliptical and quarter elliptical cracks [Nishioka and Atluri (1983)]. The approach for a part elliptical crack, such as at location B or C, is now described. With reference to Fig. 1.165, the stress distribution along the line O-P is extended into the fictitious portion of the second quadrant such that it remained constant in the x direction. This is illustrated by the stress distribution in the section Z-Z (Fig. 1.165). In the fictitious region  $-c < y < 0$ , the distribution remained constant in the y direction and varied in the x direction in accordance with the distribution on  $y = 0$ . Finally, in the region  $-a < x < 0$ ,  $-c < y < 0$ , the stress is constant having the value at the origin and this is consistent with the extensions into the other fictitious regions.

#### *Results*

The rivet hole configuration of Fig. 1.163 was analyzed here under the action of remote tensile loading (unit loading unless otherwise stated). Both the X-X and Y-Y axes were planes of symmetry. Although not illustrated in Fig. 1.163, this implies that there are diametrically opposed cracks in the component. Because of the two planes of symmetry, it is only necessary to analyze one quarter of the structure. A detail of the crack plane geometry is shown in Fig. 1.166 and this indicates the relative dimensions that were used in the analysis. The half width of the plate is 6.5 times the hole radius, R and the half length is 13 times the hole radius. In each

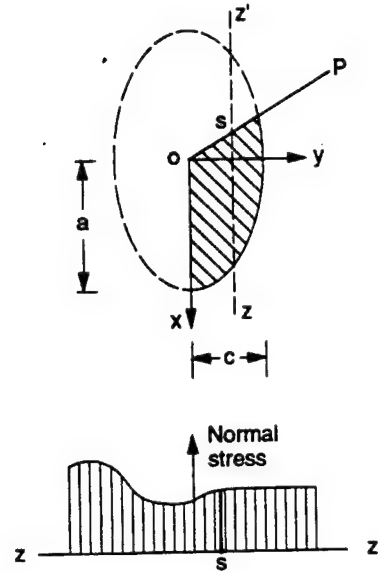


Figure 1.165: Extension of crack surface stresses to fictitious region

analysis just a single crack was considered to exist, at location A, B or C. Thus there are no multiple flaws and no interaction effects between the cracks arise in the present analysis. The finite element models consisted of conventional twenty node isoparametric three dimensional elements. All results reported in this section are plotted as a normalized stress intensity factor variation along the crack front. The crack front position is given as a function of the elliptical angle,  $\theta$ , and the sign convention for this is given in Fig. 1.166. The normalizing factor in these analyses is given by

$$K_o = \frac{\sigma_o \sqrt{\pi a}}{\sqrt{(1 + 1.464(a/c)^{1.65})}} \quad \frac{a}{c} \leq 1$$

$$K_o = \frac{\sigma_o \sqrt{\pi a}}{\sqrt{(1 + 1.464(c/a)^{1.65})}} \quad \frac{a}{c} > 1 \quad (1.83)$$

where  $\sigma_o$  is the remote tension,  $c$  the major axis and  $a$  the minor axis.

The first study investigated the convergence of the numerical solution. The results in Fig. 1.167 clearly illustrate the excellent convergence that was obtained with the FEAM. Here,  $a/t = 0.2$  and  $a/c = 0.4$  and the crack is at location A. Three analyses have been conducted using 216 elements, 372 elements and 496 elements

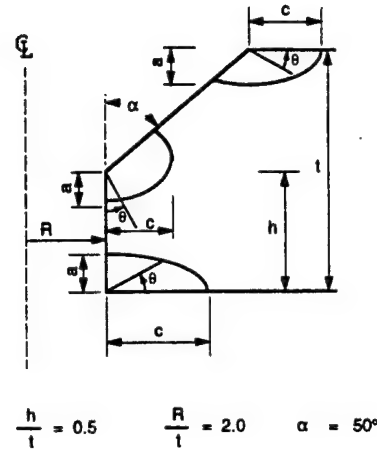


Figure 1.166: Rivet geometry detail in vicinity of crack location

(1265, 2047 and 2655 nodes respectively). The maximum variation between the three solutions is just a few percent at most. This demonstrates that accurate solutions can be obtained with the FEAM using relatively few elements.

A number of studies illustrating typical parametric results (normalized stress intensity factor as a function of elliptical angle,  $\theta$ ) for cracked countersunk rivets are shown in Figs. 1.168, 1.169 and 1.170. Note the sign convention for the elliptical angle in Fig. 1.166 differs for each crack location. The results for a crack at location B with  $a/t = 0.2$  and four different crack aspect ratios are given in Fig. 1.168. The corresponding result for  $a/t = 0.4$  is given in Fig. 1.169. Fig. 1.170 illustrates the normalized stress intensity factor variation for a crack at location C with  $a/t = 0.2$  and four different crack aspect ratios.

### § 1.12.3 Fatigue crack growth

This section describes the integration of a fatigue crack growth model into SAFE-FLAW to be used in conjunction with the FEAM. This is used here to analyze the countersunk rivet configuration under constant amplitude loading.

#### Implementation

A general form for fatigue crack growth is as follows

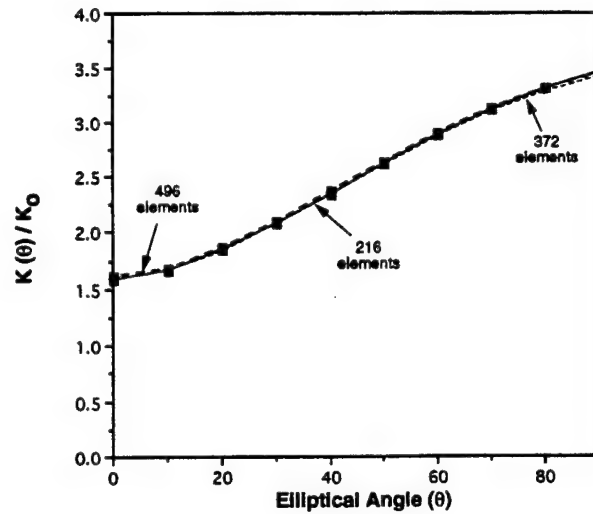


Figure 1.167: Illustration of good convergence of normalized stress intensity factor computation for crack at location A near rivet hole;  $a/t = 0.2$ ;  $a/c = 0.4$ ;  $R/t = 2.0$

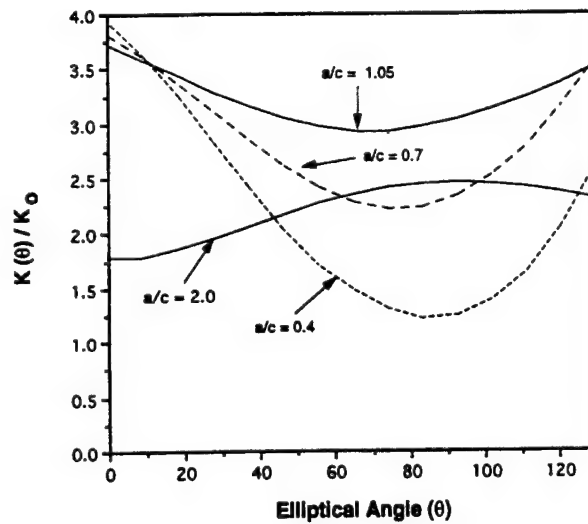


Figure 1.168: Normalized stress intensity factor variation along crack front for different aspect ratios; crack at location B near rivet hole;  $a/t = 0.2$ ;  $R/t = 2.0$

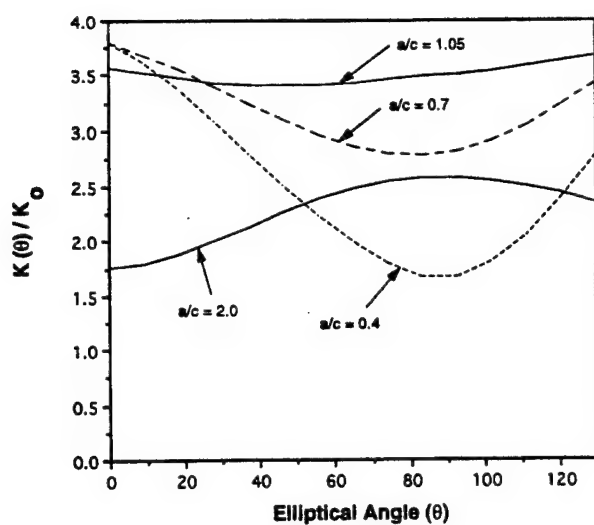


Figure 1.169: Normalized stress intensity factor variation along crack front for different aspect ratios; crack at location B near rivet hole;  $a/t = 0.4$ ;  $R/t = 2.0$

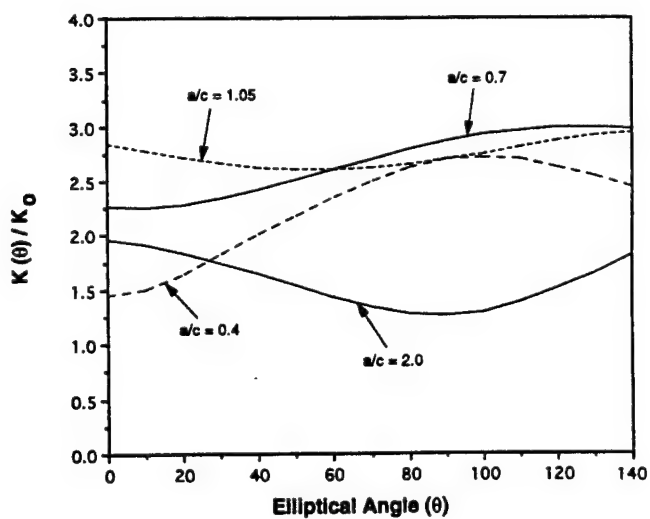


Figure 1.170: Normalized stress intensity factor variation along crack front for different aspect ratios; crack at location C near rivet hole;  $a/t = 0.2$ ;  $R/t = 2.0$

$$\frac{da}{dN} = \frac{A(1-R)^m(\Delta K)^n\{\Delta K - (\Delta K)_{th}\}^p}{\{(1-R)K_c - \Delta K\}^q} \quad (1.84)$$

where  $a$  is the crack length,  $N$  is the number of cycles for crack growth,  $R$  is the stress intensity factor ratio and  $\Delta K$  is the stress intensity factor difference. The fracture toughness of the material is  $K_c$ , the threshold stress intensity factor is  $\Delta K_{th}$  and  $A$ ,  $n$ ,  $m$ ,  $p$  and  $q$  are constants in the fatigue relation. Some of the more common fatigue relations such as Paris, Gomez, and Anderson (1961); Paris and Erdogan (1963); Forman, Kearney, and Engle (1967); Walker (1970) are special cases of Eq. (1.84). For example, the Paris relation can be obtained by setting  $p = q = m = 0$ . In the case of a part elliptical crack, the distance from the origin to the crack front varies from point to point. Here the definition of crack length is very important. When performing a fatigue calculation, such as to determine the number of cycles for crack growth, it is best to take the crack length as the major axis or the minor axis.

As a part elliptical crack begins to grow, it will generally have different growth rates in the different directions. This is to be anticipated since the stress intensity factor ( $\Delta K$ ) will vary along the crack front. Therefore the shape of the crack will change during the growth process. It is appropriate to assume that the crack will always maintain an elliptical or part elliptical shape. In this case the shape change of the ellipse will be completely described by the major and minor axis lengths. Therefore, Eq. (1.84) can be viewed as an equation that describes the change of length of the major and minor axes.

A fatigue calculation generally involves either the calculation of the number of cycles for a crack to grow a specified length or else the amount of crack growth in a given number of cycles. To calculate the number of cycles during crack extension, it is necessary to integrate Eq. (1.84) for  $N$ . The limits for this integration will represent the starting and ending crack lengths. Generally these will be the initial and final minor axis lengths. This integration is performed numerically by subdividing into a number of crack growth intervals (twenty or less is usually sufficient). This sets the minor axis growth increment for each step. The stress intensity factor distribution is calculated at each interval. Using an integrated form of Eq. (1.84), the number of cycles for this increment is calculated. Substituting this into Eq. (1.84), the major axis growth increment is calculated for this step. While the minor axis increment is constant for each step, the major axis increment is generally different for each step. It is in this manner that changes in the crack aspect ratio during crack growth can be considered. The total number of cycles is obtained by summing the values from each step. This computational approach is valid for constant amplitude

loading but is not directly applicable to variable amplitude loadings. An approach that considers the latter is presented in the next section. A somewhat similar procedure can be used to calculate the amount of crack growth when the number of load cycles is known.

Fatigue analyses using conventional finite element techniques can be very laborious since a separate mesh must be generated for each crack configuration and the changing aspect ratio will then add to the complexity of this analysis. Fortunately, the FEAM overcomes this difficulty. Since the finite element mesh does not have to explicitly model the crack front, it is sufficient to use just a single mesh for the entire fatigue simulation even though the crack size increases during the growth process. The only requirement is that the finite element mesh has sufficient resolution for the uncracked stress distributions in the vicinity of the crack location. In addition to eliminating the manual effort in recreating the finite element mesh, resolution procedures can be used at the calculation stage, necessitating just a single reduction of the element stiffness matrix. Therefore the alternating method offers several distinct advantages to efficiently carry out fatigue crack growth calculations for complex three dimensional components.

### Results

To illustrate these constant amplitude fatigue crack growth concepts, the counter-sunk rivet configuration of Fig. 1.163 was subjected to a remote tensile cyclic load with a single crack at location A. The maximum load was 69 MPa and the minimum value was zero. The half width of the plate is 43.4 mm and the half height of the plate is 70.6 mm. The plate thickness,  $t$ , was 1.73 mm with the hole radius being 5.18 mm. The initial minor axis length was 0.173 mm and  $a/c = 2$  with reference to Fig. 1.166. The crack was allowed to grow such that the minor axis doubled in length to 0.346 mm. The Paris growth relation was used in this case (ie.  $m = p = q = 0$ ) and this is given by.

$$\frac{da}{dN} = A (\Delta K)^n \quad (1.85)$$

The constants in the Paris relation were  $n = 4$  and  $A = 1.8 \times 10^{-8}$  mm/cycle  $(\text{MPa m}^{1/2})^{-4}$ . These values are typical for the 2024-T3 aluminum used for aircraft fuselages. Fig. 1.171 shows the stress intensity factor variation (not normalized) along the crack front as a function of the elliptical angle at three values of the major and minor axis lengths during crack growth. In the actual calculations, the stress intensity factors were calculated at nine aspect ratios during the growth process.



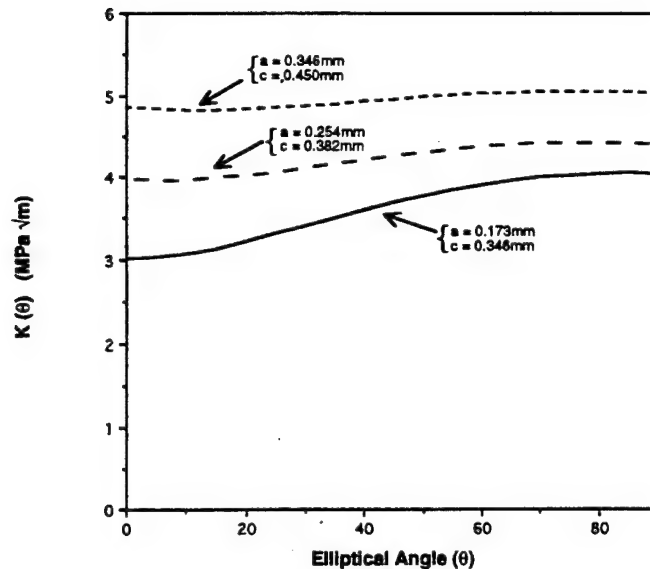


Figure 1.171: Stress intensity factor variation with elliptical angle with increasing crack size during fatigue for crack at location A near rivet hole

The fatigue life calculation then gave 25,110 as the number of cycles for the crack minor axis to double in length. In this period, the major axis increased to 0.450 mm. Thus the crack shape changed from an initial aspect ratio of 2 to a final aspect ratio of 1.3.

#### § 1.12.4 Variable amplitude loading

In many practical applications, engineering components are subjected to variable amplitude loading. A computational strategy to calculate the fatigue behavior under this loading category is now outlined here for the C-141B weep hole configuration of Fig. 1.164. However this approach can also be used for any other cracked component subject to variable amplitude loading.

#### Implementation

The complexities associated with fatigue analyses under variable amplitude loading have not been included in SAFEFLAW. Consequently, it was necessary to link this code with NASA-FLAGRO to facilitate the calculation of the fatigue life under

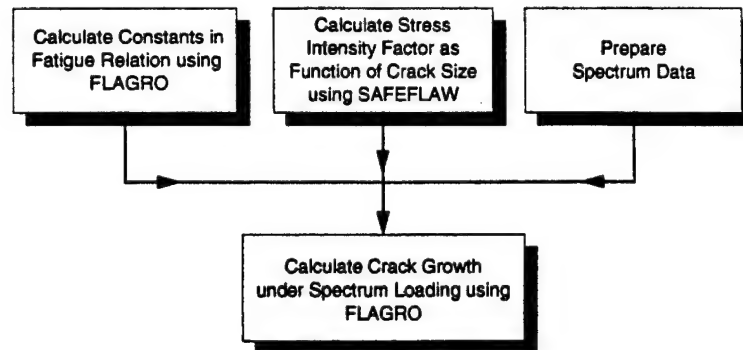


Figure 1.172: Flowchart illustrating approach to variable amplitude loading analysis

this loading category. NASA-FLAGRO has many advanced fatigue features that are ideally suited to variable amplitude loading. However, while FLAGRO contains built in solutions to a number of commonly occurring fracture configurations, it does not include complex configurations such as the weep hole. Thus, it is necessary to integrate the capabilities of NASA-FLAGRO and SAFEFLAW to obtain the solution.

Fig. 1.172 illustrates the various elements involved in the analysis for variable amplitude loading. The steps in this analysis are as follows:

1. FLAGRO is used to calculate the constants in the fatigue crack growth relation.
2. Stress intensity factors are calculated for a wide range of crack sizes using SAFEFLAW.
3. Spectrum loading data are prepared.
4. The results from the first three steps serve as input to FLAGRO in the computation of the fatigue life.

These steps are now explained in detail. This scheme is valid for variable amplitude loading acting on an arbitrary component. However, the discussion here focuses on the application to a corner crack emanating from a weep hole in a C-141B aircraft.

Firstly, experimental fatigue crack growth data for the C-141B aircraft aluminum (7075 T651) were available and these were used to determine the constants

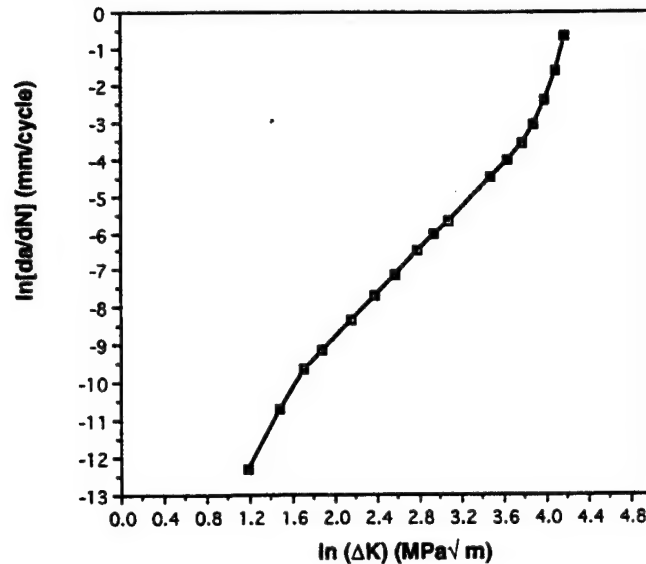


Figure 1.173: Data used to determine constants in fatigue crack growth relation

in the fatigue crack growth relation. The Forman model for fatigue was used here and crack closure was allowed. Since there was very little load reversal (negative end levels) for the flight load data in this example, crack closure effects were not very significant in this instance. The Forman relation is obtained from Eq. (1.84) by setting  $m = p = 0$  and  $q = 1$ . The Forman relation is given by:

$$\frac{da}{dN} = \frac{A(\Delta K)^n}{(1-R)K_c - \Delta K} \quad (1.86)$$

The material constants were calculated using FLAGRO. The  $(da/dN)$  vs.  $\Delta K$  data used to determine these constants are given in Fig. 1.173. The yield stress was taken as 448 MPa, the plane strain fracture toughness as 29.7 MPa m<sup>1/2</sup> and the wall thickness in the riser was 4.57 mm. These data resulted in a critical stress intensity for fracture of 63.3 MPa m<sup>1/2</sup>. This quantity is of course thickness dependent. The constants  $A$  and  $n$  were determined to be  $4.31 \times 10^{-5}$  mm/cycle (MPa m<sup>1/2</sup>)<sup>-2.531</sup> and 2.531 respectively.

In step 2, these constants were then input into SAFEFLAW and the weep hole fracture test configuration was analyzed. The purpose of these analyses is to obtain the stress intensity factor distribution for the range of crack sizes that are likely to be encountered during fatigue crack growth. Curve fits for these data will then be used

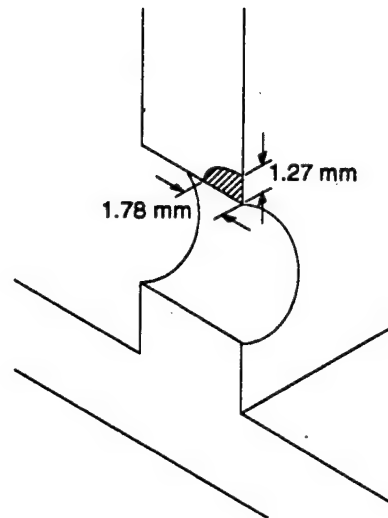


Figure 1.174: Detail of crack emanating from weep hole vertically up the riser

in step 4 to calculate the fatigue life under variable amplitude loading. Because of symmetry about the crack plane, only one half of the test configuration need be analyzed. The geometrical dimensions for the specimen are given in Fig. 1.164. A uniform load of 100 MPa was applied at both ends of the specimen. In reality, this is just a reference value as the actual flight spectrum loads will be applied in the step 4 analyses. A quarter elliptical crack was assumed to be located on the top of the hole and this would subsequently grow along the bore and up along the riser. The initial crack dimensions were 1.78 mm along the bore and 1.27 mm in the radial direction (up the riser), which is typical of the component under test. A detail of this crack configuration is shown in Fig. 1.174. A further set of analyses were conducted for a crack on the lower end of the hole and growing down the riser towards the wing skin. This analysis is also described in the results section. Comparisons are made between the latter and some test data.

For the crack on the top of the weep hole, two separate finite element meshes were used in the analysis, having 596 and 868 twenty node block elements respectively. Fig. 1.175 indicates that convergence has been obtained in view of the very good agreement between the two sets of results with the maximum discrepancy being four percent at most. Here the stress intensity factor is given as a function of the elliptical angle where this angle is measured from the bore of the weep hole. With the good agreement between the two meshes, it was decided to use the smaller

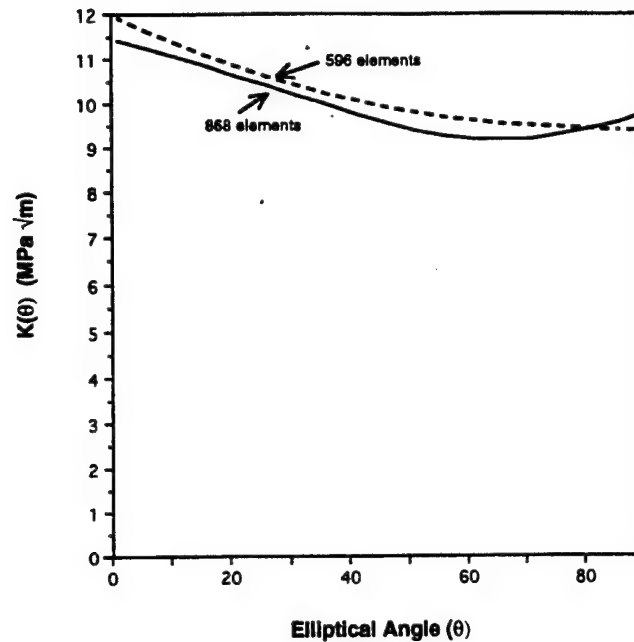


Figure 1.175: Illustration of good convergence of stress intensity factor computation for weep hole crack

mesh in all subsequent calculations. A typical stress intensity factor computation with this model took 11 minutes on a HP workstation.

The analysis focused on growth of the crack along the bore and the three dimensional phase was considered to be complete when the crack reached the end of the bore and broke through the riser. The loading in the SAFEFLAW computational simulation was limited to constant amplitude with a maximum value of 100 MPa and  $R = 0$ . This fatigue load was applied until the crack grew along the bore through the riser. Clearly this was different from the spectrum loading in the actual tests. The important point however is that the change of shape of the quarter elliptical crack during the growth process is relatively independent of the type of loading (constant amplitude or spectrum). Thus the analysis calculates the correct change in crack shape and the correct stress intensity factors during growth but makes no attempt to calculate the number of cycles for growth. It is necessary to use FLAGRO to perform the latter computation. Specifically, the stress intensity factors at the tips of the major and minor axes have been computed for different crack sizes.

Table 1.17: Computed stress intensity factors and the major and minor axis locations during fatigue crack growth of constant amplitude 100 MPa load

Major Axis (mm)	K (MPa m <sup>1/2</sup> )	Minor Axis (mm)	K (MPa m <sup>1/2</sup> )
1.93	11.78	1.35	9.37
2.38	12.50	1.61	10.20
2.81	13.55	1.86	10.58
3.25	13.93	2.12	11.27
3.67	14.64	2.37	11.94

These data are given in Tab. 1.17 for the crack emanating from the top of the weep hole.

Step 3 involves preparation of the flight load spectrum. The loading spectrum was used for both the test and the numerical simulation. These data are comprised of peak-valley pairs representing six 504.5 equivalent flight hours passes or 3027 total flight hours. In the tests, this spectrum is repeated on a number of occasions resulting in through wall crack growth up the riser or growth into the wing skin depending on the initial crack location. The number of peak-valley pairs is somewhat different for each pass in order to account for cycles that occur as little as once in 3027 flight hours and for an accumulation of fractional occurrences in the correct sequence. The data has been filtered such that stress differences of less than 14 MPa were filtered out. In the data, the highest peak was 123.3 MPa. The Forman relation for fatigue crack growth is likely to give better results than the Paris relation for this spectrum as the R ratio is relatively large for many of the cycles. The Paris relation will generally over predict the fatigue life in this instance.

### Results

In step 4, FLAGRO uses the major and minor axis stress intensity factor results from SAFEFLAW to calculate the number of cycles for the crack growth process under variable amplitude loading. Cubic spline curve fits of these two sets of data are developed and these are input into FLAGRO. The loading in this instance is the

Table 1.18: Computed major and minor crack lengths during fatigue crack growth as a function of equivalent flight hours (C-141B spectrum loading)

Equivalent Flight Hours	Major Axis (mm)	Minor Axis (mm)
0	1.78	1.27
504.5	2.40	1.65
1009	3.19	2.14
1513.5	4.18	2.79
2018	Breakthrough	

flight load spectrum that was also used in the experimental work. The constants in the Forman relation, as described above, are also used here. The number of cycles for crack growth under the spectrum loading can then be calculated. This relatively simple and straightforward approach for spectrum loads is valid since, as expected, the predicted crack shape change is relatively independent of the loading. The results are presented in Tab. 1.18 where major and minor crack lengths are given as a function of equivalent flight hours. Between 1513 hours and 2018 hours, the crack (major axis) grows to the end of the bore and through the riser. This marks the end of the three dimensional stage of the crack growth. The subsequent analysis of through wall crack growth up the riser is essentially two dimensional. This was not considered in the present effort but would allow a more extensive comparison with the experimental data.

A similar coupled SAFEFLAW/FLAGRO analysis was carried out for a crack emanating from the bottom of the weep hole and propagating down the riser towards the wing skin. Limited comparison was possible between these data and a weep hole test specimen referred to as RN0001 [O'Donoghue, Nishioka, and Atluri (1982)]. In this case, the initial major axis along the bore is 1.73 mm while the initial minor axis into the riser is 1.45 mm as in test RN0001. Tab. 1.19 gives the SAFEFLAW computed stress intensity factors (596 elements) at the tips of the major and minor axes of this crack as a function of crack lengths for a nominal maximum load of 100 MPa. These data, along with the flight spectrum loading and the constants in the Forman relation, are input to FLAGRO and the number of cycles

Table 1.19: Computed stress intensity factors and the major and minor axis locations during fatigue crack growth of constant amplitude 100 MPa load

Major Axis (mm)	K (MPa m <sup>1/2</sup> )	Minor Axis (mm)	K (MPa m <sup>1/2</sup> )
1.73	12.23	1.45	8.44
2.08	12.30	1.62	9.15
2.39	12.68	1.76	9.50
2.69	13.29	1.92	9.67
3.03	13.48	2.06	10.18
3.33	13.86	2.21	10.28
3.64	14.26	2.35	10.69
3.95	14.58	2.50	10.90
4.25	15.32	2.65	11.18



taken for the crack to propagate along the bore of the hole is calculated. Tab. 1.20 gives the relevant crack lengths as a function of flight hours. Thus breakthrough of the riser is predicted to occur between 1513 and 2018 hours. The experimental data from test RN0001 however predicted breakthrough between 3027 and 6054 hours; about twice the length of the computed lifetime. A more precise test measurement was not available. It must be noted however that direct comparison is not possible as some details of the test configuration and relevant material and geometric parameters were not fully known.

Several reasons are likely to contribute to discrepancies that exist between the computational model and the test data. A difficulty with the data used to establish the growth rate constants is that it was generated for the case of  $R = 0$ . Much of the actual spectrum loading is for much higher values of  $R$  such as  $R = 1/2$ . Further, the constants in the fatigue crack growth relation came from a planar test specimen where properties such as the fracture toughness are thickness dependent. The applicability of these data to a three dimensional configuration may not be strictly correct. In addition, there appeared to be some difficulty in obtaining a uniform load over the specimen cross section in the experimental work. Thus, the actual load experienced by the specimen in the crack region may be different to that applied in the computational model.

In a further effort to check the accuracy of the numerical approach, an analysis was carried out using FLAGRO directly for a corner crack emanating from a hole in a rectangular plate. This geometry, particularly in the vicinity of the crack front, is similar to the weep hole configuration for a crack emanating from the top of the hole. In this analysis, the spectrum loading and fracture properties are identical to that described earlier. However, the stress intensity factors in this instance come from a well validated pre-existing solution that is already contained in FLAGRO. This analysis gave stress intensity factors that were typically 5% different from SAFEFLAW and the number of cycles for crack growth differed by less than 20% from the coupled SAFEFLAW/FLAGRO analysis presented above. This agreement is highly encouraging in view of the fact that the geometries are slightly different and lends further credibility to the combined SAFEFLAW/FLAGRO approach that has been used.

#### § 1.12.5 Discussion

The finite element alternating method has been applied here to calculate stress intensity factors for cracks emanating from rivet holes in aircraft fuselages. Fatigue calculations have also been carried out. The FEAM is ideally suited to performing

Table 1.20: Computed major and minor crack lengths during fatigue crack growth as a function of equivalent flight hours (C-141B spectrum loading)

Equivalent Flight Hours	Major Axis (mm)	Minor Axis (mm)
0	1.73	1.45
504.5	2.38	1.75
1009	3.19	2.13
1513.5	4.14	2.61
2018	Breakthrough	

these calculations and offers significant advantages when compared to other analysis techniques. This is primarily due to the fact that the finite element model is for the uncracked component and it is not necessary to explicitly model the crack front. Therefore a large number of elements is not required, reducing both the pre and post processing effort in addition to the computation time. Another major advantage is that the same mesh can be used to analyze cracks of different size, clearly beneficial in the case of fatigue.

The methodology described here can be easily used for three dimensional fatigue crack growth under spectrum loading in components of complex shape. FLAGRO and SAFEFLAW are combined to obtain the solution to problems that are beyond the individual scope of either code; FLAGRO is limited to a set of predefined 3-D configurations while SAFEFLAW is restricted to constant amplitude loading. Therefore the methodology exploits the principal features of the two packages; superior fatigue crack growth capabilities in FLAGRO and efficient stress intensity factor calculation for complex three dimensional structures with SAFEFLAW. These developments now make three dimensional fatigue calculations a relatively simple task.

The FEAM also addresses other aspects relating to crack growth in aircraft components. The schematic of Fig. 1.163 indicates a number of possible crack initiation locations. In each of the analyses reported earlier, it was assumed that only one crack existed in the initiation region. It is plausible however that cracks might co-exist; for example at locations A and B. In this instance, the interaction effects

can become important resulting in stress intensity factor amplification. The technology for this has already been included in the alternating method [O'Donoghue, Nishioka, and Atluri (1982)]. Remote tensile loads were assumed to act on the fuselage in the cases presented here. Additional loads can result from rivet bearing pressure acting on the edges of the hole. These loads can have a significant influence on the stress intensity factors. An approach that considers rivet bearing pressure has been developed for SAFEFLAW but the results have not been reported here.

### **§ 1.13 Composite Patch Repair Technology**

In this section, the problems of composite-patch repair of (i) center and edge-cracked panels loaded in the far field; and (ii) cracks emanating from pin-loaded fastener holes are examined in thorough detail. The effects of various non-dimensional design parameters on the reduction in the stress-intensity factors near the crack-tip are determined, and are presented in the form of design charts. Both analytical and numerical methods are employed in this study. In the analytical method, the cracked metallic plate was considered to be infinitely large and the composite patch was modeled as a long orthotropic strip of finite height (in the direction perpendicular to the crack axis). Next, by using the FEAM, a more general analysis capability that can treat arbitrary shapes of the cracked metallic sheet as well as the composite patches, is developed. This general FEAM is applied to:

1. composite patch repairs of cracks emanating from loaded fastener holes (the MSD problem)
2. composite patch repairs of semi-elliptical shaped surface flaws in thick-section plates
3. composite patch repairs of quarter-elliptical shaped surface flaws emanating from fastener holes.

The problem (1) is two-dimensional in nature, while problems (2) and (3) are fully three-dimensional. In all these cases, the effects of various design parameters on the reduction of the crack-tip (front) stress-intensity, due to repair, are fully discussed.

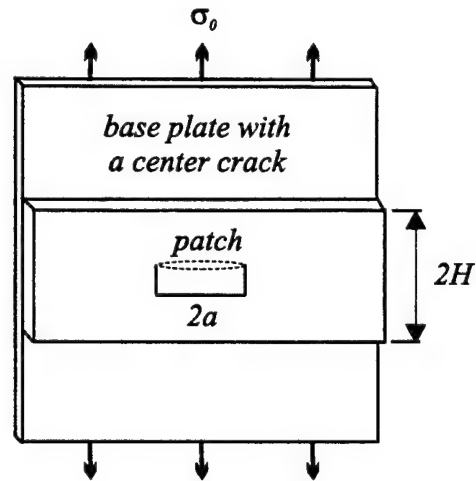


Figure 1.176: Schematic of a cracked metallic sheet repaired with a composite patch

#### § 1.13.1 Repair of center or edge cracks in unstiffened panels

Due to the fact that, in general, an analytical (as opposed to purely numerical) approach is more conveniently employed to examine the effects of each design parameter on the mechanical behavior of a repaired crack, a model problem of a repaired crack is first analyzed. Fig. 1.177 depicts the problem of an infinite isotropic (metal) sheet containing a crack of length  $2a$ , repaired by an adhesively bonded infinitely long orthotropic (composite) patch of height  $2H$  (height is measured normal to the crack-axis). It is assumed that the crack lies along the  $x$ -axis and that the principal material directions of the patch coincide with the geometric  $x$  and  $y$  axes. Let the thickness of the metal plate, the composite patch and the adhesive layer, be, respectively,  $h_s$ ,  $h_p$  and  $h_a$ .

The metal sheet is subjected to a hoop stress of  $\sigma_0$  as in Fig. 1.176. This mode I symmetric problem can be solved by a superposition of the two following problems:

Problem A: Determine the stress field in an isotropic metal sheet without a crack, to which is bonded an orthotropic patch as in Fig. 1.177a.

Problem B: When the tractions at the location of the crack, as determined from the solution of Problem A above, are erased, determine the stress-intensity factors at the crack-tips. This problem is sketched in Fig. 1.177b.

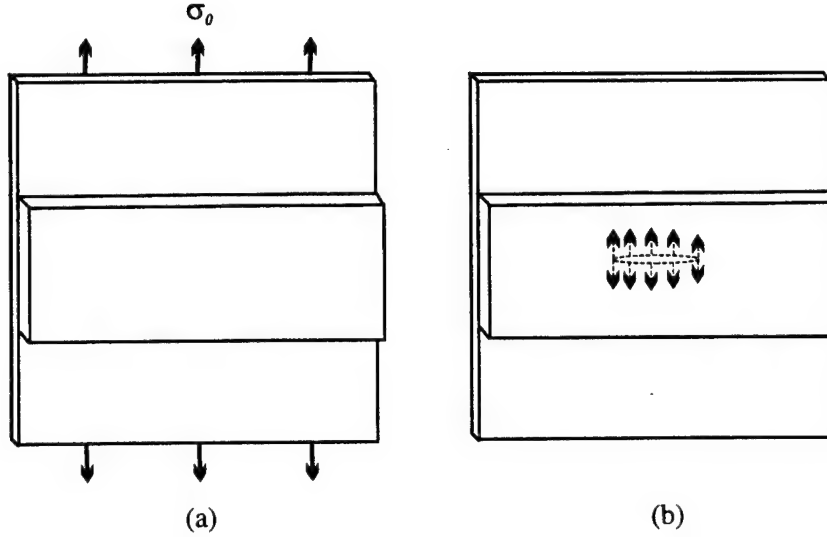


Figure 1.177: Linear superposition of problem A and problem B to solve the problem in Fig. 1.176

The relevant material and geometric parameters from Problems A and B are as follows:

1. The Young's modulus  $E_s$ , and Poisson's ratio  $\nu_s$  for the isotropic sheet.
2. Thickness  $h_s$  of the isotropic sheet.
3. The Young's modulus  $E_x$  and  $E_y$  of the orthotropic patch; the Poisson ratio  $\nu_y$  and the shear modulus  $G_{xy}$  of the orthotropic patch.
4. The height  $H$ ; and thickness  $h_p$  of the orthotropic patch; and
5. The thickness  $h_a$ , and the shear modulus  $G_a$  of the adhesive layer.

By using the Buckingham's  $\Pi$  theorem, the grouping of non-dimensional parameters that arise from the above geometric and material data is determined to be:

$$\left( \frac{G_s F}{h_s} \right), \left( \frac{a}{h_s} \right), \left( \frac{h_p E_y}{h_s G_s} \right), (\nu_s), \left( \frac{E_y}{E_x} \right), \left( \frac{E_x}{G_{xy}} \right), (\nu_y), \left( \frac{H}{a} \right). \quad (1.87)$$

It is the objective of the present analysis to determine the stress-intensity factor as a function of the above 8 non-dimensional parameters. This ensemble of curves

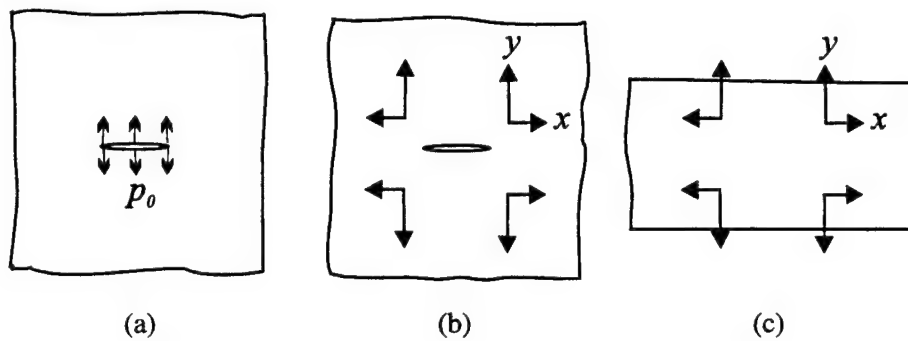


Figure 1.178: Basic problems needed in solving the problems of Fig. 1.177b

would then lead to a design procedure to select the appropriate composite patch, and adhesive, for a given crack in a metallic sheet. This is the first comprehensive treatment of this problem in the literature.

*Problem A (Fig. 1.177a)*

Since the base plate and the patch have infinite lengths in the  $x$ -direction and since there is no crack, we can treat this problem as a one-dimensional patch problem. Here it is assumed that the shear stresses in the adhesive layer are only in the  $y$ -direction (i.e.,  $\tau_{xz} = 0$ ), the base plate and the patch are in states of plane stress, and that the shear stresses in the adhesive layer are applied on the base plate and the patch as body forces (Fig. 1.178).

The equilibrium equations for a metal sheet and the composite patch are, respectively:

$$\frac{d\sigma_{yy}^s}{dy} = \frac{\tau_{yz}}{h_s}, \quad (1.88)$$

$$\frac{d\sigma_{yy}^p}{dy} = -\frac{\tau_{yz}}{h_p}. \quad (1.89)$$

Here  $\sigma_{yy}^s$  and  $\sigma_{yy}^p$  are the normal stresses in the  $y$  direction in the base sheet and in the patch respectively, and  $\tau_{yz}$  is the shear stress in the adhesive layer.

The stress-strain relations of the base sheet and the patch are given by:

$$\epsilon_{xx}^s = \frac{1}{E_s} (\sigma_{xx}^s - \nu_s \sigma_{yy}^s), \quad (1.90)$$

$$\epsilon_{yy}^s = \frac{1}{E_s} (\sigma_{yy}^s - \nu_s \sigma_{xx}^s), \quad (1.91)$$

$$\epsilon_{xx}^p = \frac{1}{E_x} (\sigma_{xx}^p - \nu_x \sigma_{yy}^p), \quad (1.92)$$

$$\epsilon_{yy}^p = \frac{1}{E_y} (\sigma_{yy}^p - \nu_y \sigma_{xx}^p). \quad (1.93)$$

Here  $E_s$  and  $\nu_s$  are Young's modulus and Poisson's ratio of a base sheet respectively; and  $E_x, E_y$  and  $\nu_x, \nu_y$  are the moduli and Poisson's ratios of an orthotropic patch. Among these variables, the relation  $\nu_x/E_x = \nu_y/E_y$  is satisfied.

As a compatibility condition between the metal sheet and the composite patch, the following relations proposed by Mitchell, Wooley, and Chivirut (1975), Jones and Callinan (1979) were used

$$\tau_{yz} = \frac{\nu^s - \nu^p}{F} \quad (1.94)$$

Here

$$F = \frac{h_a}{G_a} + \frac{3h_s}{8G_s} + \frac{3h_p}{8G_p}, \quad (1.95)$$

$\nu_s$  and  $\nu^p$  are the  $y$  displacements in the sheet and the plate respectively, and  $G_a, G_s$  and  $G_p$  are the shear moduli of the adhesive, the base sheet and the patch, respectively. We assume that  $G_p$  has the same value as  $G_{xy}$  in the patch plate. From the elaborate numerical results presented later, it will be seen that this assumption has little effect on the stress intensity factors.

By using Eq. 1.94 and the following boundary conditions:

$$\sigma_{yy}^s = \sigma_0 \quad \sigma_{yy}^p = 0 \quad \text{at } y = H, \quad (1.96)$$

we can solve Eqs. 1.88 and 1.89 easily. The stresses are obtained as

$$\sigma_{yy}^s = \sigma_0 - \frac{(1 - \nu_s^2) \sigma_0}{FE_s h_s A^2 \cosh AH} (\cosh AH - \cosh Ay), \quad (1.97)$$

$$\sigma_{yy}^p = \frac{(1 - \nu_s^2) \sigma_0}{FE_s h_p A^2 \cosh AH} (\cosh AH - \cosh Ay), \quad (1.98)$$

$$\tau_{yz} = \frac{(1 - \nu_s^2) \sigma_0}{FE_s A \cosh AH} \sinh Ay. \quad (1.99)$$

Here, to simplify the problem, the additional assumptions  $\epsilon_{xx}^s = 0$  and  $\epsilon_{xx}^p = 0$  were used.  $A^2$  is defined as

$$A^2 = \frac{1}{F} \left( \frac{1 - \nu_s^2}{E_s h_s} + \frac{1 - \nu_x \nu_y}{E_y h_p} \right). \quad (1.100)$$

From Eqs. (1.97-1.99), we can notice that  $\sigma_{yy}^s$  and  $\tau_{yz}$  have their maximum values at  $y = H$ , and decrease exponentially as  $(H - y)$  becomes larger than zero. On the other hand,  $\sigma_{yy}^p$  is zero at  $y = H$ , but it increases exponentially as  $(H - y)$  becomes larger than zero.

When  $\cosh AH \gg 1$ , the stresses near  $y = 0$  can be expressed as

$$\sigma_{yy}^s = \sigma_0 - \frac{(1 - \nu_s^2)}{F E_s h_s A^2} \sigma_0, \quad (1.101)$$

$$\sigma_{yy}^p = \frac{(1 - \nu_s^2)}{F E_s h_p A^2} \sigma_0, \quad (1.102)$$

$$\tau_{yz} = 0. \quad (1.103)$$

These stresses are the same as those when the patch is considered to be of an infinite height. Thus, when the value of  $\cosh AH$  is much greater than 1, we can assume that the patch has an infinite height, because this assumption gives nearly the same values for the stress intensity factors at the cracktip, and induced stresses near  $y = 0$ .

#### *Problem B (Fig. 1.177b)*

In order to solve this problem, a superposition of the basic problems shown in Fig. 1.178a, b and c may be used.

Fig. 1.178a is the case where uniform surface pressure  $p_0$  is applied on the crack surface in a metal sheet of infinite size. Its solution is well known [Gladwell and England (1977)]. Let the displacement field of this problem be  $u^{sA} = f_1(x, y)$ ,  $v^{sA} = f_2(x, y)$ . Here  $u^s$  is the displacement in the  $x$  direction and  $v^s$  is the displacement in the  $y$  direction, in the sheet.

Fig. 1.178b is the problem wherein point loads  $X, Y$  are applied symmetrically at the points  $(x_0, y_0)$ ,  $(-x_0, y_0)$ ,  $(x_0, -y_0)$  and  $(-x_0, -y_0)$  on an infinite isotropic plate with a central crack. Let this solution be  $u^{sB}$  and  $v^{sB}(x, y)$ . The solutions can be found in Erdogan and Arin (1972) and Roderick (1980). By using the solution in Roderick (1980), the displacements at a point  $(x, y)$  for this problem can be expressed as:

$$u^{sB}(x, y) = H_{11}(x, y; x_0, y_0)X + H_{12}(x, y; x_0, y_0)Y \quad (1.104)$$



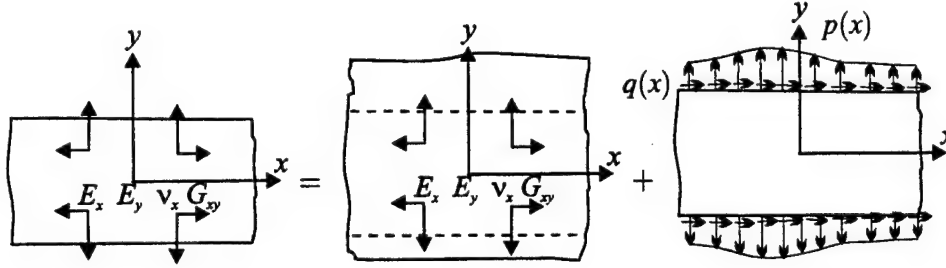


Figure 1.179: Green's function solution for a finite orthotropic plate, through superposition

$$v^B(x, y) = H_{21}(x, y; x_0, y_0)X + H_{22}(x, y; x_0, y_0)Y \quad (1.105)$$

The problem of Fig. 1.178c is where the point loads  $X, Y$  are applied symmetrically at the points  $(x_0, y_0)$ ,  $(-x_0, y_0)$ ,  $(x_0, -y_0)$  and  $(-x_0, -y_0)$  on an orthotropic patch of height  $2H$ . The problem of Fig. 1.178c can again be solved through a linear superposition of two other problems as in Fig. 1.179b and c. Fig. 1.179b is of the problem of an infinite orthotropic sheet; and Fig. 1.179c is of a finite height composite patch with residual tractions, from the solution of the problem in Fig. 1.179b, acting on the edges  $y = \pm H$ . The displacement field for the problem in Fig. 1.179b can be found in Lekhnitskii (1968). Now we consider the problem of Fig. 1.179c. Here,  $-p(x)$  and  $-q(x)$  are the normal and shear stresses acting on the  $y = H$  plane. Since, for the problem in Fig. 1.179c, the displacements  $u^{pc}(x, y)$  and  $v^{pc}(x, y)$  are odd and even functions, respectively, with respect to  $x$ , we may define:

$$u^{pc}(x, y) = \frac{2}{\pi} \int_0^\infty \phi(\alpha, y) \sin \alpha x d\alpha, \quad (1.106)$$

$$v^{pc}(x, y) = \frac{2}{\pi} \int_0^\infty \psi(\alpha, y) \cos \alpha x d\alpha, \quad (1.107)$$

where  $\phi(\alpha, y)$  and  $\psi(\alpha, y)$  are the Fourier transforms of  $u^{pc}(x, y)$  and  $v^{pc}(x, y)$  respectively. Since there are no further body forces, the equilibrium equations for the patch in Fig. 1.179c are written in terms of  $u^{pc}$  and  $v^{pc}$  for this component problem of Fig. 1.179c, as:

$$\left( \frac{v_x E_y}{1 - v_x v_y} \right) \frac{\partial^2 u^{pc}}{\partial x \partial y} + \left( \frac{E_y}{1 - v_x v_y} \right) \frac{\partial^2 v^{pc}}{\partial y^2} + G_{xy} \left( \frac{\partial^2 u^{pc}}{\partial x \partial y} + \frac{\partial^2 v^{pc}}{\partial x^2} \right) = 0 \quad (1.108)$$

$$\left(\frac{E_x}{1-v_x v_y}\right) \frac{\partial^2 u^{pc}}{\partial x^2} + \left(\frac{v_y E_y}{1-v_x v_y}\right) \frac{\partial^2 v^{pc}}{\partial x \partial y} + G_{xy} \left(\frac{\partial^2 u^{pc}}{\partial y^2} + \frac{\partial^2 v^{pc}}{\partial x \partial y}\right) = 0. \quad (1.109)$$

Substituting Eq. 1.106-1.107 into Eq. 1.108-1.109, we obtain:

$$\frac{\partial^4 \phi}{\partial y^4} + \alpha^2 \left(-\frac{E_x}{G_{xy}} + 2v_x\right) \frac{\partial^2 \phi}{\partial y^2} + \alpha^4 \frac{E_x}{E_y} \phi = 0, \quad (1.110)$$

$$\frac{\partial^4 \psi}{\partial y^4} + \alpha^2 \left(-\frac{E_x}{G_{xy}} + 2v_x\right) \frac{\partial^2 \psi}{\partial y^2} + \alpha^4 \frac{E_x}{E_y} \psi = 0, \quad (1.111)$$

The general solutions of Eqs. 1.110-1.111 are:

$$\phi = e_1 A_1 \cosh \beta_1 y + e_2 A_2 \cosh \beta_2 y + e_1 A_3 \sinh \beta_1 y + e_2 A_4 \sinh \beta_2 y \quad (1.112)$$

$$\psi = A_1 \sinh \beta_1 y + A_2 \sinh \beta_2 y + A_3 \cosh \beta_1 y + A_4 \cosh \beta_2 y, \quad (1.113)$$

where

$$e_k = \frac{\alpha \beta_k [v_x E_y + G_{xy} (1 - v_x v_y)]}{G_{xy} \beta_k^2 (1 - v_x v_y) - \alpha^2 E_x}, \quad k = 1, 2 \quad (1.114)$$

and  $\beta_1$  and  $\beta_2$  are roots of

$$\beta^4 - \alpha^2 \left(\frac{E_x}{G_{xy}} - 2v_x\right) \beta^2 + \alpha^4 \frac{E_x}{E_y} = 0 \quad (1.115)$$

Considering the symmetry conditions,  $u^{pc}(x, y) = u^{pc}(x, -y)$ , and  $v^{pc}(x, y) = -v^{pc}(x, -y)$ , we see that the constants  $A_3$  and  $A_4$  must be zero in Eqs. 1.112-1.113. Using Eqs. 1.112-1.113 in Eq. 1.106-1.107, we obtain the displacements  $u^{pc}$  and  $v^{pc}$ . From these, the corresponding stresses can be determined as:

$$\begin{aligned} \sigma_{xx}^{pc} &= \frac{2}{\pi} \int_0^\infty [(\alpha M_1 e_1 + M_2 \beta_1) A_1 \cosh \beta_1 y + \\ &\quad (\alpha M_1 e_2 + M_2 \beta_2) A_2 \cosh \beta_2 y] \cos \alpha x d\alpha \\ \sigma_{yy}^{pc} &= \frac{2}{\pi} \int_0^\infty [(\alpha M_2 e_1 + M_3 \beta_1) A_1 \cosh \beta_1 y + \\ &\quad (\alpha M_2 e_2 + M_3 \beta_2) A_2 \cosh \beta_2 y] \cos \alpha x d\alpha \\ \sigma_{xy}^{pc} &= \frac{2}{\pi} \int_0^\infty [G_{xy} (e_1 \beta_1 - \alpha) A_1 \sinh \beta_1 y + \\ &\quad G_{xy} (e_2 \beta_2 - \alpha) A_2 \sinh \beta_2 y] \sin \alpha x d\alpha, \end{aligned} \quad (1.116)$$

where

$$M_1 = \frac{E_x}{1 - \nu_x \nu_y}, \quad M_2 = \frac{\nu_y E_x}{1 - G \nu_x \nu_y} = \frac{\nu_x E_y}{1 - \nu_x \nu_y}, \quad M_3 = \frac{E_y}{1 - \nu_x \nu_y}.$$

If  $P(\alpha)$  and  $Q(\alpha)$  are the Fourier transforms of the tractions  $p(x)$  and  $q(x)$  in Fig. 1.179c, such that

$$p(x) = \frac{2}{\pi} \int_0^\infty P(\alpha) \cos \alpha x dx, \quad (1.117)$$

$$q(x) = \frac{2}{\pi} \int_0^\infty Q(\alpha) \sin \alpha x dx, \quad (1.118)$$

then the boundary conditions at  $\sigma_{yy}^{pc}(x, H) = +p(x)$  and  $\sigma_{xy}^{pc}(x, H) = +q(x)$  result in the following equations:

$$(\alpha M_2 e_1 + M_3 \beta_1) (\cosh \beta_1 H) A_1 + (\alpha M_2 e_2 + M_3 \beta_2) (\cosh \beta_2 H) A_2 = P(\alpha) \quad (1.119)$$

$$G_{xy} (e_1 \beta_1 - \alpha) (\sinh \beta_1 H) A_1 + G_{xy} (e_2 \beta_2 - \alpha) (\sinh \beta_2 H) A_2 = Q(\alpha) \quad (1.120)$$

from which  $A_1$  and  $A_2$  are solved for. Thus, the displacement solution  $u^{pc}(x, y)$  and  $v^{pc}(x, y)$  is obtained for the problem in Fig. 1.179c.

Let the displacement solution for the patch problem of Fig. 1.178c, obtained as a superposition of problems in Fig. 1.179b and c, be written as:

$$u^{pc}(x, y) = \frac{1}{h_p} \int_D [K_{11}(x, y; x_0, y_0) \tau_{xz}(x_0, y_0) + K_{12}(x, y; x_0, y_0) \tau_{yz}(x_0, y_0)] dx_0 dy_0 \quad (1.121)$$

$$v^{pc}(x, y) = \frac{1}{h_p} \int_D [K_{21}(x, y; x_0, y_0) \tau_{xz}(x_0, y_0) + K_{22}(x, y; x_0, y_0) \tau_{yz}(x_0, y_0)] dx_0 dy_0 \quad (1.122)$$

wherein, the adhesive shear stresses  $(\tau_{xz}/h_p)$  and  $(\tau_{yz}/h_p)$  are treated as body forces per unit volume, acting on the composite patch, as in Fig. 1.178c.

The sheet displacements from problems 1.178A and 1.178B may be written as:

$$\begin{aligned} u^s(x, y) &= u^{sA}(x, y) + u^{sB}(x, y) \\ &= f_1(x, y) - \frac{1}{h_s} \int_D [H_{11}(x, y; x_0, y_0) \tau_{xz}(x_0, y_0) + H_{12}(x, y; x_0, y_0) \tau_{yz}(x_0, y_0)] dx_0 dy_0 \end{aligned} \quad (1.123)$$

$$v^s(x, y) = f_2(x, y) - \frac{1}{h_s} \int_D [H_{21}(x, y; x_0, y_0) \tau_{xz}(x_0, y_0) + H_{22}(x, y; x_0, y_0) \tau_{yz}(x_0, y_0)] dx_0 dy_0 \quad (1.124)$$

where  $D$ , the domain of integration, is the size of the composite patch. The body forces on the sheet are  $(-\tau_{xz}/h_s)$  and  $(-\tau_{yz}/h_s)$  in the  $x$  and  $y$  directions, respectively.

The compatibility condition between the sheet and the patch is expressed as

$$\tau_{xz} = \left( \frac{u^s - u^p}{F} \right) \text{ and } \tau_{yz} = \left( \frac{v^s - v^p}{F} \right). \quad (1.125)$$

By substituting Eqs. 1.121-1.122 and Eqs. 1.123-1.124 into Eq. 1.125, one obtains the following integral equations for  $\tau_{xz}$  and  $\tau_{yz}$ :

$$F \tau_{xz}(x, y) + \int_D [k_{11}(x, y; x_0, y_0) \tau_{xz}(x_0, y_0) + k_{12}(x, y; x_0, y_0) \tau_{yz}(x_0, y_0)] dx_0 dy_0 = f_1(x, y) \quad (1.126)$$

$$F \tau_{yz}(x, y) + \int_D [k_{21}(x, y; x_0, y_0) \tau_{xz}(x_0, y_0) + k_{22}(x, y; x_0, y_0) \tau_{yz}(x_0, y_0)] dx_0 dy_0 = f_2(x, y) \quad (1.127)$$

where

$$\begin{aligned} k_{11} &= \left( \frac{H_{11}}{h_s} + \frac{K_{11}}{h_p} \right), \quad k_{12} = \left( \frac{H_{12}}{h_s} + \frac{K_{12}}{h_p} \right) \\ k_{21} &= \left( \frac{H_{21}}{h_s} + \frac{K_{21}}{h_p} \right), \quad k_{22} = \left( \frac{H_{22}}{h_s} + \frac{K_{22}}{h_p} \right) \end{aligned} \quad (1.128)$$

In integral Eqs. 1.126 and 1.127, the domain of integration  $D$  is the size of the orthotropic patch, which is finite in the  $y$  direction, but  $\infty$  in the  $x$  direction. For numerical purposes, however, the domain  $D$  in the  $x$  direction is also truncated to some finite value. In order to solve Eqs. 1.126 and 1.127, the domain  $D$  is discretized into a number of small sub-elements. In each subelement,  $\tau_{xz}$  and  $\tau_{yz}$  are assumed to be constant. Thus a system of linear equations, for discrete values of  $\tau_{xz}$  and  $\tau_{yz}$ , is obtained. By solving these, the shear stresses  $\tau_{xz}$  and  $\tau_{yz}$  are determined. Since the stress-state on the sheet, as in Fig. 1.178a and b, is thus completely known, the  $k$ -factors can be evaluated from the analytical solutions for problems 1.178A and B.

One example of discretization of  $D$  is shown in Fig. 1.180, for the case when  $(H/a) = 4$ . By varying the size of this  $D$ , it was determined that the obtained  $k$ -factors are insensitive to the size of  $D$ , as long as the dimensions of  $D$  are about five

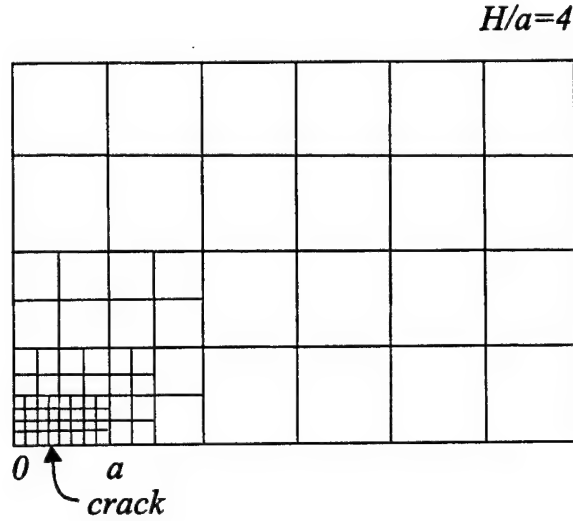


Figure 1.180: A typical finite element mesh of the adhesive layer

times as large as  $a$ . Note also the finer mesh near the crack, in Fig. 1.180, as the adhesive shear stresses are expected to be maximum near the crack itself.

#### *Behavior of patched cracks in unstiffened panels*

Attention is focused in this study, on the variation of:

1. non-dimensional stress intensity, i.e.,  $K_I/\sigma_0\sqrt{\pi a}$
2. non-dimensional adhesive shear,  $\tau_{xz}/\sigma_0$  and  $\tau_{yz}/\sigma_0$
3. non-dimensional patch stress,  $[\sigma_{yy}^p h_p]/(\sigma_0 h_s)$

as a function of the non-dimensional parameters:

$$\left(\frac{G_s F}{h_s}\right), \left(\frac{h_p E_y}{h_s G_s}\right), \left(\frac{a}{h_s}\right), \left(\frac{H}{a}\right), (v_s), \left(\frac{E_y}{E_x}\right), \left(\frac{E_x}{G_{xy}}\right), (v_y).$$

From the computed results, it was found that the more significant parameters are:

1.  $(G_s F/h_s)$ : which characterizes the adhesive flexibility. The “smaller” this number is, the “stiffer” is the adhesive.

2.  $(h_p E_y / h_s G_s)$ : which characterizes the patch stiffness in the direction normal to the crack axis.

The "larger" this number, the "stiffer" is the patch in the direction normal to the crack-axis.

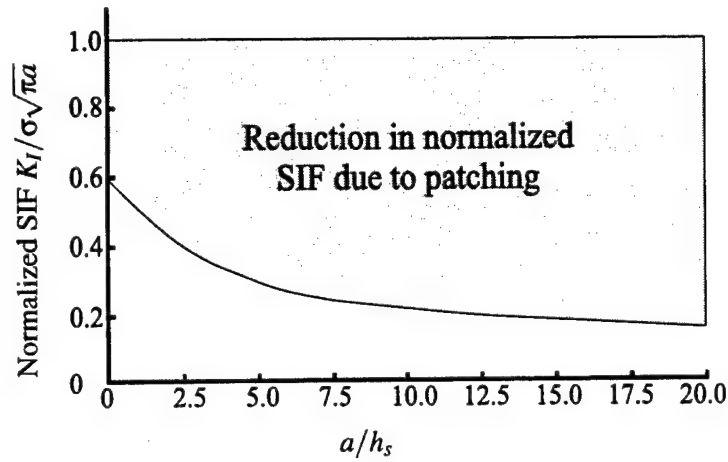
Fig. 1.181a shows the variation of the normalized stress-intensity factor as the crack-length increases, for the case of a very large composite patch,  $(H/a) \rightarrow \infty$ ;  $(h_p E_y / h_s G_s) = 2$ ; and  $(G_s F / h_s) = 3.0$ . Note that, in the absence of a composite patch, the normalized  $k$ -factor, i.e.,  $[K_I / \sigma \sqrt{\pi a}] = 1.0$ . Thus, the vertical distance between the horizontal straight line [normalized  $k$ -factor = 1.0] for the unpatched crack, and the curve for the repaired crack, indicates the reduction in the normalized  $k$ -factor due to patching. Fig. 1.181a clearly shows that more and more reduction in the normalized  $k$ -factor results as the crack-length increases.

Also it is seen from Fig. 1.181a that, as  $(a/h_s) \ll 1$ , the normalized  $k$ -factor converges to that in a center-cracked sheet with the crack-face pressure of  $p_0$  (see Fig. 1.178a), which is smaller than the applied far-field stress  $\sigma_0$  in the sheet (see Fig. 1.177a). Thus, when the crack length in the metal sheet is very small, the reduction in  $k$ -factor is achieved by the reduction in the crack-face pressure,  $p_0$ , in the metal sheet, due to the pressure of the composite patch. From Eq. 1.97 it is seen that  $p_0$  in Fig. 1.177b is given by

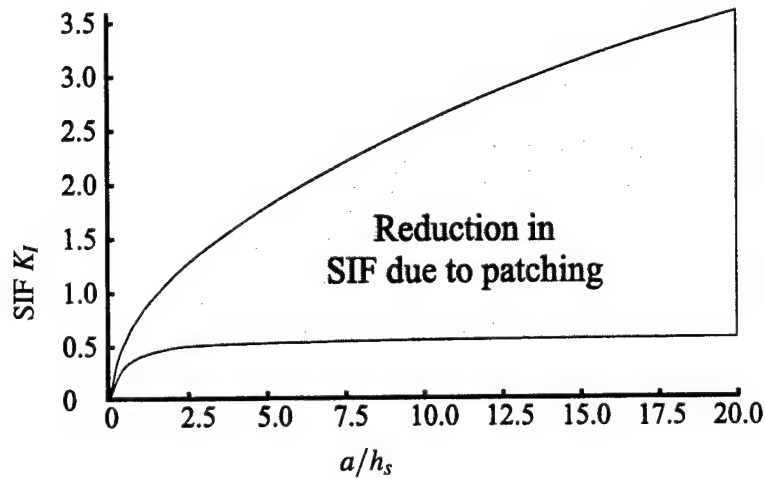
$$p_0 = \sigma_{yy}^s(y=0) = \sigma_0 - \frac{(1 - v_s^2) \sigma_0}{F E_s h_s A^2 \cosh AH} (\cosh AH - 1) \quad (1.129)$$

Substituting for  $A^2$  from Eq. 1.100 into 1.129, it is seen that  $p_0$  is independent of the adhesive flexibility parameter " $F$ "; for large values of  $H$  when  $\cosh AH \gg 1$ . Thus, for short cracks, the reduction in the normalized  $k$ -factor is unaltered by the adhesive flexibility. As the crack becomes longer, the adhesive shear stresses acting on the metal sheet have more dominant effect on the crack-tip  $k$ -factor, and the reduction in the  $k$ -factor depends on the adhesive flexibility parameter  $F$ .

Fig. 1.181b shows the variation of the actual  $k$ -factor as the crack grows, with and without the presence of a composite patch. It is seen that without the patch, the  $k$ -factor increases as  $\sqrt{a}$  as expected, but in the presence of a patch, the  $k$ -factor levels off to a constant value as the crack grows. This result has also been noted earlier by Rose (1981) and Atluri and Kathiresan (1978). It should be noted, however, that in the present analysis, the adhesive bond between the metal sheet and the composite patch is assumed to be perfect. However, the shear stress in the adhesive is maximum near the center of the crack, where the crack-opening displacement  $v^s$  in the sheet is maximum. Thus, for all adhesives whose maximum



(a)



(b)

Figure 1.181: (a) Reduction in normalized  $k$ -factor due to patching, as a function of the crack length; (b) reduction in the actual  $k$ -factor (for  $\sigma_o = 1$ ) due to patching as a function of the crack length.  $h_p E_y / h_s G_s = 2$ ,  $G_s F / h_s = 3$ ,  $H/a = \infty$ ,  $E_y/E_x = 8$ ,  $E_x/G_{xy} = 3.5$ ,  $\nu_s = 0.32$  and  $\nu_y = 0.16$ .

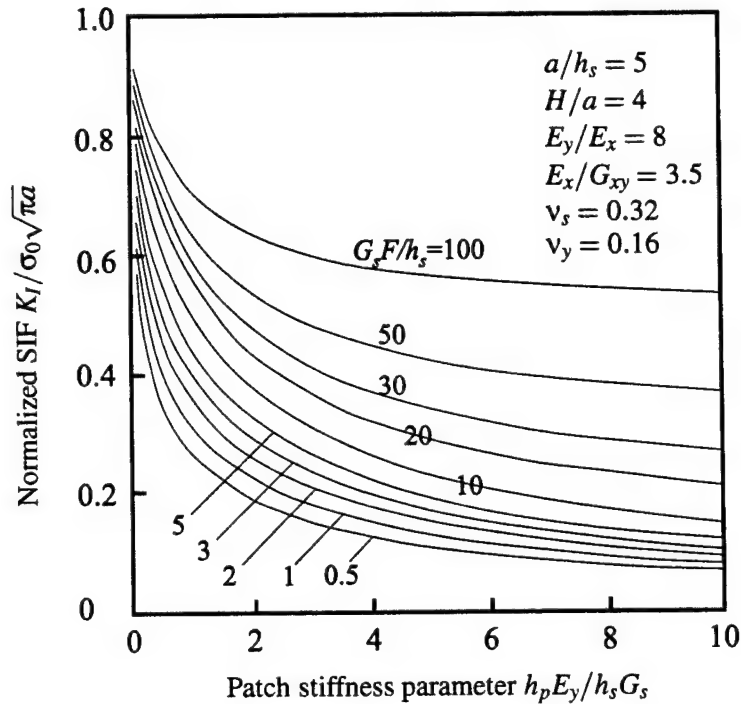


Figure 1.182: Reduction in normalized  $k$ -factor for a given crack length, as a function of the patch stiffness and adhesive flexibility

shear-strength is a finite value, a disbond can be expected to occur between the metal sheet and the composite patch near the center of the crack at  $y = 0$ , as well as possibly at  $y = H$ . When this disbonding is modeled properly, its effect is to increase the actual  $k$ -factor of the repaired crack, as the crack length increases.

Fig. 1.182 shows the effects of the “patch-stiffness” parameter and the “adhesive-flexibility” parameter on the normalized stress-intensity factor of the patched crack, for a given crack length ( $a/h_s$ ) = 5.0, and a given patch-height, ( $H/a$ ) = 4.0.

For a fixed “adhesive-flexibility” value, the stress-intensity factor (S.I.F.) of the patched crack decreases rapidly from its “unpatched” value, as the patch-stiffness increases. This S.I.F. reduction is, however, smaller as the adhesive flexibility increases.

From Fig. 1.182, it is evident that the S.I.F. reduction due to a patch is maximum when one uses a very stiff composite patch, as well as a very stiff adhesive layer.



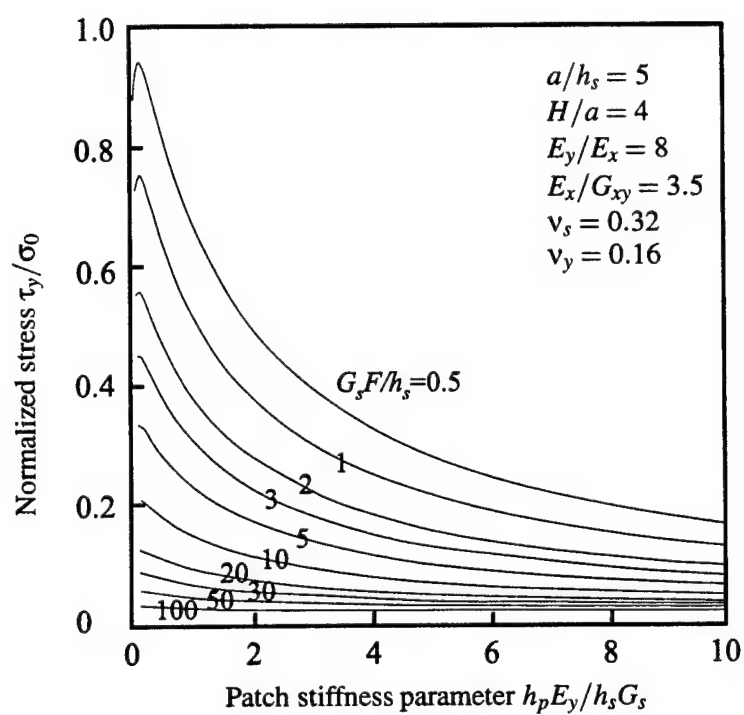


Figure 1.183: Variation of  $\tau_{yz}$  at  $x = 0$ ,  $y = 0$  as a function of the patch-stiffness and adhesive flexibility

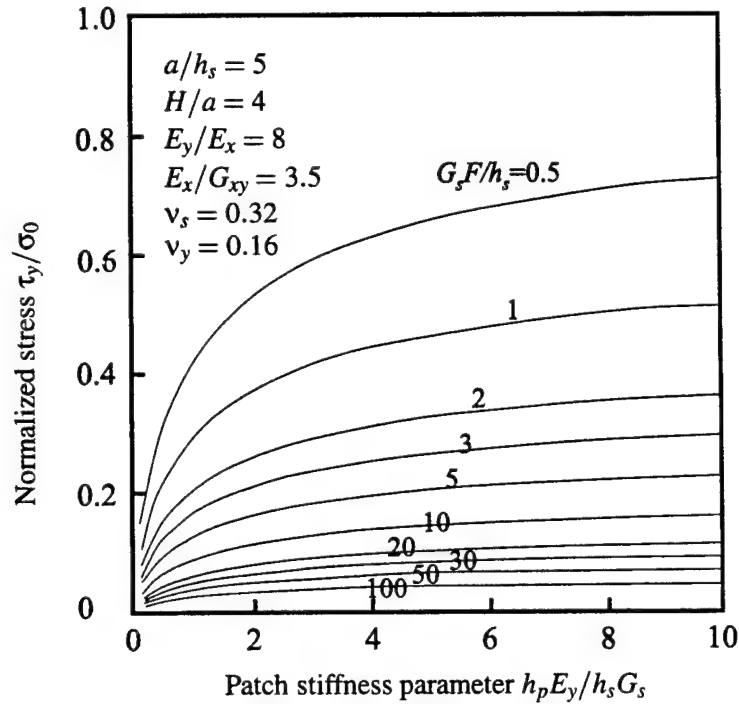


Figure 1.184: Variation of  $\tau_{yz}$  at  $x = 0$ ,  $y = H$  as a function of the patch-stiffness and adhesive flexibility

However, a stiff adhesive layer has a deleterious effect on the integrity of the bond itself as the adhesive shear stresses increase in such a case, as seen from Fig. 1.183 and 1.184.

Fig. 1.183 shows the non-dimensional shear stress ( $\tau_{yz}/\sigma_0$ ) in the adhesive layer, at the center of the crack, i.e.,  $x = 0$  and  $y = 0$ ; while Fig. 1.184 shows the corresponding value at the end of the patch, i.e.,  $x = 0$  and  $y = H$ . It is noted that in all cases,  $\tau_{xz} \ll \tau_{yz}$  and hence  $\tau_{xz}$  is not shown. It is seen that  $\tau_{yz}$  at  $y = 0$  arises only from the problem in Fig. 1.177b. Since  $\tau_{yz} = (\nu^s - \nu^p)/F$  and since  $(\nu^s - \nu^p)$  is maximum at  $x = 0$  and  $y = 0$  in Fig. 1.177b, the maximum value for the problem in Fig. 1.177b also occurs at  $x = 0$  and  $y = 0$ . Also, the stress  $\tau_{yz}$  at  $x = 0$  and  $y = H$  for the problem in Fig. 1.176 are nearly the same as that for the problem in Fig. 1.177a, and given by Eq. 1.99 when  $y = H$ .

From Fig. 1.183 it is seen that  $\tau_{yz}$  at  $x = 0$  and  $y = 0$  increases rapidly as the adhesive becomes stiffer (i.e., as  $F$  decreases), especially for moderate values of

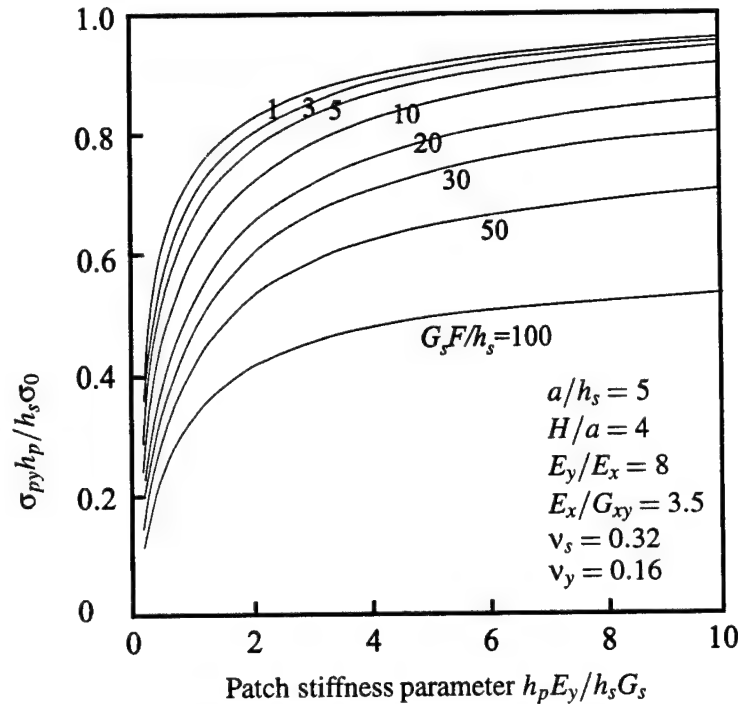


Figure 1.185: Variation of  $\sigma_{yy}^p$  at  $x = 0$ ,  $y = H$  as a function of the patch-stiffness and adhesive flexibility

patch stiffness. For fixed values of  $F$ ,  $(\tau_{yz}/\sigma_0)$  at  $x = 0$  and  $y = 0$  decreases as the patch stiffness increases. For large values of adhesive flexibility, the maximum shear stress is nearly constant regardless of the value of the patch stiffness.

From Fig. 1.184 it is seen that  $\tau_{yz}$  at  $x = 0$  and  $y = H$  also increases as the adhesive layer becomes stiffer. However, for fixed values of  $F$ , this shear stress increases as the patch increases.

Thus, we note that when a patch with a low stiffness  $((h_pE_p)/(h_sG_s) < 3.0)$  is used, the value of  $\tau_{yz}$  at  $x = y = 0$  is larger than the value of  $\tau_{yz}$  at  $x = 0$  and  $y = H$ . As the patch becomes stiffer,  $\tau_{yz}$  at  $x = 0$  decreases, while  $\tau_{yz}$  at  $x = 0$  and  $y = H$  increases. Thus as the patch becomes very stiff,  $\tau_{yz}(x = 0, y = H) > \tau_{yz}(x = 0, y = 0)$ .

Thus, in general, depending of the values of the patch stiffness, the likelihood of a disbond between the metal plate and the patch exists both at the locations  $(x = 0, y = 0)$  and  $(x = 0, y = H)$ .

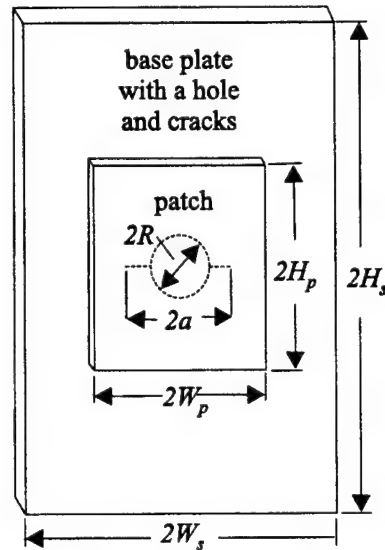


Figure 1.186: Schematic of repaired cracks near a loaded fastener hole in a metal sheet

Fig. 1.185 shows the effect of the patch-stiffness and adhesive flexibility on the values of  $(\sigma_{yy}^p h_p) / (\sigma_0 h_s)$ . The value of  $(\sigma_{yy}^p / \sigma_0)$  changes, on the other hand, according to the value of  $(h_s / h_p)$ . For fixed value of adhesive flexibility,  $(\sigma_{yy}^p h_p) / (\sigma_0 h_s)$  increases as the patch-stiffness increases. For fixed patch-stiffness,  $(\sigma_{yy}^p h_p) / (\sigma_0 h_s)$  increases as the adhesive stiffness increases.

So far, we have assumed that the metal sheet is infinite, and the composite patch is of a finite height but infinitely long. In reality however, the base sheet as well as the patch are finite in size; moreover, the patch can be arbitrary in shape. To account for these size and shape effects, one may use the FEAM to determine the displacement fields in each of the component problems such as in Fig. 1.178a, b, c wherein each problem may have a finite, arbitrary, shape. The integral equations for  $\tau_{xz}$  and  $\tau_{yz}$  in these finite arbitrary shapes may be formulated in much the same way as described earlier.

### § 1.13.2 Repair of cracks near loaded fastener holes in a lap joint

Consider the model problem of repairing of symmetrical cracks emanating from a loaded fastener hole, as shown in Fig. 1.186.

A circular hole of radius  $R$  is located at the center of a rectangular plate of

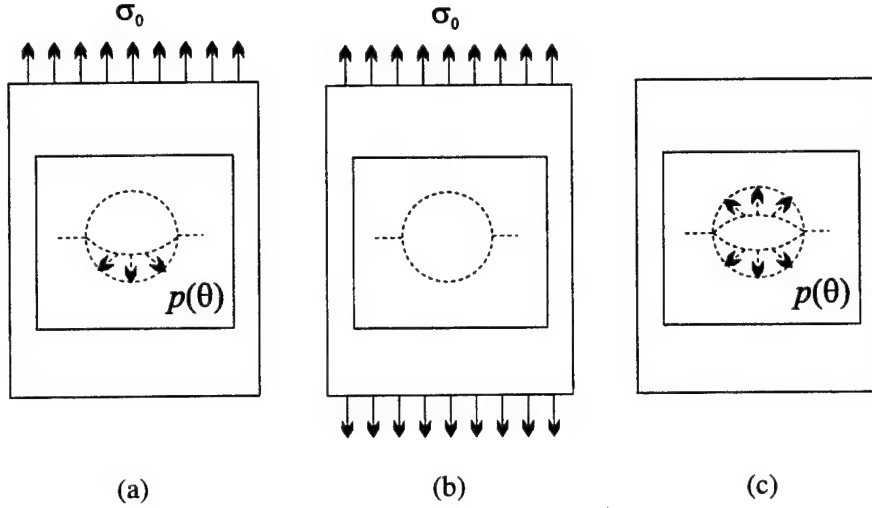


Figure 1.187: Linear superposition of problem B and C to solve a problem A:  
 $K_{IA} = (K_{IB} + K_{IC})/2$

width  $2W_s$ , height  $2H_s$  and thickness  $h_s$ . Two radial cracks of equal lengths  $(a - R)$  each emanate from the hole, along the  $x$  axis. To repair these cracks, a rectangular orthotropic patch of width  $2W_p$ , height  $2H_p$  and thickness  $h_p$  is assumed to be bonded onto the metal sheet. The thickness of the adhesive is  $h_a$ . The metal sheet is assumed to be subject to a far-field hoop stress  $\sigma_0$  as well as the pin-loading  $p(\theta)$  of the type:

$$p(\theta) = \frac{4W_s\sigma_0}{\pi R} |\sin\theta| \quad (1.130)$$

as Fig. 1.187a. Since the applied loading ( $\sigma_0$  and  $p(\theta)$ ) is not symmetric in the  $y$  direction, the crack may exhibit mode II behavior also. However, this mode II  $k$ -factor may be expected to be much smaller than the mode I component, and will be ignored hence forth.

The problem of Fig. 1.187a can be solved by a superposition of the two symmetric problems of Fig. 1.187b and c. If the crack-tip  $k$ -factor in Fig. 1.187b is  $K_{IB}$  and that in Fig. 1.187c is  $K_{IC}$ , respectively, then the  $k$ -factor of Fig. 1.187a may be written as:

$$K_{IA} = \frac{1}{2} (K_{IB} + K_{IC}). \quad (1.131)$$

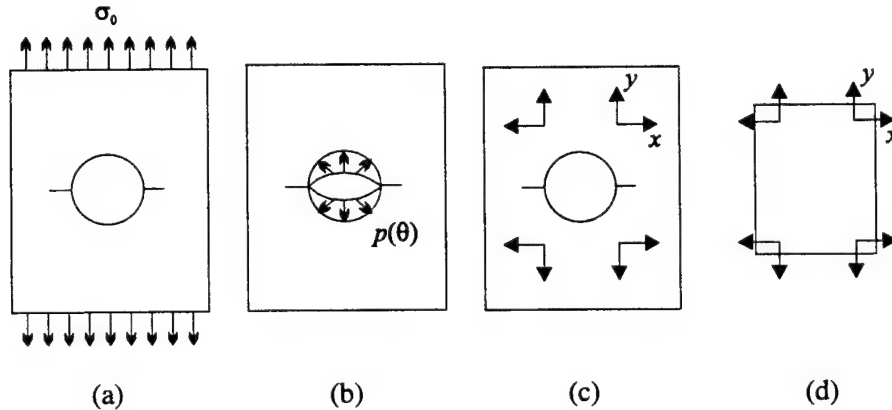


Figure 1.188: Basic problems to be solved in solving the problems of Fig. 1.187

Note that both the problems of Fig. 1.187b and c involve finite geometries.

The problems in Fig. 1.187b and c, can, in turn, be solved by a linear superposition of the basic problems in Fig. 1.188: (A) the problem of a finite sized isotropic metal sheet with radial cracks emanating from an unloaded hole, the sheet being subject to far-field hoop stress  $\sigma_0$ ; (B) the problem of a finite-sized isotropic metal sheet with radial cracks emanating from a hole, the hole surface being subject to symmetric load  $p(\theta)$  (Fig. 1.188b); (C) the problem of a finite-sized isotropic metal sheet with cracks emanating from a hole, the plate being subjected to shear tractions  $\tau_{xz}$  and  $\tau_{yz}$  (from the adhesive layer) on its surface (Fig. 1.188c); and (D) the problem of a finite-sized orthotropic composite patch, subjected to shear tractions  $\tau_{xz}$  and  $\tau_{yz}$  (from the adhesive layer) on its surface (Fig. 1.188d).

In order to solve the above four basic problems, the FEAM is employed. In the case of the problem in Fig. 1.188a, the FEAM procedure is as follows:

First consider the analytical solution for the problem of a central crack in an infinite sheet, the crack-faces being subjected to arbitrary tractions. Earlier in this book, the solution of Gladwell and England (1977), wherein the crack-face pressure was assumed to be a sum of Chebyshev polynomials, was presented. However, in the present problem of cracks emanating from a hole, as in Fig. 1.188a, in the FEAM procedure, residual tractions would arise on the crack-faces,  $|x| \geq (R - a)$  (for a traction-free hole), and further, there will be steep stress gradient near  $|x| = R$  because of the stress-concentration near the hole. Thus, in order to use the Gladwell and England (1977) solution, tractions on the fictitious crack-face  $|x| < a$  will have

to be interpolated with Chebyshev polynomials which is not desirable, since the residual tractions on the fictitious crack-faces  $|x| < R$  are zero, while those on  $|x| \geq (R_a)$  have a steep gradient. Due to this fact, an alternate analytical solution for a central crack in an infinite sheet, the crack faces being subject to equal and opposite point-loads at an arbitrary location  $x$  as discussed in Chapter ??, is considered.

*Formulation of integral equations for the problem of repair of cracks near loaded fastener holes*

By using the FEAM outlined in Sec. § 1.13.2, we obtain the displacement fields in each of the four basic problems sketched in Fig. 1.188a-d, respectively. Let the displacement field of the problem in Fig. 1.188a be given by  $u^{sA} = F_{1A}(x, y)$  and  $v^{sA} = F_{2A}(x, y)$ ; and that for problem in Fig. 1.188b be given by  $u^{sB} = F_{1B}(x, y)$  and  $v^{sB} = F_{2B}(x, y)$ . Let the displacement field for the problem in Fig. 1.188c be given by:

$$u^{sC}(x, y) = -\frac{1}{h_s} \int_D [H_{11}(x, y; x_0, y_0) \tau_{xz}(x_0, y_0) + H_{12}(x, y; x_0, y_0) \tau_{yz}(x_0, y_0)] dx_0 dy_0 \quad (1.132)$$

and

$$v^{sC}(x, y) = -\frac{1}{h_s} \int_D [H_{21}(x, y; x_0, y_0) \tau_{xz}(x_0, y_0) + H_{22}(x, y; x_0, y_0) \tau_{yz}(x_0, y_0)] dx_0 dy_0 \quad (1.133)$$

where  $D$  is the domain of the finite patch (and of the adhesive layer). Likewise, the displacement field in the patch is given by

$$u^p = u^{pD}(x, y) = \frac{1}{h_p} \int_D [K_{11}(x, y; x_0, y_0) \tau_{xz}(x_0, y_0) + K_{12}(x, y; x_0, y_0) \tau_{yz}(x_0, y_0)] dx_0 dy_0 \quad (1.134)$$

$$v^p = v^{pD}(x, y) = \frac{1}{h_p} \int_D [K_{21}(x, y; x_0, y_0) \tau_{xz}(x_0, y_0) + K_{22}(x, y; x_0, y_0) \tau_{yz}(x_0, y_0)] dx_0 dy_0 \quad (1.135)$$

The total displacement in the metal sheet (see Fig. 1.188a-c) is given by:

$$u^s = \frac{1}{2} (u^{sA} + u^{sB}) + u^{sC} = \frac{1}{2} (f_{1A} + f_{1B}) + u^{sC} \quad (1.136)$$

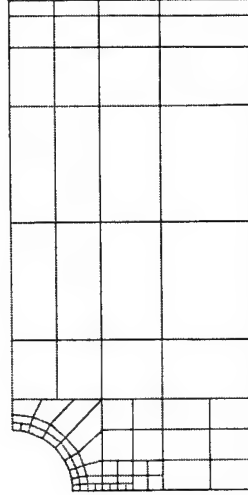


Figure 1.189: A typical finite element mesh of the adhesive layer

and

$$v^s = \frac{1}{2} (v^{sA} + v^{sB}) + v^{sC} = \frac{1}{2} (f_{2A} + f_{2B}) + v^{sC} \quad (1.137)$$

The conditions of compatibility between the metal sheet and the orthotropic patch are given, again, by:

$$\tau_{xz} = \frac{u^s - u^p}{F} \quad \text{and} \quad \tau_{yz} = \frac{v^s - v^p}{F} \quad (1.138)$$

where  $F$  is the adhesive flexibility as defined in Eq. 1.95. By substituting Eqs. 1.132 to 1.137 in Eq. 1.138, one obtains the integral equations for  $\tau_{xz}$  and  $\tau_{yz}$ . Once these integral equations are solved for  $\tau_{xz}$  and  $\tau_{yz}$ , the free-body diagram of the stress-intensity factors near the crack-tips, as effected by the repair patch, can be computed.

By assuming constant values of  $\tau_{xz}$  and  $\tau_{yz}$  within each subdomain, the integral equations in Eqs. 1.137 and 1.138 are solved for. One example of the mesh used for solving the integral equation over  $D$ , for the case  $W_p/R = 2$  and  $H_p/W_p = 2.0$  is shown in Fig. 1.189.

In the problems of Fig. 1.187, the  $k$ -factor of the problems in Fig. 1.187a-c are identified as  $K_{IA}$ ,  $K_{IB}$  and  $K_{IC}$  respectively,  $[K_{IA} = \frac{1}{2} (K_{IB} + K_{IC})]$ . In the following, the results for the normalized  $k$ -factors, as functions of the material parame-



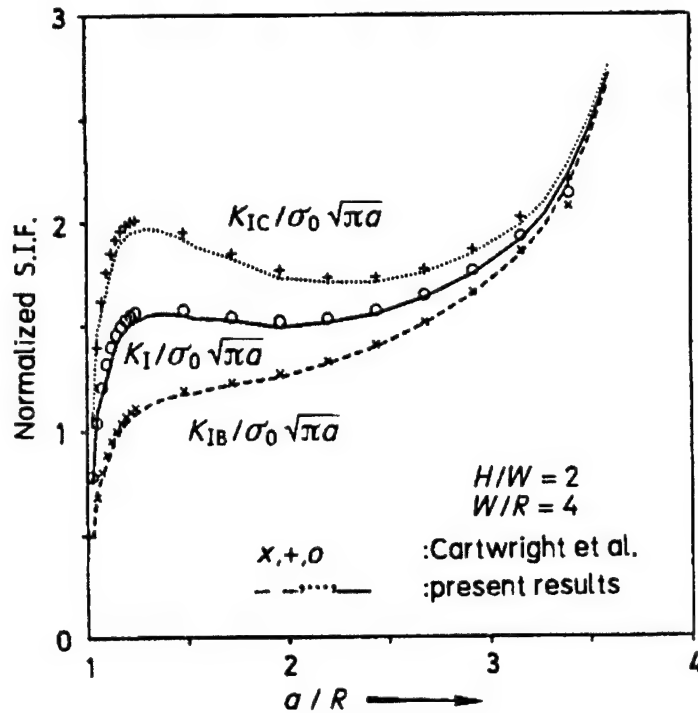


Figure 1.190: Variation of normalized  $k$ -factor as a function of the crack-length (unrepaired case)

ters ( $G_s F / h_s$ ), ( $h_p E_y / h_s G_s$ ) and the geometrical parameters  $a/R$ ,  $R/h_s$ ,  $W/R$ , and  $H/W$ , are discussed for the patched and unpatched cases.

#### Results and discussions

In order to examine the accuracy of the presently developed FEAM, first the problem of cracks emanating from a loaded fastener hole, without the presence of the repair patch, is solved first. The present results are compared with those of Cartwright and Parker (1972), for the case when  $H/W = 2$ , and  $W/R = 4.0$ . In the present FEAM, 65 eight-noded isoparametric elements were used, and the CPU time required to solve one crack case was about 55 seconds on a MicroVAX Station II. The present results are seen from Fig. 1.190 to agree excellently with those of Cartwright and Parker (1972).

Fig. 1.191a shows the effect of patching on the normalized stress-intensity fac-

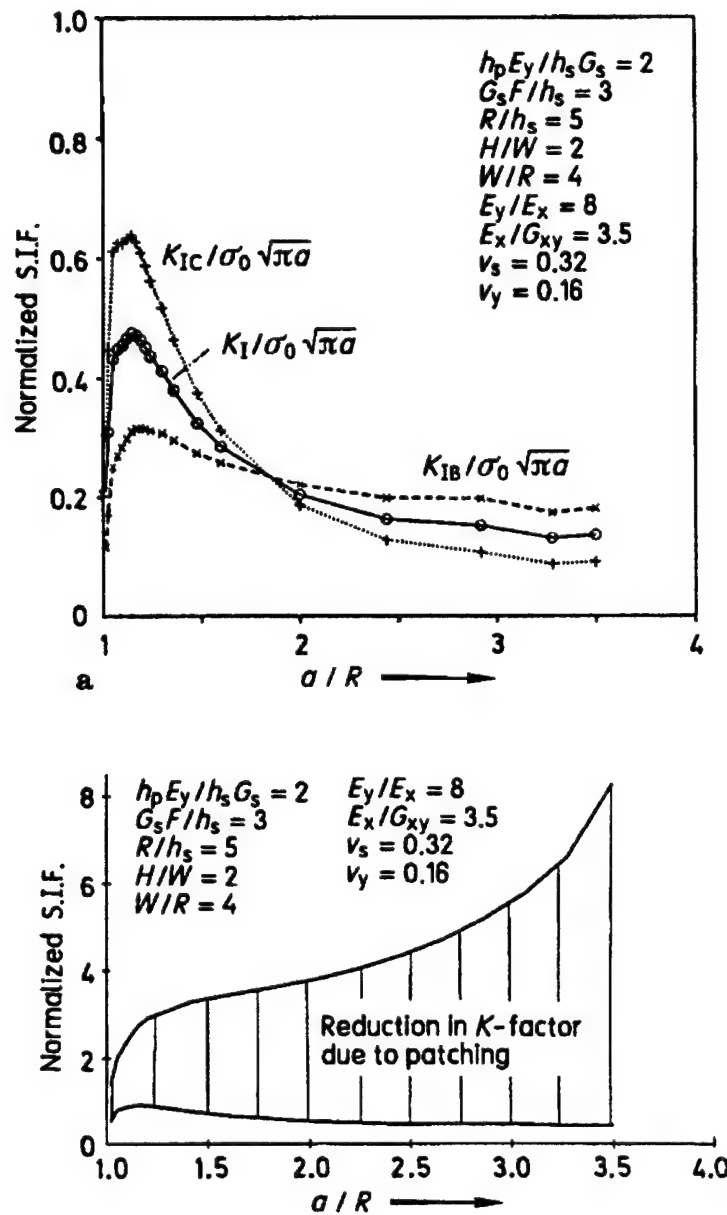


Figure 1.191: (a) Variation of normalized  $k$ -factor as a function of the crack-length (repaired case); (b) reduction in  $k$ -factor (for  $\sigma_o = 1$ ), due to repair, for cracks emanating from a loaded fastener hole

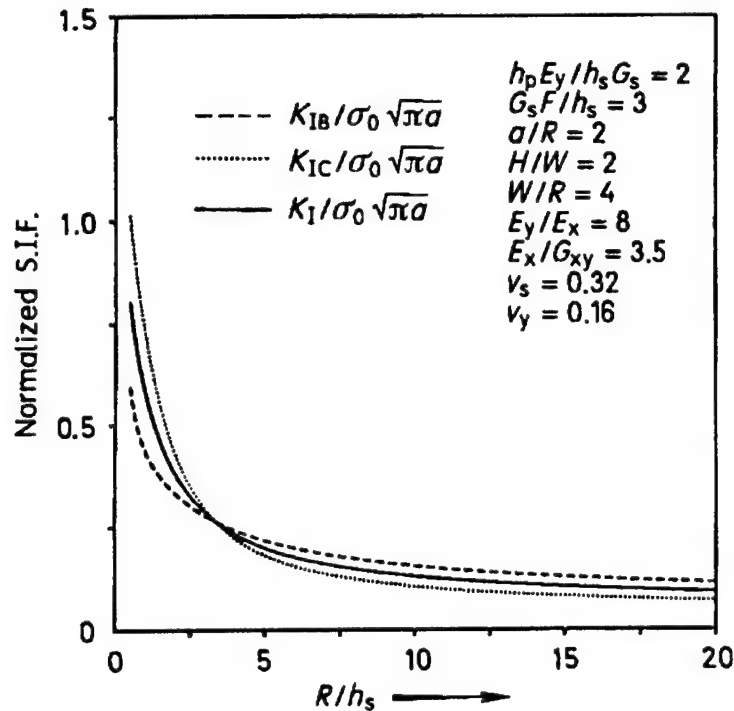


Figure 1.192: Variation of normalized  $k$ -factor for a given crack length, as a function of the hole radius(repaired case)

tor, as the crack length increases, for given material and geometrical parameters of the patch as identified in the inset of Fig. 1.191a. Comparing Fig. 1.190 and 1.191a, the reduction in the normalized  $k$ -factor, as the crack grows, due to the presence of the composite patch, can be observed. For small cracks this reduction is not much, but as  $(a/R)$  increases, the effects of patching increases as well.

Fig. 1.191b shows the effect of patching on the actual stress-intensity factor, as the crack length increases, for given geometrical and material parameters as identified in the inset of Fig. 1.191b. Once again it is seen that even for a repaired crack near a loaded fastener hole, the actual  $k$ -factor becomes a constant as the crack-length increases under the patch. This appears to be a salient feature of all cases when the crack in a fuselage skin is repaired with a stiff composite patch. Fig. 1.192 shows the effect of the hole radius on the normalized  $k$ -factors for the repaired cracks.

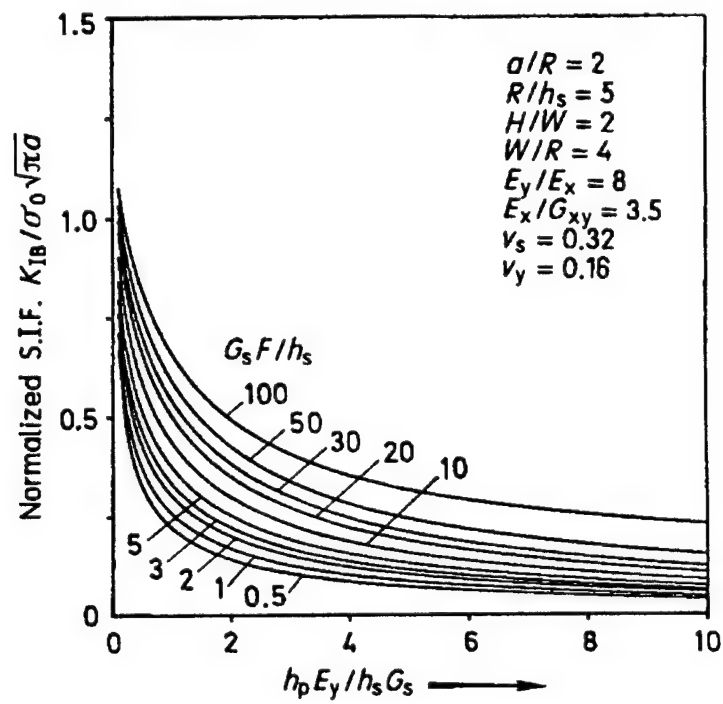


Figure 1.193: Variation of nomalized  $k$ -factor,  $K_{1B}$ , for a given crack length, as a function of the patch stiffness and adhesive flexibility

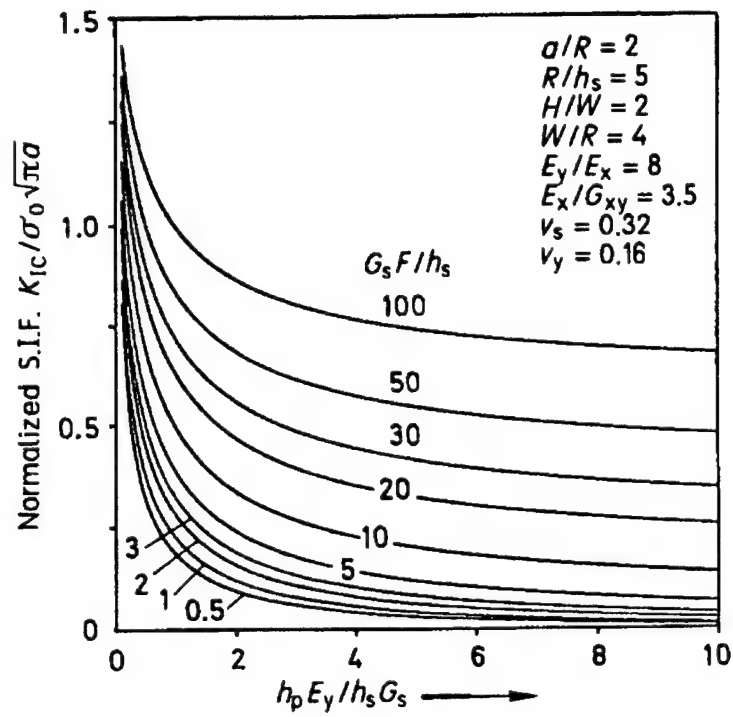


Figure 1.194: Variation of normalized  $k$ -factor,  $K_{IC}$ , for a given crack length, as a function of the patch stiffness and adhesive flexibility

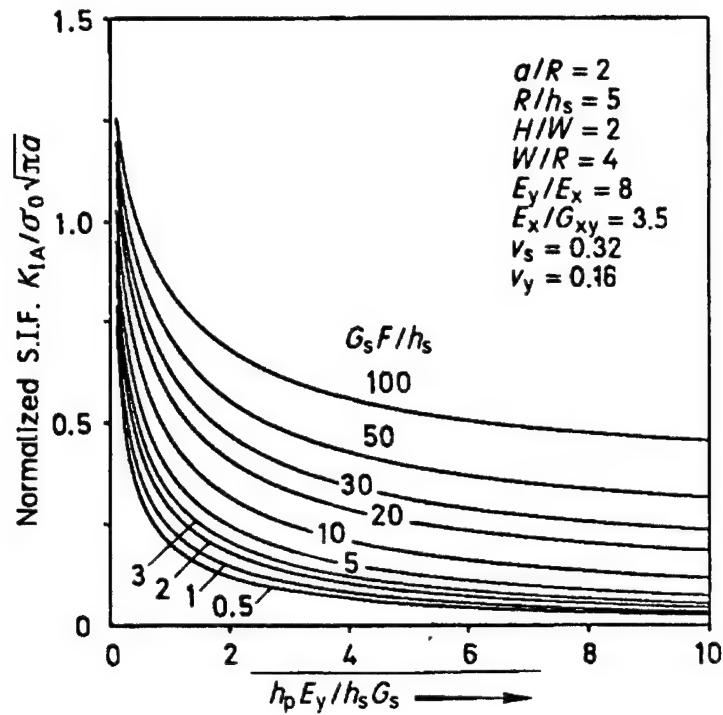


Figure 1.195: Variation of normalized  $k$ -factor,  $K_{IA}$ , for a given crack length, as a function of the patch stiffness and adhesive flexibility

Fig. 1.193 shows the effect of the adhesive layer flexibility and patch-stiffness on the normalized stress-intensity near the crack-tip, for the case of far-field hoop-stress loading  $\alpha_0$ . Fig. 1.194 shows similar results for the case of the fastener loading on the hole, while Fig. 1.195 shows the combined effect of far-field loading as well as the fastener loading. As in the case of the central crack discussed in Sec. § 1.13.1, the stiffer the adhesive layer and the stiffer the patch, the more reduction is achieved in the  $k$ -factor near the patched crack-tip. On the other hand, a stiff adhesive layer has a deleterious effect on the integrity of the patch itself, as the adhesive shear stresses also increase as the adhesive stiffness increases.



*Multiple-site-damage in a fuselage lap-joint*

A model of a typical lap joint, and a typical multiple site damage near a row of fastener holes, are illustrated in Fig. 1.196 and b, respectively. Taking into account the fastener flexibility, the fastener reaction forces on the upper (or lower) skin can be determined for the lap-splice joint configuration of Fig. 1.196, through the finite element method [see Sec. § 1.2.2]. Once these reaction forces, treated as concentrated forces, are determined, one may use the known elasticity solution, to approximate the stress field on the hole-surface in the skin, that is equivalent to these concentrated forces. Under the action of these fastener-interaction stress fields and the far-field hoop tension, the stress-intensity factors for multiple cracks near fastener holes can be determined using the FEAM described in this section. The corresponding reduction in  $k$ -factors due to patching can be obtained again, using the FEAM, as described in this section.

*§ 1.13.3 Three-dimensional analysis of surface-flaws with and without repairs*

In the FEAM applied to three-dimensional problems of embedded and/or surface flaws (of elliptical or part-elliptical shapes) in structural components, the key ingredient is the analytical solution for an embedded elliptical flaw in an isotropic elastic solid, the crack-faces being subjected to arbitrary tractions [Atluri (1986); Nishioka and Atluri (1983); Atluri and Tong (1991)]. Here we describe some applications of the three-dimensional FEAM to the analysis of surface-flaws in aircraft structural components, with and without composite-patch repairs.

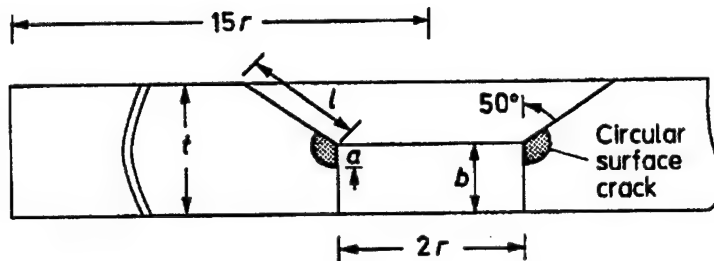
*Corner flaw near a counter-sunk rivet hole*

The problem of a counter-sunk rivet hole with a surface-flaw emanating from the corner is shown in Fig. 1.198. This is a typical situation in an aircraft-fuselage lap-joint. In the early stages of fatigue, this surface flaw grows into a through-the-thickness crack emanating from the fastener hole leading ultimately to the development of multiple-site-damage near a row of such fastener holes.

Fig. 1.199 shows a comparison of two different finite-element models:

1. Fig. 1.199a shows a finite element model of  $(1/4)$  of the plate when two surface cracks are assumed to emanate symmetrically from either side of the hole. In this finite element model, crack-tip elements are used in an explicit numerical modeling of the crack-tip singularity. Because of this, this model





Configurations:  $a/l = 0.2, 0.5, 0.8$   
 $r/t = 2.0, 1.0, 0.5$   
 $b/t = 0 \text{ \& } b/t > 0.0$

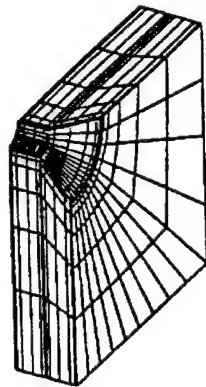
Loading: Remote tension  
 Remote bending

Figure 1.198: Schematic of a counter sunk rivet hole with a surface crack

#### Counter - sunk Rivet

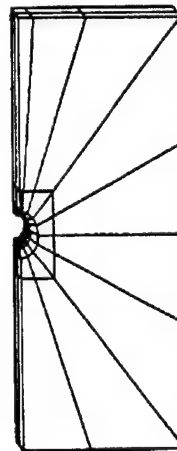
Elements: 1,430 20-node elements  
 Nodes: 6,828  
 D.O.F.: 20,484

(Assumes symmetry of plate & cracks)



Conventional FEM

90 Elements only  
 ( 20 nodes )  
 202 Nodes  
 606 D.O.F.



Present model  
 (Finite Element Alternating Method)

Figure 1.199: Typical finite element models

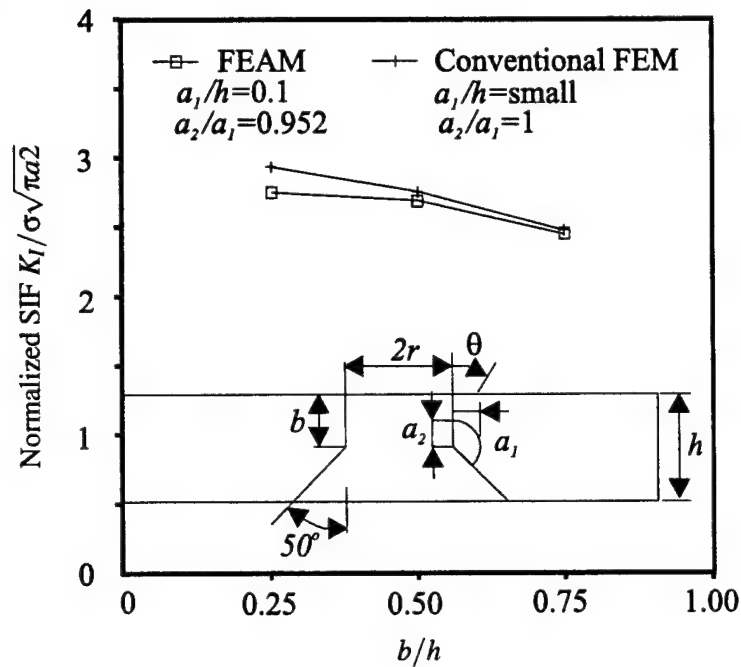


Figure 1.200: Variation of  $k$ -factor at minor axis of ellipse as a function of hole depth

involves 1430 twenty-node finite elements, with a total of 20,484 degrees of freedom;

2. Fig. 1.199b shows the finite element model in the present FEAM. In this model, only one surface crack is assumed to emanate from one side of the hole; and the crack-tip singularity is treated analytically through the solutions given in Vijayakumar and Atluri (1981) and Nishioka and Atluri (1983).

Because of this, the finite element model involves only 90 twenty-node elements with a total of only 606 degrees of freedom. Thus, the savings in computational time, as well as in the data preparation time, in the present FEAM are truly significant.

In Fig. 1.200, a comparison of the results from a conventional FEM, and the present FEAM, is shown for the normalized  $k$ -factor at the tip of the minor axis of the quarter-elliptical flaw, as a function of the ratio of the depth of the hole (without counter-sink) to the depth of the plate. The FEAM with only 1575 DOF gives as good a set of results as the conventional FEM with 20,484 DOF.

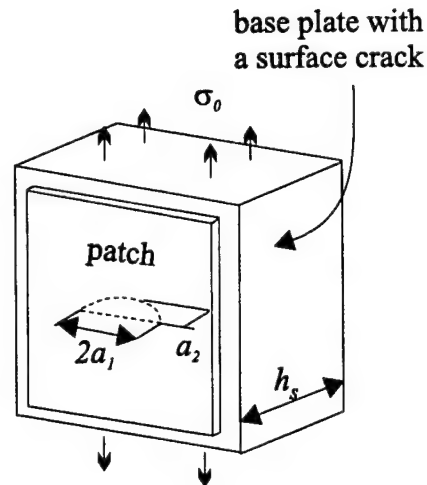


Figure 1.201: Schematic of a patched, surface-flawed thick plate

*Three-dimensional problem of a plate with a surface crack: effect of patching*

Consider the problem of a base plate with a surface crack, with a composite patch, as shown in Fig. 1.201. We assume that the sizes of the base plate and patch are infinite (this assumption is reasonable as long as the widths and lengths of the plate as well as the patch are about five times the length of the semi-major axis of the elliptical surface flaw, as in Fig. 1.201), but that the thicknesses of the base plate as well as the patch are finite. Let the thicknesses of the base plate and the patch be  $h_s$  and  $h_p$  respectively. The loading is assumed to be far-field tension, as in Fig. 1.201.

The problem in Fig. 1.201 can be solved by using the superposition principle as shown in Fig. 1.202. In this case, the displacement fields of the basic problems as shown in Fig. 1.202 need to be solved for.

Fig. 1.203a is the case wherein uniform stress  $\sigma_0$  is applied on the crack-surface. The displacement field for this problem is generated by using an analytical alternating technique, wherein the analytical solution for an infinite body containing an embedded elliptical flaw, subjected to arbitrary crack-face tractions, is employed. This analytical solution has been previously obtained by Nishioka and Atluri (1983).

Fig. 1.203b shows the problem wherein point loads  $X, Z$  are applied symmetrically at the points  $(x_0, z_0)$ ,  $(x_0, -z_0)$ ,  $(-x_0, z_0)$ ,  $(-x_0, -z_0)$  on the plate with a semi-elliptical surface crack. Let the displacements at a point  $(x, z)$  on the front

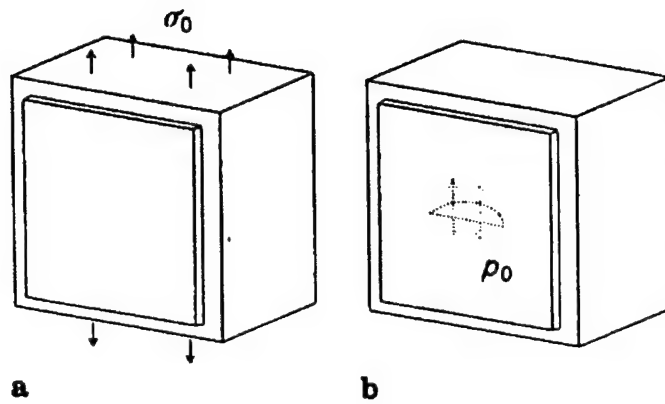


Figure 1.202: Linear superposition of (a) a patched plate without a crack subjected to far-field stress, and (b) patched plate with a crack subjected to crack-face pressure

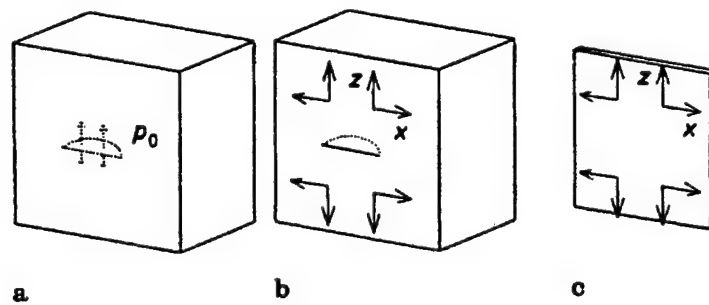


Figure 1.203: Linear superposition of basic problems

surface ( $y = 0$ ) be expressed as

$$\begin{aligned} u &= H_{11}(x, z; x_0, z_0)X + H_{12}(x, z; x_0, z_0)Z \\ w &= H_{21}(x, z; x_0, z_0)X + H_{22}(x, z; x_0, z_0)Z \end{aligned}$$

The problem of Fig. 1.203c is one wherein point loads  $X, Z$  are applied symmetrically on an infinite orthotropic plate. This solution has been reported on previously. Let the displacements at a point  $(x, z)$  for this problem be expressed as:

$$\begin{aligned} u^p &= K_{11}(x, z; x_0, z_0)X + K_{12}(x, z; x_0, z_0)Z \\ w^p &= K_{21}(x, z; x_0, z_0)X + K_{22}(x, z; x_0, z_0)Z \end{aligned}$$

Let the displacements  $U^s$  and  $w^s$  denote the total displacements from problems 1.203A and B. The compatibility conditions between the base plate and the composite patch are expressed as

$$\tau_{xz} = \frac{u^s - u^p}{F}, \quad \tau_{yz} = \frac{w^s - w^p}{F}$$

where  $F$  is the adhesive flexibility, defined as earlier, as

$$F = \frac{h_a}{G_a} + \frac{3h_p}{8G_p}$$

By using these compatibility conditions, integral equations are derived for  $\tau_{xz}$  and  $\tau_{yz}$ . Once these are solved for, the  $k$ -factors are obtained in a manner described in earlier sections.

Fig. 1.204 shows the effect of the thickness of the base plate on the normalized stress-intensity factors for both the unrepaired and repaired cases. When the base plate thickness is small, about 50% reduction in  $k$ -factor is obtained. As the base plate becomes thicker, however, the effect of the patch is reduced (to about 40%), and the  $k$ -factor converges to a constant value. (Note that in the case of the surface-flaw, the  $k$ -factor that is considered is at the intersection of the crack-front with the front face of the base plate). From Fig. 1.204 it is also noted that if one uses a very stiff patch, a better reduction in the  $k$ -factor is obtained. However, a stiff patch may increase the adhesive shear stresses.

Fig. 1.205 shows the effect of patch-stiffness parameters and adhesive flexibility parameters on the normalized  $k$ -factors.

Fig. 1.206 shows the effect of patch stiffness and adhesive flexibility on the adhesive shear stresses,  $\tau_{yz}/\sigma_0$  at  $x = 0$ ,  $y = 0$  and  $z = 0$ . Finally Fig. 1.207 shows the effect of the patch-stiffness and adhesive flexibility on the values of  $\sigma_{yy}^p$ .

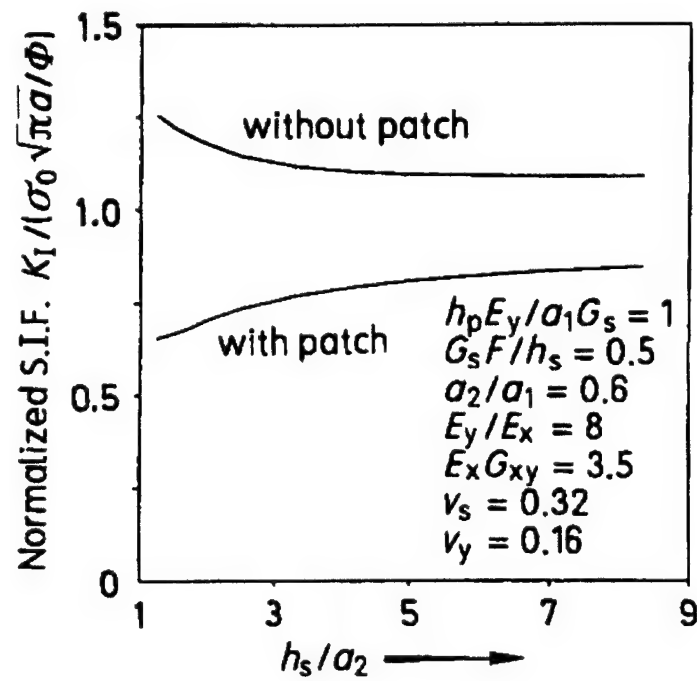


Figure 1.204: Reduction in  $k$ -factor due to patching as a function of crack-depth ratio

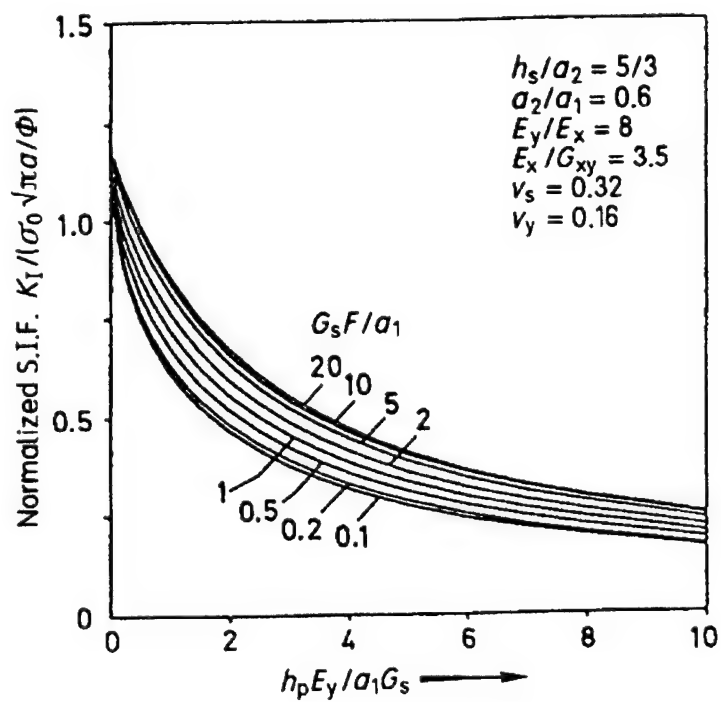


Figure 1.205: Effects of patch stiffness and adhesive flexibility on the  $k$ -factor of a surface flaw

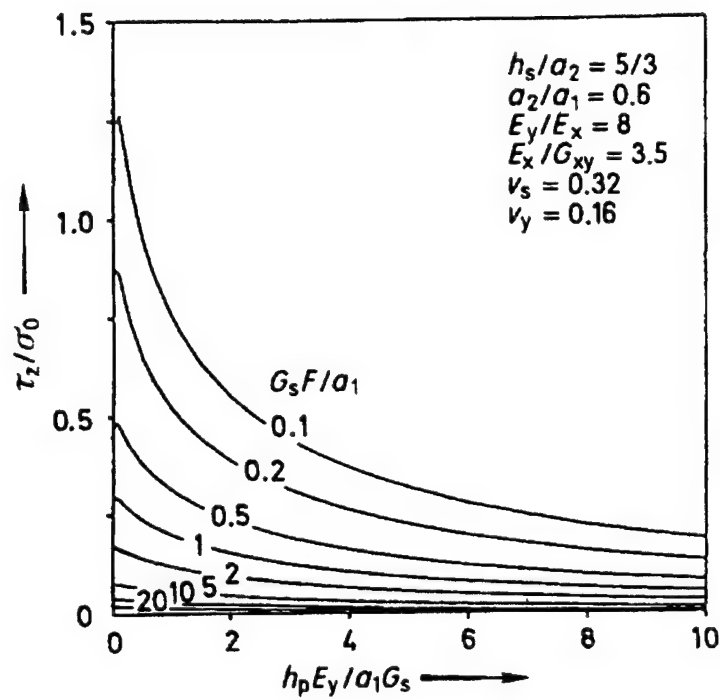


Figure 1.206: Effects of patch stiffness and adhesive flexibility on the shear stress in the adhesive at  $x = y = z = 0$



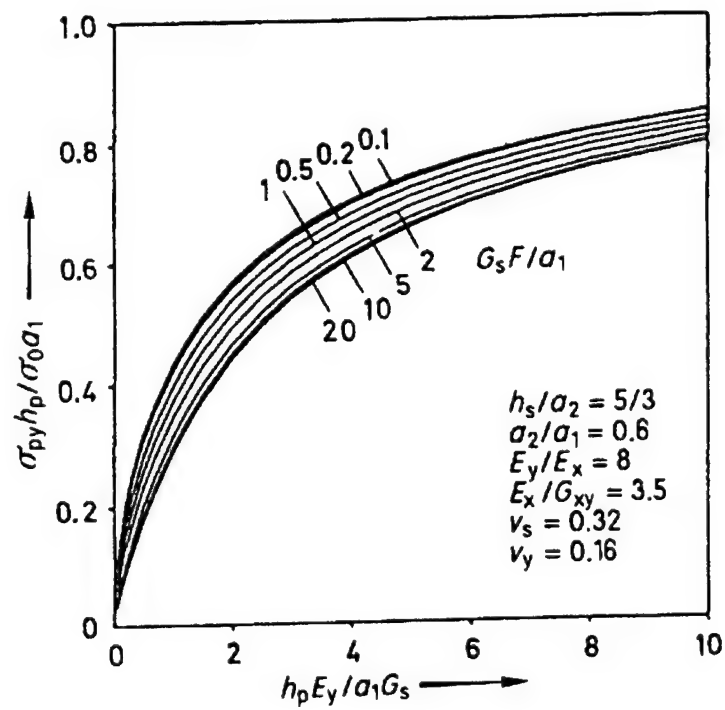


Figure 1.207: Effects of patch stiffness and adhesive flexibility on the tensile stress in the patch

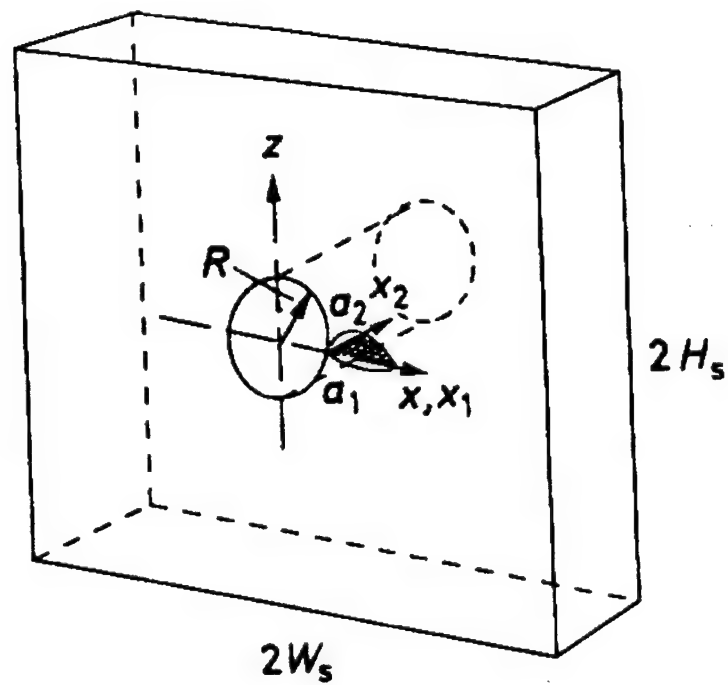


Figure 1.208: Schematic of a surface flaw near a fastener hole

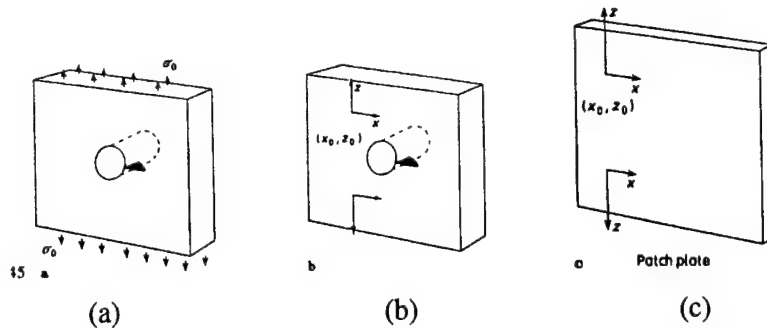


Figure 1.209: Linear superposition of basic problems in the analysis of patching of a surface flaw near a fastener hole

#### *Repair of a surface crack near a hole*

The problem is shown schematically in Fig. 1.208. To repair the crack, a patch of width  $2W_p$  and height  $2H_p$  is applied, such that the center of the patch coincides with the center of the hole.

The basic component problems to be analyzed are shown in Fig. 1.209a-c. For problem 1.209a, the displacement fields on the front surface and the stress intensity factors can be obtained by using the 3D finite element alternating technique [Atluri (1986)].

As for problem 1.209b, when a point force  $(X, Z)$  is applied at the point  $(x_0, z_0)$  and a symmetrical point load  $(X, -Z)$  is applied at  $(x_0, -z_0)$ , once again the 3D finite element alternating technique can be used.

In problem 1.209c, the displacement field in the patch is determined as before.

The finite element mesh used for problems 1.209a and b are shown in Fig. 1.210. The finite element mesh used for problem 1.209c is shown in Fig. 1.211.

The variations of the stress intensity factor along the crack front, with and without repair patch, are shown in Fig. 1.212. Once again, the significant reduction in the crack-growth retardation, achieved by the application of the patch, is evident.

### § 1.14 Analysis of Repaired Cracks in Pressurized Aircraft Fuselages

Repairs to pressurized fuselages have been done traditionally by using mechanical doublers. While bonding of metal structures and bonded repair techniques have existed for about 50 years now, bonded repairs have not gained as much acceptance as the mechanical doubler repairs. This is mainly due to the disappointing early ex-

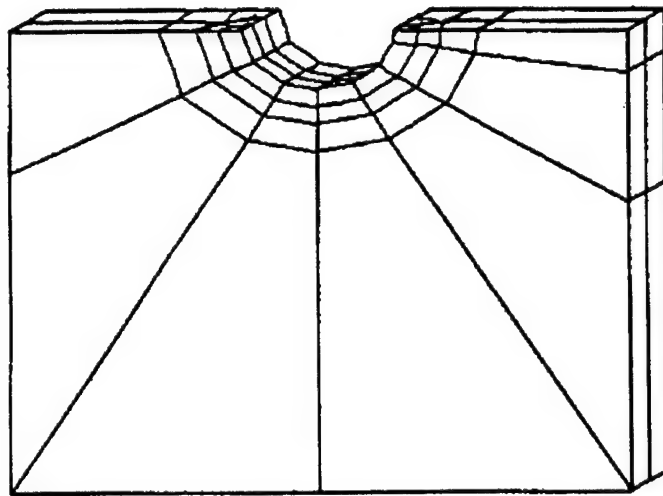


Figure 1.210: FEM mesh for base plate (56 ele., 401 nodes)

perience with bonding and the lack of widespread understanding of bonded repairs among technicians. This provides the motivation for the development of effective analysis techniques that can be implemented on low end workstations. In this investigation, the mechanical doubler repairs have been compared with bonded repairs in the repair of cracks in the fuselage skin. To analyze the effect of global loading (viz. pressure loading in the fuselage shell), on the essentially local feature of repair, a hierarchical approach has been used. This allows the fuselage to be modeled with increasing detail over smaller regions. At the global level, the fuselage is modeled as a shell, with stiffeners modeled as beams, and with flexible fasteners. In the intermediate stage the degree of modeling is improved. A section of the fuselage from the global stage is now analyzed, with the stiffeners being modeled with shell elements. The kinematic boundary conditions applied to this smaller intermediate region are obtained from the global solution. The stress results from this intermediate zone are later applied to a still smaller zone that is analyzed in the local stage; and this local analysis is used to evaluate the stress intensity factors for repaired or unrepaired cracks. The local stage uses a 2D finite element alternating method (FEAM) to model the crack. At this stage, the bending effects caused by a bonded patch on one side of the skin are ignored. This assumption is considered

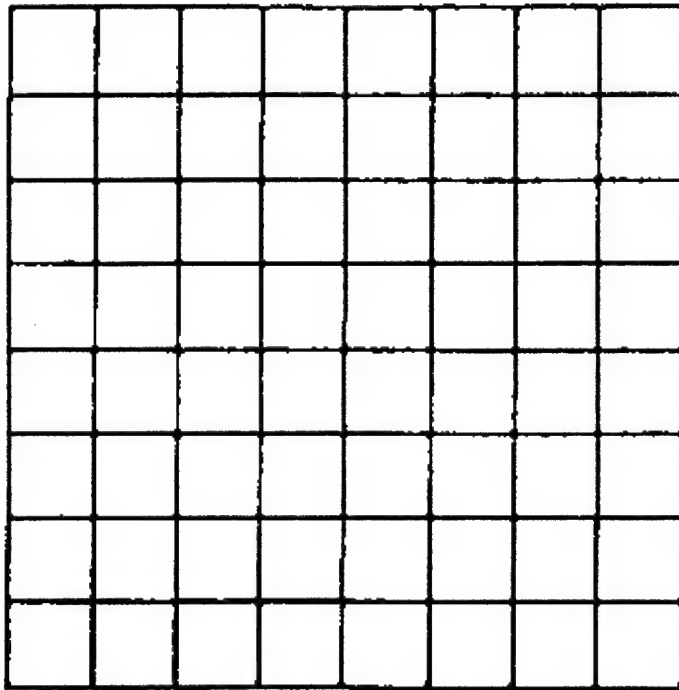


Figure 1.211: FEM mesh for patch plate, 64 2D 8 node isoparametric elements, 225 nodes

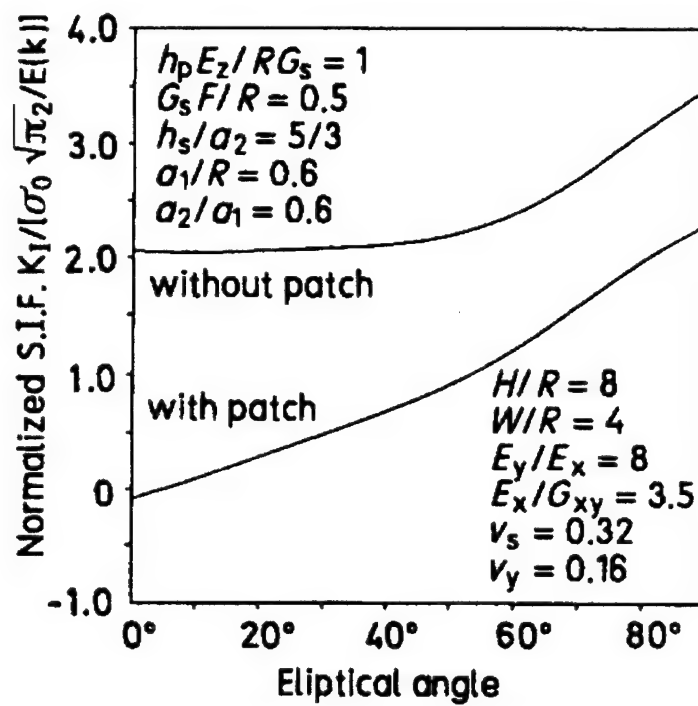


Figure 1.212: Variation of S.I.F near the border of a surface flaw near a fastener hole, with and without patching

sufficient as the substructure of the fuselage will restrict the effect of bending from being of any significance. The local analysis accounts for the non-linearity of the adhesive material by modeling it as an elastic perfectly plastic material. A large difference in the extensional stiffness of patch and the skin results in large strains being induced in the adhesive. Therefore, the necessity to model the adhesive as an elastic perfectly plastic material becomes more critical when the patch extensional stiffness is large when compared to the skin extensional stiffness. Using this approach the stress redistribution caused by mechanical doubler repair is compared with that caused by composite patch repairs. The residual strength and fatigue life of fuselages with composite patch repairs have been compared with those of the un-repaired case. The stress intensity factors have been evaluated by considering the adhesive as elastic material and as an elastic perfectly plastic material. Parametric studies of composite repairs are conducted using this methodology.

Most of the present day repairs to cracked aircraft fuselages are performed by using mechanical doublers. The cracked portion is cutout, a sheet is placed in the region thus created; and finally, another sheet is riveted to this cutout portion and the skin.

From the Second World War, successful applications of adhesive bonding have been made in aircraft structures. The Fokker F-27 aircraft is an example of successfully operating aircraft that has employed adhesive bonding for primary structure [Baker and Jones (1988)]. While such success stories exist, doubts about adhesive bonded repairs still exist. In this section we study such bonded repairs and compare them with mechanical doubler repairs.

There are several methods for the analysis of patched cracks. They can be broadly divided as

1. Analytical
2. Finite Element Approach

The analytical approach of Rose (1981) is an elegant method based on Hart-Smith (1974) theory of bonds, elastic inclusion analogy, and on some simplifying assumptions. Fredell (1994), in his exhaustive thesis, has extended this analysis to include thermal effects. He has also carried out an evaluation of mechanical doubler repairs. Erdogan and Arin (1972) have used integral equations approach to study the patched cracks. The assumptions of Erdogan and Arin were subsequently used by Ko (1978) and Hong and Jeng (1985) in the analysis of sandwich plates with part-through crack.

Jones and co-workers [Jones and Callinan (1979)], Mitchell, Wooley, and Chivirut (1975); Chu and Ko (1989) used finite element method to study patched cracks. Park, Ogiso, and Atluri (1992) have used an integral approach combined with FEAM to estimate the stress intensity factors for patched panels. Tarn and Shek (1991) have combined boundary element method approach (for the plate) and finite element method (for the patch) to estimate the stress intensity factors. Other work in this area includes Atluri and Kathiresan (1978); Sethuraman and Maiti (1989); Kan and Ratwani (1981).

In most of these approaches, only patches of infinite size, or very narrow strip type patches, or infinite sheet cases are considered. All of these cases are valid only for flat sheets. The loading for all these analyzes are hoop stresses evaluated from basic thin shell theory. While, in most cases this is a good approximation, this does not take into account the stress re-distributions due to the curvature and due to the presence of stiffeners.

The present work addresses the problem of the study of patched cracks in actual commercial airliner fuselages. A hierarchical modeling strategy is used to study the repairs to fuselages. The methodology is as follows. The whole of the fuselage is studied in the first stage. In the next stage, a portion of this is studied with an increase in complexity of the model. Finally a small portion around the crack and the repairs is studied to estimate the stress intensity factors. The procedure used to analyze the local zone is the finite element alternating method. This methodology to study repairs to fuselages. The stress re-distributions caused by mechanical doubler repairs is contrasted with those by patch repairs. The effect of various parameters such as the patch dimensions, patch material, patch thickness, adhesive material and adhesive thickness on patch efficiency is studied.

#### § 1.14.1 *Methodology*

The problem of cracks and their repairs is a localized phenomenon. The known loading conditions on the fuselage are essentially global – viz. the pressure loading. Therefore the analysis requirements are conflicting – a global loading and an essentially local phenomenon. This necessitates a hierarchical modeling strategy [Starnes and Britt (1991)]. Fig. § 1.14.1. This allows an increasing level of complexity and fidelity in the modeling without a prohibitively high computational effort.



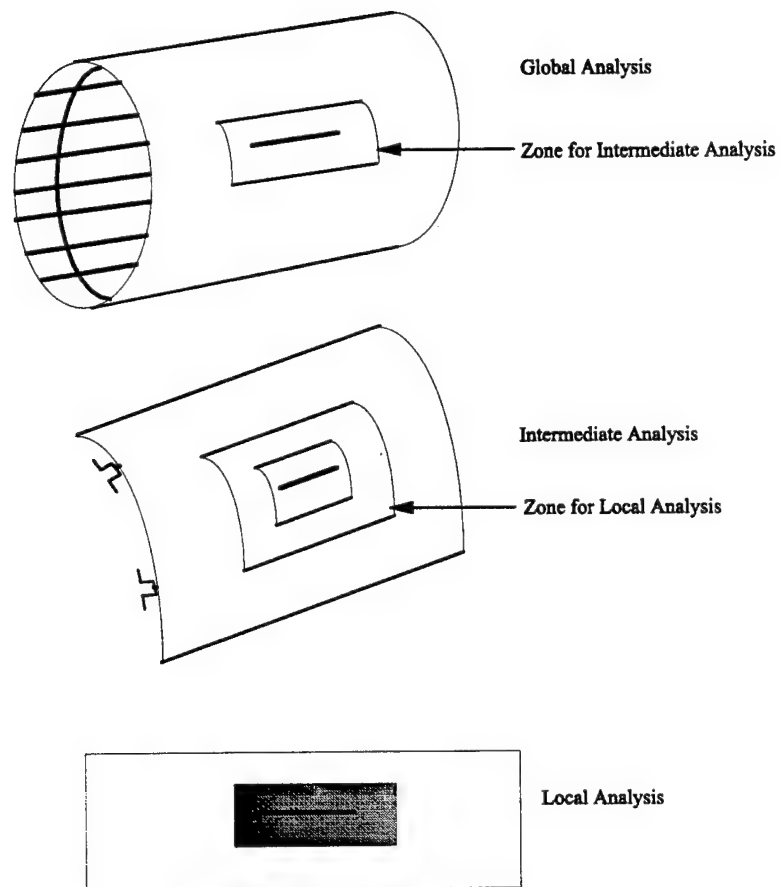


Figure 1.213: Schematic of the Hierarchical Modeling Strategy

### Local Analysis

The local analysis is a two stage analysis. They are

1. Evaluation of the stresses exerted by the adhesive and patch on the sheet, using a coarse mesh.
2. The stresses obtained from stage 1 are applied as body forces on the base sheet, and the finite element alternating method is used to find the stress intensity factor.

In step 1, a traditional finite element methodology is used to deduce the stresses exerted by the patch. As the crack tip is not meshed for the singularity, a coarse mesh is sufficient for this purpose. The sheet and the patch are modeled with eight noded 2D elements. The adhesive is modeled by elements as in Jones and co-workers [Jones and Callinan (1979)], Mitchell, Wooley, and Chivirut (1975). This element is obtained by assuming a constant shear stress in the adhesive. Under the present conditions the shear stress can be obtained from

$$\tau_{xz} = \frac{u_s - u_p}{\frac{t_a}{g_a} + \frac{3}{8} \left( \frac{t_s}{g_s} + \frac{t_p}{g_p} \right)} \quad (1.139)$$

$$\tau_{yz} = \frac{v_s - v_p}{\frac{t_a}{g_a} + \frac{3}{8} \left( \frac{t_s}{g_s} + \frac{t_p}{g_p} \right)} \quad (1.140)$$

where  $u$  and  $v$  are the displacements in the  $x$  direction and  $y$  direction respectively,  $t$ ,  $g$  are the thickness and shear modulus respectively. The subscripts  $a$ ,  $s$  and  $p$  refer to the adhesive, sheet and the patch respectively.

Large strains are induced in the adhesive when the difference between the patch stiffness and sheet stiffness is large. Therefore, this results in the yielding of the adhesive. This reduces the patched efficiency, and a linear elastic analysis would grossly overestimate the efficiency and would be anti-conservative. Therefore, the adhesive is modeled as an elastic perfectly plastic material. As there is no unloading (crack growth is not considered), a deformation theory of plasticity is considered sufficient. An initial stress algorithm [Nayak and Zienkiewicz (1972)] has been implemented. In view of the model as in Jones and co-workers [Jones and Callinan (1979)], Mitchell, Wooley, and Chivirut (1975), the Von Mises yield criterion reduces to

$$\sqrt{\tau_{yz}^2 + \tau_{xz}^2} = \sigma_{yp} / \sqrt{3} = \tau_{yp} \quad (1.141)$$

The algorithm for this is as follows

1. A load step is taken and the displacements are found.
2. The stresses are computed at each Gauss Point and yielding is checked for.
3. The residual load is computed.
4. The displacements for this residual load are then computed.
5. Repeat steps 2, 3 and 4 for convergence. Convergence is reached when there is no yielding at any Gauss point.
6. Repeat the steps 1, 2, 3, 4 and 5 for more load steps till the desired load is reached.

In finite element alternating method, the stresses in the uncracked body are first analyzed, by a traditional finite element method, for the given system of external loading. To model the crack, the tractions at the locations of the crack in an otherwise uncracked body must be erased.

#### § 1.14.2 *Analysis of repaired cracks*

The fuselage as described by Tab. 1.21 is used for the various test cases studied. The stringers used are of hat cross section and the frames are of Zee cross section. The stiffener properties are given in Tab. 1.22. It is noted that the frame is attached to the sheet on the tearstraps. This is considered as an approximation to attaching the frame to the sheet with shear clips. In view of the unavailability of the exact stiffener dimensions this is considered sufficient. The crack is assumed to be a mid-bay crack. The rivets used are NAS1097DD6 rivets of 0.15625 in diameter.

The dimensions of the different models are given in Tab. 1.23. The finite element meshes used for various models are shown in Fig. 1.214, Fig. 1.215 and Fig. 1.216.

#### *Patch repairs*

The above fuselage is repaired with a patch of dimensions 5 in X 3 in as shown in Fig. 1.217. The patch is 0.04 in thick and is made of Boron Epoxy. The adhesive is 0.004 in thick and has a shear modulus of 104.73 ksi with 5.250 ksi being the Yield Point in shear.

To analyze the effect of the patch, the crack length was varied from 1 in to 16 in. The variation of the stress intensity factor,  $K_I$ , with the crack length is shown in Fig. 1.218. (Unless otherwise noted all the stress intensity factors are in  $\text{ksi}\sqrt{\text{in}}$  and the crack lengths are in in.) The efficiency of crack patching is plotted in Fig. 1.219.

Table 1.21: Properties of The Fuselage Shell

Internal Pressure	9.0 psi
Radius	78 in
Thickness	0.036 in
Material	Al 2024T3
Young's Modulus	10,500 ksi
Poisson's Ratio	0.33
Yield Point	47.0 ksi

Table 1.22: Stiffener Properties

Rivet Specification	NAS1097DD6
Rivet Diameter	0.15625 in
Stringer Spacing	9.25 in
Stringer Area	0.0384 in <sup>2</sup>
Stringer Moment of Inertia	0.162 in <sup>4</sup>
Axis to skin distance	0.465 in
Frame Spacing	20.0 in
Frame Area	0.1248 in <sup>2</sup>
Frame Moment of Inertia	0.3271 in <sup>4</sup>
Axis to skin distance	1.148 in
Tear Strap Thickness	0.036 in
Tear Strap Width	2 in

Table 1.23: Dimension of different fuselage models

Global Region Length	100 in
Global Region Arc Length	46.25 in
Intermediate Region Length	40 in
Intermediate Region Arc Length	18.5 in
Local Region Length	10 in
Local Region Width (Arc Length)	8 in

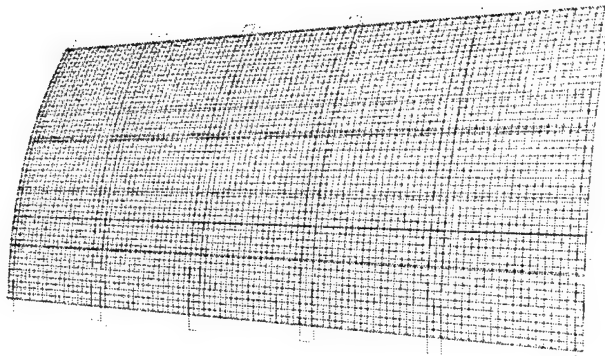


Figure 1.214: Mesh for Global Analysis

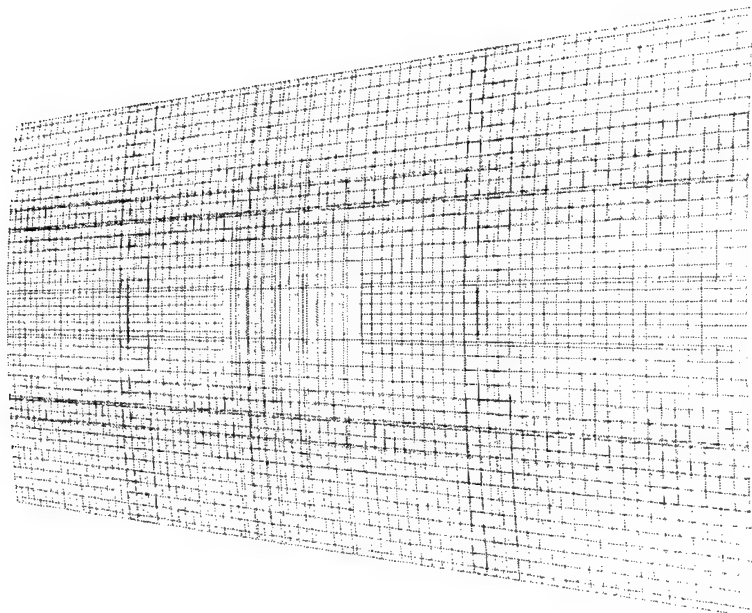


Figure 1.215: Mesh for Intermediate Analysis

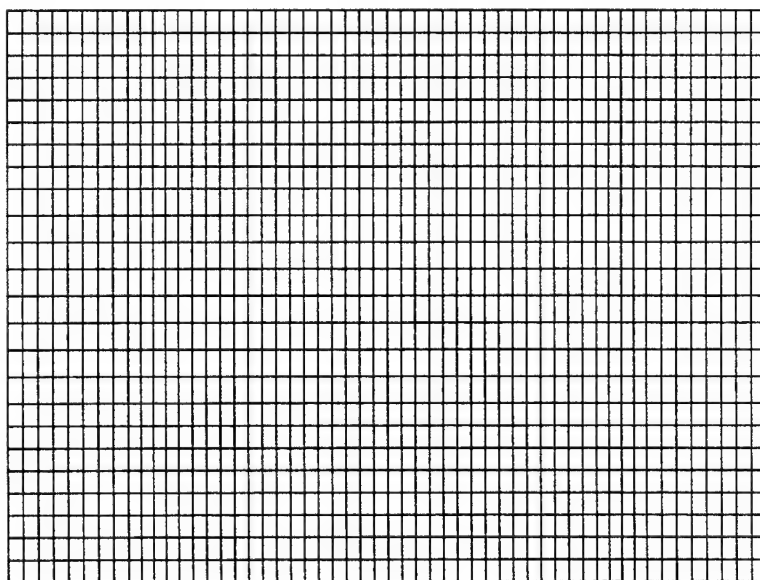


Figure 1.216: Mesh for Local Analysis

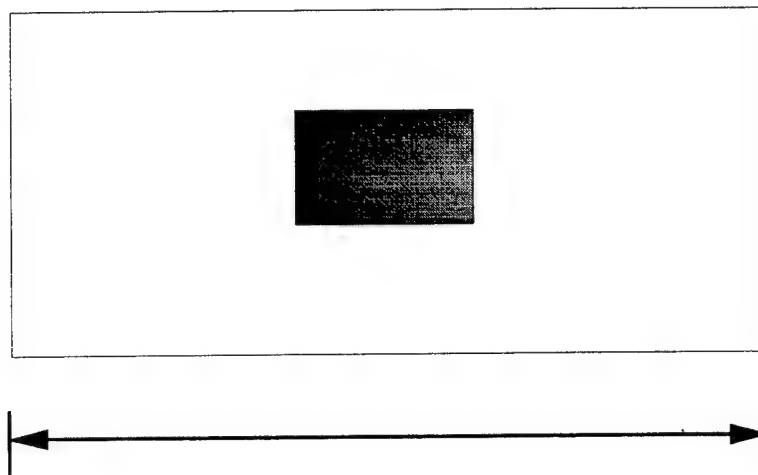


Figure 1.217: Geometry of the Local Zone showing the patch

The efficiency is defined as

$$= \frac{SIF_{unpatched} - SIF_{patched}}{SIF_{unpatched}} \times 100$$

The asymptotic nature of the stress intensity factor, as in Fredell (1994) and Baker and Jones (1988) is clearly observed. Unlike the methodology of Rose (1981) and Fredell (1994), the present methodology can analyze cracks longer than the width of the patch. It is seen that while the stress intensity factors show a significant increase as the crack emerges from the patch, it still demonstrates an asymptotic behavior. In these two situations, viz. crack shorter than the width of the patch and longer than the width of the patch, the patch transfers load in significantly different ways. When the crack is shorter than the width of the patch, most of the load is transferred by the edges of the patch parallel to the crack. This is seen from the Fig. 1.221, where the effective stress in the adhesive has been plotted. As the crack grows longer than the width of the patch, the regions near the crack tips also start to transfer the load and the patch transfers the load as in bonded overlap joints. This is shown in the effective stress in the adhesive contour plot Fig. 1.222. This increase in the effective stress lead to a final yielding of the adhesive. Once the adhesive yields, a very significant reduction in the effectiveness in seen. (Fig. 1.219 and Fig. 1.220).

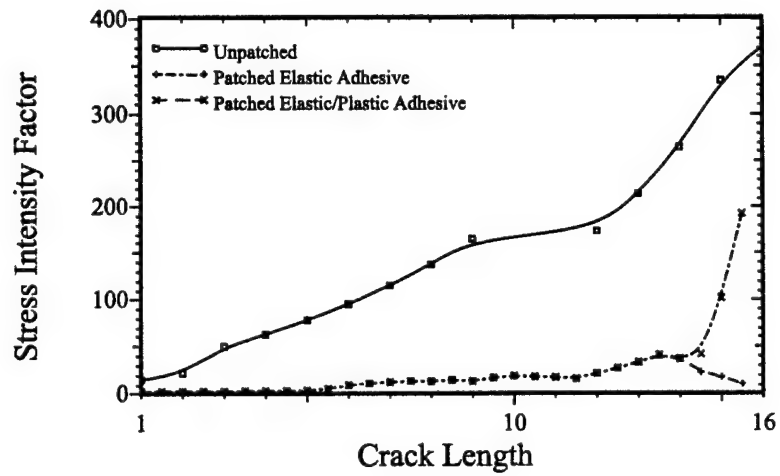


Figure 1.218: Stress Intensity factors Vs. Crack Length

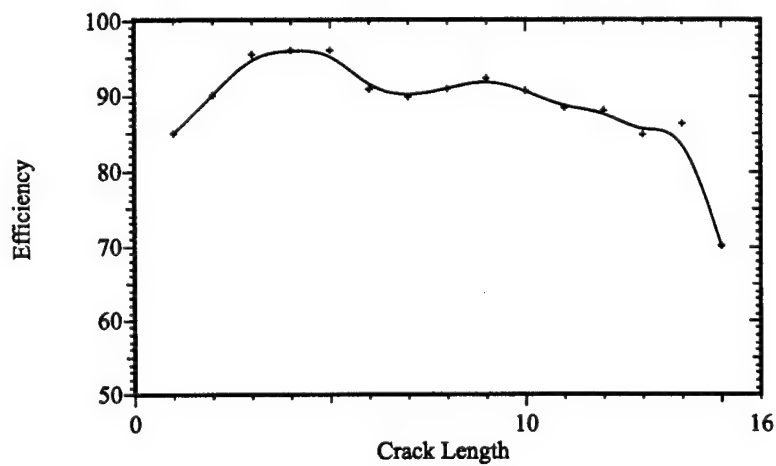


Figure 1.219: Efficiency of Crack Patching



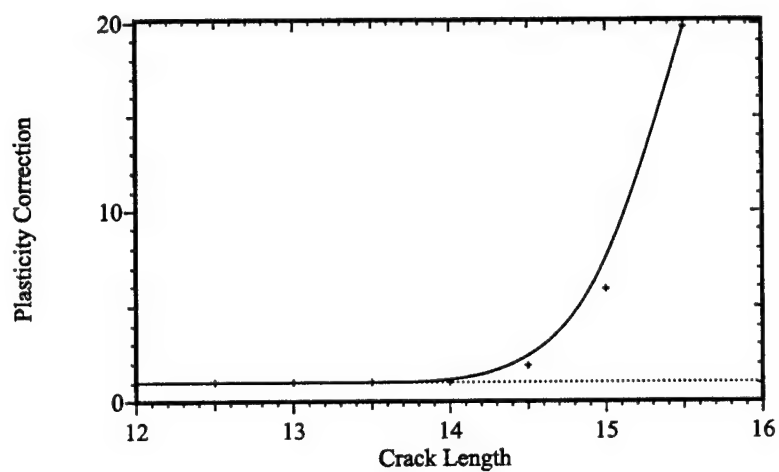


Figure 1.220: Effect of Plasticity



Figure 1.221: Effective Stress in the Adhesive for Crack Length 3 in

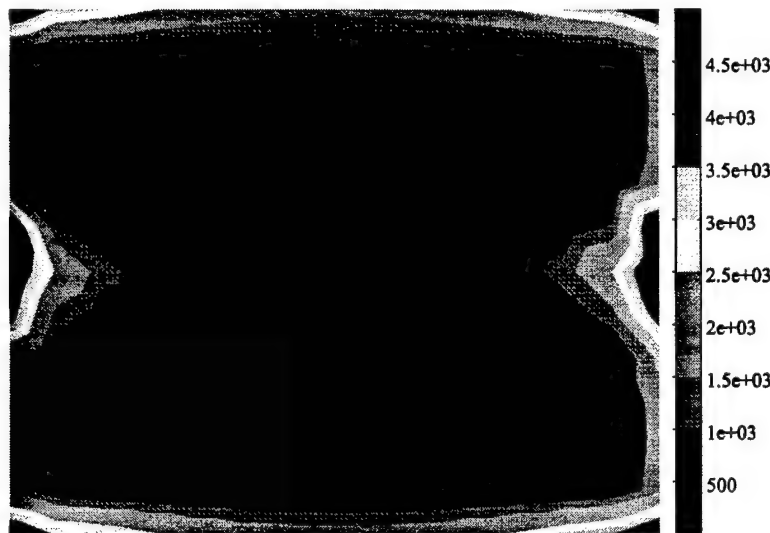


Figure 1.222: Effective Stress in the Adhesive for Crack Length 15 in

#### *Patch repairs and mechanical doubler repairs*

A mechanical doubler repair, Fig. 1.223, for the above mid-bay cracked fuselage is also analyzed. The axial (Fig. 1.224) and hoop stress (Fig. 1.225) resultants for the doubler repaired fuselage has been compared with that of the composite patch (Fig. 1.226 and Fig. 1.227) repaired fuselage and the intact fuselage (Fig. 1.228 and Fig. 1.229). As can be seen, a patch repair, despite the presence of the singularity involves a much lower value stress. In the doubler repair case, the cutout provides a site for stress concentration. Therefore, the maximum hoop stress in the doubler repair case increases from 19.1 ksi in the intact fuselage to 30 ksi. Whereas, in the fuselage repaired with a patch, the hoop stress went up marginally to 19.4 ksi. A similar pattern is also seen in the axial stresses where the stresses went up from 6.5 ksi to 11.7 ksi.

#### *Effect of patch geometry*

To study the effect of the patch overlap length of the patch (the length along the y direction), it was varied from 1.5 in to 3.5 in. The results are in Fig. 1.230. The patch is 5 in wide and 0.04 in thick and is made of Boron/Epoxy composite. The adhesive is 0.004 in thick and has a shear modulus of 104.73 ksi.

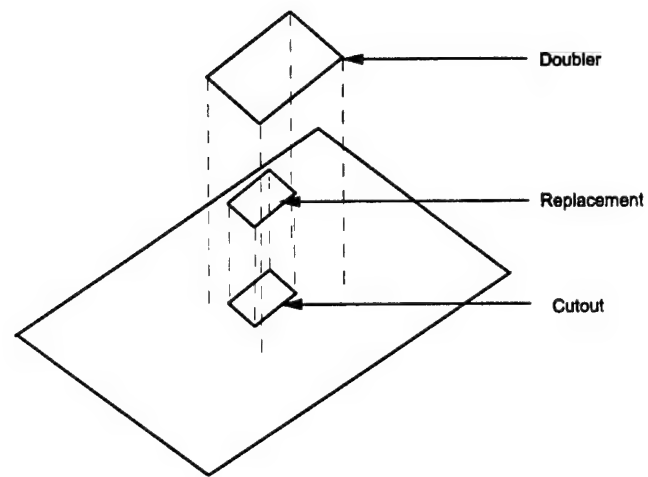


Figure 1.223: Geometry of the doubler repair

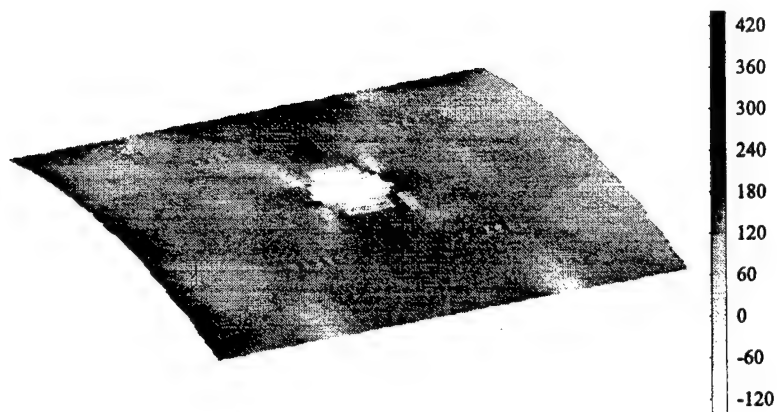


Figure 1.224: Axial Stress Resultant for Doubler Repair

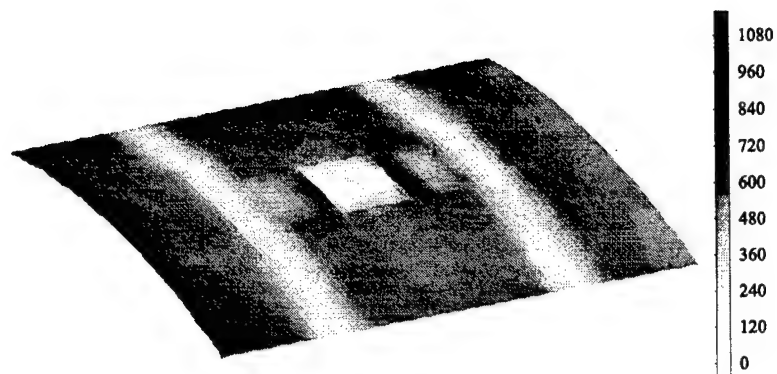


Figure 1.225: Hoop Stress Resultant for Doubler Repair

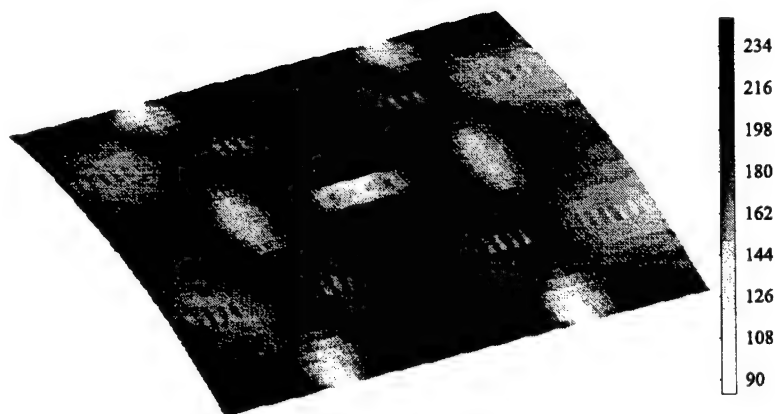


Figure 1.226: Axial Stress Resultant for Patch Repair

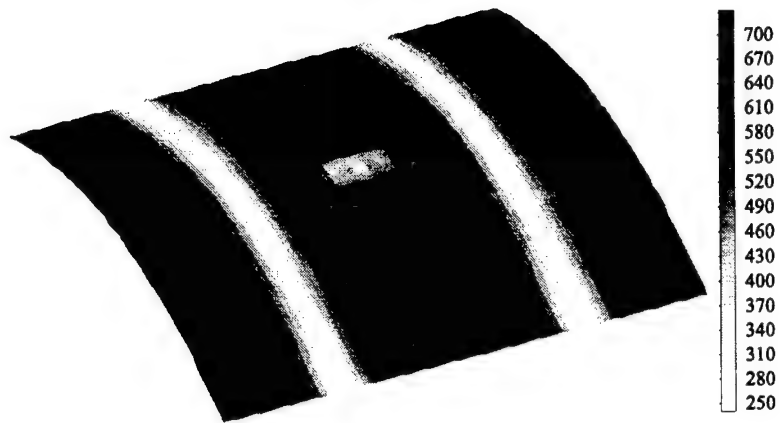


Figure 1.227: Hoop Stress Resultant for Patch Repair

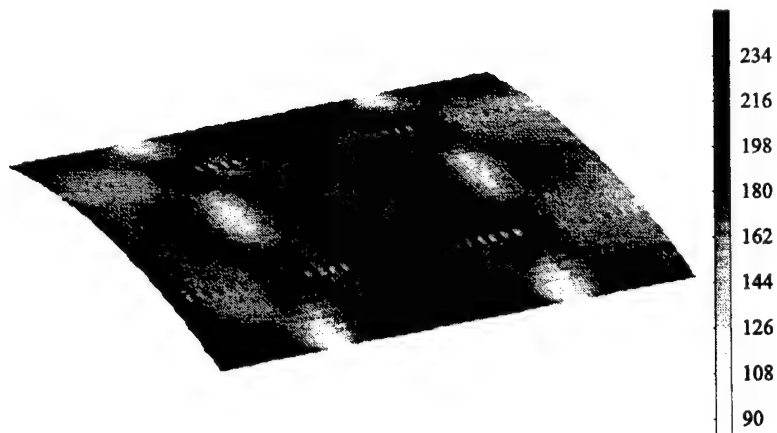


Figure 1.228: Axial Stress Resultant for Intact fuselage

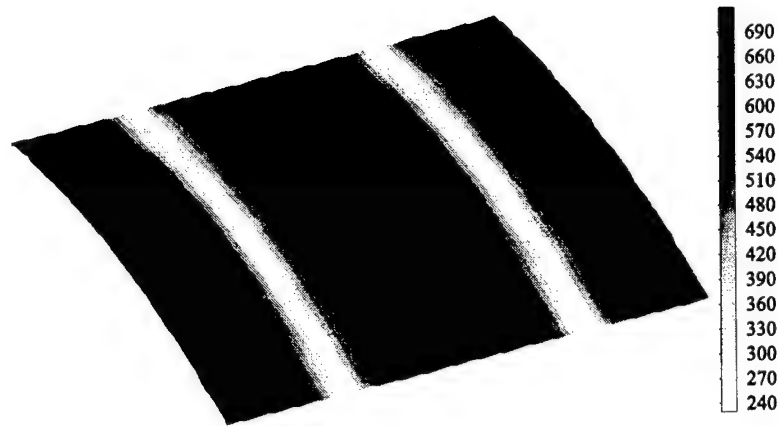


Figure 1.229: Hoop Stress Resultant for Intact Fuselage

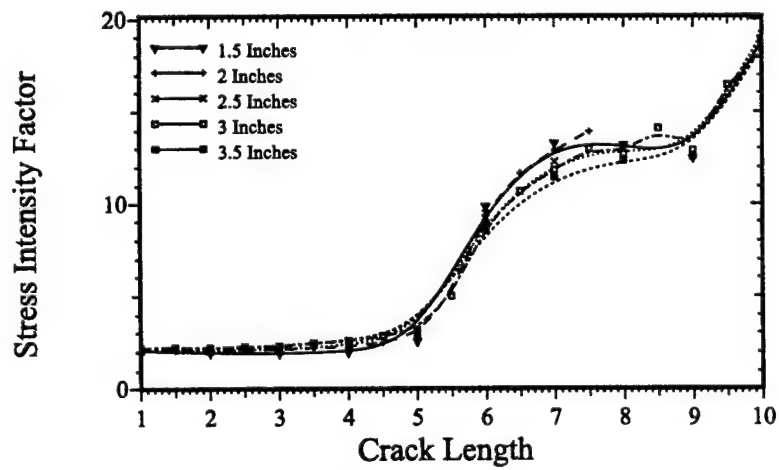


Figure 1.230: Effect of Patch Overlap Length on Stress Intensity Factor

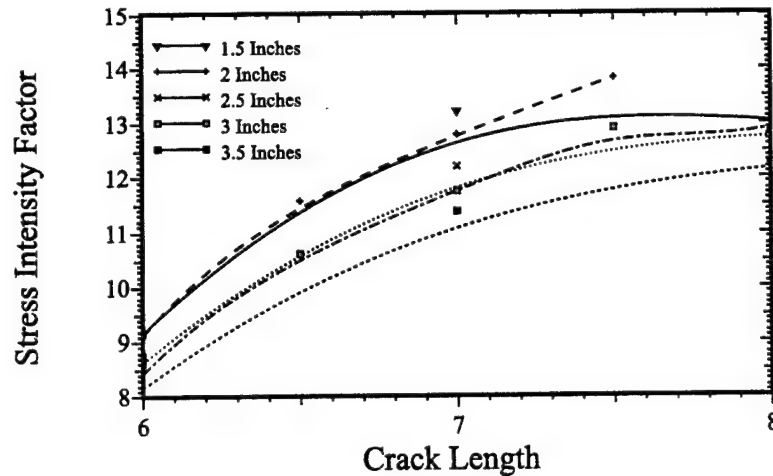


Figure 1.231: Effect of Patch Overlap Length on Stress Intensity Factor

When the crack is longer than the width of the patch, the patch serves to transfer the load across the crack and reduce the ligament stress near the crack tip. Therefore, a longer patch, having a longer overlap length and therefore larger area transfers this stress better and therefore perform better than the shorter patches (Fig. 1.230 and Fig. 1.231). Whereas, when the crack is shorter than the width of the patch, the longer patches perform poorly (Fig. 1.232). The composite system of the patch, adhesive and the sheet attracts parasitic load from other regions in the sheet, [Baker and Jones (1988)]. When the crack is shorter than the width of the patch, this parasitic load attraction, increases the load near the crack tip. Larger patches attract larger parasitic loads, therefore they perform poorly when compared to shorter ones. When the crack is longer, this parasitic load attraction does not increase the load near the crack tip, therefore a similar behavior is not seen in those cases.

The patch width is varied from 4 in to 8 in. The results are shown in Fig. 1.233. The patch is 3 in long, and 0.04 in thick and is made of Boron/Epoxy. The adhesive properties remain the same as above. As was illustrated earlier, the stress intensity factors show two asymptotic values, one obtained when the crack is shorter than the width of the patch and the other when the crack is longer than the width of the patch. When the crack is shorter than the width of the patch, the asymptotic value reached does not vary much with the patch width. While wider patches cause the second asymptotic value to be reached at a longer crack length (the cracks emerge

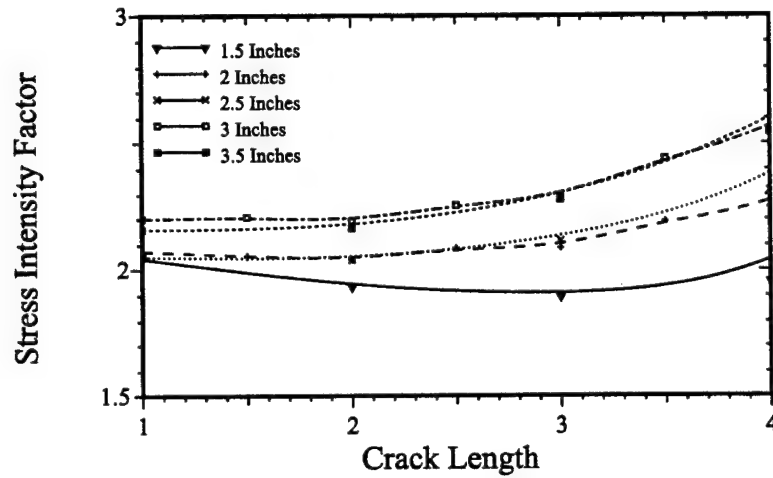


Figure 1.232: Effect of Patch Overlap Length on Stress Intensity Factor

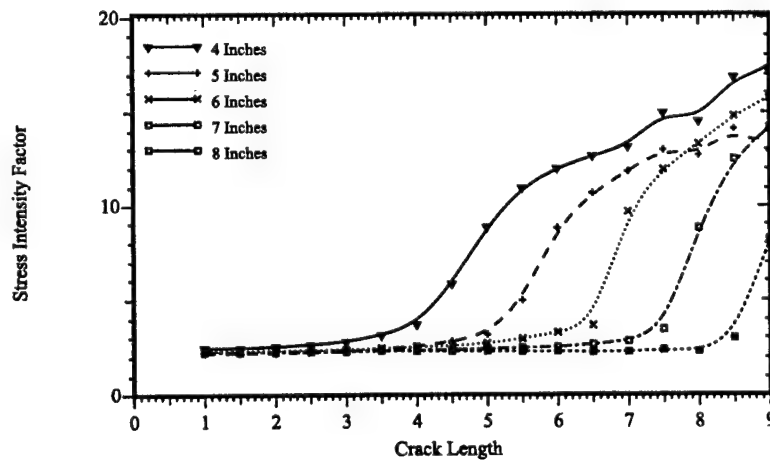


Figure 1.233: Effect of Patch Width on Stress Intensity Factor



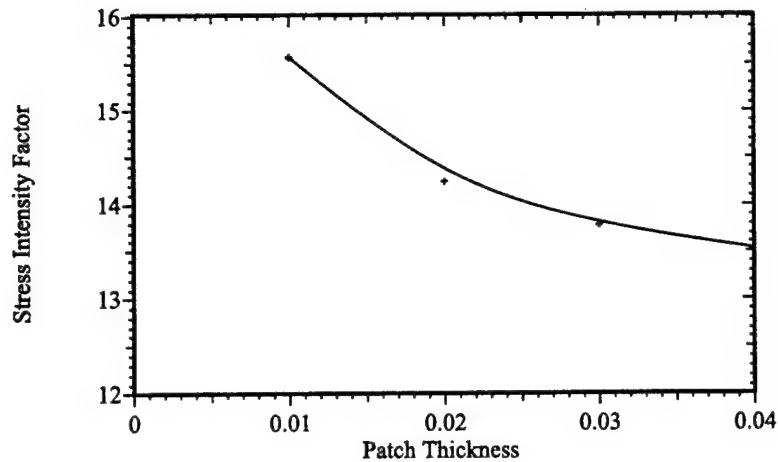


Figure 1.234: Effect of Patch Thickness on Stress Intensity Factor

from the patch later with wider patches), the asymptotic value reached does not appear to change. Therefore the narrower patches also seem to perform adequately. Wider patches, because of larger areas, have better damage tolerance.

The patch thickness was varied from 0.01 in thick to 0.04 in. The patch is 5 in wide and 3 in long and is made of Boron/Epoxy. As expected, thicker patches perform better (Fig. 1.234).

#### *Effect of patch material*

To evaluate different materials as possible candidates for patching materials several are investigated, following Fredell (1994). The properties of the materials are given in Tab. 1.22. In each of the cases the patch is 5 in wide and 3 in long and 0.04 in thick. The adhesive shear modulus is 104.7 ksi and the thickness considered is 0.004 in. The Yield Strength of the adhesive is taken as 5254 psi. The results are depicted in Fig. 1.235.

The composite patches perform the best, followed by Al 2024-T3, and finally the metal laminate GLARE. When the crack is under the patch, the difference is marked. But once the crack becomes longer than the width of the patch, the difference is marginal. When the crack is shorter than the width of the patch, the induced strains cause larger stress to be transferred in stiffer patches. Therefore, the load near the crack tip is reduced and the stress intensity factor reduction is more pronounced for stiffer patches. On the other hand when the crack is longer than the

Table 1.24: Properties of Various Patching Materials Considered

Material	$E_1$	$E_2$	$\nu_{12}$	$G_{12}$
Boron/Epoxy	$3.02 \times 10^7$ psi	$3.69 \times 10^6$ psi	0.1677	$1.05 \times 10^6$ psi
Carbon/Epoxy	$1.97 \times 10^7$ psi	$1.814 \times 10^6$ psi	0.30	$1.015 \times 10^6$ psi
Al 2024-T3	$1.05 \times 10^7$ psi	$1.05 \times 10^7$ psi	0.32	$3.977 \times 10^6$ psi
GLARE	$9.565 \times 10^6$ psi	$7.358 \times 10^6$ psi	0.33	$2.685 \times 10^6$ psi

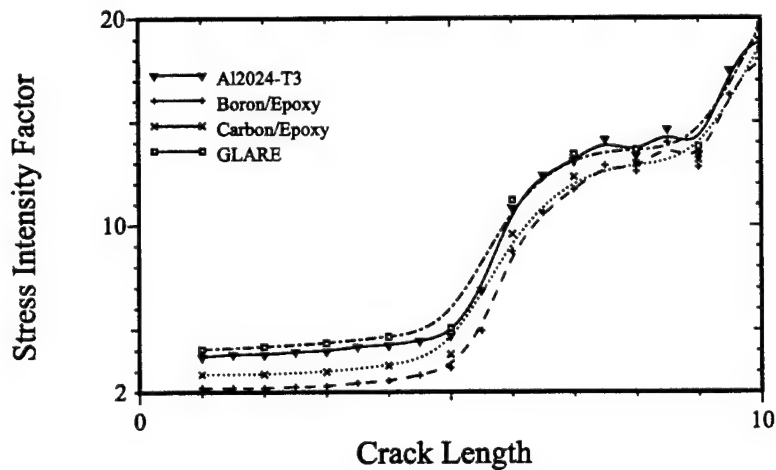


Figure 1.235: Comparison of Different Patching Materials

width, the patch transfers the load as in a bonded lap joint and the load transferred is the ligament stress and has little relationship with the stiffness. This is confirmed by the fact that when the crack is extremely long, the stress intensity factor for patched cracks, with patch of various materials is almost the same.

#### *Effect of adhesive properties*

With the effect of the patch material and geometry determined the effect of the adhesive is now examined. With the boron-epoxy patch of 5 in X 3 in X 0.04 in, the adhesive thickness is varied from 0.001 to 0.005 for a crack of length 8 in. The results are shown in Fig. 1.236. Thin adhesive layers perform better than thick

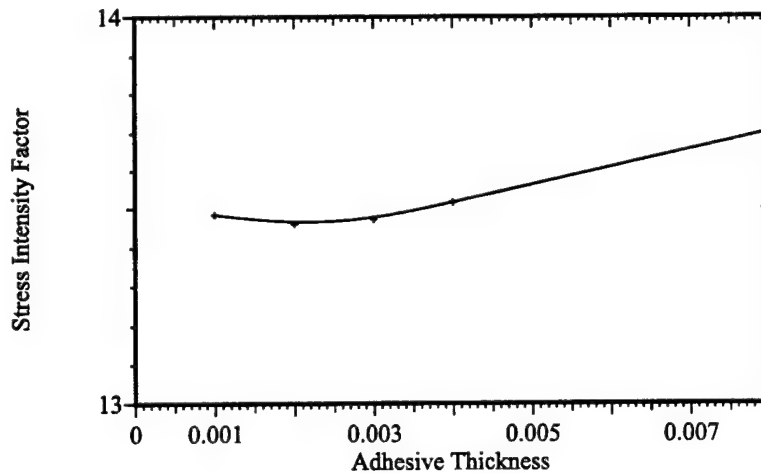


Figure 1.236: Effect of Adhesive Thickness on Patching Materials

adhesive layers because, a thick adhesive makes the composite system of the sheet, adhesive layer and patch softer. Often, a thick adhesive layer is needed for good durability as a thick adhesive will experience lesser strains. As can be seen from Fig. 1.237 the detrimental effect of having a thick adhesive is not severe.

The shear modulus of the adhesive is varied for the same patch dimensions and for 0.004 in thick adhesive. The result is shown in Fig. 1.237. As can be seen, stiffer adhesives were found to perform better. While, the conditions considered were insufficient for adhesive yield, a stiffer adhesive would result in the yield point being reached earlier. Thus, the material would yield and reduce the patch effectiveness as illustrated earlier. This being the case, it is also noted that the advantage in using a stiffer adhesive (in terms of stress intensity reduction) is not significant.

#### § 1.14.3 *Effects of Adhesive Nonlinearity, thermal Cycling & Debonding*

Comparison with the experimental data obtained by Denny (1995) has been carried out to determine the ability of the finite element alternating method in predicting the fatigue response of a cracked metal panel with a partially debonded composite patch. There is a total of 15 different specimens considered in this comparison. Some of the parameters that are varied in these specimens include the disbond location, the disbond area, the initial crack length, the maximum stress loading and the stress ratio. For all these specimens, it has been found that the numerical results

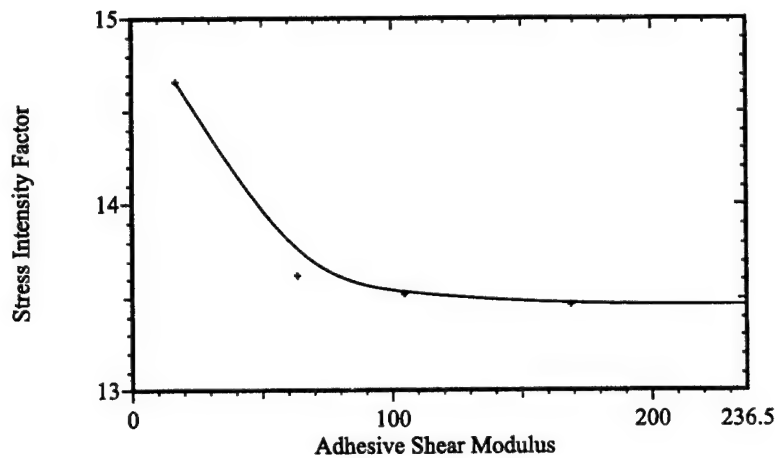


Figure 1.237: Effect of Adhesive Shear Modulus on Stress Intensity Factor

correlate very well with the experimental data, when the adhesive nonlinearity is properly accounted for in the analysis. In addition to this comparison with the experimental data, numerical studies have been carried out to examine the effect of the thermal cycling on the fatigue response of a bonded repair. It was found that due to the strong difference in the thermal expansion coefficient of the boron/epoxy patch and the aluminum panel, the fatigue life of a specimen which undergoes cycles of high-stress-at-low-temperature and low-stress-at-high-temperature loading is dramatically reduced. It was also found that the fatigue life of a specimen which undergoes a thermal-fatigue cycle is more sensitive to disbonds in the adhesive layer than a similar specimen which undergoes fatigue loading at a constant temperature. In addition to this study, numerical analysis has been carried out to study the interaction between two nearby composite patches. The study found very little interactions between the two patches when these two patches lie horizontal to each other. On the other hand, when the two patches lie vertical to each other, the fatigue life of this specimen can increase substantially when these two patches are very close to each other; however this may lead to failure of the metal in between the patches, but this is not considered in the present study.

In general, the analysis of fatigue crack growth for composite repairs can be broadly categorized as either analytical or numerical. Based on the elastic inclusion analogy, Rose (1982) has obtained the solution for strip type patches by using a successive approximation method to deduce the asymptotic behavior of the

modeled Fredholm integral equation. Rose (1988) further extended this method to obtain an approximate solution for a crack inside an elliptical patch. The solution for the elliptical patch is further extended by Fredell (1994) to include the effect of temperature. While the solution for Rose's model is simple and easy to implement, these solutions have strong limitations. Some of the limitations of the Rose's model include the assumptions that:

- the patch has to be either an infinite strip type or an elliptical shape type,
- the material behavior for the adhesive layer is linear elastic,
- the load transfer length must be significantly smaller than the patch size, i.e. the adhesive must be relatively stiff, or the size of the patch must be significantly large,
- the bonding of the patch is perfect without disbonds, and
- the size of crack is small compared to the size of the patch.

All of these assumptions limit the ability of the Rose's model to adequately analyze the effectiveness of most composite patches in reducing the fatigue crack growth. Therefore to overcome these limitations, numerical methods have been employed in analyzing the effectiveness of repairs using composite patches. Jones and Callinan (1979); Mitchell, Wooley, and Chivirut (1975); Chu and Ko (1989) have used the finite element method to study bonded patch repairs. Tarn and Shek (1991) have combined the boundary element method (for the plates) and finite element method (for the patch) to estimate the stress intensity factors. Park, Ogiso, and Atluri (1992) have applied the integral equation approach in conjunction with the Schwartz-Neumann alternating method to calculate the stress intensity factors. In extending this work, the approach of the finite element alternating method was applied by Nagaswamy, Pipkins, and Atluri (1996) to model a rectangular composite patch on a curved fuselage panel where the stress distributions due to curvature as well as the presence of stiffeners are accounted for. While these studies provide the methods to analyze a composite patch with perfect bonding, there have been few studies which concentrate on the verification of numerical analysis against experimental results especially when delaminations exist on bonded repairs.

Roderick (1980) have examined the cyclic growth of a crack inside an elliptical disbond of a composite patch. Baker (1993) has studied experimentally the effectiveness of composite repairs with disbond that occur during manufacturing. Denny (1995) has experimentally investigated the fatigue life of composite patch with intentional disbond of various locations and size. This experiment also studies

Table 1.25: Material properties for the aluminum panel, boron/epoxy patch, and adhesive layer

Material	$E_L/E_T/G$ (GPa)	Poisson Ratio	CTE $\alpha_L(10^{-6}/^{\circ}C)$	Thickness (mm)
2024-T3	72.4/72.4/27.2	0.33	22.7	1
Boron/Epoxy	210/25/72.4	0.168	4.5	0.127
AF-163-2	NA/NA/0.405	-	-	0.127

the effect of initial crack length, maximum applied fatigue stress and stress ratio. In this section, analyses are performed using the finite element alternating method (FEAM) to study the fatigue life of partially bonded patches under different loading conditions. These numerical results are compared with the experimental data obtained by Denny (1995) to determine the ability of FEAM in predicting the fatigue life of partially bonded patches. Since debonds in bonded repairs are found frequently and the replacement of defective patches remains very difficult, the ability to predict the fatigue characteristic of partially bonded patches, and hence determining the safety of the repaired structure would be an extremely important issue to be resolved before bonded repairs can be used widely in the aerospace industry. In addition to the comparison with the experimental results, this paper also evaluates the effects of (i) temperature cycles, (ii) initial stresses due to the curing of the patch, and (iii) adhesive nonlinearity, on the fatigue characteristics of partially bonded patches. Furthermore, the interaction of two composite patches on fatigue life is also studied.

The composite patch analysis presented in this section is to demonstrate the ability of the finite element alternating method in predicting the fatigue response of a cracked panel with partially bonded composite patch. For the present study, numerical analysis has been carried out to model the experiment performed by Denny (1995) on partially bonded composite repairs. In his experiment, the patch (made of three plies of unidirectional boron/epoxy laminate) is bonded to a 2024-T3 aluminum panel with AF-163-2 film adhesive. The dimensions of the geometry for the composite patch and aluminum panel are given in Fig. 1.238. The material properties of the boron/epoxy laminate, aluminum panel and adhesive layer are given in Tab. 1.25. In the current analysis, the patch and the panel are modeled with 8-noded isoparametric plane stress elements. The adhesive film is modeled

Table 1.26: Details of the specimens modeled

Specimen	Configuration	Disbond Area(%)	Peak Load (MPa)	$R$ $\sigma_{min}/\sigma_{max}$
3	CBP	0	120	0.15
4	FWD	20	120	0.10
5	FWD	20	120	0.10
6	CTD	20	120	0.10
7	CTD	20	120	0.10
10	CBP	0	120	0.10
11	FWD	10	120	0.10
13	FWD	20	100	0.10
14	FWD	5	120	0.10
16	CD	10	120	0.10
17	CD	5	120	0.10
20	CBP	0	120	0.10
21	CBP	0	120	0.10
23*	CBP	0	120	0.10
24*	CBP	0	100	0.10

\* Initial crack length = 12.7 mm instead of 25.4 mm in other specimens.

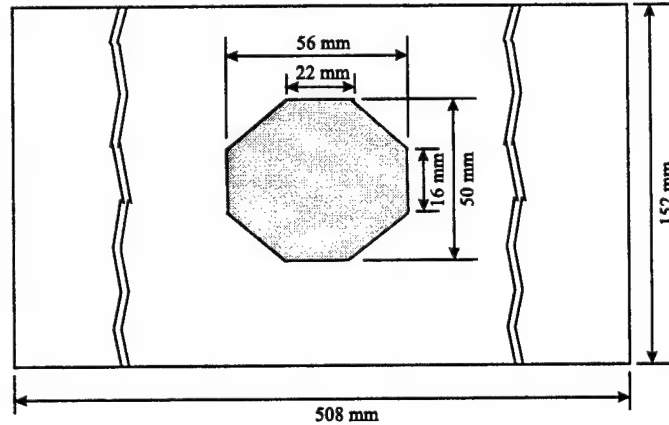


Figure 1.238: Geometry of the aluminum patch with the boron/epoxy patch

with isoparametric 16-noded adhesive elements developed by Chu and Ko (1989). The adhesive element is based on a linear adhesive relationship between the shear stress and the difference of displacements between the patch and the panel:

$$\tau = K_{ADHE} (u_{patch} - u_{panel}) \quad (1.142)$$

$$K_{ADHE} = \left[ \frac{t_{adhe}}{G_{adhe}} + \frac{3}{8} \left( \frac{t_{patch}}{G_{patch}} + \frac{t_{panel}}{G_{panel}} \right) \right]^{-1} \quad (1.143)$$

Here  $u$  is the displacement,  $t$  is the thickness and  $G$  is the shear modulus. In general, the shear modulus of an adhesive material is strongly nonlinear, but due to the lack of experimental data available, this nonlinear behavior can be approximated with an effective linear shear modulus. This effective modulus would be a function of the average shear strain on the adhesive layer.

The finite element mesh for the composite patch on the aluminum panel is shown in Fig. 1.239. The mesh contains 4176 elements and 9337 nodes. To calculate the stress intensity factors of a cracked panel under a composite patch, two steps are involved. In the first step, the crack in the panel along with the composite patch and the adhesive layer are explicitly modeled in the finite element mesh. From the finite element solution, the shear stress on the adhesive layer is calculated using Eqn. 1. In the second step, the stress intensity factors of the cracked panel are solved using the finite element alternating method which uses the same finite element mesh except the crack is not modeled explicitly. The shear traction on the cracked panel (transferred through the adhesive layer) calculated in Step 1 is converted to nodal force to be applied in Step 2. Since this shear traction accounts for



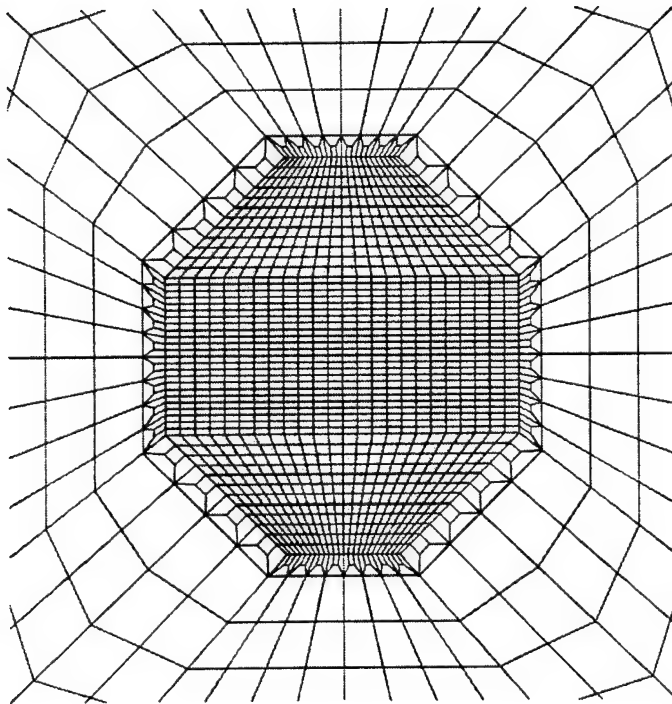


Figure 1.239: The finite element mesh of the composite patch on the aluminum panel

the "closing" force of the composite patch, only the cracked panel is required to be modeled in Step 2. Note that since finite element alternating method is used in Step 2, very fine mesh near the crack tip is not required.

The fatigue growth of a crack in general, can be calculated as a function of loading cycles. To take into account the effect of stress ratio, the Forman's crack growth equation [Forman, Kearney, and Engle (1967)] is used. This equation is given as

$$\frac{da}{dN} = \frac{C (\Delta K)^n}{(1-R) K_C - \Delta K} \quad (1.144)$$

Here  $a$  is the crack length,  $N$  is the number loading cycles,  $\Delta K$

is the range of the equivalent stress intensity factor, and  $R$  is the stress ratio in the cyclic loading. For 2024-T3 aluminum alloy, the values of,  $K_C = 91 \text{ MNm}^{-3/2}$  (83,000  $\text{psi}\sqrt{\text{in}}$ )  $C = 6.3 \times 10^{21} \text{ Pa}^{-2}$  ( $3 \times 10^{-13} \text{ psi}^{-2}$ ) and  $n = 3$  are used as given in Forman, Kearney, and Engle (1967). In general, a fatigue calculation involves the calculation of the number of cycles for a crack to grow to a specified length. Using a simple linear integration scheme to solve for the Eqn. 3, the fatigue life cycle of the crack is subdivided into a number of interval steps based on the finite element mesh. The total number of cycles is obtained by summing the values from each step.

To account for the temperature effect during the curing process, two analyses are required for each interval step of the fatigue crack growth analysis; one for the load applied at  $\sigma_{max}$  and the other is for the load applied at  $\sigma_{min}$ . In the numerical model, it is assumed that the cure would fully solidify at  $121^\circ\text{C}$  and the specimen would undergo fatigue cycling between  $\sigma_{min}$  at  $T_1$  temperature and

$\sigma_{max}$  at  $T_2$  temperature. Due to the difference in the coefficient of thermal expansion,  $\alpha_L$ , between the boron/epoxy patch and the aluminum panel, residual stresses would be induced on the repaired area when the temperature of the specimen differ from the cure temperature. And these residual stresses, which is dependent upon the temperature of the specimen, would be superimposed with the mechanical loading applied on the specimen. Hence, in this numerical model, both the mechanical loading as well as the loading induced by thermal cycling are accounted for in the fatigue crack growth analysis. It is to be noted here that even if the specimens were to undergo fatigue cycling at a constant temperature where  $T_1 = T_2$  (which is the case in the comparison analysis with the experiment performed by Denny (1995)), the drop in temperature after the curing process must be accounted for to properly model the fatigue crack growth of the specimens. Though

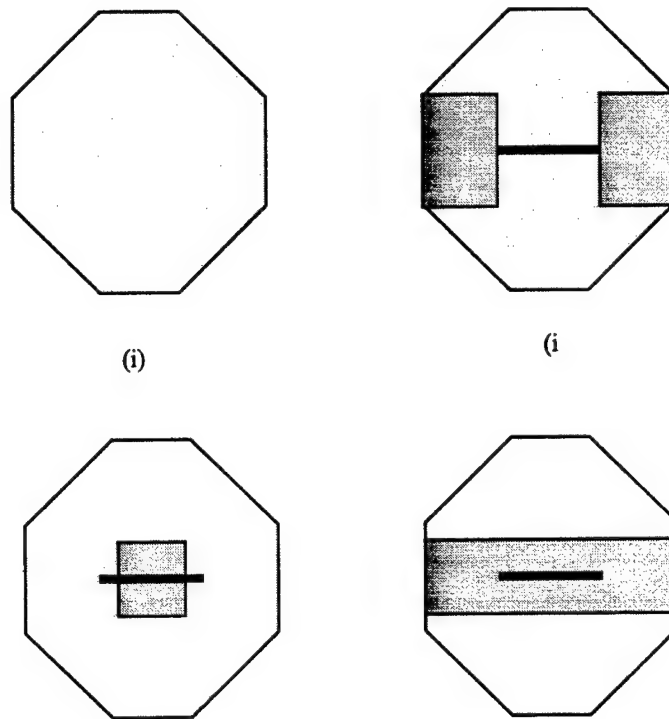


Figure 1.240: Disbond configuration types (i) a completely bonded patch (CBP); (ii) crack tip disbonds (CTD); (iii) a center disbond (CD); and (iv) a full width disbond (FWD)

is not effected by the temperature drop after the curing process (because the fatigue cycle is at a constant temperature), the ratio of stress intensity factor,  $R = K_{min}/K_{max}$ , would be affected by this temperature drop. Because of the boron/epoxy patch has a much smaller  $\alpha_L$  than the aluminum panel, the patch contracts much less than the panel when the temperature drops. The residual stresses generated would cause the crack surface to open resulting a higher stress intensity factor and hence a higher stress ratio  $R$ . This higher stress ratio,  $R$ , would cause a faster crack growth in the Forman's crack growth equation [Eq. 1.144].

### Results

#### Comparison of Numerical Result with Experimental Data

This study involves the analyses of four different intentional disbond configurations as shown in Fig. 1.240: (i) a completely bonded patch (CBP); (ii) crack tip

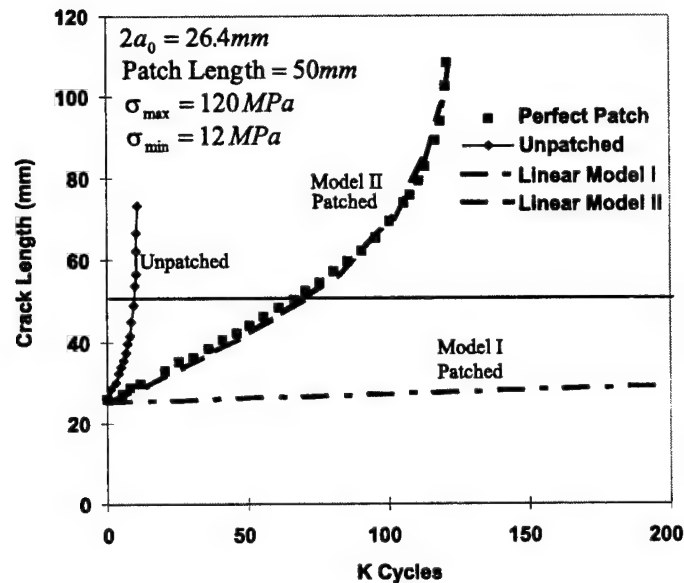


Figure 1.241: Comparison of results from numerical model I and II with the experimental data for completely bonded patch (CPB)

disbonds (CTD) at both ends of the crack; (iii) a center disbond (CD) over the crack length; and (iv) a full width disbond (FWD) extending the full width of the patch and covering the crack. In some of the configurations listed above, disbond areas of 20%, 10%, and 5% of the total bond area of the patch were investigated. These specimens would undergo fatigue cycling at room temperature, 20°C.

In the first configuration, there is no disbond on the patch repair. As has been determined from the Denny's experiment, the fatigue life of a perfectly patched specimen is about ten times longer than the unpatched specimen as shown in Fig. 1.241. However, using the material data provided in Denny (1995), it was found that the predicted fatigue life differs considerably from the experiment data for Specimen 20. In the numerical model of the completely bonded patch (CPB), the predicted fatigue crack growth is notably slower than the experimental result, approximately by a factor of five (shown in Fig. 1.241 as linear model I). Since the material data for the boron/epoxy laminate and the aluminum panel are considered to be quite reliable, it would be easy to conclude that either the adhesive model or the material data for the adhesive film is not accurate. By simple trial and error, it was found that by reducing the shear stiffness,  $K_{ADHE}$ , of the adhesive layer, the predicted fatigue growth curve would correspond very well to the experimental result

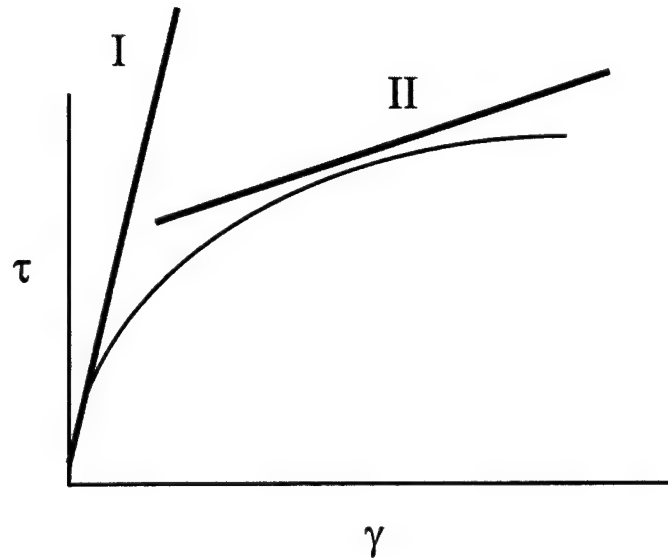


Figure 1.242: The nonlinear material behavior of adhesive layer where the shear modulus is strongly dependent on the shear strain

as shown in Fig. 1.241 as linear model II. In this model, the adhesive stiffness,  $K_{ADHE} = 0.2 \times 10^{12} \text{Pa/m}$  ( $0.73 \times 10^6 \text{psi/in}$ ), is an order of magnitude less than the adhesive stiffness calculated from the material data,  $K_{ADHE} = 2.9 \times 10^{12} \text{Pa/m}$  ( $10.6 \times 10^6 \text{psi/in}$ ). The reason for the difference in the adhesive stiffness between these two models can be partly attributed to the fact that the shear modulus of a soft adhesive tends to be strongly nonlinear. In most cases, the shear modulus directly obtained from experiments is valid only for very small shear strain. However, the adhesive layer on the composite patch may undergo a much higher shear strain and hence has a much lower shear modulus as shown in Fig. 1.242. Nonetheless, a simple linear approximation (to the slope of the nonlinear stress-strain level at the current average operating stress level in the adhesive) seems to be sufficient in predicting the fatigue response of a bonded repair.

Unlike the Rose's model which is only valid when the crack is well within the size of the patch, the numerical model based on the finite element alternating method was able to predict the fatigue response when the crack grows within the size of the patch as well as when the crack grows outside of the patch. Fig. 1.243 plots the stress intensity factor,  $K_I$ , as a function of the crack length calculated (i) based on the finite element alternating method (FEAM) and (ii) based on the Rose's model. In this figure, both models are based on the same adhesive stiffness,  $K_{ADHE}$

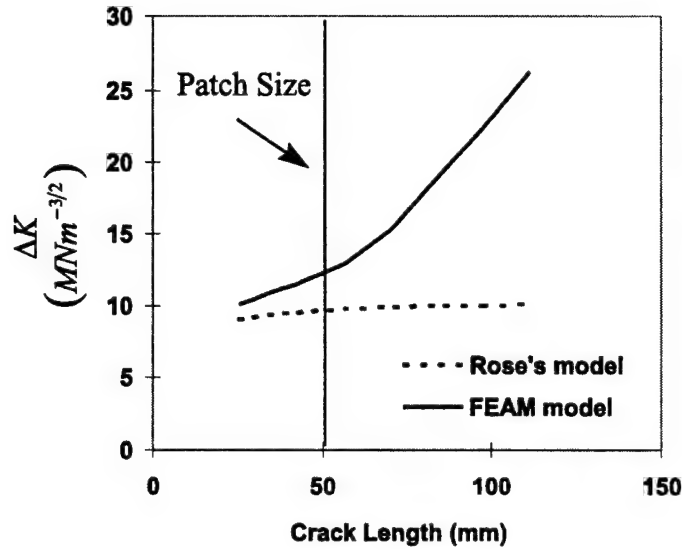


Figure 1.243: The stress intensity factor as a function of crack length for FEAM and Rose's models

(material model II). As shown in Fig. 1.243, when the crack size is small relative to the patch, the difference between these two models is about 10%. However, as the crack grows longer, the difference between these two models increases substantially, especially when the crack tip grows beyond the boundary of the patch. The difference between these two models is magnified even greater on the fatigue curve plotted in Fig. 1.244. It is to be noted here that one of the assumptions in Rose's model<sup>3</sup> as is the characteristic load-transfer length,  $\Lambda$ , is not satisfied in this analysis. To obtain the asymptotic behavior of a crack under a composite patch, Rose had to assume that the load-transfer length has to be significantly smaller than the size of patch:

$$\Lambda = \left[ \frac{G_{adhe}}{t_{adhe}} \left( \frac{E_{patch}t_{patch} + E_{panel}t_{panel}}{E_{patch}t_{patch} - E_{panel}t_{panel}} \right) \right]^{1/2} \ll h_{patch} \quad (1.145)$$

where  $E$  is the elastic modulus and  $h_{patch}$  is the height of the composite patch.

As described in the earlier section, the curing process of the composite patch on the aluminum panel has been modeled. Due to the incompatibility of the coefficient of thermal expansion between the boron/epoxy patch and the aluminum panel, residual stresses would be induced when the temperature is dropped after the curing process. Fig. 1.245 shows the contour plot of the residual stress,  $\sigma_{22}$ , on the aluminum panel generated after the panel has been cooled from the cure tempera-

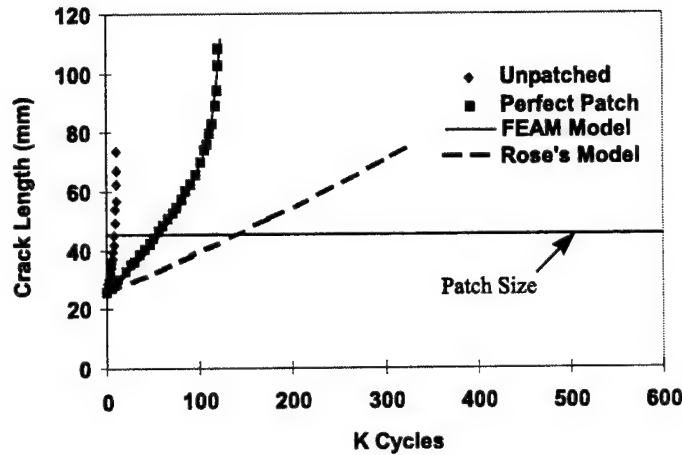


Figure 1.244: Fatigue response based on FEAM and Rose's models

ture of 121°C to the room temperature, 20°C. The deformed shape in Fig. 1.245 has been magnified by a factor of 100. Since the panel contracts much more than the composite patch, the crack surfaces would be opened by the residual stress generated and hence resulting high stress concentrations on the crack tips as shown in Fig. 1.245.

Unlike the Rose's model where disbonds cannot be modeled, the FEAM is used to predict the fatigue response of partially bonded patches. Using the adhesive stiffness obtained from the perfect patched specimen, the fatigue response of a composite patch with crack tip disbonds (CTD) is analyzed. In this configuration, two specimens were tested; Specimen 6 and 7. In both specimens, the disbond area is 20% of the patch area. Fig. 1.246 shows that the predicted fatigue curve correlates very well the experimental data from Specimen 6 and 7. Even though the disbond areas on both crack tips are quite large, both the analysis and the experiment show that the fatigue life of the specimens would be reduced by no more than 20%.

In the next analysis, the fatigue crack growth of specimens with a center disbond is evaluated. Specimen 16 has a disbond area of 10% and Specimen 17 has a disbond area of 5%. Fig. 1.247 shows that the fatigue responses predicted with FEAM agree quite well with the experimental data from Specimen 16 and 17. The predicted number of cycles to failure for Specimens 16 and 17 are 99,411 and 114,707 respectively. These results correspond well with the experimental data where the number of cycles to failure for Specimens 16 and 17 are found to be 92,624 and 116,817 respectively. Since the fatigue life of Specimen 16 (center dis-

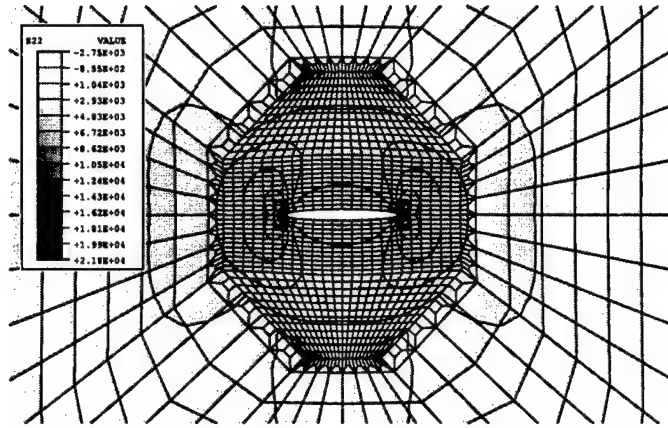


Figure 1.245: Contour plot of the residual stress,  $\sigma_{22}$ , due to the curing process

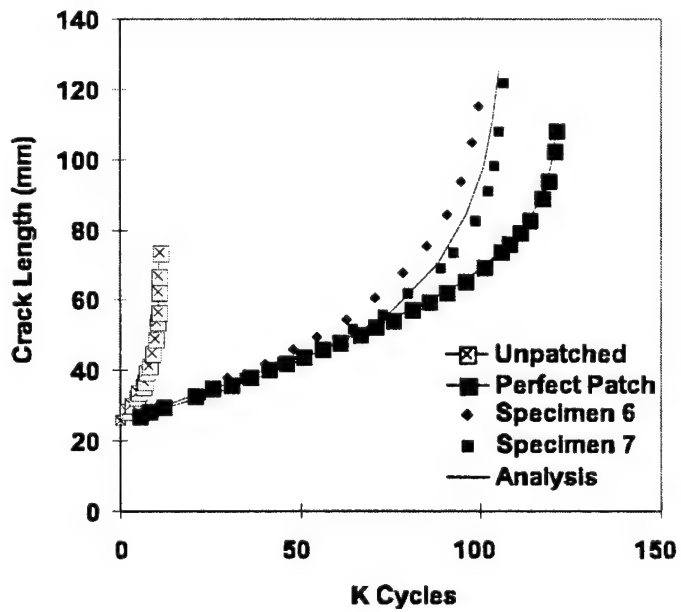


Figure 1.246: Comparison of numerical result with experimental data for Crack Tip Disbond (CTD)



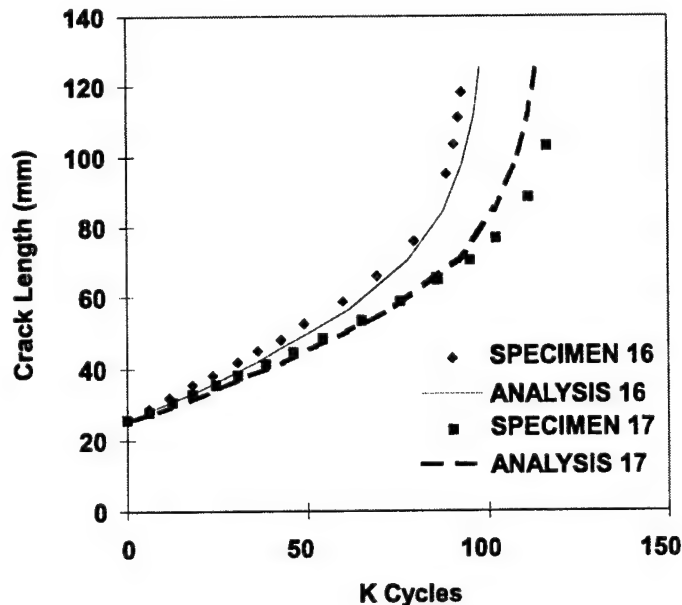


Figure 1.247: Comparison of numerical result with experimental data for Crack Disbond (CD)

bond with disbond area of 10%) is less than the Specimen 6 or 7 (crack tip disbond with disbond area of 20%), it can be inferred that the effectiveness of the composite patch is more sensitive to the disbands located at the center of the crack rather than the disbands located at the crack tips.

Four full width disbond (FWD) specimens have been investigated by Denny; Specimens 4, 5, 11 and 14. These specimens have disbond areas of 20% (for Specimen 4 & 5), 10% (for Specimen 11), and 5% (for Specimen 14). The numerical analysis seems to provide good correlation with the experiment when the disbond area is small. However, for specimens with larger disbond area, the numerical solution seems to over predict the reduction in the fatigue life as shown in Fig. 1.248. The predicted number of cycles to failure for Specimens 4, 5, 11 and 14 are 73,404, 73,404, 95,048 and 115,108 respectively. These results correspond with the experimental data where the number of cycles to failure for Specimens 4, 5, 11 and 14 are found to be 86,995, 82,324, 97,278 and 114,423 respectively.

To summarize the ability of finite element alternating method in predicting the fatigue response of partially bonded patch repair, the predicted results are displayed along with experimental data on a bar chart shown in Fig. 1.249. The parameters that are varied in these specimens include the disbond shape, the disbond area,

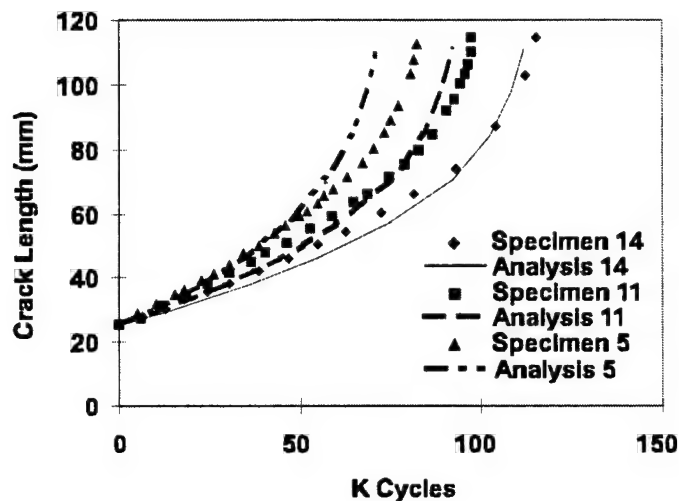


Figure 1.248: Comparison of numerical result with experimental data for full width disbond (FWD)

the initial crack length, the maximum applied stress, and the applied stress ratio. The details of each specimen are given in Tal. 1.26. Fig. 1.249 shows that overall, FEAM can effectively predict the fatigue life of the aluminum panels with partial bonded composite patch. The overall error of prediction is found to be 7.5%.

#### *Effect of Temperature Cycles*

In general, an aircraft would undergo a thermal cycle during each single flight. As the aircraft climbs to the cruising altitude, the air temperature can drop to less than  $-50^{\circ}\text{C}$ . However, when the aircraft is parked in a depot under a heated sun, the temperature can rise to  $70^{\circ}\text{C}$ . Since the boron/epoxy patch has a lower thermal expansion coefficient, the patch would contract much less than the aluminum panel when the air temperature drops. This induces a cyclic thermal tensile loading on the crack tip at a time when the mechanical stress is highest. In the current analysis, the sensitivity of the adhesive stiffness to the temperature is not considered, however as pointed out in the earlier section, the initial stresses due to the curing process (at  $121^{\circ}\text{C}$ ) are accounted for in this numerical model. Fig. 1.251 shows the fatigue response of a completely bonded patch (CBP) for Case I where the fatigue load is applied at room temperature, and Case II where the maximum load,  $\sigma_{max}$ , is applied at  $-50^{\circ}\text{C}$  and the minimum load,  $\sigma_{min}$ , applied at  $70^{\circ}\text{C}$ . As shown in Fig. 1.251, the fatigue life of the specimen undergoing the thermal cycles would be reduced by more than 60% when compared to the specimen loaded at room temperature. Furthermore, it

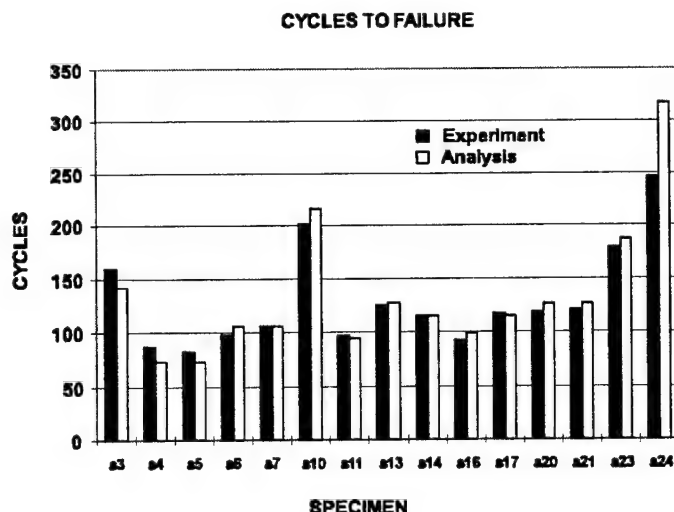


Figure 1.249: The predicted fatigue lives against the experimental data

was found that when crack tip disbond (CTD) is considered (where the disbond area is 20%), the fatigue life of the specimen undergoing the thermal cycles is further reduced by another 30% as shown in Fig. 1.250. In contrast, the fatigue life of the CTD specimen loaded at room temperature is reduced by no more than 20% when compared with a perfect patched specimen. This model seems to indicate that the specimen undergoing a typical thermal cycle would be more affected by partial disbond than the specimen loaded at constant temperature.

#### *Interaction of Two Composite Patches*

Given that cracks are sometimes found quite close to each other, it is important to study how two composite patches would interact with each other. In this section, two types of patch interaction are considered. In both configurations, the two patches are considered to be perfectly patched. In the first configuration, both patches would lie on the same horizontal line as shown in Fig. 1.252. When the patches are 100mm apart, there seems to be very little interactions between these two cracks. As shown in Fig. 1.253, the fatigue response of the specimen with two patches is quite similar to the specimen with a single patch. When the distant between the two patches is reduced to 25mm, similar fatigue response is found in which there is very little interactions between these two cracks as shown in Fig. 1.253.

In the second configuration, both patches would lie on the same vertical line as shown in Fig. 1.254. When the patches are 100mm apart, there seems to be very

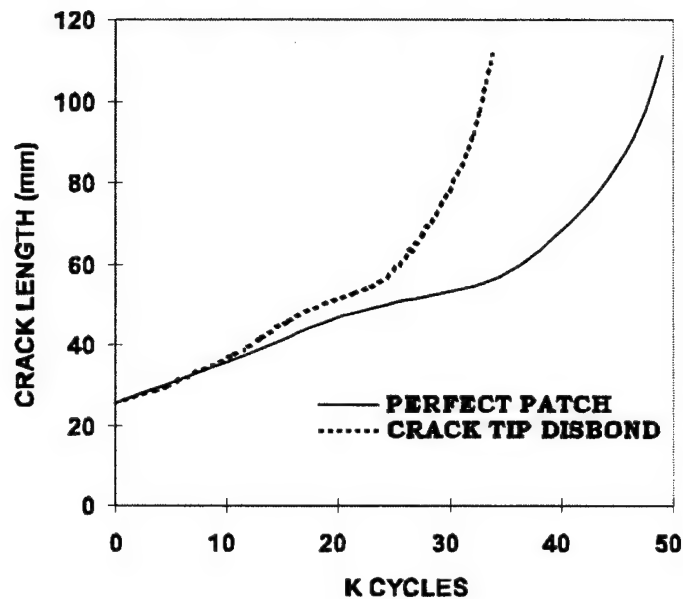


Figure 1.250: The fatigue life of the specimen undergoing the thermal cycles with Crack Tip Disbond (CTD)

little interactions between these two cracks as shown in Fig. 1.255. However, when the distant between the two patches is reduced to 25mm, the fatigue crack growth is slowed by a factor of three as shown in Fig. 1.255. Therefore, the specimen with two patches would have a longer fatigue life than the specimen with a single patch. However, it is possible that the metal in between the patches may fail in such situation; and this is not considered here.

### *Conclusion*

Numerical analyses based on the finite element alternating method have been performed on several cracked panels with partially bonded composite patches. The numerical results are compared with the experimental data obtained by Denny (1995) and the comparison indicates that the numerical results correlate quite well with the experimental data. Furthermore, a numerical study has been carried out to study the effect of high stress low temperature and low stress high temperature cycles. The result shows a very significant drop in the fatigue life when the specimen undergoes the thermal-fatigue cycle. This numerical result also shows that the specimen which undergoes the thermal-fatigue cycles is more sensitive to partial disbond than a specimen which undergoes the fatigue cycles at constant temperature. Further-

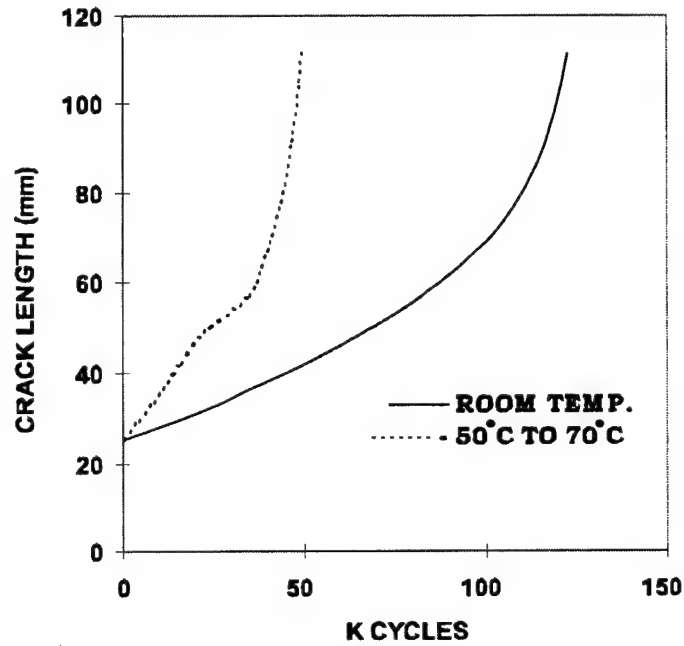


Figure 1.251: The fatigue response of a completely bonded patch (CBP) for Case I where the fatigue load is applied at room temperature, and Case II where the maximum load,  $\sigma_{max}$ , is applied at  $-50^{\circ}\text{C}$  and the minimum load,  $\sigma_{min}$ , applied at  $70^{\circ}\text{C}$

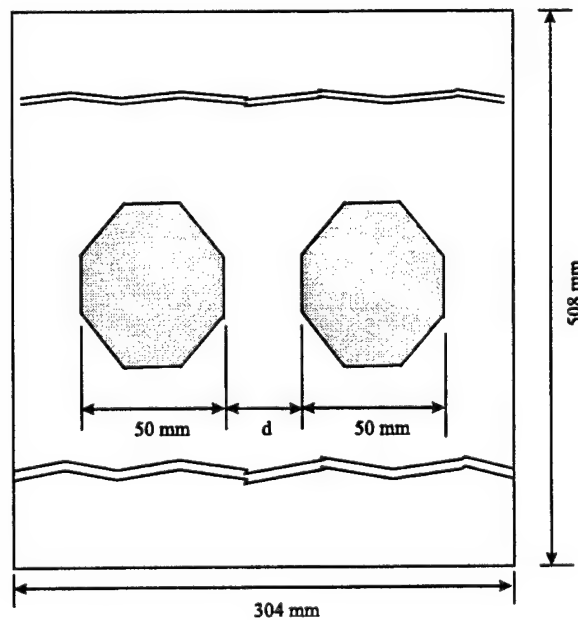


Figure 1.252: Geometry of the aluminum patch with two patches lying horizontally

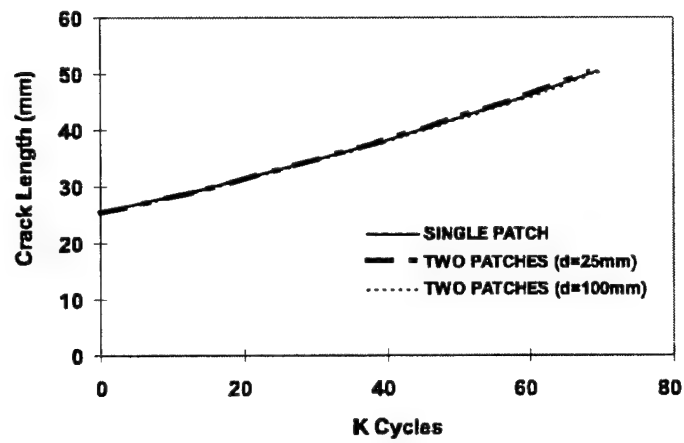


Figure 1.253: Interaction of two patches lying on a horizontal line

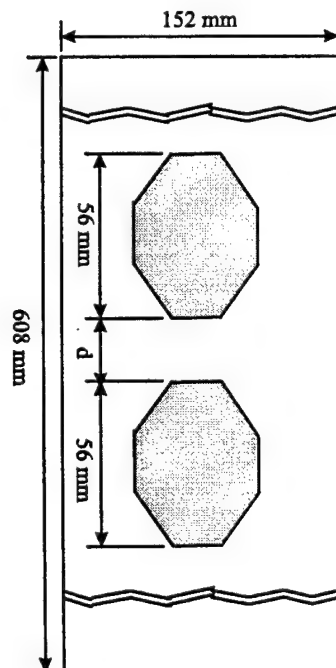


Figure 1.254: Geometry of the aluminum patch with two patches lying vertically

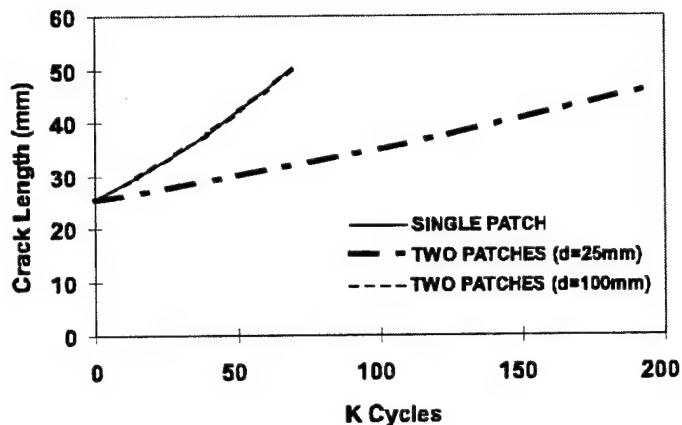


Figure 1.255: Interaction of two patches lying on a vertical line

more, numerical study has been carried out to examine the interaction between two nearby patches. It has been found that the interactions between two nearby patches do not reduce the fatigue life of the specimen.

### § 1.15 Fracture and Fatigue Analysis of Curved or Kinked Cracks Near Fastener Holes

Cracks emanating from fastener holes in a rivet lap joints of a fuselage do not always grow in a straight trajectory but sometimes do deviate and become moderately curved. Possible reasons for these cracks to kink out of a straight trajectory include material irregularity, unexpected impact-type loading, and in particular the misfit between the rivets in the fastener holes. This section presents a study of fracture and fatigue growth of moderately curved cracks emanating from fastener holes in a pressurized fuselage. Realistic geometric dimension and loading will be applied on the lap joints as well as the fastener holes. This study will determine how well a straight crack can be used to approximate a moderately curved crack in a MSD analysis.

Consider a central crack in an infinite body in which the normal of the crack makes a small angle with the direction of remote tensile loading as shown in Fig. 1.256. Since the crack is not perpendicular to the tensile loading, the asymptotic stress fields near the crack tip would demonstrate both mode I and mode II behavior. As a result of this mix-mode behavior, there is a tendency for the crack not to propagate tangent to the crack tip but with a kink angle from the crack di-

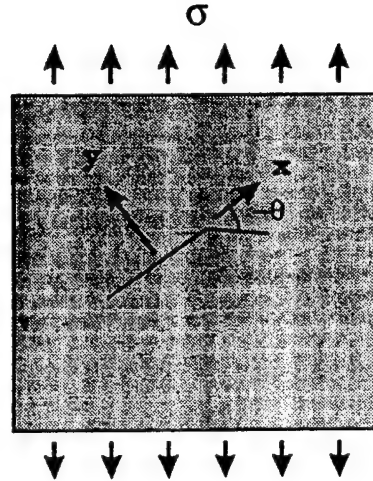


Figure 1.256: A central crack in a infinite body in which the normal of the crack makes a small angle with the remote tensile loading and the kinking of the crack by an angle  $\theta$  as result of the mixed-mode loading.

rection. In this study, the criterion based on the investigation by Erdogan and Sih (1963) is used to predict the kink angle. This criterion assumes the crack will grow in the direction where the singular circumferential stress near the crack tip is maximum. The relation between the kink angle,  $\theta$ , and the stress intensity factors,  $K_I$  and  $K_{II}$ , is given as

$$K_I \left[ \sin \frac{\theta}{2} + \sin \frac{3\theta}{2} \right] + K_{II} \left[ \cos \frac{\theta}{2} + \cos \frac{3\theta}{2} \right] = 0 \quad (1.146)$$

This criterion also assumes that the crack will fracture when the maximum circumferential stress of the mix-mode fracture matches the equivalent circumferential stress of a pure mode I fracture. As a result, the equivalent stress intensity factor used in the fracture and fatigue analysis becomes

$$K_I^{eq} = K_I \left[ \frac{3}{4} \cos \frac{\theta}{2} + \frac{1}{4} \cos \frac{3\theta}{2} \right] - K_{II} \left[ \frac{3}{4} \sin \frac{\theta}{2} + \frac{3}{4} \sin \frac{3\theta}{2} \right] \quad (1.147)$$

This equation would satisfy the condition that  $K_I^{eq} = K_I$  if the crack propagation is self-similar that is, the kink angle  $\theta = 0$ .

Having obtained the equivalent stress intensity factor, the fatigue growth of the curvilinear cracks emanating from the fastener holes can be calculated as a function



of loading cycles. To take into account the effect of stress ratio, the Forman's crack growth equation [Forman, Kearney, and Engle (1967)] is used. This equation is given by

$$\frac{da}{dN} = \frac{C (\Delta K)^n}{(1-R) K_C - \Delta K} \quad (1.148)$$

Here  $a$  is the crack length,  $N$  is the number loading cycles,  $\Delta K$  is the range of the equivalent stress intensity factor, and  $R$  is the stress ratio in the cyclic loading. For 2024-T3 aluminum alloy, the values of  $K_C = 83,000 \text{ psi } \sqrt{\text{in}}$ ,  $C = 3 \times 10^{-13} \text{ psi}^{-2}$  and  $n = 3$  are used as given in Forman, Kearney, and Engle (1967).

### § 1.15.1 A computational model

Consider a lap joint in a pressurized fuselage which holds two overlapping skins together with three rows of fastener as illustrated in Fig. 1.257. As a result of fatigue growth due to the pressurized cycle, multiple cracks would emanate from these fastener holes and is often found that some these cracks are slightly kinked. Singh, Park, and Atluri (1994b) have performed a global, intermediate and local analysis to obtain the load distribution near the fastener holes and found that the maximum cyclic hoop stress on the skin for a typical aircraft fuselage due to the pressure cycle would vary from 0 ksi to 13.5 ksi. In the load-transfer analysis between the two skins, they have found that the top row of the fasteners would carry the most load (35% of the total load) in comparison with the middle and bottom rows. Using this load data, the present study would model a single fastener hole with two cracks of equal length under periodic boundary conditions as illustrated in Fig. 1.258. At the maximum applied loading state, the fastener accounts for 35% of the total load and the contact normal stress due to the fastener is approximated with

$$\sigma_r = \frac{2.6\sigma W}{\pi R} \sin \theta \quad (1.149)$$

where  $W$  is half of the distance between the holes, and  $R$  is the radius of the holes. The geometric dimensions of the model are as follow:  $2W = 1.2 \text{ in}$ ,  $2R = 0.1875 \text{ in}$ , the height of the model is  $2H = 1.5 \text{ in}$ , and the crack length emanating from the hole is  $2a = 0.2625 \text{ in}$ . Three sets of initial cracks are considered; the first set of initial cracks are straight, the second set of initial cracks kinked upward with the initial kink angle being  $+30$  and the third set of initial cracks kinked downward with the initial kink angle being  $-30$  as illustrated in Fig. 1.259. Due to the symmetry condition that exist in the specimen as well as the loads, only half of the specimen is modeled with finite element method. The half model of

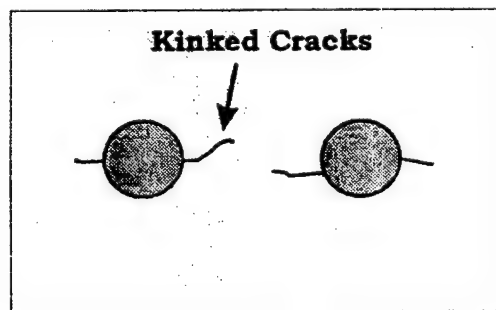
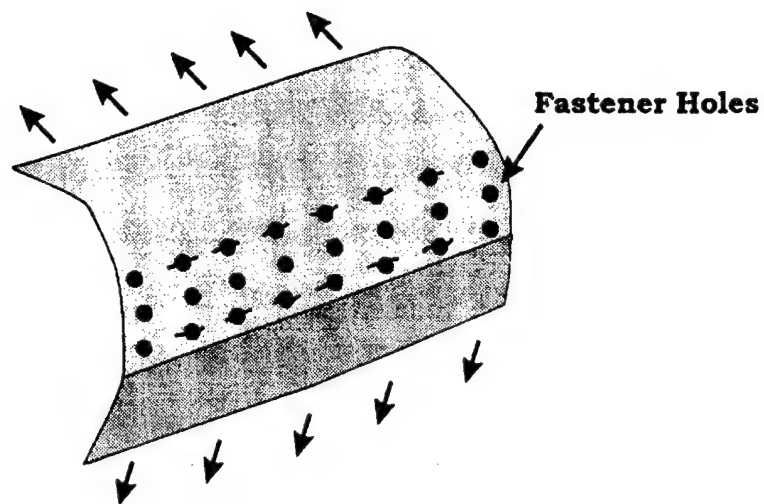


Figure 1.257: Multiple Site Damage problem in a lap-splice joint in which some of the cracks are moderately kinked.

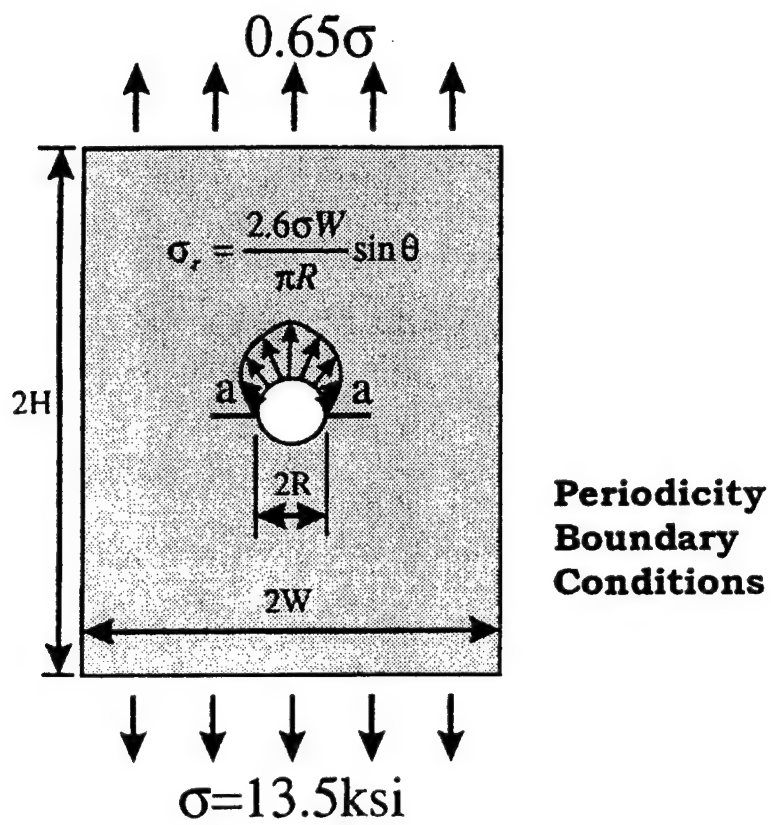
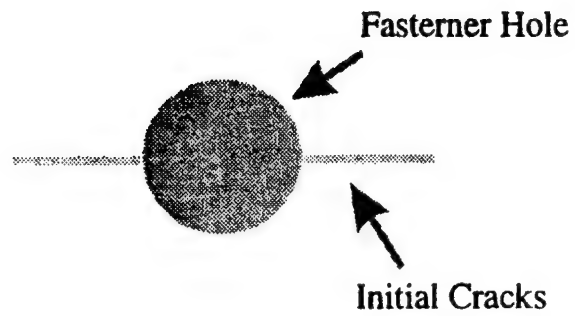
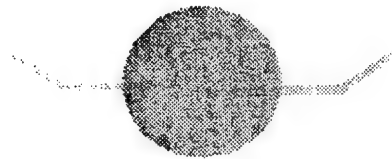


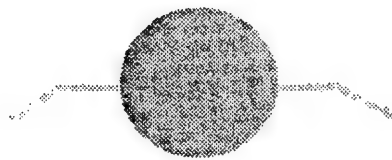
Figure 1.258: Two cracks of equal length emanating from the fastener hole.



(a) Initial kink angle=0



(b) Initial kink angle=+30



(c) Initial kink angle=-30

Figure 1.259: Cracks emanating from the fastener hole with the initial kink angle of 0, +30, and -30 degree

the 30 kinked crack under plane stress condition is discretized with isoparametric quadratic elements as shown in Fig. 1.260.

Using Eq.?? through ?? and 1.147, the mixed-mode stress intensity factors as well as the equivalent stress intensity factor of the crack tip are calculated and listed in Tab. 1.27. The result shows that even when the crack emanating from the fastener hole is straight, mode II behavior is not negligible as the ratio  $K_I/K_{II} = -0.04$ . However, the calculated result also shows that the equivalent stress intensity factor and the stress intensity factor for mode I of the straight crack have the same value. This would mean that the prediction of fracture for the case of initial kink angle=0 can be solely based on the value of  $K_I$ . Therefore, the alternating method can be effectively used in the fracture analysis of straight cracks for MSD problem even though it can only calculate the value of  $K_I$  and not  $K_{II}$ . Furthermore, the result from Tab. 1.27 also shows that the equivalent stress intensity factors,  $K_I^{eq}$ , for the initial kink angle of +30 and -30 are within 2% of  $K_I$  for the initial kink angle of 0. Hence, the alternating method can still be effectively used to perform the fracture analysis for moderately curved cracks by using the fracture solution which assumes the cracks to be straight.

In addition to the fracture analysis, this study also include the fatigue analysis of these moderately kinked cracks. The crack's trajectory is computed using Eq. 1.146 and the crack growth propagation for the initial kink angle of +30 is shown in Fig. 1.261. The figure shows that as the crack propagates, the crack tends to straighten out and resemble a straight crack. As the crack grows, the stress intensity factors of the crack tip are calculated. Fig. 1.262 shows that the calculated equivalent stress intensity factors,  $K_I^{eq}$ , for the initial kink angle +30 and -30 are very close to the mode I stress intensity factor,  $K_I$ , for initial kink angle 0. Based on the calculated stress intensity factor and the Forman's crack propagation equation, Eq. 1.148, the fatigue life of each specimen is calculated. Since the equivalent stress intensity factors of all three specimens are very close to each other, it is expected that the fatigue life of the specimens with kinked cracks is very close to the fatigue life of the specimen with straight crack;  $N_{+30}/N_{+0} = 0.984$  and  $N_{-30}/N_{+0} = 0.991$ . As a result, it can be argued that the alternating method can be used to perform the fatigue analysis for moderately curved cracks by using the solution which assumes straight cracks.

The present study also include the example of two fastener holes in which the kink angle of the cracks emanating from the left and right holes are +30 and -30 respectively as shown in Fig. 1.263. The loading and boundary conditions of this specimen is similar to the specimens of a single hole described earlier. It is found

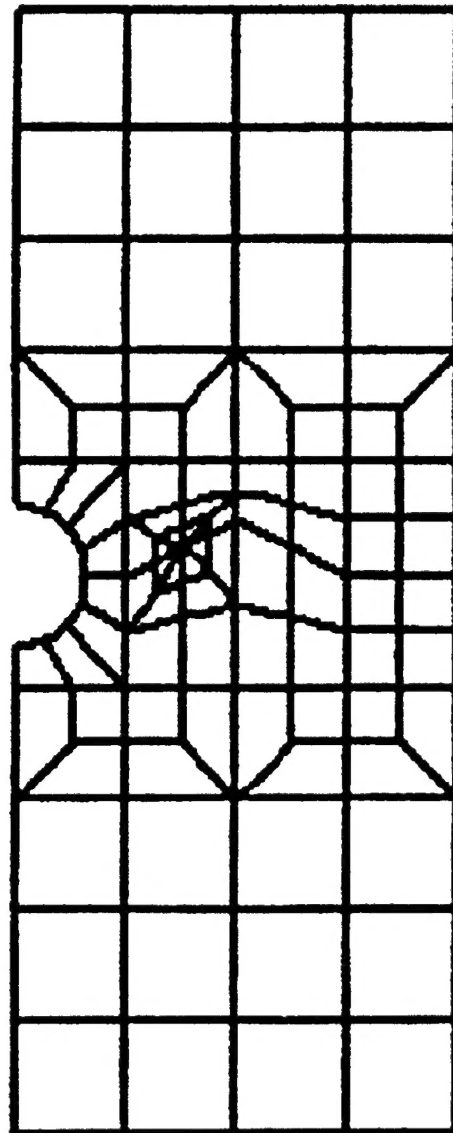


Figure 1.260: Half model of the +30 degree kinked cracked discretized with 8 noded isoparametric elements.

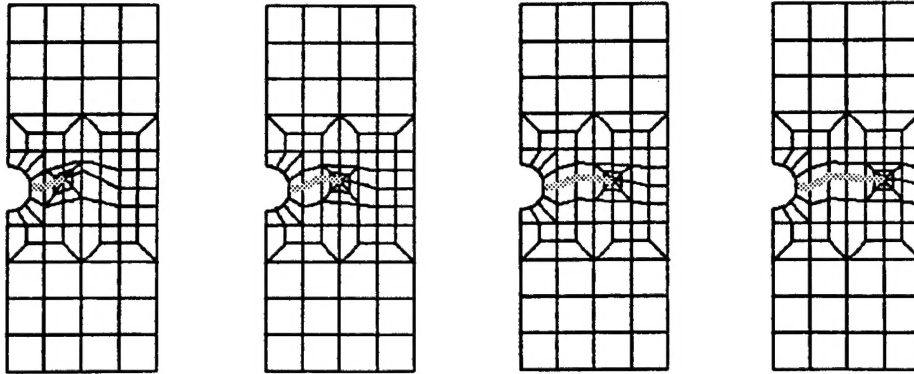


Figure 1.261: Crack growth analysis of the 30 degree kinked crack.

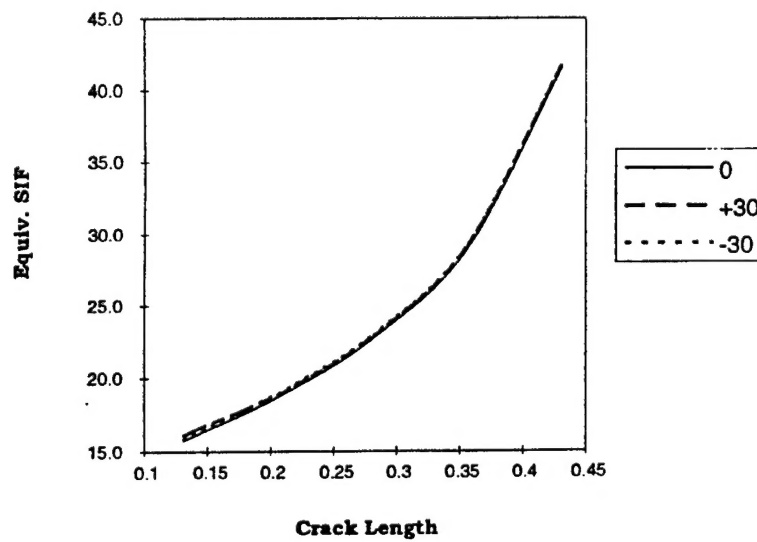


Figure 1.262: The equivalent stress intensity factor of the initial kinked angles of  $+30^\circ$  and  $-30^\circ$  in comparison to a straight crack with initial kinked angle of  $0^\circ$ .

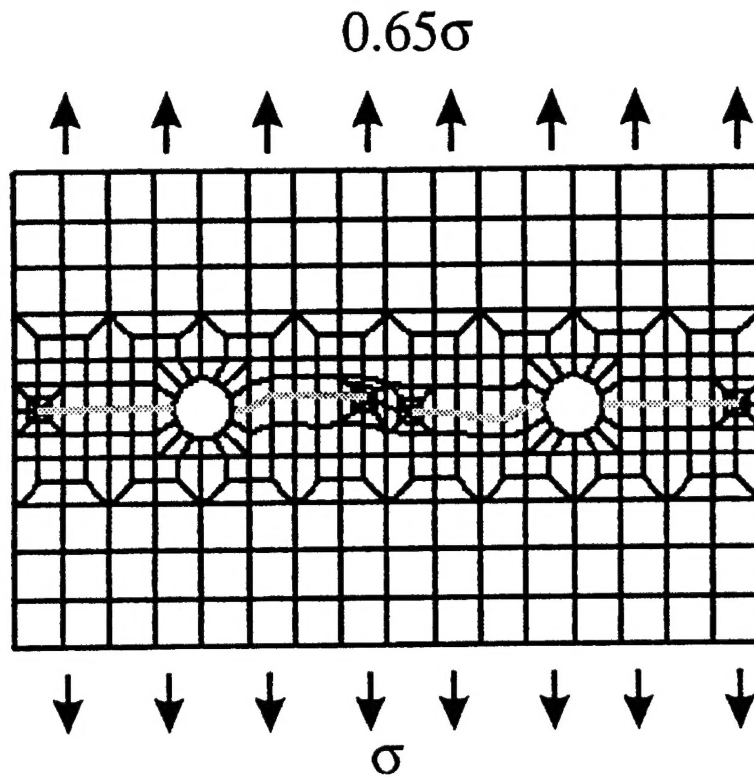


Figure 1.263: Fatigue crack growth near two fastener holes under uniaxial load with the initial kink angle of the cracks emanating from the left and right holes being  $+30$  and  $-30$  degrees respectively.

that the fatigue life of this specimen with kinked cracks are very close to the fatigue life of a specimen with straight cracks;

$N_{KINK}/N_{STRAIGHT} = 0.976$ . The study also include another similar example of two fastener holes with kinked cracks but loaded in both directions as shown in Fig. 1.264. Using the approximation of a pressurized tube, the applied longitudinal stress is assumed to be a quarter of the applied hoop stress. Again, it is found that the fatigue life of this specimen with kinked cracks are very close to the fatigue life of a specimen with straight cracks;  $N_{KINK}/N_{STRAIGHT} = 0.973$ .



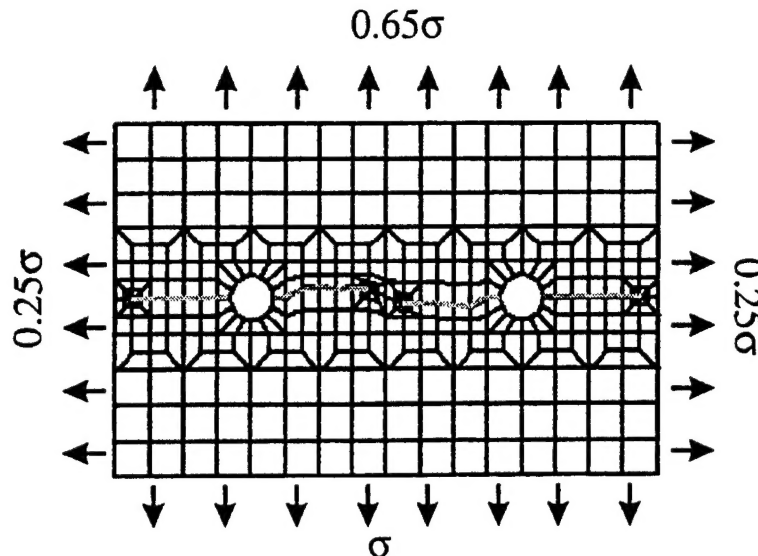


Figure 1.264: Fatigue crack growth near two fastener holes under biaxial load with the initial kink angle of the cracks emanating from the left and right holes being +30 and -30 degrees respectively.

### § 1.15.2 Conclusion

The present analysis has shown that the fracture and fatigue life for a slightly kinked crack near a fastener hole can be very well approximated using the stress intensity factor for pure mode I behavior obtained by replacing the slightly kinked cracks with simple straight cracks. Henceforth, the alternating method can be applied in modeling moderately curved cracks that often exist in Multiple Site Damage problem, and therefore significantly reduce and simplify the fracture and fatigue analysis of such problem.

### § 1.16 Interaction of Engine Rotor Fragments with Containment Structures

#### § 1.17 Finite Element Analysis of Engine Rotor Failure and Containment

The complex dynamical interactions among failed rotor fragments and the engine containment structure is studied by the finite element method. DYNA3D is used for the finite element analysis which is an explicit, three-dimensional, transient finite element code. A number of different rotor fragments are considered for this study